

# Design and Control of an Ergonomic Wearable Full-Wrist Exoskeleton for Pathological Tremor Alleviation

Jiamin Wang

Dissertation submitted to the Faculty of the  
Virginia Polytechnic Institute and State University  
in partial fulfillment of the requirements for the degree of

Doctor of Philosophy  
in  
Mechanical Engineering

Oumar R. Barry, Chair

Andrew J. Kurdila

Corina Sandu

Sujith Vijayan

Lei Zuo

December 1, 2022

Blacksburg, Virginia

Copyright 2023, Jiamin Wang

# Design and Control of an Ergonomic Wearable Full-Wrist Exoskeleton for Pathological Tremor Alleviation

Jiamin Wang

(ABSTRACT)

Activities of daily living (ADL) such as writing, eating, and object manipulation are challenging for patients suffering from pathological tremors. Pathological tremors are involuntary, rhythmic, and oscillatory movements that manifest in limbs, the head, and other body parts. Among the existing treatments, mechanical loading through wearable rehabilitation devices is popular for being non-invasive and innocuous to the human body. In particular, a few exoskeletons are developed to actively mitigate pathological tremors in the forearm. While these forearm exoskeletons can effectively suppress tremors, they still require significant improvements in ergonomics to be implemented for ADL applications. The ergonomics of the exoskeleton can be improved via design and motion control pertaining to human biomechanics, which leads to better efficiency, comfort, and safety for the user.

The wrist is a complicated biomechanical joint with two coupled degrees of freedom (DOF) pivotal to human manipulation capabilities. Existing exoskeletons either do not provide tremor suppression in all wrist DOFs, or can be restrictive to the natural wrist movement. This motivates us to explore a better exoskeleton solution for wrist tremor suppression. We propose TAWA - a wearable exoskeleton that provides alleviation of pathological tremors in all wrist DOFs. The design adopts a 6-DOF rigid linkage mechanism to ensure unconstrained natural wrist movements, and wearability features without extreme tight-binding or precise positioning for convenient ADL applications.

When TAWE is equipped by the user, a closed-kinematic chain is formed between the exoskeleton and the forearm. We analyze the coupled multibody dynamics of the human-exoskeleton system, which reveals a few robotic control problems - (i) The first problem is the identification of the unknown wrist kinematics within the closed kinematic chain. We realize the real-time wrist kinematic identification (WKI) based on a novel ellipsoidal joint model that describes the coupled wrist kinematics, and a sparsity-promoting Extended Kalman Filter for the efficient real-time regression; (ii) The second problem is the exoskeleton motion control for tremor suppression. We design a robust adaptive controller (IO-RAC) based on model reference adaptive control and inverse optimal robust control theories, which can identify the unknown model inertia and load, and provide stable tracking control under disturbance; (iii) The third problem is the estimation of voluntary movement from tremorous motion data for the motion planning of exoskeleton. We develop a lightweight and data-driven voluntary movement estimator (SVR-VME) based on least square support vector regression, which can estimate voluntary movements with real-time signal adaptability and significantly reduced time delay.

Simulations and experiments are carried out to test the individual performance of robotic control algorithms proposed in this study, and their combined real-time performance when integrated into the full exoskeleton control system. We also manufacture the prototype of TAWE, which helps us validate the proposed solutions in tremor alleviation exoskeletons. Overall, the design of TAWE meets the expectations in its compliance with natural wrist movement and simple wearability. The exoskeleton control system can execute stably in real-time, identify unknown system kinematics and dynamics, estimate voluntary movements, and suppress tremors in the wrist. The results also indicate a few limitations in the current approaches, which require further investigations and improvements. Finally, the proposed exoskeleton control solutions are developed based on generic formulations, which can be applied to not only TAWE, but also other rehabilitation exoskeletons.

# Design and Control of an Ergonomic Wearable Full-Wrist Exoskeleton for Pathological Tremor Alleviation

Jiamin Wang

(GENERAL AUDIENCE ABSTRACT)

Activities of daily living (ADL) such as writing, eating, and object manipulation are challenging for patients suffering from pathological tremors, which affect millions of people worldwide. Tremors are involuntary, rhythmic, and oscillatory movements. In recent years, rehabilitation exoskeletons are developed as non-invasive solutions to pathological tremor alleviation. The wrist is pivotal to human manipulation capabilities. Existing exoskeletons either do not provide tremor suppression in all wrist movements, or can be restrictive to natural wrist movements. To explore a better solution with improved performance and ergonomics, we propose TAWE - a wearable exoskeleton that provides tremor alleviation in full wrist motions. TAWE adopts a high-degree-of-freedom mechanism to ensure unconstrained natural wrist movements, and wearability features for convenient ADL applications. The coupled dynamics between the forearm and TAWE leads to a few robotic control problems. We propose novel real-time robotic control solutions in the identification of unknown wrist kinematics, robust adaptive exoskeleton control for tremor suppression, and voluntary movement estimation for motion planning. Later, simulations and experiments validate the TAWE prototype and its exoskeleton control framework for tremor alleviation, and reveal limitations in the current approaches that require further investigations and improvements. Finally, the proposed exoskeleton control solutions are developed based on generic formulations, which can be applied to not only TAWE, but also other rehabilitation exoskeletons.

# Dedication

*To My Parents, My Grandparents, and My Love Ms. Wu, Fan.*

*“The greatest virtue is like water, nourishing all things gently and competing with none.  
Water is content to be in low places not sought by people, and therefore, being closer to the  
truth of the world...” - Laozi*

# Acknowledgments

I would like to express my utmost gratefulness to my Ph.D. advisor, Dr. Oumar Barry, for his teaching, guidance, insights, encouragement, and support throughout my study. Dr. Barry has also been a life mentor who constantly cares about me, and inspires me to be better in both work and life.

I would like to sincerely thank the members of my Ph.D. committee, Dr. Andrew Kurdila, Dr. Corina Sandu, Dr. Sujith Vijayan, and Dr. Lei Zuo for their teaching, insights, and supports that help me greatly improve my work.

I am deeply grateful to Dr. Sunit Gupta, Dr. Mohammad Bukhari, Raghuraj Chauhan, Andrew Choi, Zijian Ding, and other members of the VibRo Lab for their help and support in my research and daily life.

I would like to thank Dr. Hailin Ren, Dr. Yujiong Liu, Dr. Xinyue Wang, Dr. Yuan Li, and other friends at Virginia Tech who journeyed with me in this challenging and rewarding Ph.D. "odyssey". I would also like to thank the Mechanical Engineering and Physics Departments at Virginia Tech, and the NSF Grant for partially funding my study.

I was not able to visit home during my Ph.D. study. However, I can always feel the love and support from my family. My special thanks go to my parents, Ningjun Wang and Hong Liu, who constantly care about me and support me to pursue my dream. I would also like to extend my deep appreciation to my aunt, Wei Liu, and cousins, Michelle Wang and Joanna Wang, for being by my side all this time.

Finally, my special gratitude goes to my girlfriend, Fan Wu, for your love and support at the highest and lowest points of my life. I love you and I cannot wait to be by your side again.

# Contents

<b>List of Figures</b>	<b>xiv</b>
<b>List of Tables</b>	<b>xx</b>
<b>Nomenclature</b>	<b>xxi</b>
<b>1 Introduction</b>	<b>1</b>
1.1 Background - Pathological Tremors . . . . .	2
1.1.1 Pathophysiologies and Symptoms . . . . .	2
1.1.2 Surgical, Pharmacological and Therapeutic Treatments . . . . .	4
1.1.3 Summary . . . . .	5
1.2 Background - Tremor Control via Exoskeletons . . . . .	5
1.2.1 Forearm Motions and Wrist Anatomy . . . . .	6
1.2.2 Forearm Tremor Rehabilitation Exoskeletons . . . . .	8
1.2.3 Tremor Signal Processing and Prediction . . . . .	9
1.2.4 Summary . . . . .	11
1.3 Motivations . . . . .	11
1.3.1 Wearable Exoskeleton Design for Full-Wrist Actuation . . . . .	12
1.3.2 Control Problems . . . . .	13

1.4	Research Objectives . . . . .	16
1.5	Organization of the Dissertation . . . . .	17
<b>2</b>	<b>Tremor Alleviating Wrist Exoskeleton &amp; Human-Exoskeleton Dynamics</b>	<b>19</b>
2.1	Design Considerations . . . . .	20
2.1.1	Mechanism and Wearability . . . . .	21
2.1.2	Sensors and Actuators . . . . .	23
2.2	Coupled Kinematics of TAWWE and the Wrist . . . . .	24
2.2.1	3D Kinematic Transformation . . . . .	25
2.2.2	Kinematics of TAWWE . . . . .	27
2.2.3	Kinematics of the Wrist . . . . .	28
2.2.4	Nonholonomic Kinematic Constraints . . . . .	32
2.3	Human-Exoskeleton Multibody Dynamics . . . . .	34
2.3.1	Coupled Dynamical Model . . . . .	35
2.3.2	Base Excitation and Actuation . . . . .	38
2.3.3	Numerical Modeling Validation . . . . .	41
2.3.4	Workspace and Controllability . . . . .	42
2.4	Summary . . . . .	45
<b>3</b>	<b>Real-Time Wrist Kinematics Identification</b>	<b>47</b>
3.1	Ellipsoidal Joint Model for Wrist Kinematics . . . . .	48

3.1.1	Relationship to Sequential Rotational Joints . . . . .	50
3.1.2	Ellipsoid-Based Translational Constraints . . . . .	51
3.1.3	General Model for Wrist Kinematics Identification . . . . .	52
3.2	Real-Time Wrist Kinematics Identification . . . . .	55
3.2.1	Extended Kalman Filter . . . . .	56
3.2.2	Promoting Sparsity in Extended Kalman Filter . . . . .	58
3.2.3	The 6-DOF Wrist Motion Measurement Tool . . . . .	60
3.2.4	Wrist Kinematics Regression via Sparsity Promoting EKF . . . . .	63
3.3	Numerical Simulation . . . . .	64
3.3.1	Solutions of the Ellipsoidal Joint Model . . . . .	65
3.3.2	Parameter Identification via EKF . . . . .	67
3.3.3	Characteristics of FLC and SP-EKF . . . . .	69
3.4	Experimental Validation . . . . .	74
3.4.1	Regression Performance . . . . .	76
3.4.2	Analysis of the Identified Model . . . . .	79
3.5	Summary . . . . .	81
<b>4</b>	<b>Exoskeleton Control for Tremor Alleviation</b>	<b>82</b>
4.1	Tremor Dynamics and Assumptions . . . . .	83
4.1.1	Experimental Tremor Time Series Observation . . . . .	84

4.1.2	Frequency Components of Tremor . . . . .	87
4.2	Human-Exoskeleton Control System . . . . .	89
4.2.1	Control System based on Nonholonomic Outputs . . . . .	90
4.2.2	Uncertainties and Disturbances . . . . .	92
4.3	Model-Based Controller for Tremor Suppression . . . . .	94
4.3.1	Assumptions on User Control Input . . . . .	94
4.3.2	Model Reference Adaptive Controllers for Exoskeletons . . . . .	96
4.3.3	Inverse Optimal Robust Control Theory . . . . .	99
4.3.4	Inverse Optimal Robust Adaptive Controller . . . . .	101
4.3.5	Passive and Active Tremor Suppression . . . . .	103
4.4	Numerical Simulation . . . . .	104
4.4.1	Stationary Exoskeleton . . . . .	106
4.4.2	TAWA . . . . .	112
4.5	Summary . . . . .	116
<b>5</b>	<b>Voluntary Movement Estimation for Exoskeleton Motion Planning</b>	<b>118</b>
5.1	Voluntary movement estimation and Time-Delay . . . . .	119
5.1.1	Low-Pass Filtering of Voluntary Movement . . . . .	120
5.1.2	Adaptive Filtering with BMFLC . . . . .	122
5.2	Voluntary Movement Estimation via Support Vector Regression . . . . .	124

5.2.1	Least Square Support Vector Regression . . . . .	126
5.2.2	Recursive Kernel Matrix Inversion . . . . .	128
5.2.3	Delay Reduction in Voluntary Movement Estimation . . . . .	130
5.3	Numerical Analysis . . . . .	131
5.3.1	Synthesized Tremor Movement Signals . . . . .	132
5.3.2	Experimental Tremor Movement Signals . . . . .	137
5.4	Summary . . . . .	141
<b>6</b>	<b>Prototype, System Integration and Experiment</b>	<b>142</b>
6.1	Prototype of TAWÉ . . . . .	143
6.1.1	Design Updates . . . . .	143
6.1.2	Mechanism and Wearability . . . . .	145
6.2	Control System Integration . . . . .	150
6.2.1	Mechatronic System of TAWÉ . . . . .	151
6.2.2	Control Software on ROS2 . . . . .	152
6.2.3	Real-Time Exoskeleton Control Simulation . . . . .	154
6.3	Experimental Validations . . . . .	159
6.3.1	Voluntary Movement Estimation from Real-Time Data . . . . .	159
6.3.2	Passive Tremor Suppression on Forearm Mannequin . . . . .	162
6.4	Summary . . . . .	168

<b>7 Conclusion</b>	<b>169</b>
7.1 Contribution . . . . .	170
7.1.1 The Design of Tremor Alleviating Wrist Exoskeleton . . . . .	170
7.1.2 Analysis of Coupled Human-Exoskeleton Dynamics . . . . .	171
7.1.3 Real-Time Identification of Wrist Kinematic . . . . .	171
7.1.4 Exoskeleton Controllers for Tremor Suppression . . . . .	172
7.1.5 Voluntary Movement Estimation for Motion Planning . . . . .	172
7.1.6 Prototyping, Control Integration and Experiments . . . . .	173
7.2 Future Work . . . . .	173
7.2.1 Improved Ergonomics in Mechanism and Wearability . . . . .	173
7.2.2 Reliable Exoskeleton Actuators . . . . .	174
7.2.3 Nonlinear Analysis of Tremor Dynamics . . . . .	174
7.2.4 Advanced Exoskeleton Control for Tremor Suppression . . . . .	175
7.2.5 Motion Planning with Better Compliance . . . . .	176
7.2.6 Extensive Experimental Validations . . . . .	176
<b>Bibliography</b>	<b>177</b>
<b>Appendices</b>	<b>203</b>
<b>Appendix A Mathematical Proofs and Results</b>	<b>204</b>

A.1	Explicit Solution of Translational Displacement in the Ellipsoidal Joint Wrist Model . . . . .	204
A.2	Lyapunov Stability of User PID Controller . . . . .	205
A.3	Lyapunov Stability of PD and SMC Controllers . . . . .	207
A.4	Lyapunov Stability of IO-RAC . . . . .	209
A.5	Optimality of IO-RAC . . . . .	211
<b>Appendix B Symbolic-Numerical Formalism of Multibody Dynamics</b>		<b>214</b>
B.1	Recursive Kinematics and Kane's Method . . . . .	215
B.2	Software Design of ANDY . . . . .	218

# List of Figures

1.1	Symptoms of Parkinson’s Disease and Essential Tremor, and Existing Treatments . . . . .	3
1.2	Forearm DOFs and musculoskeletal anatomy . . . . .	7
1.3	Tremor rehabilitation exoskeleton prototypes and concepts . . . . .	8
1.4	Examples of the 6-DOF mechanism implemented in wrist wearable devices . . . . .	13
2.1	CAD model of the conceptual design of TAWÉ . . . . .	19
2.2	Overview of the TAWÉ conceptual design . . . . .	22
2.3	Wearability of the TAWÉ conceptual design . . . . .	23
2.4	Kinematics of TAWÉ conceptual design . . . . .	27
2.5	Kinematics of the Wrist . . . . .	29
2.6	3D models from the simulations in (a) V-REP and (b) ANDY [177]. . . . .	41
2.7	Simulation validation between the models in V-REP and ANDY, . . . . .	42
2.8	Eigenvalue norm ratio of control input Jacobian in the workspace . . . . .	44
3.1	Illustration of an ellipsoidal joint . . . . .	49
3.2	Demonstration of Sparsity Promoting Function . . . . .	60
3.3	The design of wrist kinematics measurement tool . . . . .	61
3.4	Solution of Ellipsoidal Joint Model . . . . .	66

3.5	Motion Trajectory from Reference Model for Simulation . . . . .	67
3.6	Trajectories of parameter estimation errors in the regression of the simplified model via EKF . . . . .	68
3.7	The performance of WKI algorithm on regressing two reference models . . . . .	70
3.8	Comparison of regression performances with FLC and SP-EKF (no noise) . . . . .	71
3.9	The comparison of parameter sparsities (zeros versus non-zeros) of the models respectively updated by regular EKF and SP-EKF . . . . .	72
3.10	Comparison of regression performances with FLC and SP-EKF (noise) . . . . .	73
3.11	The experimental setup of the author wearing the WKMT . . . . .	74
3.12	The experimental wrist motion data for WKI . . . . .	75
3.13	Estimation of wrist kinematics based on regression by the proposed WKI algorithm . . . . .	76
3.14	Comparison of the translational displacement estimation error among different WKI algorithm configurations . . . . .	77
3.15	Comparison of the rotational constraint estimation error among different WKI algorithm configurations . . . . .	78
3.16	The estimated primary parameters from the model with FLC trained by SP-EKF . . . . .	79
3.17	The comparison between wrist rotation presented in Frame A1 and Frame W1 . . . . .	80
4.1	“Motus” kinetic tremor time series . . . . .	84
4.2	“Motus” kinetic tremor time series autocorrelation . . . . .	85

4.3	“Motus” resting tremor time series . . . . .	86
4.4	“Motus” kinetic tremor amplitude spectrum . . . . .	87
4.5	“Motus” resting tremor amplitude spectrum . . . . .	88
4.6	The 3D model of the 4-DOF stationary exoskeleton for control simulation . .	105
4.7	Trajectory tracking performance of the stationary exoskeleton with uncertain Body 2 only . . . . .	107
4.8	Tracking and estimation errors from the stationary exoskeleton simulation with uncertain Body 2 only . . . . .	108
4.9	Estimation errors of uncertain parameters from Body 1 and Body 2 . . . . .	109
4.10	Tracking error comparison on the stationary exoskeleton simulation with dif- ferent feedback controller designs . . . . .	110
4.11	Input effort comparison on the stationary exoskeleton simulation with differ- ent feedback controller designs . . . . .	111
4.12	The 3D model of TAWÉ control system . . . . .	112
4.13	The performances of IO-RAC on TAWÉ with known human kinematics and zero-disturbance . . . . .	113
4.14	The performances of IO-RAC on TAWÉ with unknown human kinematics and disturbance . . . . .	114
4.15	The comparison of passive and active tremor suppression with IO-RAC from TAWÉ simulations . . . . .	115

5.1	Comparison between causal (IIR) and non-causal (zero-phase) low-pass filtering of an example synthesized tremor signal . . . . .	121
5.2	The performance of KF-BMFLC in voluntary movement estimation . . . . .	123
5.3	The performance of SVR-VME algorithm on synthesized tremor movement signal in comparison to KF-BMFLC . . . . .	132
5.4	Quantitative analysis of SVR-VME performance on synthesized tremor movement signals . . . . .	133
5.5	The performance of SVR-VME in Trial No. 9 from the quantitative analysis on synthesized tremor signals . . . . .	134
5.6	Comparison between SVR-VME algorithms with different prediction horizons	135
5.7	The performance of SVR-VME algorithm on a noise overlaid synthesized signal	136
5.8	The performance of SVR-VME algorithm on synthesized signal in with transient behaviors . . . . .	137
5.9	Quantitative analysis of SVR-VME performance on experimental tremor movement signals . . . . .	138
5.10	The performance of SVR-VME on experimental tremor movement angular velocity signal (Trial No. 1) . . . . .	139
5.11	The performance of SVR-VME on experimental tremor movement angular position signal (Trial No. 1) . . . . .	139
5.12	The performance of SVR-VME on experimental tremor movement angular position signal (Trial No. 2) . . . . .	140
6.1	The finalized design of TAWA Prototype . . . . .	144

6.2	The views of TAWE Prototype attached to the right forearm . . . . .	146
6.3	TAWE at different natural wrist poses . . . . .	147
6.4	TAWE at natural forearm pronation and supination . . . . .	148
6.5	The full control framework of TAWE . . . . .	150
6.6	The mechatronic system of TAWE . . . . .	151
6.7	The architecture of TAWE control software in ROS2 . . . . .	152
6.8	Visualization of TAWE in Rviz from ROS2 . . . . .	153
6.9	Human-TAWE system actuated by user input with fixed-frequency tremor excitation . . . . .	154
6.10	Real-time simulation of TAWE on active suppression of tremor with fixed- frequency harmonic components . . . . .	156
6.11	Human-TAWE system actuated by user input with varying-frequency tremor excitation . . . . .	157
6.12	Real-time simulation of TAWE on active suppression of tremor with varying- frequency harmonic components . . . . .	158
6.13	Experimental setup for real-time movement data collection using TAWE . . .	159
6.14	Real-time performance of SVR-VME on wrist movements with intentional tremors . . . . .	160
6.15	Real-time performance of SVR-VME on smooth voluntary wrist movements	161
6.16	TAWE on a forearm mannequin with robotic wrist . . . . .	162
6.17	The compliance of TAWE towards user-guided movement . . . . .	164

6.18	TAWÉ servomotor behaviors in passive tremor suppression experiment . . .	165
6.19	Robotic wrist servomotor behaviors in passive tremor suppression experiment	166
B.1	The multibody formulation framework is shown in (a); the software architecture of TAWÉ is shown in (b) [180]. . . . .	219

# List of Tables

2.1	Properties of homogeneous transformations for coordinate frames in TAFE Conceptual Design . . . . .	28
2.2	Properties of homogeneous transformations for coordinate frames in the Wrist	29
3.1	Properties of transformations between coordinate frames in the WKMT kinematic system. . . . .	62
4.1	True values of uncertain parameters and default controller parameters for stationary robot simulation. . . . .	106

# Nomenclature

## Abbreviations

ADL Activities of daily living

AR Auto-regressive

BMFLC Band-limited multi-frequency Fourier linear combiner

CLF Control Lyapunov function

DBS Deep brain stimulation

DOF Degree of freedom

EFE Elbow flexion-extension

EKF Extended Kalman filter

EMG Electromyography

ET Essential Tremor

FLC Fourier linear combiner

IIR Infinite impulse response

IMU Inertial measurement unit

KF Kalman filter

MCU Micro-controller Unit

MRAC Model reference adaptive control

P(I)D Proportional-(Integral)-Derivative (Controller)

PS Pronation-supination (of the forearm)

PT Parkinsonian Tremor

RAC Robust adaptive controller

ROS2 Robot Operating System 2 (Software)

RUD Radial-ulnar-deviation (of the wrist)

SP Sparsity-promoting

SVM(R) Support vector machine (regression)

TAWE Tremor-Alleviating Wrist Exoskeleton (a device proposed in this project)

VME Voluntary Movement Estimation

WFE Wrist flexion-extension

WFLC Weighted-frequency Fourier linear combiner

WKI Wrist kinematics identification

WKMT Wrist Kinematics Measurement Tool (a device proposed in this project)

## Mathematical Notations

$\|\mathbf{Z}\|_n$   $n$ -norm of a matrix  $\mathbf{Z}$  ( $n = 2$  if not specified)

$\bar{\mathbf{z}}$  Statistical mean of a vector  $\mathbf{z}$

$\mathbf{c}_{m \times n}$   $m \times n$  matrix whose elements equal to  $\mathbf{c} \in \mathbb{R}$  ( $m, n$  fit automatically into the equation if not specified)

$\mathbf{c}_m$   $m \times 1$  vector whose elements equal to  $\mathbf{c} \in \mathbb{R}$

$\hat{\mathbf{z}}$  Estimated value of a vector  $\mathbf{z}$

$\mathbf{I}_n$  Identity matrix of dimension  $n$  ( $n$  fits automatically into the equation if not specified)

$\mathbf{L}_{\mathbf{Y}}\mathbf{Z}$  Lie derivative :  $\mathbf{L}_{\mathbf{Y}}\mathbf{Z} = (\partial\mathbf{Z}/\partial\mathbf{x})\mathbf{Y}$

$\text{lpf}_c(\mathbf{Z})$  The low-pass filtering of time-dependent matrix  $\mathbf{Z}$ , where  $c$  is the delay in discrete time steps.

$\text{diag}(\mathbf{z})$  Convert an  $m$ -dimensional vector  $\mathbf{z}$  into an  $m \times m$  diagonal matrix where the diagonal elements are the elements of  $\mathbf{z}$

$\text{skew}(\mathbf{z})$  Convert an  $3 \times 1$  vector  $\mathbf{z}$  into an  $3 \times 3$  skew symmetric matrix

$\text{vec}(\mathbf{Z})$  Reshape a matrix  $\mathbf{Z}$  elements into a column vector

$\tilde{\mathbf{z}}$  Estimation error of a vector  $\mathbf{z}$

$\mathbf{Z} > 0$  A square matrix  $\mathbf{Z}$  is positive definite

$\mathbf{Z}^m$  Elemental-wise matrix  $\mathbf{Z}$  to the power of  $m$

$\mathbf{Z}^+$  The Moore-Penrose pseudo inverse of  $\mathbf{Z}$

$\mathbf{Z}^{-\text{T}}$  Transposed inverse of  $\mathbf{Z}$  (since  $(\mathbf{Z}^{-1})^{\text{T}} = (\mathbf{Z}^{\text{T}})^{-1}$ )

$\mathbf{Z}_1 * \mathbf{Z}_2$  Elemental-wise product of matrices  $\mathbf{Z}_1$  and  $\mathbf{Z}_2$

$\mathbf{z}_1 \times \mathbf{z}_2$  Product of quaternions  $\mathbf{z}_1$  ( $4 \times 1$ ) and  $\mathbf{z}_2$  ( $4 \times 1$ )

$\mathbf{Z}_{[m,n]}$  The  $m$ th row,  $n$ th column element of matrix  $\mathbf{Z}$

$\mathbf{z}^*$  Conjugation of quaternion  $\mathbf{z}$  ( $4 \times 1$ )

## Symbols for Specified Vectors and Matrices

<b>b</b>	Bias vector
<b>C</b>	Constant coefficient matrix (for various purpose)
<b>c</b>	Constant coefficient vector (for various purpose)
<b>F</b>	General function that outputs a matrix
<b>f</b>	General function that outputs a vector
<b>Z</b>	Intermediate/Temporary variable matrix (for various purpose)
<b>z</b>	Intermediate/Temporary variable vector (for various purpose)
<b>C</b>	Coriolis and centripetal matrix (also abbreviated as C-Matrix)
<b>d</b>	$3 \times 1$ 3D translational displacement
<b><math>\epsilon</math></b>	Tracking/Estimation error (for controls and optimizations)
<b>F</b>	Jacobian related to model process function
<b>f</b>	Model process function
<b>g</b>	Generalized force
<b>H</b>	Jacobian related to model observable function
<b>h</b>	Model observable function
<b>J</b>	Jacobian Matrix
<b><math>\kappa</math></b>	Intrinsic $\vec{z} - \vec{y} - \vec{x}$ Euler angle for rotation description
<b>K</b>	Gain matrix (for controls and optimizations)

$\lambda$	Lagrange Multiplier (for dynamical constraints and optimizations)
$\mathbf{M}$	Inertia matrix that satisfies $\mathbf{M} = \mathbf{M}^T > 0$
$\mu$	Movement measurement (which may not possess a physical unit)
$\Omega$	$3 \times 3$ Rotation matrix
$\omega$	$3 \times 1$ 3D angular velocity
$\mathbf{P}$	Covariance matrix of state estimation
$\mathbf{p}$	Model parameter (for dynamical systems and optimizations)
$\mathbf{Q}$	Covariance matrix of process noise
$\mathbf{q}$	Generalized coordinate
$\rho$	Nonholonomic state for multibody dynamical system
$\mathbf{R}$	Covariance matrix of observation noise
$\mathbf{r}$	Reference (for constraints, controls, and optimizations)
$\mathbf{T}$	$4 \times 4$ 3D Homogeneous transformation matrix
$\mathbf{u}$	Input (for dynamical systems and optimizations)
$\mathbf{v}$	Observation noise (for dynamical systems and optimizations)
$\mathbf{w}$	Perturbation/disturbance or process noise (for dynamical systems and optimizations)
$\xi$	Unit quaternion vector for rotation description
$\mathbf{x}$	State (for dynamical systems and optimizations)
$\mathbf{y}$	Output/Observable (for dynamical systems and optimizations)

## Subscripts for Specified Properties

eigen	Eigenvalue
base	Base frame (of a kinematic chain)
cp	Coupled (Dynamics)
ct	Control-targeting (Dynamics)
dep	Dependent variable/coordinate
end	End frame (of a kinematic chain)
est	Estimation
exo	Exoskeleton
fb	Feedback (for control)
ff	Feedforward (for control)
indep	Independent variable/coordinate
nh	Nonholonomic
sp	Sparsity-promoting
$\vec{w}$	Property/Operation along $\vec{w}$ axis/direction (for quaternion)
wrist	Wrist
$\vec{x}$	Property/Operation along $\vec{x}$ axis/direction
$\vec{y}$	Property/Operation along $\vec{y}$ axis/direction
$\vec{z}$	Property/Operation along $\vec{z}$ axis/direction

$\Omega$	Rotation
vol	Voluntary
$a$	Forearm subsystem (including base)
$d$	Translation
$e$	Exoskeleton subsystem (including base)
$f$	Process function (for control and estimation)
$h$	Observation function (for control and estimation)
$i$	Object/Target Number $i$
$j$	Object/Target Number $j$
$k$	Object/Target Number $k$
$m$	Dimension $m$
$n$	Dimension $n$
$u$	Input
$v$	Observable/Output noise
$w$	Disturbance/Perturbation
$x$	Control/Process system state
$y$	Observable/Output state

# Chapter 1

## Introduction

Activities of daily living (ADL) such as writing, eating, and object manipulation are challenging for patients suffering from pathological tremors. The primary symptom of pathological tremor is shaking palsy that can manifest in limbs, heads, and other body parts. Among the existing treatments for tremors, mechanical loading through wearable rehabilitation devices is popular for its non-invasiveness to the human body. In particular, a few exoskeletons are developed to actively mitigate pathological tremors in the forearm using control inputs from actuators. While the tremor suppression effectiveness of these forearm exoskeletons has been validated through prototypes, they still require significant improvements in ergonomics to be implemented for ADL applications. The ergonomics of the exoskeleton can be improved via design and motion control pertaining to human biomechanics, which leads to better efficiency, comfort, and safety for the user.

The wrist is a complicated biomechanical joint with two coupled degrees of freedom (DOF) pivotal to human manipulation capabilities. Some existing exoskeletons do not provide active tremor suppression in all wrist DOFs, while others can restrict the natural motion of the user. This motivates us to explore a better exoskeleton solution for wrist tremor suppression. We propose TAWÉ - a wearable exoskeleton that provides alleviation of pathological tremors in all wrist DOFs. This project also establishes generalized frameworks modeling, analysis, and control that aim for better exoskeleton ergonomics, which are applicable to not only TAWÉ but also other exoskeletons.

The remaining Introduction Chapter is arranged as follows. Section 1.1 summarizes the background of pathological tremor and its existing treatment. Section 1.2 reviews the forearm motions and wrist anatomy, compares existing forearm tremor rehabilitation exoskeletons, and discusses tremor signal processing and prediction method. Section 1.3 discusses the motivations of this project to develop an ergonomic tremor suppression exoskeleton for the wrist. Section 1.4 provides the research objectives and contributions of this work. Finally, Section 1.5 lays out the remaining content of this dissertation.

## 1.1 Background - Pathological Tremors

Millions of people around the world suffer from pathological tremors. Parkinson's Disease [37, 68, 79, 82, 131], which leads to Parkinsonian Tremor (PT), and Essential Tremor (ET) [7, 35, 105, 190] are the two most common adult tremors. The prevalence of Parkinson's Disease is estimated up to 10 million worldwide in 2017 [78], and 930,000 among the age $\geq$ 45 population in the US in 2020 [116]. ET is estimated to affect approximately 1% of the people worldwide in 2010, and around 7 Million of the US population in 2014 [106, 107].

### 1.1.1 Pathophysiologies and Symptoms

Tremors are generally summarized as involuntary, rhythmic, and oscillatory movements [119], whose characteristics and behaviors vary among different pathological tremors [10, 165]. As examples, the common frequency bands of PT and ET are 3~6 Hz [82] and 4~12 Hz [7], respectively. Also, PT is significant during resting [20], while ET is mainly categorized as kinetic and postural tremor [18]. Such distinctive behaviors result from the different pathophysiologies of PT and ET [7, 79, 82, 190]. Studies indicated that PT is related to

Lewy bodies [82] and the deficiency of Dopaminergic neurons in the substantia nigra [29, 140], which are neurons related to motor control information relay. Parkinsonian Tremors are also accompanied by other symptoms such as bradykinesia (i.e., slowness of movement) [9], muscle rigidity [8], and postural instability [72]. ET mainly results from toxins or familial genetic diseases [7, 35], and may also be related to the dysfunction in the cerebellum [36]. Despite these differences, misdiagnosis [77] of these two pathological tremors can still occur, since PT and ET are related and may co-exist [165, 166].

The majority of Parkinson’s Disease and ET patients come from the elderly population. Poor posture and joint deformity [6, 40, 79] have been frequently observed in Parkinson’s Disease patients, as shown in Fig. 1.1. While no mortality is directly induced by Pathological tremors, tremors and postures instability can lead to vulnerability to potential environmental threats. This is critical to elderly patients suffering from other aging diseases such as sarcopenia (i.e., the decline of muscle power) [122] and osteoporosis (i.e., fragile bone structure)

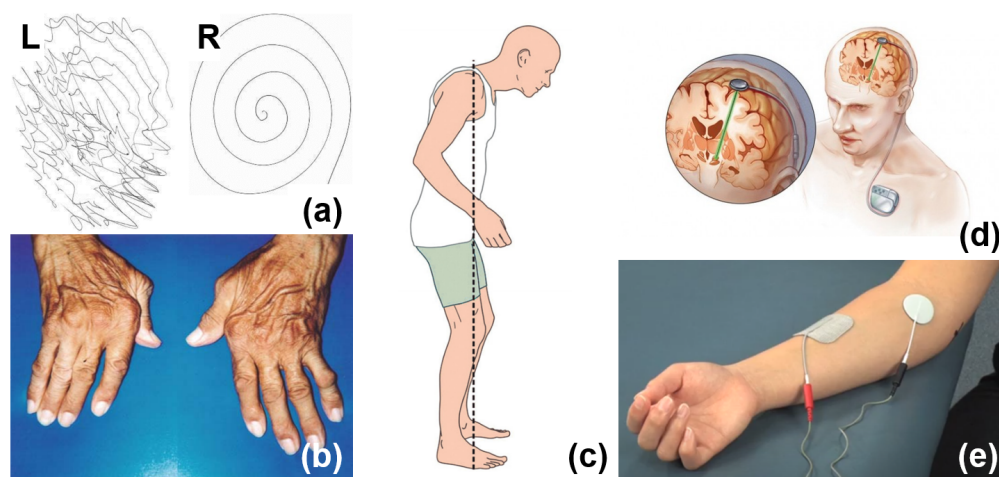


Figure 1.1: Symptoms of Parkinson’s Disease and Essential Tremor, and Existing Treatments - (a): an Essential Tremor patient is incapable of drawing archimedean spiral (L) as smoothly as a health person (R) [7]; (b): joint deformities on the hands of a Parkinson’s Disease patient suffering [6]; (c): typical postural deformity in Parkinson’s Disease patients featuring shoulder rounding and hip/knee flexion [40]; (d): an illustration of Deep Brain Stimulation [45, 162]; and (e) a demonstration of functional electrical stimulation setup [41, 53].

[91, 157], making them susceptible to falling [169], which can lead to severe injuries.

### 1.1.2 Surgical, Pharmacological and Therapeutic Treatments

Researchers are dedicated to exploring cures to relieve the patients from pathological tremors. In the cases of Parkinson's Disease and ET, the complete cures have not yet been discovered [82, 190]. The most common surgical treatments of Parkinson's Disease and ET include thalamotomy and deep brain stimulation (DBS) [145, 162]. In general, DBS has better efficacy (up to 90%) in tremor reduction [45]. However, both major surgeries are expensive and accompanied by surgical risks, neuropsychiatric adverse events [60], and loss of efficacy (experienced by 16% of the patients [93]).

The tremor reduction by pharmacological treatments can reach up to 59% for Parkinson's Disease and 68% for ET [45, 92]. But similar to surgery, medications also have the problems of side effects and drop in efficacy. Common side effects of these medicines include nausea, hypotension, and dizziness. Particular medicines for PT and ET can also lead to other neurological disorders, heart-related complications, and effectiveness reduction [46, 56].

The alternatives to surgical and pharmacological treatments include various types of therapies [128]. In particular, functional electrical stimulation (FES) [41, 53, 193]) and sensory electrical stimulation (SES) [38, 64]) are developed to stimulate the peripheral nervous system to generate muscle contractions that mitigate the effects of tremor. Both FES and SES can reduce the power of tremors by approximately 50% [38, 53]. However, subjects can experience muscle fatigue, discomfort, and interference with voluntary movements from FES. The variability of SES is relatively high, and some patients may not respond to the stimulation. Finally, the efficacy of electrical stimulation can drop over the long term due to neural adaptation.

### 1.1.3 Summary

Pathological tremors afflict millions of people around the world, causing a significant reduction in their quality of life. The causes and symptoms are distinctive among different tremors, which are extremely complicated and have not yet been fully understood. For the majority of the tremor patients that come from the elderly population, complications can develop from tremors and other elderly diseases, leading to more vulnerabilities in daily living.

Existing treatments for pathological tremors such as surgeries, medications, and stimulative therapies are effective. However, they are also invasive to the human body, and have the problems of side effects and a drop in efficacy. Therefore, non-invasive and reliable treatments of pathological tremors would greatly benefit society. This leads to the development of tremor suppression exoskeletons, which are discussed in the next section.

## 1.2 Background - Tremor Control via Exoskeletons

In recent years, mechanical loading through wearable orthoses and exoskeletons has emerged as a popular approach to alleviate pathological tremors [51, 111, 128]. Unlike the aforementioned interventions of tremors, tremor suppression via mechanical loading is non-invasive and innocuous, since it does not involve modification of the human body or stimulation of the neural system. By considering tremor movements as vibrations of the human body, the orthoses and exoskeletons can be categorized into:

- (1) Passive devices based on fixed mechanisms for vibration isolation and absorption [94, 161].
- (2) Semi-active devices that can adaptively tune the parameters of the isolator/absorber

mechanism based on tremor behaviors [23, 66, 108, 151, 187].

- (3) Active devices that mitigate tremors through control inputs from actuators [30, 67, 73, 87, 118, 137, 146, 158, 159, 188].

Since semi-active and active devices involve the application of mechatronics and robotics, they are referred to as *exoskeletons* hereinafter.

The design of tremor suppression exoskeletons primarily focuses on the forearm. Therefore, this section first summarizes the forearm motions and, specifically, the wrist musculoskeletal anatomy. The existing forearm exoskeletons for tremor suppression are then presented and compared. Finally, we discuss the tremor signal processing and prediction techniques applied to semi-active and active devices.

### 1.2.1 Forearm Motions and Wrist Anatomy

The forearm is involved in four major upper limb DOFs [42, 144] - wrist flexion-extension (WFE), wrist abduction (radial-ulnar-deviation) (RUD), forearm pronation-supination (FPS), and elbow flexion-extension (EFE). The approximate rotation axes of these motions are shown in Fig. 1.2(a). The EFE and FPS motions are relatively distinctive, where the rotation of EFE is categorized as a hinge joint, and the rotation of FPS is classified as a pivot joint. The flexor and extensor muscle groups respectively contribute to the elbow flexion (up to 145 degrees) and extension (0 degrees); the forearm pronation (up to 70 degrees) and supinations (up to 85 degrees) are mainly actuated by the pronator and supinator muscles [114], respectively.

The wrist motions are more complicated. The wrist possesses multiple coupled DOFs, which are generalized into the WFE and RUD motions. Both wrist flexion and extension can reach

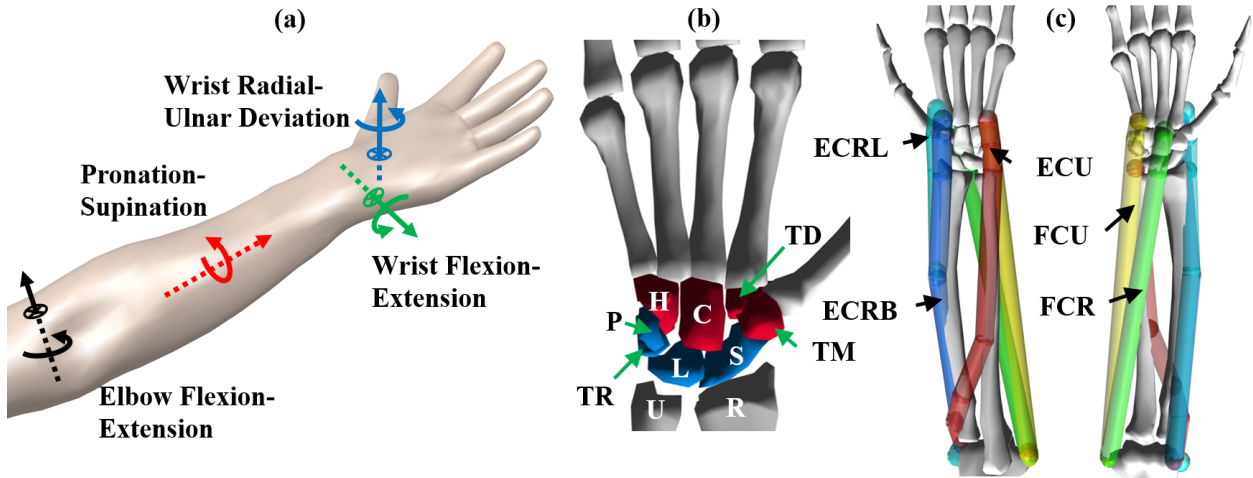


Figure 1.2: Forearm DOFs and musculoskeletal anatomy acquired from OpenSim [148], where (a) presents approximate rotation axes of the four major DOFs that involve the forearm; (b) shows the radial (R) bone, the ulnar (U) bone, the proximal carpal bones (blue): S - Scaphoid, L - Lunate, TR - Triquetrum, P - Pisiform; and the distal carpal bones (red): TM - Trapezium, TD - Trapezoid, C - Capitate, H - Hamate; (c) illustrates the muscles that actuates the wrist joints: ECRB - Extensor Carpi Radialis Brevis, ECRL - Extensor Carpi Radialis Longus, ECU - Extensor Carpi Ulnaris, FCU - Flexor Carpi Ulnaris, FCR - Flexor Carpi Radialis. Wrist motions are actuated by: (1) flexion: FCR and FCU; (2) extension: ECRB, ECRL and ECU; (3) radial deviation: ECRB, ECRL and FCR; and (4) ulnar deviation: FCU and ECU.

up to 70 degrees, while the radial and ulnar deviations can reach up to 20 and 30 degrees, respectively [104]. As shown in Fig. 1.2(b), these two motions are primarily generated by the radiocarpal joint (between the radial-ulnar row and the proximal row) and midcarpal joint (between the proximal and distal row [84, 85], which are categorized by the multi-DOF ellipsoidal and gliding joints, respectively. In many studies, the wrist kinematics is often approximated by sequential rotational joints (e.g., universal joints), where multiple rotations take place one after another [11, 26, 42, 49, 104, 141]. However, we can observe from Fig. 1.2(c) that the actuation of the wrist joint is contributed by different combinations of carpal muscles. Unlike the sequential rotation joints, there are no distinctive mechanical axes for the WFE and RUD motion. As a result, the approximate rotation axes of WFE and RUD can shift translationally and rotationally during wrist movements [2, 121].

## 1.2.2 Forearm Tremor Rehabilitation Exoskeletons

All aforementioned forearm motions are crucial to human manipulation capabilities, and can be affected by pathological tremors [51, 123]. Therefore, forearm tremor suppression devices are developed to assist patients in essential daily activities such as writing, eating, and object manipulation. A few wearable semi-active and active exoskeletons are shown in Fig. 1.3, which are developed for tremor suppression in one or multiple DOFs.

For active tremor suppression, the majority of exoskeletons employ rigid mechanisms actuated through electrical motors (e.g., Figs. 1.3(a), (b), and (e)) [73, 137, 146]. Electrical motors are energy-efficient and easy to control. However, electrical motors are usually located on the upper limb, introducing significant gravitational loads to the user.

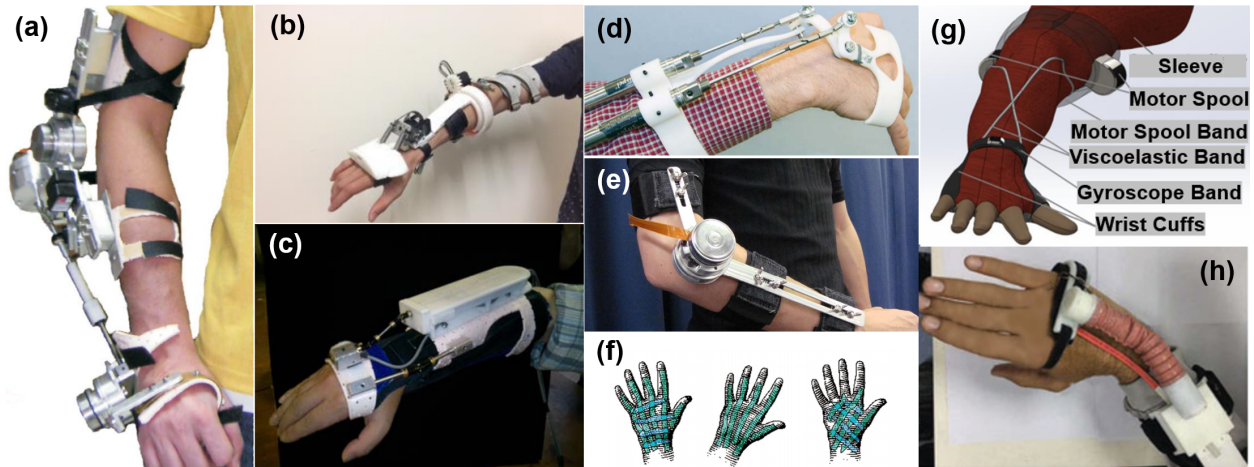


Figure 1.3: Tremor rehabilitation exoskeleton prototypes (a-e, h) and concepts (f, g): (a) WOTAS [137] - actuates EFE, FPS, and WFE with motors (active); (b) Work by Huen/Lou [73] - actuates FPS and WFE with motors (active); (c) DRIFT [108] - impedes WFE and RUD with double magnetorheological fluid viscous beam (semi-active); (d) Work by Taheri/Richer [159] - actuates EFE, FPS, WFE, and RUD with linear actuators (pneumatic); (e) Elbow EMG Exoskeleton [146] - actuates EFE with motor (active); (f) Piezoelectric Fibre Glove [158] - controls WFE and RUD with piezo-actuators (active); (g) Work by Shamroukh et al. [151] - impedes FPS using viscoelastic tendons (semi-active); (h) SETS [187] - impedes WFE and RUD with magnetorheological fluid damper (semi-active).

Fluid-based actuators are adopted in both semi-active and active tremor control devices. The pneumatic actuators in Fig. 1.3(d) [159] lead to significantly less gravitational load in the upper limb and allows larger actuation torques. However, pneumatic actuators require additional hardware including air compressors and valves, which make loud operation noises. Magnetorheological (MR) fluid actuators (e.g., Figs. 1.3(c, h) [108, 187]) are more commonly used in semi-active exoskeletons to create damping forces. The properties of MR fluid actuators can be actively adjusted for optimal tremor-damping performances.

Finally, following the rising popularity of soft robotics research, more tremor control exoskeletons developed in recent years begin to incorporate soft structures and actuators for potentially improved ergonomics and flexibility. The devices shown in Fig. 1.3(f, g, h) [151, 158, 187] adopt piezoelectric fabric actuators, viscoelastic soft tendons, and soft MR fluid actuators, respectively. However, soft structures and actuators are more difficult to model and control [19, 195]. Some soft materials also have limited ranges of motions, making them unable to follow the human body in full ranges of motion [120]. Hence, many soft tremor suppression devices remain in the conceptual design stage [151, 158].

### 1.2.3 Tremor Signal Processing and Prediction

Both semi-active and active tremor suppression devices depend on the processing and prediction of tremor signals, which are carried out based on the understanding that tremors are the dynamical behavior of the human neuromusculoskeletal system [142, 192]. The dynamics of tremor is extremely complicated. Previous works indicated that while tremors show patterns of limit cycles that sometimes resemble the effects of time delay [129], tremor oscillations are not strictly periodic [54, 136, 167]. These studies also suggest that tremor signals are nonlinear and involve stochasticity.

Therefore, existing semi-active and active tremor suppression devices mainly adopt the short-term (i.e., a window of deciseconds) prediction of tremor signals based on the delayed time series. The tremorous motion of the user is often collected by encoders within the motors and inertia measurement units (IMU) [52, 171]. Some studies also measure the neuromuscular signal with surface EMG sensors, which can be used to estimate the muscle input [191]. The data contains the voluntary motion of the user overlaid with tremors. The voluntary movements are extracted from the true motion through estimation models including Benedict–Bordner filter [137] and auto-regressive (AR) model [13].

The filtered tremor movements are then regressed by models such as weighted-frequency Fourier linear combiner (WFLC) [1, 135], band-limited multi-frequency Fourier linear combiner (BMFLC) [171], AR model [163], support vector machine (SVM) [164], and neural networks [74, 150]. For short-term prediction, these regression models are designed to approximate the dynamics of tremors based on a limited window of delayed time series. The regression processes are often carried out in real-time using Kalman filters as the online optimizer [163, 171], so that the parameters of the regression model are constantly updated. It should be also noted that these tremor signal processing techniques are often shared in the control of hand-held surgical tools for physiological tremor suppression [135, 163].

For tremor suppression exoskeletons, both tremor and voluntary motion predictions are used in tremor alleviation following the user movement. The efficacy of active exoskeletons can reach up to 90% [51, 137]. Semi-active exoskeletons utilize tremor prediction algorithms to tune the damping parameters. The efficacy of these exoskeletons can reach up to 98% [51, 108]. On the other hand, the damping in semi-active devices can also encumber voluntary motions.

### 1.2.4 Summary

Mechanical loading via rehabilitation orthoses and exoskeletons is a non-invasive and innocuous approach to mitigate pathological tremors. Based on the designs and utilities, these orthoses and exoskeletons can be categorized into passive, semi-active, and active (specifically referred to as exoskeletons) devices. The design of tremor suppression devices primarily focuses on forearm motions (i.e., WFE, RUD, FPS, and EFE). The semi-active and active forearm exoskeletons can provide effective tremor suppression based on the prediction of tremor signals. With the control input provided by various actuators, active exoskeletons can also mitigate tremors while following the natural movement of the user.

While the existing exoskeleton prototypes are proved effective in upper limb tremor suppression, they still require significant improvement in ergonomics to be implemented for ADL applications [51]. The ergonomics of the exoskeleton can be improved via reasonable design and motion control, which lead to better efficiency, comfort, and safety of the user. Therefore, the next section discusses the motivations of this project to develop an ergonomic tremor suppression exoskeleton for the wrist.

## 1.3 Motivations

As explained in Section 1.1.1, elderly patients with pathological tremors (Parkinson's Disease in particular) may also suffer bradykinesia, muscle rigidity, and declined muscle powers. It would be beneficial to develop wearable exoskeletons that can mitigate tremors with minimal encumbrance of the movements of patients in daily activities. Hence, this project focus on the development of active tremor suppression devices.

In general, the design constraints for wearable rehabilitation exoskeletons are more restric-

tive than the stationary ones [16, 132, 139, 152]. Unlike stationary exoskeletons installed on fixed/moving platforms, wearable exoskeletons have tight design boundaries in dimensions and weights, which leads to limits in workspace and output capacity. However, these exoskeletons are still expected to fulfill the ergonomic criteria that apply to all exoskeletons. Here, ergonomics is a generalized concept that covers the efficiency, comfort, and safety of the interplay between users and exoskeletons. Exoskeletons that lack ergonomics are not only incapable of providing tremor suppression, but can also encumber voluntary user movements. Hence, the following subsections explain the motivations to develop an ergonomic full-wrist tremor suppression exoskeleton through design and motion control pertaining to human biomechanics.

### 1.3.1 Wearable Exoskeleton Design for Full-Wrist Actuation

As explained in Section 1.2.1, the wrist motions are extremely complicated. The coupled WFE and RUD motions challenge the development of wearable exoskeletons with full-wrist actuation. In general, many active exoskeletons from previous studies only provide partial wrist actuation [111]. As examples, the devices shown in Fig. 1.3(a, b) [73, 137] from Section 1.2.2) focus on the tremor suppression in the WFE but not RUD [51]. While there are exoskeletons that provide full-wrist actuation, the majority of these exoskeletons are stationary (e.g., RiceWrist [58], OpenWrist [139], and (CADEN)-7 [132]) and not designed for tremor alleviation [111].

For wearable full-wrist exoskeletons, a major ergonomic concern is the compatibility between the mechanism design and wrist musculoskeletal model. Some mechanisms have two actuated joints between three linkages from the distal end of the forearm to the hand (e.g., Fig. 1.3(d)) [47, 132, 159]. Due to the difference between the wrist joint and sequential rotational joints,

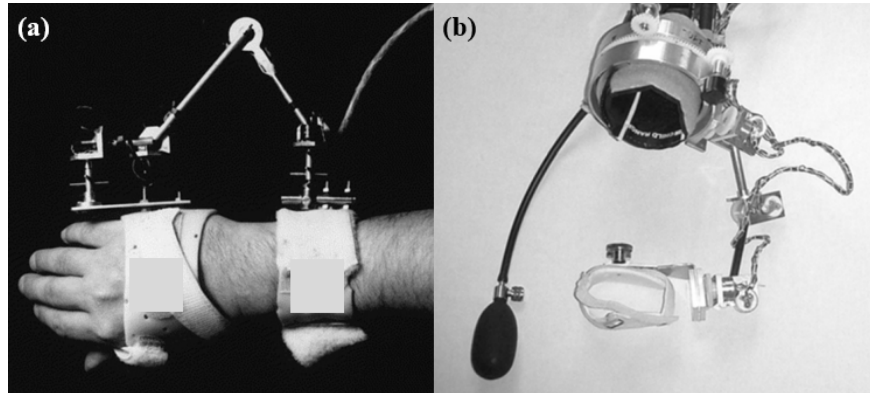


Figure 1.4: Examples of the 6-DOF mechanism implemented in wrist wearable devices, where (a) shows a measurement device for modeling of the wrist [141], and (b) presents the wrist section of the ergonomic wearable exoskeleton that adopts the 6-DOF mechanism [144].

these mechanisms may not fully align with the axes of WFE and RUD rotations. Hence, these mechanisms may confine the natural wrist movements. The key to this problem is to ensure that the mechanism between the distal end of the forearm and wrist has at least six DOFs, which satisfies the minimal requirement for unconstrained translations and rotations between two bodies in the 3D space. Therefore, one solution is using soft mechanisms (e.g., Fig. 1.3(h)) [187]. It is also possible to adopt 6-DOF rigid-linkage mechanisms (RLM), which are easier to design, manufacture, and control than soft mechanisms. Note that only two of the six DOFs are required for full-actuation of the wrist. The idea of 6-DOF RLM has been adopted in the measurement and modeling of complex human joints [141]. The mechanism has also been implemented for the wrist in an ergonomic wearable exoskeleton [144]. These examples are shown in Fig. 1.4. Therefore, the 6-DOF rigid-linkage mechanism can be a potential candidate for the design of a wearable full-wrist tremor alleviation exoskeleton.

### 1.3.2 Control Problems

The implementation of a 6-DOF mechanism in the wearable wrist exoskeleton can lead to a few robotic control problems, which are crucial to the practicality and ergonomics of the

wearable exoskeleton. The major control problems are (1) multibody analysis, (2) wrist kinematics identification, (3) trajectory tracking controller design, and (4) motion planning of tracking reference.

When a 6-DOF rigid-linkage wrist exoskeleton is equipped, the exoskeleton and human skeletal mechanisms form a closed kinematic chain [144]. All six DOFs of the mechanism will be fully constrained to the natural wrist motion, where the joints of the mechanism can be fully expressed by wrist rotations. Hence, the first problem is workspace validity. The desired workspace should not contain regions where the exoskeleton loses controllability, i.e., the control inputs being unable to actuate all individual wrist motions. Therefore, the multibody analysis of the human-exoskeleton system may serve as a preliminary validation for the exoskeleton design.

To establish the control system, a 6-DOF wearable wrist exoskeleton also requires the full information of the closed kinematic chain. However, the wrist kinematics involved in the closed kinematic chain is initially unknown in practice and can vary among different users. If the binding between the exoskeleton and the user is not tight, the exoskeleton attachment locations on the forearm and hand can also slowly change during user movements. Hence, the information on the wrist kinematics involved in the human-exoskeleton system needs to be updated in real-time. Due to different research focuses, however, most wrist kinematics analyses were performed offline [121, 141, 186]. Hence, the exoskeleton requires real-time wrist kinematics identification to obtain the information for controller design.

Solving the previous two problems lays the foundation for controller development, which enables the exoskeleton to track a designed reference trajectory. The multibody dynamics of the human-exoskeleton system is nonlinear. According to the nonlinear control theory, a stabilizing controller for the tracking problem of the human-exoskeleton system needs to guarantee the convergence of a positive-definite Lyapunov function [90]. The control

performance and stability are crucial to the reliability and safety of exoskeleton operations. Exoskeleton control in practice also faces model uncertainties and disturbances that originate in the human system. For stationary rehabilitation exoskeletons, previous works adopted model reference adaptive controller (MRAC) for the inertia, force, and input uncertainties [16, 63, 183]. A few studies also take into consideration the robustness towards the disturbance, and introduced robust adaptive sliding-mode controllers (SMC) that provide good performance under uncertainties and disturbances [17, 22]. On the other hand, the downside of SMC is the chattering problem [168], which may damage the exoskeleton hardware and undermine the safety of the user.

The controller design for tremor alleviation exoskeletons was not investigated in many existing works. A few papers investigated the mitigation of tremor oscillations with adaptive controller [88, 160, 189], which are designed by considering tremors as uncertain oscillators. However, these studies adopt linearized single-DOF systems that do not involve voluntary human movements, and the control algorithms are mainly validated in simulation and experimental devices. Therefore, it is necessary to explore efficient controller designs that support tremor suppression and potential movement assistance under model uncertainties and disturbances.

The compliance between the user and exoskeleton is an important topic in the development of rehabilitation robotics. Unlike the stationary exoskeletons where the tracking reference is manually designed by physiotherapist [17], in user-guided operation, it is desirable that the tracking reference can closely follow the user intention, so that the exoskeleton is compliant with the human motion [81, 196]. For stationary exoskeletons, some earlier studies effectively improved the exoskeleton compliance through model-based feedforward compensations and disturbance observer-based controllers [81, 103]. Other studies adopted user motion predictions for more compliant exoskeleton control or motion planning [28, 80, 153, 196].

Motion planning of tracking reference is also necessary for the suppression of kinetic tremor where the user voluntary movement exists. The key to motion planning is the accurate real-time estimation of voluntary movement with minimal time delay. Earlier studies on the tremor signal processing mainly focus on the modeling of tremor [52, 135, 163, 164, 171]. For the real-time estimation of voluntary movements, most techniques can introduce significant time delay [52, 171]. The design of wearable exoskeletons is also constrained in processor and measurement availability. Therefore, it may be difficult to apply algorithms that require advanced hardware [74, 150]. Hence, there also exists a need for developing a lightweight real-time voluntary movement estimator for the motion planning of the exoskeleton.

## 1.4 Research Objectives

In this dissertation, we investigate the design and control of an ergonomic wearable exoskeleton for full-wrist tremor suppression. The research objectives are listed as follows:

1. The design of a novel wearable exoskeleton that provides active tremor alleviation in all wrist movements. The design requires the exoskeleton mechanism to allow unrestricted natural wrist motions, and aims for applications in daily activities.
2. Multibody modeling and analysis of the human-exoskeleton system, which verifies the preliminary feasibility of the exoskeleton design, and lays the foundation for the control system development.
3. The development of a real-time wrist kinematics identification algorithm that can accurately regress the wrist kinematic model, estimate wrist movements, and provide the information for controller design.
4. The design of an exoskeleton motion controller for active tremor suppression. The

controller should be able to identify and compensate for model uncertainties, and maintain stability under perturbations/disturbances.

5. The development of a motion planning algorithm for user-guided operation based on the estimation of voluntary wrist movements. The algorithm needs to be real-time efficient, and the voluntary movement estimation should have minimal time delays.
6. The prototyping of exoskeleton hardware and control software, and their validations through simulations and experiments.

The primary goal of this project is to explore the design and control of an ergonomic exoskeleton that can potentially lead to quality-of-life improvements for patients suffering from pathological tremors. This study will also establish generalized frameworks of exoskeleton modeling, analysis, and control, which apply to not only the proposed tremor alleviating wrist exoskeleton, but also other rehabilitation exoskeletons.

## 1.5 Organization of the Dissertation

The rest of this dissertation is organized as follows. Chapter 2 discusses the design of the tremor alleviating wrist exoskeleton and the multibody dynamical analysis of the human-exoskeleton coupled dynamics, which lays the foundation for the exoskeleton control system development. The real-time modeling and identification of the wrist kinematics are explained in Chapter 3, where we proposed a real-time wrist kinematic identification based on a novel ellipsoidal joint model that describes the coupled wrist kinematics, and a sparsity-promoting Extended Kalman Filter for the efficient real-time regression. Chapter 4 discusses the design of exoskeleton controllers for tremor alleviation. Specifically, we introduce a robust adaptive controller based on model reference adaptive control and inverse optimal robust

theories. The proposed controller can compensate for inertia and load uncertainties and possess robustness toward perturbation/disturbances. The estimation of voluntary movement from tremorous motion signals is explored in Chapter 5, where we developed a lightweight and data-driven voluntary movement estimator based on least square support vector regression, which can estimate voluntary movements with real-time signal adaptability and significantly reduced time delay. Chapter 6 presents the exoskeleton prototype, the control system integration, and experimental validations, which demonstrate the performance of the proposed methods and reveal their limitations. Finally, Chapter 7 summarizes the findings of this study and proposes future work. Additional information on mathematical proofs and multibody formulations are explained in Appendices A and B, respectively.

## Chapter 2

# Tremor Alleviating Wrist Exoskeleton & Human-Exoskeleton Dynamics

This project begins with the conceptual design of Tremor Alleviating Wrist Exoskeleton (TAWE) - a high-degree-of-freedom wearable exoskeleton designed for pathological tremor suppression in the wrist [177]. The CAD model of the conceptual design is shown in Fig. 2.1. As mentioned in Section 1.3.1, unlike many active exoskeletons mainly focuses on tremor suppression in the WFE motion. The novelty of TAWE is taking into consideration the coupling of WFE and RUD movements, and providing tremor alleviation in both WFE and

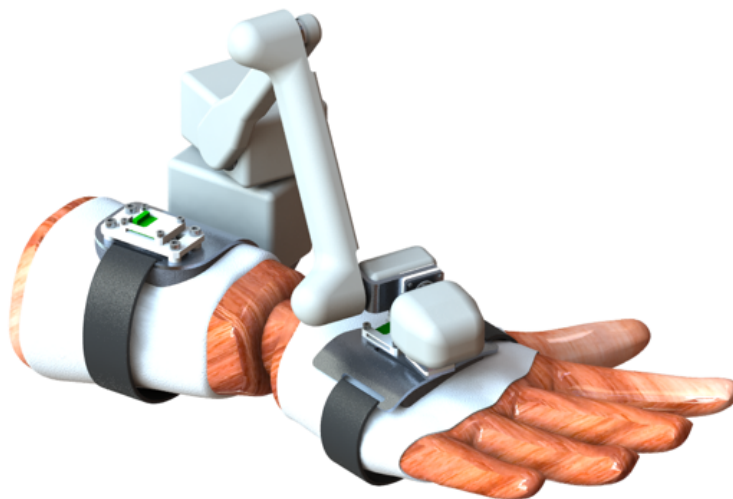


Figure 2.1: The CAD model of the conceptual design of TAWE attached to a right human forearm mannequin [177].

RUD without constraining the natural wrist motion. TAWE is designed with necessary sensors and actuators for tremor measurement and active control, as well as wearability features suitable for ADL applications. The estimated weight of the exoskeleton is 390 grams excluding the battery, which is mainly contributed by the servomotors and rigid linkages.

The feasibility of TAWE is determined by not only the design, but also its dynamical interplay with the user forearm. When the user wears the exoskeleton, a closed-kinematic chain is formed between the forearm and TAWE mechanisms based on the constraints introduced at the attachments. The modeling and analysis of the coupled dynamics between the forearm and exoskeleton lay the foundation for the control system development of TAWE in the later chapters.

This chapter discusses the features of TAWE conceptual design and the multibody dynamical analysis of the human-exoskeleton coupled dynamics, which are used in later parts of the research. Section 2.1 explains the design considerations including mechanism, wearability, sensors, and actuators. Section 2.2 models the kinematics of the human-exoskeleton system. Section 2.3 explains the modeling and coupling of the forearm and exoskeleton dynamics, which reveals the control problems to be addressed in later chapters. Finally, Section 2.4 summarizes the findings of this study. (The study in this chapter has been partially reported in [176, 177].)

## 2.1 Design Considerations

This section discusses the design consideration of the conceptual design of TAWE. The design choices on the mechanism, wearability, sensors, and actuators take into consideration of ergonomics, observability, and controllability, which also constructs the system setup for the following studies.

### 2.1.1 Mechanism and Wearability

As previously mentioned in Section 1.3.1, an essential requirement of TAWÉ is the compliance with natural wrist motions of the user. As the exact 3D kinematics of the wrist is initially unknown, the hand and the distal end of the forearm are treated as two individual bodies. Hence, an exoskeleton that links these two bodies requires at least 6 DOFs to ensure unconstrained natural wrist motion. Another benefit of using a high-DOF mechanism is the compatibility with user profiles of moderately different wrist musculoskeletal geometries. In this case, a single exoskeleton may be used by different users without frequent customization of the linkage dimensions. Finally, compared to soft mechanisms that may also realize high-DOF, rigid mechanisms are more efficient in force/torque transmission, and they can also be reliably modeled, measured, and controlled.

The design of TAWÉ is realized based on the 6-DOF rigid linkage mechanism. Figure 2.2 presents the conceptual design of TAWÉ, where two linkages in the middle bridge the components attached to the distal part of forearm and the dorsum of hand. The motors and linkages (i.e., Joint 1 to Joint 3) support the 3D translational displacements between the hand components and the forearm components. The axes of the remaining 3 joints (i.e., Joint 4 to Joint 6) are perpendicular to each other, which leads to the formulation of the “Euler Joint”. The Euler Joint is similar to a ball-and-socket joint as they both are 3D rotational joints. On the other hand, the Euler Joint is a sequential rotational joint, where each of the joint angles is similar to Euler angles and can be directly measured. Euler joint allows the exoskeleton to adapt to any relative rotation between forearm and hand. Hence, TAWÉ can follow to both natural WFE and RUD movements without imposing restrictions on the user. The standard poses of the exoskeleton are shown in Fig.2.2(b-e). By assuming the current mannequin wrist as a common ball-and-socket joint, the exoskeleton can reach  $-75^\circ \sim 75^\circ$  in FE and  $-45^\circ \sim 25^\circ$  in RUD without geometric collision between parts.

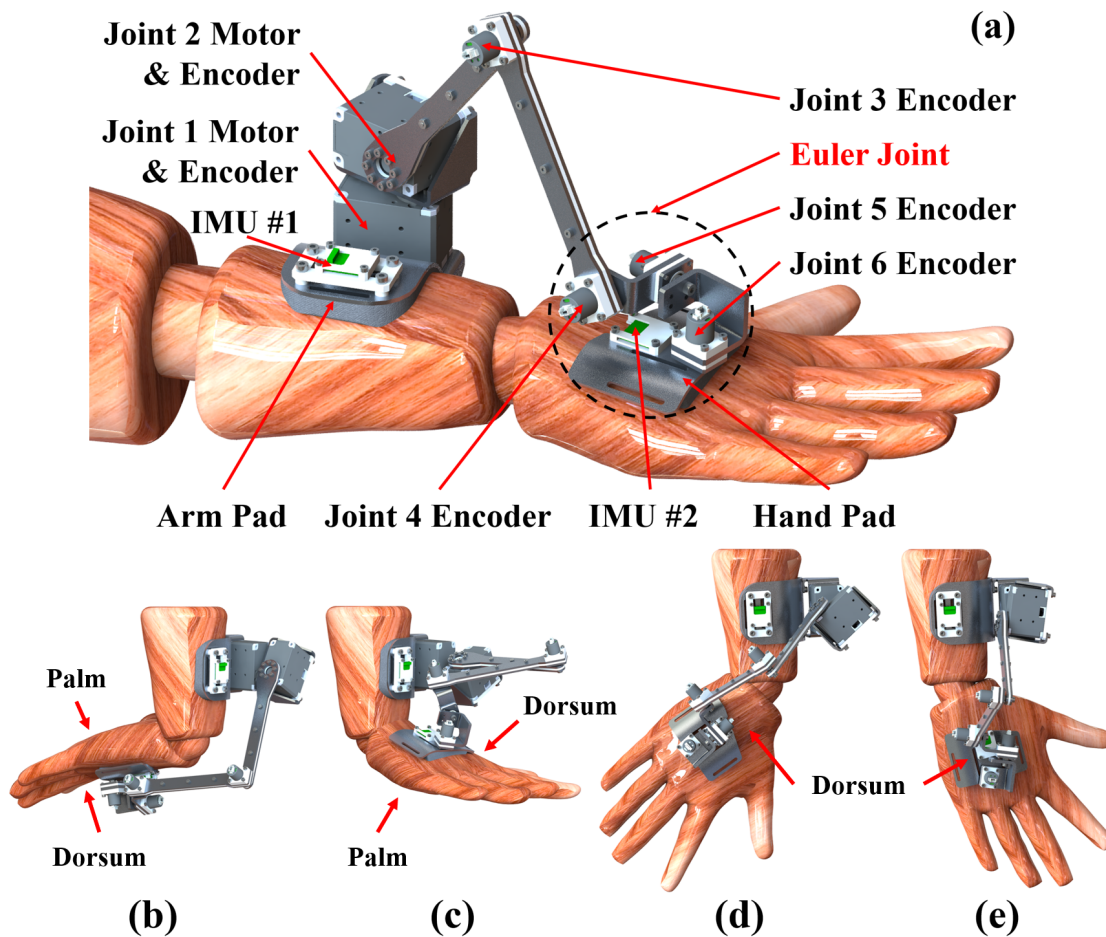


Figure 2.2: The overview of TAWEx (Conceptual Design) installed on a right forearm mannequin [177], where (a) shows the mechanism design with all the major components labeled. The standard poses of TAWEx at different wrist position is shown in: (b):  $-75^\circ$  in WFE (Flexion); (c):  $75^\circ$  in WFE (Extension); (d):  $-45^\circ$  in RUD (Ulnar Deviation); and (e):  $25^\circ$  in RUD (Radial Deviation). In (b-e), the palm and dorsum of the right hand are marked.

The wearability of TAWEx is another design consideration. For ADL applications, we expect that TAWEx can be easily equipped and unequipped. Therefore, the current designs of TAWEx employ user-friendly wearability features. As shown in Fig. 2.2, the forearm and hand attachment pads are respectively located at the base and the end of TAWEx. The forearm pad is attached to the distal end of the forearm, and the hand pad is attached to the hand dorsum. As demonstrated in Fig. 2.3, sleeves, gloves, and Velcro tapes are installed with the attachment pads for the user to convenient equip the device without extreme tight-binding

or precise positioning. These setups allow the users to freely use their fingers and palms, and perform some tasks in daily life. The designs of the attachment pads and the dimensions of all mechanism linkages can be customized to better fit the user profile (size, range of motion, etc.). The design of TAWE can also be improved using safe casings with smooth and soft surfaces to cover the mechanism, sensors, and electrical wiring.

### 2.1.2 Sensors and Actuators

The sensors of TAWE need to provide full measurements of wrist movements and joint angles in the exoskeleton. The positional sensors used in the design from Fig. 2.2 are absolute rotary encoders (US Digital MAE3) installed at the rotary joints, and the two inertial measurement units (IMU) (STMicroelectronics LSM9DS1) fixed on the forearm and hand pads. All of these sensors can reach measurement resolutions higher than  $0.1^\circ$  and sampling frequencies higher than 250 Hz, which is sufficient for movement measurement to realize tremor control. This setup provides two different measurements of the orientation difference between the hand and the forearm. Since the base of the exoskeleton is attached

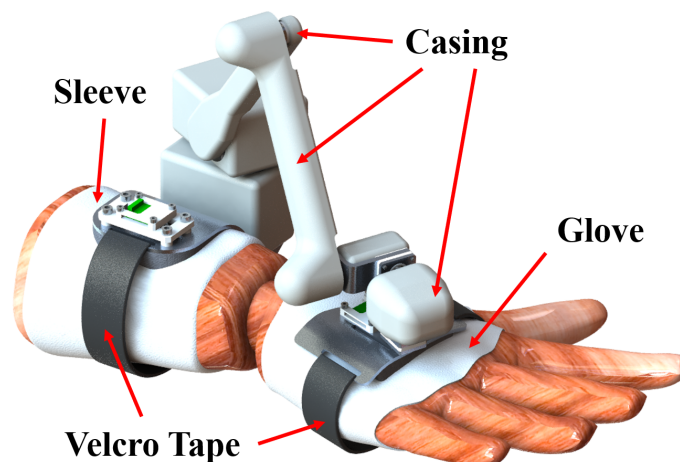


Figure 2.3: The attachment of TAWE to a right forearm mannequin model via sleeve, glove, and Velcro tapes [177]. The mechanisms and sensors are covered by safe casings.

close to the distal end of the forearm, the orientation difference between IMU 1 and IMU 2 is not affected by the FPS motion in the forearm. Hence, it is possible to apply sensor fusion based on the two measurements to provide accurate kinematic information of the wrist and exoskeleton movements [102].

For a wearable exoskeleton, the options for actuators are limited. The actuators need to provide enough torque for tremor suppression. On the other hand, unnecessarily powerful motors are usually heavy, which may pose both wearability and safety problems. For the design in Fig. 2.2, the actuation of the exoskeleton is realized by servomotors (Dynamixel XM430 Series). These servomotors are compact all-in-one actuators consisting of brushed DC motors, speed-reduction gearboxes, absolute encoders, and driver circuits with current control support. For DC motors, since current is approximately proportional to torque [113], current control is equivalent to direct torque control. For safety concerns, the maximum torque of the motors will be limited at approximately 2 N-m, which is sufficient for tremor suppression without exerting excessive load on the user. With the use of two servomotors at Joint 1 and Joint 2, the exoskeleton can provide full actuation of the wrist.

## 2.2 Coupled Kinematics of TAWÉ and the Wrist

Based on the conceptual design of TAWÉ, the kinematics of the human-exoskeleton system can be formulated. This section discusses the coupled kinematics of the TAWÉ and forearm. When the user wears TAWÉ, a closed kinematic chain is created by the coupling of TAWÉ and forearm mechanisms whose individual kinematic chains are opened. The connection points of the kinematic chains can be established at the attachment points where IMU 1 and IMU 2 are installed. Hence, we approach the kinematic modeling by defining the forearm and exoskeleton as two subsystems, which are labeled as “ $a$ ” and “ $e$ ”, respectively.

### 2.2.1 3D Kinematic Transformation

We first review the mathematical notations of 3D kinematic transformations used in this section. For any pair of Frames  $i$  and  $j$  in the 3D space, the transformation from Frame  $i$  to Frame  $j$  can be represented by a homogeneous matrix  $\mathbf{T}_{i,j} \in \mathbb{R}^{4 \times 4}$  which satisfies the following equations

$$\mathbf{T}_{i,j} = \begin{bmatrix} \boldsymbol{\Omega}_{i,j} & \mathbf{d}_{i,j} \\ \mathbf{0}_{1 \times 3} & 1 \end{bmatrix} = \mathbf{T}_{j,i}^{-1}; \quad \mathbf{T}_{j,i} = \begin{bmatrix} \boldsymbol{\Omega}_{i,j}^T & -\boldsymbol{\Omega}_{i,j}^T \mathbf{d}_{i,j} \\ \mathbf{0}_{1 \times 3} & 1 \end{bmatrix} \quad (2.1)$$

where  $\boldsymbol{\Omega} \in \mathbb{R}^{3 \times 3}$  and  $\mathbf{d} \in \mathbb{R}^3$  are the rotation matrix and translational displacement, respectively. The rotation matrix  $\boldsymbol{\Omega}_{i,j}$  is an orthogonal matrix that satisfies  $\boldsymbol{\Omega}_{i,j}^{-1} = \boldsymbol{\Omega}_{i,j}^T = \boldsymbol{\Omega}_{j,i}$ . A 3D rotation  $\boldsymbol{\Omega}_{i,j}$  can also be represented by a corresponding unit quaternion vector  $\boldsymbol{\xi}_{i,j} \in \mathbb{R}^4$  [39]. A unit quaternion  $\boldsymbol{\xi} = [\xi_{\bar{w}}, \xi_{\bar{x}}, \xi_{\bar{y}}, \xi_{\bar{z}}]^T$  that describes rotation  $\boldsymbol{\Omega}$  has the following properties

$$\boldsymbol{\xi}^* = \begin{bmatrix} \xi_{\bar{w}} & -\xi_{\bar{x}} & -\xi_{\bar{y}} & -\xi_{\bar{z}} \end{bmatrix}^T \quad (2.2a)$$

$$\|\boldsymbol{\xi}\|_2^2 = \xi_{\bar{w}}^2 + \xi_{\bar{x}}^2 + \xi_{\bar{y}}^2 + \xi_{\bar{z}}^2 = 1 \quad (2.2b)$$

$$\boldsymbol{\Omega}(\boldsymbol{\xi}) = \begin{bmatrix} -2\xi_{\bar{y}}^2 - 2\xi_{\bar{z}}^2 + 1 & 2\xi_{\bar{x}}\xi_{\bar{y}} - 2\xi_{\bar{w}}\xi_{\bar{z}} & 2\xi_{\bar{w}}\xi_{\bar{y}} + 2\xi_{\bar{x}}\xi_{\bar{z}} \\ 2\xi_{\bar{w}}\xi_{\bar{z}} + 2\xi_{\bar{x}}\xi_{\bar{y}} & -2\xi_{\bar{x}}^2 - 2\xi_{\bar{z}}^2 + 1 & 2\xi_{\bar{y}}\xi_{\bar{z}} - 2\xi_{\bar{w}}\xi_{\bar{x}} \\ 2\xi_{\bar{x}}\xi_{\bar{z}} - 2\xi_{\bar{w}}\xi_{\bar{y}} & 2\xi_{\bar{w}}\xi_{\bar{x}} + 2\xi_{\bar{y}}\xi_{\bar{z}} & -2\xi_{\bar{x}}^2 - 2\xi_{\bar{y}}^2 + 1 \end{bmatrix} \quad (2.2c)$$

where Eq. (2.2a) calculates the conjugate of the quaternion, and Eq. (2.2c) converts the quaternion to the rotation matrix.

Another representation of rotation can be Euler angles [39], which represents 3D rotation with three sequential rotations along orthogonal axes. There exists multiple sets of Euler

angles that represent the same rotation based on different rotation sequence configurations. In this work, the default Euler angles  $\boldsymbol{\kappa}$  is defined as the intrinsic  $\vec{z} - \vec{y} - \vec{x}$  (or equivalently extrinsic  $\vec{x} - \vec{y} - \vec{z}$ ), which can be calculated from the quaternion  $\boldsymbol{\xi}$  as

$$\boldsymbol{\kappa}(\boldsymbol{\xi}) = \begin{bmatrix} \kappa_{\vec{x}} \\ \kappa_{\vec{y}} \\ \kappa_{\vec{z}} \end{bmatrix} = \begin{bmatrix} \text{atan2}(2\xi_{\vec{w}}\xi_{\vec{x}} + 2\xi_{\vec{y}}\xi_{\vec{z}}, \xi_{\vec{w}}^2 - \xi_{\vec{x}}^2 - \xi_{\vec{y}}^2 + \xi_{\vec{z}}^2) \\ \text{asin}(2\xi_{\vec{w}}\xi_{\vec{y}} - 2\xi_{\vec{x}}\xi_{\vec{z}}) \\ \text{atan2}(2\xi_{\vec{w}}\xi_{\vec{z}} + 2\xi_{\vec{x}}\xi_{\vec{y}}, \xi_{\vec{w}}^2 + \xi_{\vec{x}}^2 - \xi_{\vec{y}}^2 - \xi_{\vec{z}}^2) \end{bmatrix} \quad (2.3)$$

so that it represent the rotation as

$$\boldsymbol{\Omega}(\boldsymbol{\kappa}) = \boldsymbol{\Omega}_{\vec{z}}(\kappa_{\vec{z}})\boldsymbol{\Omega}_{\vec{y}}(\kappa_{\vec{y}})\boldsymbol{\Omega}_{\vec{x}}(\kappa_{\vec{x}}) \quad (2.4)$$

where  $\boldsymbol{\Omega}_i$  is the rotation matrix along  $i$  axis (for  $i = x, y, z$ ). It should be noted that all Euler angles suffer from "Gimbal Lock", which occurs when the second rotation reaches an angle that cause the axes of the first and third rotations to coincide. This leads to lost of DOF and singularity in  $\boldsymbol{\Omega}$  when calculated based on  $\boldsymbol{\kappa}$ .

To describe the evolution of rotation along time, by defining  $\boldsymbol{\omega}_{i,j} = [\omega_{\vec{x},i,j}, \omega_{\vec{y},i,j}, \omega_{\vec{z},i,j}]^T$  as the angular velocity of Frame  $j$  in Frame  $i$ , the 1st order time-derivative of  $\boldsymbol{\Omega}_{i,j}$  can be written as

$$\dot{\boldsymbol{\Omega}}_{i,j} = \text{skew}(\boldsymbol{\omega}_{i,j})\boldsymbol{\Omega}_{i,j} = \begin{bmatrix} 0 & -\omega_{\vec{z},i,j} & \omega_{\vec{y},i,j} \\ \omega_{\vec{z},i,j} & 0 & -\omega_{\vec{x},i,j} \\ -\omega_{\vec{y},i,j} & \omega_{\vec{x},i,j} & 0 \end{bmatrix} \boldsymbol{\Omega}_{i,j} \quad (2.5)$$

where "skew()" produces a  $3 \times 3$  skew-symmetric matrix from the angular velocity. Similarly, the 1st order time-derivative of  $\boldsymbol{\xi}_{i,j}$  can be expressed as

$$\dot{\boldsymbol{\xi}}_{i,j} = 0.5 \begin{bmatrix} 0 & \boldsymbol{\omega}_{i,j}^T \end{bmatrix}^T \boldsymbol{\xi}_{i,j} \quad (2.6)$$

### 2.2.2 Kinematics of TAWE

Figure 2.4 shows the main coordinate frames in the forearm-TAWE system and their transformations. Here, Frame A1 and A2 are defined in the forearm kinematic chain for IMU 1 and IMU 2, respectively. Similarly, Frame E1 and E2 are the coordinate frames of IMU 1 and IMU 2 in the exoskeleton kinematic chain, respectively. With respect to the global frame defined as Frame G, Frames A1 and E1 are also defined as floating bases, whose coordinates  $\mathbf{q}_{a,\text{base}}$ ,  $\mathbf{q}_{e,\text{base}} \in \mathbb{R}^6$  are respectively defined in their 1st order time-derivatives as

$$\dot{\mathbf{q}}_{a,\text{base}} = \begin{bmatrix} \dot{\mathbf{d}}_{a,\text{base}}^T & \boldsymbol{\omega}_{a,\text{base}}^T \end{bmatrix}^T; \quad \dot{\mathbf{q}}_{e,\text{base}} = \begin{bmatrix} \dot{\mathbf{d}}_{e,\text{base}}^T & \boldsymbol{\omega}_{e,\text{base}}^T \end{bmatrix}^T; \quad (2.7)$$

where symbols  $\mathbf{d}_{\text{base}}$  and  $\boldsymbol{\omega}_{\text{base}}$  respectively represents the translational displacements and angular velocities of the bases defined in the global frame. The linkage kinematics of the exoskeleton can be directly acquired from the mechanism design. The transforma-

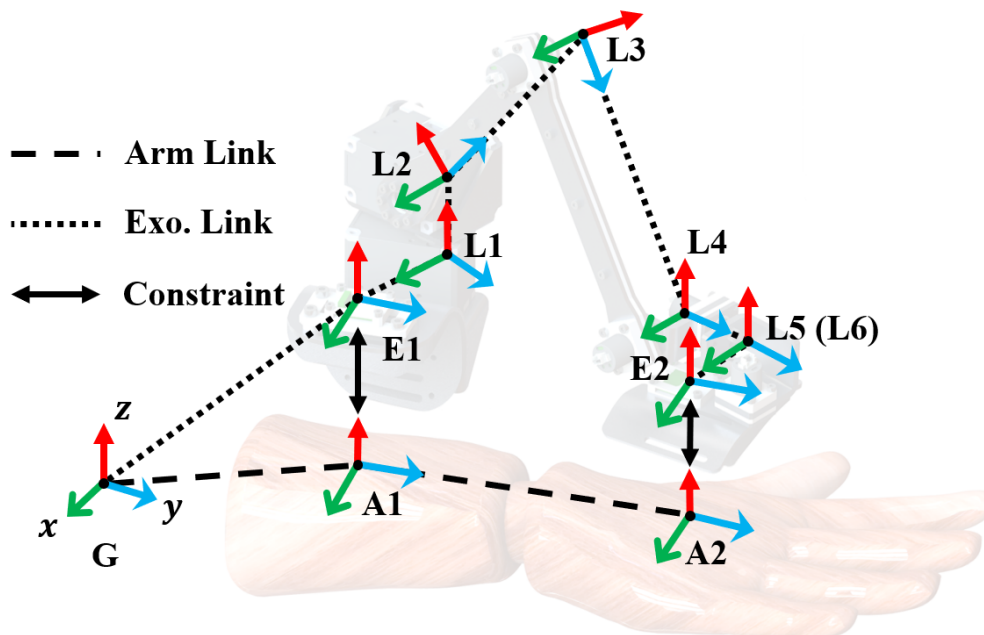


Figure 2.4: Overview of the kinematics of the forearm and TAWE [177], where the coordinate frames are labeled and the link between the frames are marked.

Table 2.1: Properties of homogeneous transformations between coordinate frames, where the numerical values are the default design parameters of TAWE.

From	To	Translation ( $\mathbf{d}$ )	Rotation ( $\mathbf{\Omega}$ )
E1	L1	$\mathbf{d}_{e,1} = [-6.8; 1.2; 0]$ cm	$\mathbf{\Omega}_{e,1}\mathbf{\Omega}_{\bar{z}}(q_{e,exo,1})$
L1	L2	$d_{\bar{z}} = 2.15$ cm	$\mathbf{\Omega}_{\bar{x}}(q_{e,exo,2})$
L2	L3	$d_{\bar{y}} = 12$ cm	$\mathbf{\Omega}_{\bar{x}}(q_{e,exo,3})$
L3	L4	$d_{\bar{y}} = 12$ cm	$\mathbf{\Omega}_{\bar{x}}(q_{e,exo,4})$
L4	L5	$d_{\bar{y}} = 3$ cm	$\mathbf{\Omega}_{\bar{y}}(q_{e,exo,5})$
L5	L6	$d_{\bar{x}} = 1$ cm	$\mathbf{\Omega}_{\bar{z}}(q_{e,exo,6})$
L6	E2	$\mathbf{d}_{e,2} = [0; -3; -0.5]$ cm	$\mathbf{\Omega}_{e,2}$

tions between the frames in the exoskeleton kinematic chain are demonstrated in Table 2.1, where the default parameters of the design are also included. In the table, the terms marked as  $\mathbf{d}_k$  and  $\mathbf{\Omega}_k$  stand for the translation and rotation along the  $k$  axis, respectively. The generalized coordinate for joint angles in the TAWE mechanism are defined in  $\mathbf{q}_{e,exo} = [q_{e,exo,1}, q_{e,exo,2}, q_{e,exo,3}, q_{e,exo,4}, q_{e,exo,5}, q_{e,exo,6}]^T \in \mathbb{R}^6$ . The rotation matrices  $\mathbf{\Omega}_e$  are constant as they are not functions of  $\mathbf{q}_{e,exo}$ .

Finally, we specify the homogeneous transformation matrix from Frame E1 to Frame E2 as

$$\mathbf{T}_{E1,E2}(\mathbf{q}_{e,exo}) = \begin{bmatrix} \mathbf{\Omega}_{e,end}(\mathbf{q}_{e,exo}) & \mathbf{d}_{e,end}(\mathbf{q}_{e,exo}) \\ \mathbf{0}_{1 \times 3} & 1 \end{bmatrix} \quad (2.8)$$

The kinematic properties  $\mathbf{d}_{e,end}$ ,  $\mathbf{\Omega}_{e,end}$ , and the corresponding unit quaternion  $\xi_{e,end}$  for rotation will be used later in the definition of kinematic constraints.

### 2.2.3 Kinematics of the Wrist

As discussed in Section 1.2.1, unlike common sequential rotational joints (e.g., universal joint), the wrist is a constrained 3D rotational joint where WFE and RUD movements are

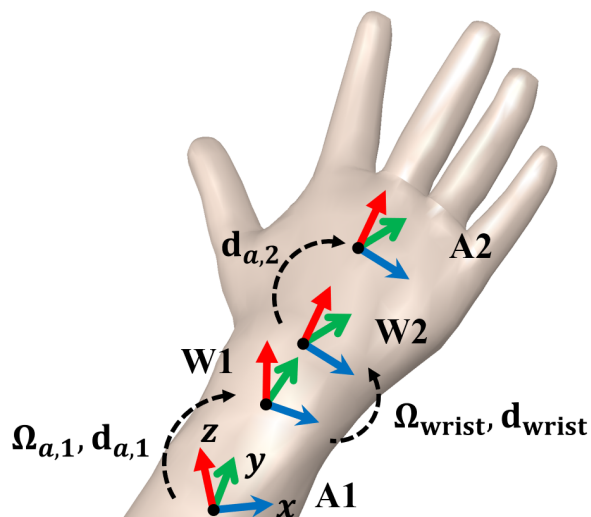


Figure 2.5: The wrist kinematic chain in a right human forearm [176], where the Frame A1 is located at the forearm, Frame A2 is located at the hand. The wrist motions take place between the intermediate frames, i.e., Frames W1 and W2.

coupled. A right human forearm is presented in Fig. 2.5. Same as in Fig. 2.4, Frames A1 and A2 are located at the forearm and hand, respectively. The wrist motions take place between the intermediate frames, i.e., Frame W1 and Frame W2. With respect to Frame W1, WFE is defined along  $\vec{x}$  direction, RUD is defined along  $\vec{z}$  direction, and  $\vec{y}$  direction is approximately the FPS direction.

The transformations between frames are shown in Tab. 2.2, where  $\mathbf{d}_{a,1}$  and  $\mathbf{d}_{a,2}$  are constant translational displacements. The coordinate frames are defined so that rotation  $\Omega_{a,1}$  between Frames A1 and W1 is fixed. Also, we assume no rotational displacement between Frames

Table 2.2: Properties of transformations between coordinate frames from the wrist kinematic system shown in Fig. 2.4.

From	To	Translation ( $\mathbf{d}$ )	Rotation ( $\Omega$ )
A1	W1	$\mathbf{d}_{a,1}$	$\Omega_{a,1}$
W1	W2	$\mathbf{d}_{\text{wrist}}$	$\Omega_{\text{wrist}}$
W2	A2	$\mathbf{d}_{a,2}$	$\mathbf{I}_3$

W2 and A2.

The transformation between Frames W1 and W2 is governed by  $\mathbf{\Omega}_{\text{wrist}}$  and  $\mathbf{d}_{\text{wrist}}$ , which are rotation of the wrist and the slight translational displacement during wrist movement, respectively. We introduce the generalized coordinates  $\mathbf{q}_{a,\text{wrist}}$  written as

$$\mathbf{q}_{a,\text{wrist}} = \begin{bmatrix} q_{a,\text{wrist},\bar{x}} & q_{a,\text{wrist},\bar{y}} & q_{a,\text{wrist},\bar{z}} \end{bmatrix}^T \quad (2.9)$$

whose elements are related to the 3D rotations, which will be specified later. We also define the unit quaternion  $\boldsymbol{\xi}_{\text{wrist}}$  that represents  $\mathbf{\Omega}_{\text{wrist}}$ , which leads to the following relationships

$$\mathbf{d}_{\text{wrist}} = \mathbf{f}_{d,\text{wrist}}(\boldsymbol{\xi}_{\text{wrist}}) \quad (2.10a)$$

$$r_{\lambda,\text{wrist}}(\boldsymbol{\xi}_{\text{wrist}}) = 0 \quad (2.10b)$$

where Eq. (2.10a) states that the  $\mathbf{d}_{\text{wrist}}$  is dependent on the rotation of the wrist, and Eq. (2.10b) indicates that a kinematic constraint  $r_{\lambda,\text{wrist}}$  exists, which constraints one of the DOF from  $\mathbf{q}_{\text{wrist}}$  to realize the 2-DOF wrist rotational movement.

In real life,  $r_{\lambda,\text{wrist}}$  is determined by the musculoskeletal model of the wrist, which is sophisticated and different among various user profiles. In earlier studies, the wrist kinematics is often approximated by sequential rotational joints, where multiple rotations take place one after another [11, 26, 42, 49, 100, 104, 141]. These models are uniquely defined by their rotation sequences. Two examples of sequential rotational joints are the first-WFE-then-RUD model [100, 104] and the first-RUD-then-WFE model [186]. Both models take the form of universal joints, where the WFE and RUD rotations are separated along two orthogonal axes. Provided that the rotation angles of WFE and RUD are  $\rho_{\text{WFE}}$  and  $\rho_{\text{RUD}}$ , for the

first-WFE-then-RUD model, the rotation matrix  $\Omega_{\text{wrist,FWTR}}$  can be written as

$$\Omega_{\text{wrist,FWTR}} = \Omega_{\vec{x}}(\rho_{\text{WFE}})\Omega_{\vec{z}}(\rho_{\text{RUD}}) \quad (2.11)$$

and for the first-RUD-then-WFE model, the rotation matrix  $\Omega_{\text{wrist,FRTW}}$  is

$$\Omega_{\text{wrist,FRTW}} = \Omega_{\vec{z}}(\rho_{\text{RUD}})\Omega_{\vec{x}}(\rho_{\text{WFE}}) \quad (2.12)$$

It is easy to observe that, for the same pair of  $\rho_{\text{WFE}}$  and  $\rho_{\text{RUD}}$ , the rotation matrices  $\Omega_{\text{wrist,FWTR}}$  and  $\Omega_{\text{wrist,FRTW}}$  are different. Hence, depending on the design of the sequential rotational joints, the resulting constraint  $r_{\lambda,\text{wrist}}$  can be different.

For both sequential rotation models above, it is possible to select  $\mathbf{q}_{\text{wrist}}$  as

$$\mathbf{q}_{\text{wrist}} = \left[ \rho_{\text{WFE}} \quad \rho_{\text{wrist},\vec{y}} \quad \rho_{\text{RUD}} \right]^T \quad (2.13)$$

so that  $\xi_{\text{wrist}}$  can also be explicit expressed by  $\mathbf{q}_{\text{wrist}}$ . Note that we define the rotation  $\rho_{\text{wrist},\vec{y}}$  as the internal rotation of the wrist that takes place between  $\rho_{\text{RUD}}$  and  $\rho_{\text{WFE}}$ . While Eq. (2.13) is used for sequential rotation models, the definition of  $\rho_{\text{WFE}}$ ,  $\rho_{\text{wrist},\vec{y}}$ , and  $\rho_{\text{RUD}}$  do not necessary follow the notion of Euler angles introduced in Section 2.2.1. The constraint for the above sequential rotational joints can simply be

$$r_{\lambda,\text{wrist}} = \rho_{\text{wrist},\vec{y}} = 0 \quad (2.14)$$

On the other hand,  $\mathbf{q}_{\text{wrist}}$  can also be selected so that its 1st order time derivative satisfies

$$\dot{\mathbf{q}}_{\text{wrist}} = \omega_{\text{wrist}} \quad (2.15)$$

where  $\boldsymbol{\omega}_{\text{wrist}}$  is the locally defined angular velocity of Frame W2 with respect to W1. This selection more generally applicable to any possible wrist rotation model regardless of rotation sequences.

Same as in the modeling of TAWK Kinematics, we also specify the homogeneous transformation matrix from Frame A1 to Frame A2 as

$$\mathbf{T}_{A1,A2}(\boldsymbol{\xi}_{\text{wrist}}) = \begin{bmatrix} \boldsymbol{\Omega}_{a,\text{end}}(\boldsymbol{\xi}_{\text{wrist}}) & \mathbf{d}_{a,\text{end}}(\boldsymbol{\xi}_{\text{wrist}}) \\ \mathbf{0}_{1 \times 3} & 1 \end{bmatrix} \quad (2.16)$$

where  $\mathbf{d}_{a,\text{end}}$ ,  $\boldsymbol{\Omega}_{a,\text{end}}$ , and the corresponding  $\boldsymbol{\xi}_{a,\text{end}}$  will be used in the constraint definition.

## 2.2.4 Nonholonomic Kinematic Constraints

Based on the above setups of the forearm and TAWK kinematics, the generalized coordinates of the two subsystems can be written as

$$\mathbf{q}_a = \begin{bmatrix} \mathbf{q}_{a,\text{base}}^T & \mathbf{q}_{a,\text{wrist}}^T \end{bmatrix}^T; \quad \mathbf{q}_e = \begin{bmatrix} \mathbf{q}_{e,\text{base}}^T & \mathbf{q}_{e,\text{exo}}^T \end{bmatrix}^T \quad (2.17)$$

which yields 21 DOFs in total. The DOF of the model can be reduced by applying the kinematic constraints. By considering the attachment between the forearm and TAWK as a rigid connection, each attachment will constrain 6 DOFs. The constraint  $\mathbf{r}_{\lambda,\text{base}} \in \mathbb{R}^6$  between Frame A1 and E1 can be written as

$$\mathbf{r}_{\lambda,\text{base}}(\mathbf{q}_{e,\text{exo}}, \boldsymbol{\xi}_{a,\text{base}}, \boldsymbol{\xi}_{e,\text{base}}) = \begin{bmatrix} \mathbf{d}_{a,\text{base}} - \mathbf{d}_{e,\text{base}} \\ \begin{bmatrix} \mathbf{0}_{3 \times 1} & \mathbf{I}_3 \end{bmatrix} (\boldsymbol{\xi}_{a,\text{base}}^* \times \boldsymbol{\xi}_{e,\text{base}}) \end{bmatrix} \quad (2.18)$$

and the constraint  $\mathbf{r}_{\lambda,\text{end}} \in \mathbb{R}^6$  between Frame A2 and Frame E2 can be written as

$$\mathbf{r}_{\lambda,\text{end}}(\mathbf{q}_{e,\text{exo}}, \boldsymbol{\xi}_{\text{wrist}}) = \begin{bmatrix} \mathbf{d}_{a,\text{end}} - \mathbf{d}_{e,\text{end}} \\ \mathbf{0}_{3 \times 1} \quad \mathbf{I}_3 (\boldsymbol{\xi}_{a,\text{end}}^* \times \boldsymbol{\xi}_{a,\text{end}}) \end{bmatrix} \quad (2.19)$$

To incorporate the constraint  $\mathbf{r}_{\lambda,\text{base}}$ , we may simply have  $\mathbf{q}_{a,\text{base}} = \mathbf{q}_{e,\text{base}}$  so that the bases of two subsystems are merged. While  $\mathbf{r}_{\lambda,\text{base}}$  constrains the TAWE mechanism DOFs to the wrist movements,  $\mathbf{q}_{e,\text{exo}}$  cannot be easily explicitly expressed by  $\mathbf{q}_{a,\text{wrist}}$  due to the complexity. Also, when we choose the general design of  $\mathbf{q}_{\text{wrist}}$  based on Eq. (2.15),  $\mathbf{q}_{a,\text{wrist}}$  cannot represent the rotation  $\boldsymbol{\Omega}_{\text{wrist}}$ , and the relationship between the unit quaternion  $\boldsymbol{\xi}_{\text{wrist}}$  and  $\mathbf{q}_{a,\text{wrist}}$  is nonholonomic. Similarly, the constraint  $r_{\lambda,\text{wrist}}$  in the wrist from Eq. (2.10b) can also be nonholonomic in terms of  $\mathbf{q}_{a,\text{wrist}}$ . Therefore, we combine the nonholonomic constraints  $\mathbf{r}_{\lambda,\text{base}}$  and  $r_{\lambda,\text{wrist}}$  into

$$\mathbf{r}_{\lambda,\text{nh}}(\mathbf{q}_{e,\text{exo}}, \boldsymbol{\xi}_{\text{wrist}}) = \begin{bmatrix} \mathbf{r}_{\lambda,\text{end}}^T & r_{\lambda,\text{wrist}} \end{bmatrix}^T \quad (2.20)$$

where “nh” stands for nonholonomic. The 1st order time-derivative of  $\mathbf{r}_{\lambda,\text{nh}}$  can be expressed by  $\dot{\mathbf{q}}_{e,\text{exo}}$  and  $\dot{\mathbf{q}}_{a,\text{wrist}}$

$$\dot{\mathbf{r}}_{\lambda,\text{nh}} = \mathbf{J}_{\lambda,\text{nh},\text{indep}}(\mathbf{q}_{e,\text{exo}}, \boldsymbol{\xi}_{\text{wrist}}) \dot{\mathbf{q}}_{\text{indep}} + \mathbf{J}_{\lambda,\text{nh},\text{dep}}(\mathbf{q}_{e,\text{exo}}, \boldsymbol{\xi}_{\text{wrist}}) \dot{\mathbf{q}}_{\text{dep}} \quad (2.21)$$

where the dependent coordinate  $\mathbf{q}_{\text{dep}} \in \mathbb{R}^7$  and independent coordinate  $\mathbf{q}_{\text{indep}} \in \mathbb{R}^2$  are defined as

$$\mathbf{q}_{\text{dep}} = \begin{bmatrix} \mathbf{q}_{e,\text{exo}}^T & q_{\text{wrist},\bar{y}} \end{bmatrix}^T ; \quad \mathbf{q}_{\text{indep}} = \begin{bmatrix} q_{\text{wrist},\bar{x}} & q_{\text{wrist},\bar{z}} \end{bmatrix}^T \quad (2.22)$$

The constraint Jacobian matrices  $\mathbf{J}_{\lambda,\text{nh},\text{indep}} \in \mathbb{R}^{7 \times 2}$  and  $\mathbf{J}_{\lambda,\text{nh},\text{dep}} \in \mathbb{R}^{7 \times 7}$  corresponds to independent and dependent coordinates, respectively. If we have  $\text{rank}(\mathbf{J}_{\lambda,\text{nh},\text{dep}}) = 7$ , we

obtain

$$\dot{\mathbf{q}}_{\text{dep}} = -\mathbf{J}_{\lambda,\text{nh,dep}}^{-1} \mathbf{J}_{\lambda,\text{nh,indep}} \dot{\mathbf{q}}_{\text{indep}} \quad (2.23)$$

which is a nonholonomic representation of  $\dot{\mathbf{q}}_{\text{dep}}$  using  $\dot{\mathbf{q}}_{\text{indep}}$ . Furthermore, by taking the derivative of Eq. (2.23), the acceleration  $\ddot{\mathbf{q}}_{\text{dep}}$  can be calculated as

$$\ddot{\mathbf{q}}_{\text{dep}} = -\mathbf{J}_{\lambda,\text{nh,dep}}^{-1} (\mathbf{J}_{\lambda,\text{nh,indep}} \ddot{\mathbf{q}}_{\text{indep}} + \dot{\mathbf{J}}_{\lambda,\text{nh,indep}} \dot{\mathbf{q}}_{\text{indep}} - \dot{\mathbf{J}}_{\lambda,\text{nh,dep}} \mathbf{J}_{\lambda,\text{nh,dep}}^{-1} \mathbf{J}_{\lambda,\text{nh,indep}} \dot{\mathbf{q}}_{\text{indep}}) \quad (2.24)$$

Therefore, provided that  $\mathbf{J}_{\lambda,\text{nh,indep}}$  is non-singular, it is possible to reduce the dimensionality of the kinematics with the use of  $\ddot{\mathbf{q}}_{\text{indep}}$ . In the next section, Eqs. (2.23, 2.24) are crucial to the modeling of the coupled human-exoskeleton dynamical system.

## 2.3 Human-Exoskeleton Multibody Dynamics

This section analyzes the coupled dynamics of TAWE and the wrist via a generalized multi-body framework. Following the kinematic modeling in the previous section, the human musculoskeletal model and the exoskeleton model can be written as

$$\begin{aligned} \mathbf{M}_a(\mathbf{q}_a, \boldsymbol{\rho}_a) \ddot{\mathbf{q}}_a &= -\mathbf{C}_a(\mathbf{q}_a, \boldsymbol{\rho}_a, \dot{\mathbf{q}}_a) \dot{\mathbf{q}}_a - \mathbf{g}_a(t, \mathbf{q}_a, \boldsymbol{\rho}_a, \dot{\mathbf{q}}_a) \\ &\quad + \mathbf{J}_{u,a}^T(\mathbf{q}_a, \boldsymbol{\rho}_a) \mathbf{u}_a + \mathbf{J}_{w,a}^T(\mathbf{q}_a, \boldsymbol{\rho}_a) \mathbf{w}_a + \mathbf{J}_{\lambda,a}^T(\mathbf{q}_a, \boldsymbol{\rho}_a) \boldsymbol{\lambda} \end{aligned} \quad (2.25a)$$

$$\dot{\boldsymbol{\rho}}_a = \mathbf{J}_{\rho,a}(\mathbf{q}_a, \boldsymbol{\rho}_a) \dot{\mathbf{q}}_a \quad (2.25b)$$

$$\begin{aligned} \mathbf{M}_e(\mathbf{q}_e, \boldsymbol{\rho}_e) \ddot{\mathbf{q}}_e &= -\mathbf{C}_e(\mathbf{q}_e, \boldsymbol{\rho}_e, \dot{\mathbf{q}}_e) \dot{\mathbf{q}}_e - \mathbf{g}_e(t, \mathbf{q}_e, \boldsymbol{\rho}_e, \dot{\mathbf{q}}_e) \\ &\quad + \mathbf{J}_{u,e}^T(\mathbf{q}_e, \boldsymbol{\rho}_e) \mathbf{u}_e + \mathbf{J}_{w,e}^T(\mathbf{q}_e, \boldsymbol{\rho}_e) \mathbf{w}_e + \mathbf{J}_{\lambda,e}^T(\mathbf{q}_e, \boldsymbol{\rho}_e) \boldsymbol{\lambda} \end{aligned} \quad (2.25c)$$

$$\dot{\boldsymbol{\rho}}_e = \mathbf{J}_{\rho,e}(\mathbf{q}_e, \boldsymbol{\rho}_e) \dot{\mathbf{q}}_e \quad (2.25d)$$

where  $t \in \mathbb{R}_+$  is time;  $\mathbf{q}$  are the generalized coordinates from Eq. (2.17);  $\boldsymbol{\rho}$  are the nonholonomic states that cannot be written in the closed-form expression of  $\mathbf{q}$ .  $\mathbf{u}$  is the generalized control input;  $\mathbf{M}$ ,  $\mathbf{C}$ , and  $\mathbf{g}$  are respectively the inertia matrix, Coriolis and centripetal matrix, and generalized force vector. We also introduce  $\mathbf{w}$  as the system disturbance. The Jacobian matrices  $\mathbf{J}_u$ ,  $\mathbf{J}_\rho$ , and  $\mathbf{J}_w$  respectively corresponding to  $\mathbf{u}$ ,  $\boldsymbol{\rho}$ , and  $\mathbf{w}$  are dependent on the kinematic properties only. Finally,  $\boldsymbol{\lambda}$  is the Lagrange Multiplier that act as the constraint forces within and between the human and exoskeleton subsystems. The Jacobian matrix  $\mathbf{J}_\lambda$  indicates the direction of the constraint forces. The specific formulation of multibody dynamics follows a symbolic-numerical formalism explained in Appendix B.

In practice, the musculoskeletal model of the forearm can be extremely complicated. The soft-tissue artifacts including skins and muscles can introduce uncertainties to the system, which are difficult to model and control. In this study, we propose two model assumptions

- (MA. 1) The soft body dynamics from the muscles and tissues in the musculoskeletal model is considered as perturbations within  $\mathbf{w}$ .
- (MA. 2) Loads from the user are generalized into direct forces/torques acting at the human joints, which are included in  $\mathbf{g}$  as a function of time.

These model assumptions limit the scope of the multibody analysis to rigid body dynamics. The upcoming subsections will explain the coupling of the forearm and exoskeleton, and the feasibility of TAWÉ in providing full actuation to wrist movements for tremor suppression.

### 2.3.1 Coupled Dynamical Model

The general multibody formulation in Eq. (2.25) outlines the structure of the governing equation for the forearm and TAWÉ. Based on the kinematics from Section 2.2, we can

specify nonholonomic states  $\boldsymbol{\rho}_a$  and  $\boldsymbol{\rho}_e$  as follows

$$\boldsymbol{\rho}_a = \begin{bmatrix} \boldsymbol{\xi}_{a,\text{base}}^T & \boldsymbol{\xi}_{\text{wrist}}^T \end{bmatrix}^T; \quad \boldsymbol{\rho}_e = \boldsymbol{\xi}_{e,\text{base}} \quad (2.26)$$

The coupled human-exoskeleton system labeled with “cp” can written as

$$\begin{aligned} \mathbf{M}_{\text{cp}}(\mathbf{q}_{\text{cp}}, \boldsymbol{\rho}_{\text{cp}}) \ddot{\mathbf{q}}_{\text{cp}} &= -\mathbf{C}_{\text{cp}}(\mathbf{q}_{\text{cp}}, \boldsymbol{\rho}_{\text{cp}}, \dot{\mathbf{q}}_{\text{cp}}) \dot{\mathbf{q}}_{\text{cp}} - \mathbf{g}_{\text{cp}}(t, \mathbf{q}_{\text{cp}}, \boldsymbol{\rho}_{\text{cp}}, \dot{\mathbf{q}}_{\text{cp}}) \\ &\quad + \mathbf{J}_{u,\text{cp}}^T(\mathbf{q}_{\text{cp}}, \boldsymbol{\rho}_{\text{cp}}) \mathbf{u}_{\text{cp}} + \mathbf{J}_{w,\text{cp}}^T(\mathbf{q}_{\text{cp}}, \boldsymbol{\rho}_{\text{cp}}) \mathbf{w}_{\text{cp}} \end{aligned} \quad (2.27a)$$

$$\dot{\boldsymbol{\rho}}_{\text{cp}} = \mathbf{J}_{\rho,\text{cp}}(\mathbf{q}_{\text{cp}}, \boldsymbol{\rho}_{\text{cp}}) \dot{\mathbf{q}}_{\text{cp}} \quad (2.27b)$$

which is a unconstrained dynamical system, where  $\mathbf{q}_{\text{cp}}$  and  $\boldsymbol{\rho}_{\text{cp}}$  are selected as

$$\mathbf{q}_{\text{cp}} = \begin{bmatrix} \mathbf{q}_{\text{base}}^T & \mathbf{q}_{\text{indep}}^T \end{bmatrix}^T; \quad \boldsymbol{\rho}_{\text{cp}} = \begin{bmatrix} \mathbf{q}_{e,\text{base}}^T & \mathbf{q}_{\text{dep}}^T & \boldsymbol{\xi}_{\text{base}}^T & \boldsymbol{\xi}_{\text{wrist}}^T \end{bmatrix}^T \quad (2.28)$$

To realize the coupling, similar as in Eq. (2.23), we need to present the dependent coordinate with the independent coordinates in the nonholonomic form. Here we define the  $\mathbf{J}_{\lambda,\text{indep}} \in \mathbb{R}^{13 \times 8}$  and  $\mathbf{J}_{\lambda,\text{dep}} \in \mathbb{R}^{13 \times 13}$  so that

$$\begin{bmatrix} \dot{\mathbf{r}}_{\lambda,\text{base}} \\ \dot{\mathbf{r}}_{\lambda,\text{end}} \\ \dot{r}_{\lambda,\text{wrist}} \end{bmatrix} = \mathbf{0} = \mathbf{J}_{\lambda,\text{indep}}(\mathbf{q}_{\text{cp}}, \boldsymbol{\rho}_{\text{cp}}) \dot{\mathbf{q}}_{\text{cp}} + \mathbf{J}_{\lambda,\text{dep}}(\mathbf{q}_{\text{cp}}, \boldsymbol{\rho}_{\text{cp}}) \begin{bmatrix} \dot{\mathbf{q}}_{e,\text{base}} \\ \dot{\mathbf{q}}_{\text{dep}} \end{bmatrix} \quad (2.29)$$

If we can obtain  $\text{rank}(\mathbf{J}_{\lambda,\text{dep}}) = 13$ , we can obtain  $\mathbf{J}_{\text{indep,dep}} \in \mathbb{R}^{13 \times 8}$  so that

$$\mathbf{J}_{\text{indep,dep}} = -\mathbf{J}_{\lambda,\text{dep}}^{-1} \mathbf{J}_{\lambda,\text{indep}}; \quad \begin{bmatrix} \dot{\mathbf{q}}_{e,\text{base}}^T & \dot{\mathbf{q}}_{\text{dep}}^T \end{bmatrix}^T = \mathbf{J}_{\text{indep,dep}} \dot{\mathbf{q}}_{\text{cp}} \quad (2.30)$$

and the 1st order time derivative  $\dot{\mathbf{J}}_{\text{indep,dep}}$  is

$$\dot{\mathbf{J}}_{\text{indep,dep}} = -\mathbf{J}_{\lambda,\text{dep}}^{-1} (\dot{\mathbf{J}}_{\lambda,\text{indep}} - \dot{\mathbf{J}}_{\lambda,\text{dep}} \mathbf{J}_{\lambda,\text{dep}}^{-1} \mathbf{J}_{\lambda,\text{indep}}) \quad (2.31)$$

Also, the specific structure of  $\mathbf{J}_{\text{indep,dep}}$  can be written as

$$\mathbf{J}_{\text{indep,dep}} = \begin{bmatrix} \mathbf{I}_6 & \mathbf{0} \\ \mathbf{0} & -\mathbf{J}_{\lambda,\text{nh,dep}}^{-1} \mathbf{J}_{\lambda,\text{nh,indep}} \end{bmatrix} \quad (2.32)$$

since  $\mathbf{q}_{a,\text{base}} = \mathbf{q}_{e,\text{base}}$ , and the base generalized coordinates are not involved in  $\mathbf{r}_{\lambda,\text{wrist}}$ .

Based on the above setup, we can further construct a coupling matrix  $\mathbf{J}_{\text{cp}} \in \mathbb{R}^{21 \times 8}$ , which can be written as

$$\mathbf{J}_{\text{cp}} = \begin{bmatrix} \mathbf{I}_7 & 0 & \mathbf{0}_{7 \times 12} & 0 \\ \mathbf{0}_{1 \times 7} & 0 & \mathbf{0}_{1 \times 12} & 1 \\ \mathbf{0}_{1 \times 7} & 1 & \mathbf{0}_{1 \times 12} & 0 \\ \mathbf{0}_{12 \times 7} & 0 & \mathbf{I}_{12} & 0 \end{bmatrix} \begin{bmatrix} \mathbf{I}_8 \\ \mathbf{J}_{\text{indep,dep}} \end{bmatrix} \quad (2.33)$$

so that the coupled constraints can be calculated as

$$\begin{aligned} \mathbf{M}_{\text{cp}} &= \mathbf{J}_{\text{cp}}^T \begin{bmatrix} \mathbf{M}_a & \mathbf{0} \\ \mathbf{0} & \mathbf{M}_e \end{bmatrix} \mathbf{J}_{\text{cp}}; & \mathbf{C}_{\text{cp}} &= \mathbf{J}_{\text{cp}}^T \begin{bmatrix} \mathbf{C}_a & \mathbf{0} \\ \mathbf{0} & \mathbf{C}_e \end{bmatrix} \mathbf{J}_{\text{cp}} + \mathbf{J}_{\text{cp}}^T \begin{bmatrix} \mathbf{M}_a & \mathbf{0} \\ \mathbf{0} & \mathbf{M}_e \end{bmatrix} \dot{\mathbf{J}}_{\text{cp}}; \\ \mathbf{g}_{\text{cp}} &= \mathbf{J}_{\text{cp}}^T \begin{bmatrix} \mathbf{g}_a \\ \mathbf{g}_e \end{bmatrix}; & \mathbf{J}_{u,\text{cp}} &= \begin{bmatrix} \mathbf{J}_{u,a} & \mathbf{0} \\ \mathbf{0} & \mathbf{J}_{u,e} \end{bmatrix} \mathbf{J}_{\text{cp}}; & \mathbf{J}_{w,\text{cp}} &= \begin{bmatrix} \mathbf{J}_{w,a} & \mathbf{0} \\ \mathbf{0} & \mathbf{J}_{w,e} \end{bmatrix} \mathbf{J}_{\text{cp}} \end{aligned} \quad (2.34)$$

and the control input  $\mathbf{u}_{\text{cp}}$  and disturbance  $\mathbf{w}_{\text{cp}}$  are selected as

$$\mathbf{u}_{\text{cp}} = \begin{bmatrix} \mathbf{u}_a^T & \mathbf{u}_e^T \end{bmatrix}^T; \quad \mathbf{w}_{\text{cp}} = \begin{bmatrix} \mathbf{w}_a^T & \mathbf{w}_e^T \end{bmatrix}^T \quad (2.35)$$

By incorporating the constraints between the forearm and TAWE, the coupled dynamical model has only 8 DOFs. The dependent coordinates and nonholonomic states are presented in a nonholonomic manner. It should be noted that in numerical simulations, the constrained dynamics can be calculated in a more general manner (see Appendix B). The constrained dynamical model, however, is crucial to the development of the control system.

### 2.3.2 Base Excitation and Actuation

This subsection discusses the further specification of forearm-TAWE dynamics in terms of base excitation and actuation. As shown in Eq. (2.27), six of the DOFs of the system are related to the acceleration of the base. While this model is more general in terms of describing musculoskeletal dynamics, it has more DOFs than that can be controlled by TAWE. Therefore, we further specify the control-targeting dynamical model for TAWE control system development, which is labeled by “ct”.

For the control-targeting dynamical model, the generalized coordinate  $\mathbf{q}_{ct} \in \mathbb{R}^2$  of this system is selected as

$$\mathbf{q}_{ct} = \mathbf{q}_{indep} = \begin{bmatrix} q_{wrist,\bar{x}} & q_{wrist,\bar{z}} \end{bmatrix}^T \quad (2.36)$$

As the inertia matrix  $\mathbf{M}_{cp}$  is symmetric and positive definite (i.e.,  $\mathbf{M}_{cp} = \mathbf{M}_{cp}^T > 0$ ) based on formulation, it can be represented in the following structure

$$\mathbf{M}_{cp} = \begin{bmatrix} \mathbf{M}_{cp,1,1} & \mathbf{M}_{cp,1,2} \\ \mathbf{M}_{cp,1,2}^T & \mathbf{M}_{ct} \end{bmatrix} \quad (2.37)$$

where the block matrix  $\mathbf{M}_{ct} \in \mathbb{R}^{2 \times 2}$  remains symmetric and positive definite. It should also be noted that  $\mathbf{M}_{ct}$  does not contain any inertial properties from floating bases, since those properties are defined on the coordinate frames that involve  $\mathbf{q}_{a,base}$  and  $\mathbf{q}_{e,base}$  only.

In the previous parts of the modeling, the dynamical properties that were not unspecified are the control input  $\mathbf{u}_{cp}$  and disturbance  $\mathbf{w}_{cp}$ . Here, based on (MA. 2), we specify the control inputs as (recall that  $\mathbf{u}_{cp} = [\mathbf{u}_a^T, \mathbf{u}_e^T]^T$ )

$$\mathbf{u}_a = \begin{bmatrix} \mathbf{u}_{base}^T & \mathbf{u}_{wrist}^T \end{bmatrix}^T ; \quad \mathbf{u}_e = \mathbf{u}_{exo} \quad (2.38)$$

where the  $\mathbf{u}_{base} \in \mathbb{R}^6$ ,  $\mathbf{u}_{wrist} \in \mathbb{R}^2$ , and  $\mathbf{u}_{exo} \in \mathbb{R}^2$  are respectively the inputs for base excitation, muscle actuations for WFE and RUD motions, and exoskeleton servomotor inputs. The disturbances can be formulated in a similar way as (recall that  $\mathbf{w}_{cp} = [\mathbf{w}_a^T, \mathbf{w}_e^T]^T$ )

$$\mathbf{w}_a = \begin{bmatrix} \mathbf{w}_{base}^T & \mathbf{w}_{wrist}^T \end{bmatrix}^T ; \quad \mathbf{w}_e = \mathbf{w}_{exo}; \quad (2.39)$$

where  $\mathbf{w}_{base}$ ,  $\mathbf{w}_{wrist}$ , and  $\mathbf{w}_{exo}$  are the model perturbations and disturbances in the base, wrist, and exoskeleton, respectively. Since disturbances can come from multiple sources, their dimensions are not specified at the current stage. For the control-targeting model, the control input is selected as

$$\mathbf{u}_{ct} = \begin{bmatrix} \mathbf{u}_{wrist}^T & \mathbf{u}_{exo}^T \end{bmatrix}^T ; \quad (2.40)$$

and correspondingly, the structure of input Jacobian matrix  $\mathbf{J}_{u,cp}$  can be written as

$$\mathbf{J}_{u,cp} = \begin{bmatrix} \mathbf{J}_{u,cp,1,1} & \mathbf{J}_{u,cp,1,2} \\ \mathbf{J}_{u,cp,2,1} & \mathbf{J}_{u,ct} \end{bmatrix}; \quad (2.41)$$

which satisfies  $\mathbf{J}_{u,cp,1,2} \in \mathbb{R}^{4 \times 2}$ .

The above setup leads to the control-targeting dynamical model as

$$\mathbf{M}_{ct} \ddot{\mathbf{q}}_{ct} = -\mathbf{C}_{ct} \dot{\mathbf{q}}_{ct} - \mathbf{g}_{ct} + \mathbf{J}_{u,ct}^T \mathbf{u}_{ct} + \mathbf{J}_{w,ct}^T \mathbf{w}_{cp} \quad (2.42)$$

where the properties are calculated as

$$\mathbf{C}_{ct} = \begin{bmatrix} \mathbf{0}_{6 \times 2} \\ \mathbf{I}_2 \end{bmatrix}^T \mathbf{C}_{cp} \begin{bmatrix} \mathbf{0}_{6 \times 2} \\ \mathbf{I}_2 \end{bmatrix}; \quad \mathbf{g}_{ct} = \mathbf{g}_{ct,base} + \begin{bmatrix} \mathbf{0}_{6 \times 2} \\ \mathbf{I}_2 \end{bmatrix}^T \mathbf{g}_{cp}; \quad \mathbf{J}_{w,ct} = \begin{bmatrix} \mathbf{0}_{6 \times 2} \\ \mathbf{I}_2 \end{bmatrix}^T \mathbf{J}_{w,cp}; \quad (2.43a)$$

$$\mathbf{g}_{ct,base} = \mathbf{M}_{cp,1,2}^T \ddot{\mathbf{q}}_{a,base} + \begin{bmatrix} \mathbf{0}_{2 \times 6} & \mathbf{I}_2 \end{bmatrix} \mathbf{C}_{cp}^T \begin{bmatrix} \mathbf{I}_6 \\ \mathbf{0}_{2 \times 2} \end{bmatrix} \dot{\mathbf{q}}_{a,base} - \mathbf{J}_{u,cp,1,2}^T \mathbf{u}_{a,base} \quad (2.43b)$$

Therefore,  $\mathbf{g}_{ct,base}$  is the generalized force from the base that is transmitted to the wrist. In real life, the exact value of  $\mathbf{g}_{ct,base}$  is difficult to observe. Hence, in this study, we consider  $\mathbf{g}_{ct,base}$  as a part of the generalized system force, which will be assumed as a part of model uncertainty in later analyses.

Equation (2.42) indicates that the input Jacobian  $\mathbf{J}_{u,ct}$  determines the controllability of the system from  $\mathbf{u}_{ct}$ . Since  $\mathbf{u}_{ct}$  is composed of the input from the wrist muscle  $\mathbf{u}_{a,wrist}$  and the exoskeleton  $\mathbf{u}_{e,exo}$  based on Eq. (2.40), we can also divide  $\mathbf{J}_{u,ct}$  accordingly. For  $\mathbf{u}_{a,wrist}$ , the generalized muscle actuation torques are defined to be directly exerted on the generalized coordinates  $\mathbf{q}_{ct}$ , we can express  $\mathbf{J}_{u,ct}$  as

$$\mathbf{J}_{u,ct} = \begin{bmatrix} \mathbf{I}_2 & \mathbf{J}_{u,exo}^T \end{bmatrix}^T \quad (2.44)$$

so that finalized the form of the control-targeting dynamical model can be written as

$$\mathbf{M}_{ct} \ddot{\mathbf{q}}_{ct} = -\mathbf{C}_{ct} \dot{\mathbf{q}}_{ct} - \mathbf{g}_{ct} + \mathbf{u}_{wrist} + \mathbf{J}_{u,exo}^T \mathbf{u}_{exo} + \mathbf{J}_{w,ct}^T \mathbf{w}_{cp} \quad (2.45)$$

Finally, it should be noted that the control-targeting dynamical model is simply an alternate representation of a part of the coupled dynamical model. During numerical evaluation, the properties in Eq. (2.45) are calculated from the original coupled dynamics in Eq. (2.27).

### 2.3.3 Numerical Modeling Validation

To verify the correctness of the above modeling process, we numerically simulate the dynamics of forearm-TAWE assembly modeled in two different engines - ANDY (see Appendix B) [180] in MATLAB and V-REP [43]. Since V-REP is a robotics toolbox based on numerical multibody formalism, it solves the simulation of multibody systems with kinematic constraints differently. The 3D visualization of simulations is demonstrated in Fig. 2.6. In both simulations, the models adopt the first-RUD-then-WFE model, which leads to

$$\mathbf{q}_{ct} = \boldsymbol{\rho}_{\text{wrist,main}} = \begin{bmatrix} \rho_{\text{WFE}} & \rho_{\text{RUD}} \end{bmatrix}^T \quad (2.46)$$

based on the holonomic generalized coordinate selection in Eq. (2.13).

As the primary goal is to verify the analytical model realized symbolically with ANDY, the control input  $\mathbf{u}_{\text{exo}}$  in each simulation is generated to track the same planned reference using PD controllers (the formulation will be discussed in Section 4.3). While the PD feedback controller components are designed based on states from each simulation, the feedforward controller components in both simulations are calculated based on dynamical properties formulated from the analytical model. The result is shown in Fig. 2.7, despite the differences

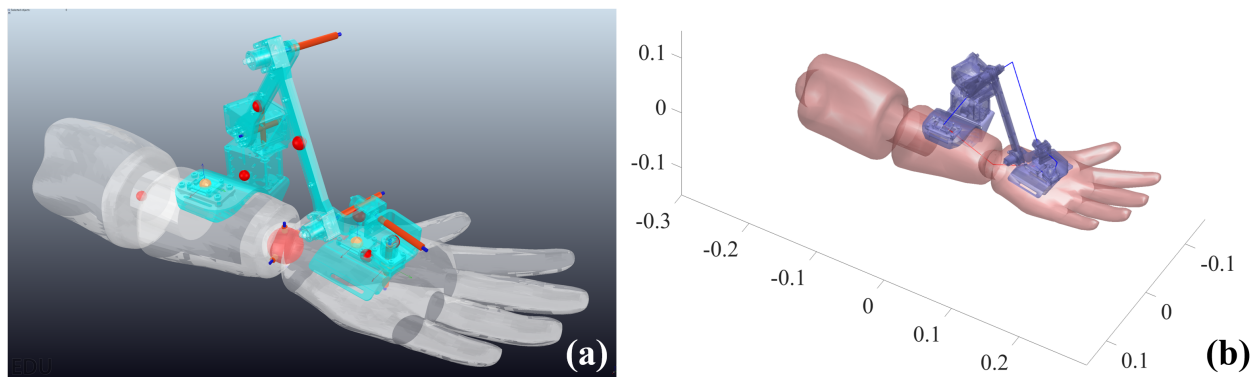


Figure 2.6: 3D models from the simulations in (a) V-REP and (b) ANDY [177].

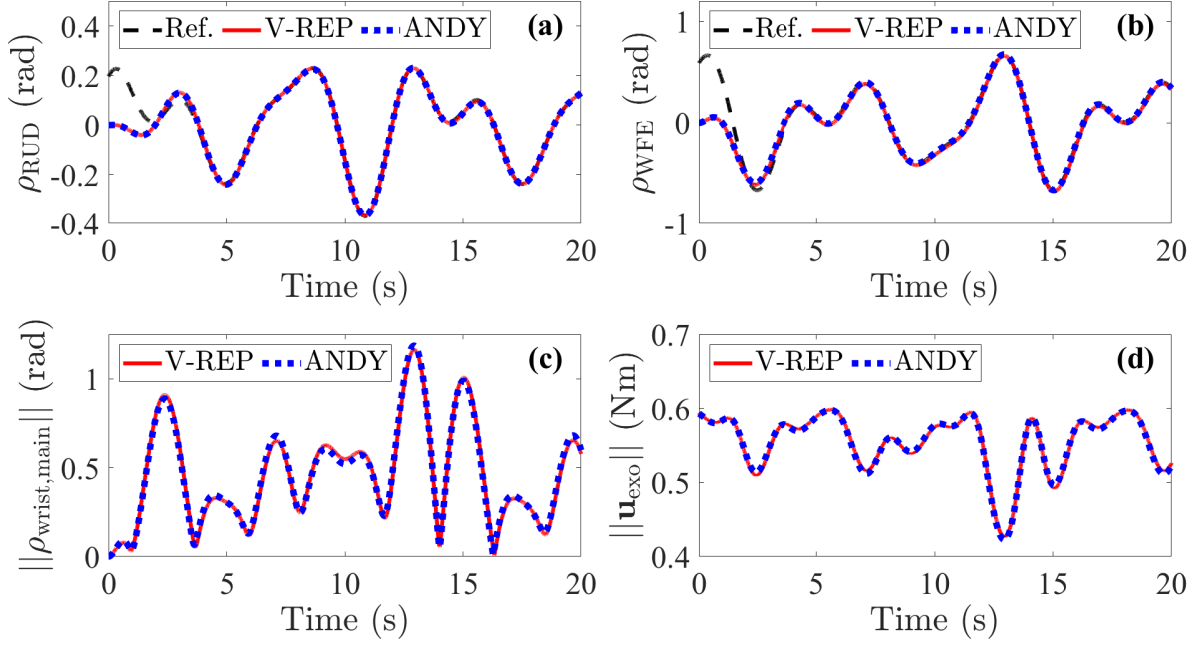


Figure 2.7: Simulation validation between the models in V-REP and ANDY, where the subplots displays: (a) the tracking trajectory of  $\rho_{\text{RUD}}$ ; (b) the tracking trajectory of  $\rho_{\text{WFE}}$ ; (c) the norm of rotation angle vector  $\|\rho_{\text{wrist,main}}\|$ ; and (d) the norm of input  $\|\mathbf{u}_{\text{exo}}\|$ .

in multibody formalism, the states and control inputs from both systems are approximately identical. This indicates the correctness of the analytical model, which makes it valid for upcoming analyses and control system development.

### 2.3.4 Workspace and Controllability

The control-targeting dynamical model also indicates the controllability of TAWE to realize full actuation of the wrist movements. Recall that from the previous derivations,  $\mathbf{J}_{\mathbf{u},\text{exo}}$  is a kinematic Jacobian based on the positional states of the system only. Since  $\mathbf{M}_{\text{ct}} = \mathbf{M}_{\text{ct}}^{\text{T}} > 0$ , the necessary condition to ensure that  $\mathbf{u}_{\text{exo}}$  can fully actuate the system is

$$\text{rank}(\mathbf{M}_{\text{ct}}^{-1}\mathbf{J}_{\mathbf{u},\text{exo}}) = \text{rank}(\mathbf{J}_{\mathbf{u},\text{exo}}) = 2 \quad (2.47)$$

Therefore, the condition of  $\mathbf{J}_{u,\text{exo}}$  determines the validity of TAWE in the workspace. If  $\mathbf{J}_{u,\text{exo}}$  has large eigenvalues, the actuators will have good input efficiency into the system. Any singularity that appears in  $\mathbf{J}_{u,\text{exo}}$  will cause incapability in controlling full wrist motion. Although it is shown in Fig. 2.2 that TAWE has adequate reachability in following wrist motion, valid control conditions may not be obtainable throughout the workspace of TAWE.

An important observation is that, for a fixed set of design parameters, the wrist model makes a significant difference in the controllability of the human exoskeleton system. To demonstrate this, we have compared the conditions of  $\mathbf{J}_{u,\text{exo}}$  in the workspaces when TAWE is respectively attached to forearms with the first-RUD-then-WFE (from Eq. (2.12)) and the first-WFE-then-RUD (from Eq. (2.11)) models. As previously mentioned, for these sequential rotational joints, the generalized coordinates are selected as the rotation angles Eq. (2.13) instead of the default selection in Eq. (2.15). In this case, we have  $\rho_{RUD}$  and  $\rho_{WFE}$  as pure RUD and WFE rotations, respectively.

The workspace condition is quantified by the ratio  $f_{u,\text{exo,eigen,ratio}}$  defined as

$$f_{u,\text{exo,eigen,ratio}}(z_{u,\text{exo,eigen},1}, z_{u,\text{exo,eigen},2}) = |z_{u,\text{exo,eigen},1}|/|z_{u,\text{exo,eigen},2}|; \quad (2.48)$$

where  $z_{u,\text{exo,eigen},1}$  and  $z_{u,\text{exo,eigen},2}$  are the two eigenvalues of  $\mathbf{J}_{u,\text{exo}}$ , which satisfies  $|z_{u,\text{exo,eigen},1}| \leq |z_{u,\text{exo,eigen},2}|$ . When  $f_{u,\text{exo,eigen,ratio}} = 1$ , the eigenvalues are complex conjugates with the same norm; when  $f_{u,\text{exo,eigen,ratio}} = 0$ , it means that  $z_{u,\text{exo,eigen},1} = 0$ , which indicates that the workspace is invalid due to singularity of  $\mathbf{J}_{u,\text{exo}}$ .

Figure 2.8 compares the maps of  $f_{u,\text{exo,eigen,ratio}}$  calculated from the models under the first-RUD-then-WFE and the first-WFE-then-RUD wrist joints and different design parameters [176]. An arbitrary contour of  $f_{u,\text{exo,eigen,ratio}} = 0.5$  is drawn to separate the areas of inadequate control conditions. Since large difference between the norms of eigenvalue can

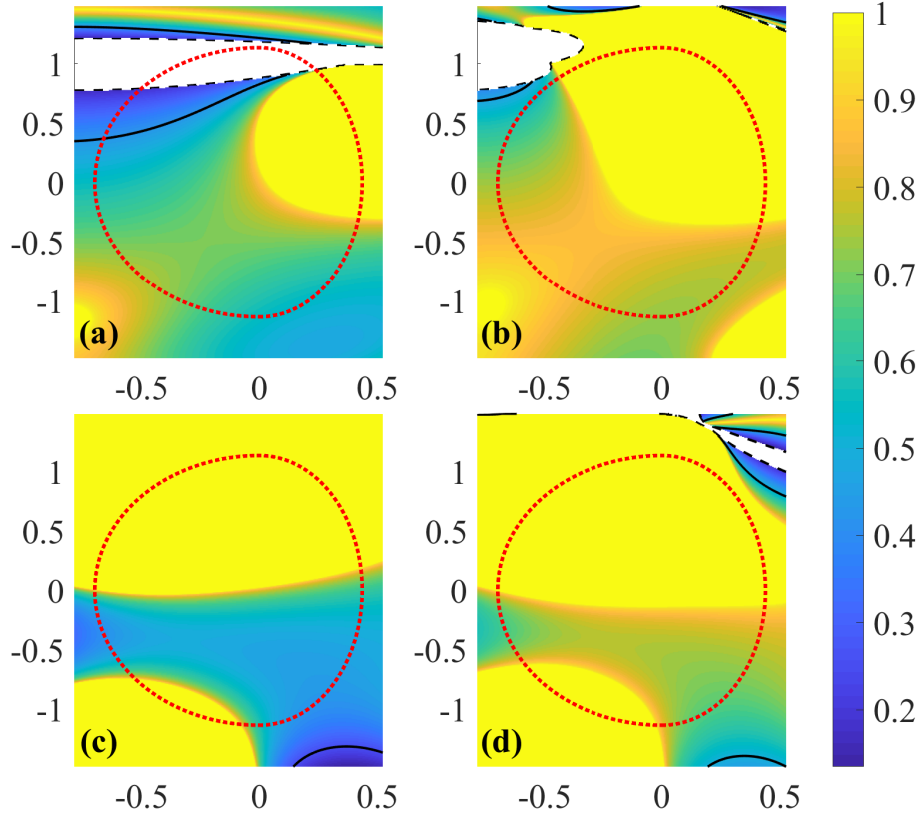


Figure 2.8: Map of the eigenvalue norm ratio  $f_{u,exo,eigen,ratio}$  calculated from  $J_{u,exo}$  under different wrist models and design parameters [177], where (a) first-RUD-then-WFE with  $d_{\bar{y}} = 0$ ,  $d_{\bar{x}} = 0$ , (b) first-RUD-then-WFE with  $d_{\bar{y}} = 3$  cm,  $d_{\bar{x}} = 1$  cm, (c) first-WFE-then-RUD with  $d_{\bar{y}} = 0$ ,  $d_{\bar{x}} = 0$ , and (d) first-WFE-then-RUD with  $d_{\bar{y}} = 3$  cm,  $d_{\bar{x}} = 1$  cm; axes: horizontal - RUD (rad), vertical - WFE (rad); black dash:  $z_{u,exo,eigen,1} < 0.25$ ; black solid:  $f_{u,exo,eigen,ratio} < 0.25$ ; red dot: approximate wrist circumduction envelope;  $d_{\bar{y}} = 0$  and  $d_{\bar{x}}$  are the translations between Frames L4 and L6 in 2.1.

lead to unbalanced actuator input load, we consider the vicinity area of singularity where  $z_{u,exo,eigen,1} < 0.25$  as workspace with bad control condition. While the examined workspace is  $-85^\circ \sim 85^\circ$  in FE and  $-45^\circ \sim 30^\circ$  in RUD, the critical workspace is contained within the contour similar to the circumduction envelope, whose contour passes through  $-65^\circ$  and  $65^\circ$  in pure FE motion as well as  $-40^\circ$  and  $25^\circ$  in pure RUD motion.

In Fig. 2.8(a) there are no axle offsets between the Euler joint of the wrist exoskeleton, i.e., the translational displacements from Frame L4 to Frame L6 in Tab. 2.1 are zeros.

The singularity region passes through the workspace when TAWE is coupled with the first-RUD-then-WFE wrist joint. This problem was also witnessed previously in [179]. However, zero-offset works well for TAWE with the first-WFE-then-RUD wrist model, as shown in Fig. 2.8(c). The Euler joint offset parameters are then modified. It is observed that by increasing  $d_{\bar{x}}$  between Frames L5 and L6, the invalid workspace can be avoided in the case of the first-RUD-then-WFE wrist joint. Doing so will, however, move the singularity region closer to the circumduction envelope in the first-WFE-then-RUD cases. Increasing  $d_{\bar{y}}$  between Frames L4 and L5 only slightly improves the control condition in the first-RUD-then-WFE case. Finally, the parameter selection of  $d_y = 30$  mm and  $d_x = 10$  mm can provide satisfying workspace conditions under both models as shown in Fig. 2.8(b) and Fig. 2.8(d).

The workspace and controllability analysis revealed the effect of wrist kinematics on the controllability of the human-exoskeleton system using control inputs from TAWE. While adjusting the design parameters may improve the control conditions, a fundamental problem to be solved is the modeling of the wrist. As discussed earlier, the musculoskeletal kinematics of the wrist is more complicated than both the first-RUD-then-WFE and first-WFE-then-RUD models. A more generalized wrist kinematic model will help explore design parameters that are more compatible with different user profiles.

## 2.4 Summary

This chapter introduced the conceptual design of TAWE - a high-degree-of-freedom wearable exoskeleton for tremor alleviation. The conceptual design demonstrated that the exoskeleton supports unconstrained wrist movements in a wide range. TAWE is also equipped with electronics to provide full measurements of wrist motions, and servomotors to realize control input. We then analyzed the kinematics of the human-exoskeleton coupled system, which

leads to the formulation of a closed kinematic chain that constrains all exoskeleton DOFs to wrist movements. The kinematics and constraints paved the road to the multibody analysis of the human-exoskeleton dynamics following a generalized framework. Through transformations and derivations, we eventually reached the control-targeting dynamical model from Eq. (2.42), which will be used for the control system development in the later chapters.

Finally, the human-exoskeleton dynamical model indicated that wrist kinematics is crucial to its controllability through actuation inputs from the servomotors in TAWÉ. Through workspace analysis, we noticed that there exist areas where TAWÉ cannot effectively actuate wrist movements. The controllability condition can be improved by adjusting the mechanism design parameters of TAWÉ.

To realize a model-based controller for the control-targeting dynamical model in Eq. (2.42), the information of the wrist is indispensable. In practice, not only is the wrist kinematics more complicated than the sequential rotational joints applied in this chapter, the wrist profile of a user is also unknown by default. This requires the TAWÉ control system to be able to identify the kinematic model of the wrist. As discussed in Section 2.1, TAWÉ is not fixed to specific locations on the user forearm for each usage, which also affects the underlying closed-loop kinematic chain information needed for controller design. Hence, the next chapter will address the solution to real-time wrist kinematics identification.

# Chapter 3

## Real-Time Wrist Kinematics Identification

This chapter discusses the real-time modeling and identification of wrist kinematics, which is a crucial part of the control system of TAWE. From the design of TAWE and the dynamics of the human-exoskeleton system explained in the previous chapter, two major challenges related the wrist kinematics are raised as follows:

1. The wrist kinematic model is crucial to exoskeleton control. While different sequential rotational joints (e.g., the first-WFE-then-RUD model [100, 104] and first-RUD-then-WFE model [186]) are applied in earlier studies, they govern different kinematic behaviors, lacks generality, and are unable to describe the coupling between rotation and internal translations in the wrist.
2. Since TAWE is wearable through sleeves, gloves, and Velcro strips, the closed kinematic chain can change every time when TAWE is attached to a different spot on the forearm. The attachment locations may also slowly shift and slide over time.

These challenges lead to the development of a real-time wrist kinematics identification (WKI) algorithm based on a novel ellipsoidal joint formulation [176]. The ellipsoidal joint, unlike sequential rotational joints, employs a quaternion-based constraint to characterize the constrained 3D rotation of the wrist [181]. With specific modifications of the expression, the

quaternion-based constraint can lead to constrained wrist rotations identical to the corresponding sequential rotations. The ellipsoidal joint also introduces geometric constraints to couple internal wrist translational motions with WFE and RUD rotations [147].

Based on the ellipsoidal joint formulation, we further generalize the WKI regression model by using 2D Fourier linear combiners (FLC) to compensate for model discrepancies. Extended Kalman Filter (EKF) is then implemented for real-time nonlinear regression. We also promote the sparsity by designing a smooth observable function that realizes  $\ell^1$ -minimization [5, 25]. The sparsity-promoting EKF (SP-EKF) ensures the accurate identification of primary wrist kinematic parameters under noisy conditions. We compare the WKI performances with different algorithm configurations through simulations that employ various reference models. A lab-developed wrist kinematics measurement tool (WKMT) is later used to collect data for experimental validations.

The rest of the chapter is arranged as follows. Section 3.1 presents the ellipsoidal joint formulation and the WKI regression model. Section 3.2 introduces the WKMT design and discusses the theories of the SP-EKF. Numerical simulations are presented in Section 3.3 to validate analytical findings and study the performance of the WKI algorithm. Section 3.4 discusses the experimental results of the WKI algorithm based on wrist motion data collected by WKMT. Finally, Section 3.5 summarizes the findings in this chapter. (The study in this chapter has been partially reported in [176].)

### 3.1 Ellipsoidal Joint Model for Wrist Kinematics

An ellipsoidal joint is illustrated in Fig. 3.1, which is similar to a ball joint except that the rotation of the oval ball can be constrained by the ellipsoidal socket. In the figure, Frames W1 and W2 are defined the same as those from Fig. 2.5. Following this idea, we introduce

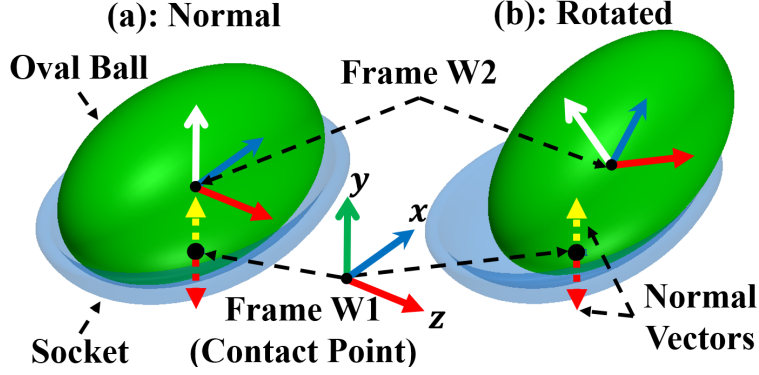


Figure 3.1: Illustration of an ellipsoidal joint [176], where the origin of Frame W1 is located at the bottom of the ellipsoidal socket, which is also the contact point between the oval ball and the ellipsoidal socket, and Frame W2 is located at the center of the oval ball. The normal vectors are respectively perpendicular to the oval ball and ellipsoidal socket surfaces at the contact point. The  $\vec{y}$  axis of Frame W1 is colinear with the normal vectors.

the quaternion-based constraint to bind the internal wrist rotation along  $\vec{y}$  direction (i.e.,  $\rho_{\text{wrist},\vec{y}}$ ) to the WFE and RUD movements (i.e.,  $\rho_{\text{WFE}}$  and  $\rho_{\text{RUD}}$ ) along  $\vec{x}$  and  $\vec{z}$  directions, respectively. The basic constraint is written as

$$r_{\lambda,\text{wrist},0} = \begin{bmatrix} 1 & \mathbf{0}_{1 \times 3} \end{bmatrix} \left( \begin{bmatrix} \mathbf{0}_{1 \times 2} & 1 & 0 \end{bmatrix}^T \times \boldsymbol{\xi}_{\text{wrist}} \right) = 0 \quad (3.1)$$

The effect of  $r_{\lambda,\text{wrist},0}$  can be interpreted from the 3D axis-angle perspective [39], i.e., the 3D rotation axis vector of  $\boldsymbol{\Omega}_{\text{wrist}}$  is constrained on the  $\vec{x}$ - $\vec{z}$  plane of Frame W1. If we define the rotation sequence as the intrinsic  $\vec{z}$ - $\vec{y}$ - $\vec{z}$  Euler angles  $\boldsymbol{\kappa}$ , so that  $\rho_{\text{wrist},\vec{y}}$  takes place between  $\rho_{\text{WFE}}$  and  $\rho_{\text{RUD}}$ , the explicit solution for  $\rho_{\text{wrist},\vec{y}}$  from Eq. (3.1) is

$$\rho_{\text{wrist},\vec{y}} = 2 \arctan \left( \frac{-\sin(\rho_{\text{WFE}}/2) \sin(\rho_{\text{RUD}}/2)}{\cos(\rho_{\text{WFE}}/2) \cos(\rho_{\text{RUD}}/2)} \right) \quad (3.2)$$

This shows that the constraint does not set  $\rho_{\text{wrist},\vec{y}} = 0$ , which also indicates that  $\rho_{\text{RUD}}$  and  $\rho_{\text{WFE}}$  are non-orthogonal rotations.

### 3.1.1 Relationship to Sequential Rotational Joints

As previously mentioned, the basic quaternion constraint in Eq. (3.1) can be modified with additional specific terms so that the wrist rotation is identical to the sequential rotation joints from previous studies. Here we present three examples.

The first example is the first-RUD-then-WFE orthogonal joint model [186]. If the quaternion-based constraint is modified into

$$r_{\lambda, \text{wrist}}(\boldsymbol{\xi}_{\text{wrist}}) = r_{\lambda, \text{wrist}, 0} + \sin(\rho_{\text{WFE}}/2) \sin(\rho_{\text{RUD}}/2) = 0 \quad (3.3)$$

then we obtain the constrained rotation  $\boldsymbol{\Omega}_{\text{wrist}}$  identical to  $\boldsymbol{\Omega}_{\text{wrist, FRTW}}$  from Eq. (2.12). Similarly, for the first-WFE-then-RUD orthogonal joint [100, 104], the equivalent constraint is

$$r_{\lambda, \text{wrist}}(\boldsymbol{\xi}_{\text{wrist}}) = r_{\lambda, \text{wrist}, 0} - \sin(\rho_{\text{WFE}}/2) \sin(\rho_{\text{RUD}}/2) = 0 \quad (3.4)$$

then we obtain the constrained rotation  $\boldsymbol{\Omega}_{\text{wrist}}$  identical to  $\boldsymbol{\Omega}_{\text{wrist, FWTR}}$  from Eq. (2.11). Finally, some studies model the wrist rotation with two serially connected orthogonal joints, which respectively approximate the radiocarpal and midcarpal joints. As an example, the WFE-RUD-WFE-RUD joint can be written as [55, 71]

$$\boldsymbol{\Omega}_{\text{wrist, half}} = \boldsymbol{\Omega}_{\bar{x}}(\rho_{\text{WFE}}/2) \boldsymbol{\Omega}_{\bar{z}}(\rho_{\text{RUD}}/2); \quad \boldsymbol{\Omega}_{\text{wrist, WRWR}} = \boldsymbol{\Omega}_{\text{wrist, half}} \boldsymbol{\Omega}_{\text{wrist, half}} \quad (3.5)$$

Hence, the modified quaternion-based constraint designed as

$$r_{\lambda, \text{wrist}} = r_{\lambda, \text{wrist}, 0} - \sin(\rho_{\text{WFE}}/2) \sin(\rho_{\text{RUD}}/2)/2 = 0 \quad (3.6)$$

yields  $\boldsymbol{\Omega}_{\text{wrist}}$  as the same rotation to  $\boldsymbol{\Omega}_{\text{wrist, WRWR}}$ .

Therefore, despite the sequential rotational joints from Eqs. (2.11, 2.12, 3.5) are different, their modified constraints shares the common element  $\sin(\rho_{\text{WFE}}/2)\sin(\rho_{\text{RUD}}/2)$ . The difference Eqs. (2.11, 2.12, 3.5) becomes significant when either  $\rho_{\text{RUD}}$  or  $\rho_{\text{WFE}}$  becomes large [176]. On the other hand, when  $\rho_{\text{RUD}}$  and  $\rho_{\text{WFE}}$  are close to zeros, the rotations represented by these models are close to each other. This is a very important property that will be used in the WKI model design.

### 3.1.2 Ellipsoid-Based Translational Constraints

The internal translational displacement  $\mathbf{d}_{\text{wrist}}$  in the ellipsoidal joint from Fig. 3.1 is coupled with  $\mathbf{\Omega}_{\text{wrist}}$ . Unlike a ball joint, the ellipsoidal socket and oval ball are not always concentric. By assuming that the oval ball and ellipsoidal socket surfaces are tangent and always in contact, we define the origins of Frames W1 and W2 at the contact point and the center of oval ball, respectively. This leads to a constraint based on the ellipsoid equation [147]

$$\begin{aligned} r_{\lambda, \text{wrist}, d, 1}(\boldsymbol{\xi}_{\text{wrist}}, \mathbf{d}_{\text{wrist}}) &= \mathbf{d}_{\text{wrist}}^{\text{T}} \mathbf{\Omega}_{\text{wrist}} \text{diag}\left(\begin{bmatrix} c_{\text{wrist}, d, 1}^2 & c_{\text{wrist}, d, 2}^2 & c_{\text{wrist}, d, 3}^2 \end{bmatrix}\right)^{-1} \mathbf{\Omega}_{\text{wrist}}^{\text{T}} \mathbf{d}_{\text{wrist}} - 1 \\ &= 0 \end{aligned} \quad (3.7)$$

where  $\mathbf{c}_{\text{wrist}, d} = [c_{\text{wrist}, d, 1}, c_{\text{wrist}, d, 2}, c_{\text{wrist}, d, 3}] > 0$  contains the radii of oval ball. It is also assumed that, the normal vector of the oval ball surface at the contact point is normal to the socket surface. The normal vector of the oval ball surface can be calculated by

$$\mathbf{z}_{\text{wrist}, \text{normal}}(\boldsymbol{\xi}_{\text{wrist}}, \mathbf{d}_{\text{wrist}}) = 2 \text{diag}\left(\begin{bmatrix} c_{\text{wrist}, d, 1}^2 & c_{\text{wrist}, d, 2}^2 & c_{\text{wrist}, d, 3}^2 \end{bmatrix}\right)^{-1} \mathbf{\Omega}_{\text{wrist}}^{\text{T}} \mathbf{d}_{\text{wrist}} \quad (3.8)$$

Hence, a second set of translational constraints is formed

$$\mathbf{r}_{\lambda, \text{wrist}, d, 2}(\boldsymbol{\xi}_{\text{wrist}}, \mathbf{d}_{\text{wrist}}) = \begin{bmatrix} 1 & 0 & 0 \\ 0 & 0 & 1 \end{bmatrix} \boldsymbol{\Omega}_{\text{wrist}} \mathbf{z}_{\text{wrist}, \text{normal}} = \mathbf{0} \quad (3.9)$$

which ensures that the  $\vec{y}$  axis in Frame W1 is colinear to the normal vector. This constraint also fixes the contact point at the bottom of the socket. Thus, the oval ball cannot be lifted from the socket. The explicit solution of  $\mathbf{d}_{\text{wrist}}$  as expressions of  $\boldsymbol{\xi}_{\text{wrist}}$  solved from Eq. (3.7, 3.9) are presented in Appendix A.1. Note that when  $c_{\text{wrist}, d, 1} = c_{\text{wrist}, d, 2} = c_{\text{wrist}, d, 3}$ , we can obtain a regular ball joint and a constant solution  $\mathbf{d}_{\text{wrist}} = [0, c_{\text{wrist}, d, 2}, 0]$ .

It is also important to note that  $\mathbf{d}_{\text{wrist}}$  primarily approximates the potential translations in the radiocarpal joint, where the proximal row of carpal bones rolls in the cavity formed by the radius bone and the articular disk [121]. The translation in midcarpal joint caused by the gliding between the proximal and distal rows of carpal bones is not considered in  $\mathbf{d}_{\text{wrist}}$ .

### 3.1.3 General Model for Wrist Kinematics Identification

The wrist kinematics in real life can be much more complicated than the proposed ellipsoidal joint model. Also, the expressions of  $\mathbf{d}_{\text{wrist}}$  in Eq. (A.2) are not numerically robust for regression, since  $c_{\text{wrist}, d}$  approaching zeros will result in singularities. Therefore, a general regression model is designed for the wrist kinematics identification (WKI) algorithm by referencing the proposed ellipsoidal joint model.

To begin with, the transformation between Frames A1 and A2 defined in Eq. (2.19) is

calculated from Table 2.2 as

$$\mathbf{d}_{a,\text{end}} = \mathbf{d}_{a,1} + \mathbf{\Omega}_{a,1} \mathbf{d}_{\text{wrist}} + \mathbf{\Omega}_{a,1} \mathbf{\Omega}_{\text{wrist}} \mathbf{d}_{a,2} \quad (3.10a)$$

$$\boldsymbol{\xi}_{a,\text{end}} = \boldsymbol{\xi}_{a,1} \times \boldsymbol{\xi}_{\text{wrist}} \quad (3.10b)$$

where  $\boldsymbol{\xi}_{a,1}$  is the quaternion that represents the rotation  $\mathbf{\Omega}_{a,1}$ . In practice, we can only measure  $\mathbf{d}_{a,\text{end}}$  and  $\boldsymbol{\xi}_{a,\text{end}}$ , and  $\boldsymbol{\xi}_{a,1}$ ,  $\mathbf{d}_{a,1}$ , and  $\mathbf{d}_{a,2}$  are unknown fixed parameters that need to be identified. Also,  $\mathbf{\Omega}_{\text{wrist}}$  and its quaternion  $\boldsymbol{\xi}_{\text{wrist}}$  are not directly available but instead estimated through

$$\boldsymbol{\xi}_{\text{wrist}} = \boldsymbol{\xi}_{a,1}^* \times \boldsymbol{\xi}_{a,\text{end}} \quad (3.11)$$

As previously discussed, since WFE ( $\rho_{\text{WFE}}$ ) and RUD ( $\rho_{\text{RUD}}$ ) are the main DOFs of the wrist, both  $\rho_{\text{wrist},\vec{y}}$  and  $\mathbf{d}_{\text{wrist}}$  are assumed to be constrained by  $\boldsymbol{\rho}_{\text{wrist},\text{main}} = [\rho_{\text{WFE}}, \rho_{\text{RUD}}]^T$ . Also, the range of motion of the wrist indicates that these movements are bounded within the WFE-RUD domain. Therefore, we introduce the Fourier linear combiners (FLC) to approximate the nonlinear wrist kinematics that is difficult to model [15, 171]. The FLC is designed based on the 2D Fourier series expansion with respect to  $\boldsymbol{\rho}_{\text{wrist},\text{main}}$  in the WFE-RUD domain. The 2D FLC vector  $\mathbf{z}_{\text{wrist},\text{FLC}}$  can be obtained from (note that “vec()” reshapes a matrix into a column vector)

$$\begin{bmatrix} 1 \\ \mathbf{z}_{\text{wrist},\text{FLC}} \end{bmatrix} = \text{vec} \left( \begin{bmatrix} 1 \\ \mathbf{z}_{\text{RUD},\text{FLC},n,\text{sin}} \\ \mathbf{z}_{\text{RUD},\text{FLC},n,\text{cos}} \end{bmatrix} \begin{bmatrix} 1 & \mathbf{z}_{\text{WFE},\text{FLC},n,\text{sin}}^T & \mathbf{z}_{\text{WFE},\text{FLC},n,\text{cos}}^T \end{bmatrix} \right) \quad (3.12)$$

based on the following vectors that contain sinusoidal terms

$$\mathbf{z}_{\text{RUD,FLC},n,\sin} = \begin{bmatrix} \sin(\rho_{\text{RUD}}) & \sin(2\rho_{\text{RUD}}) & \cdots & \sin(n\rho_{\text{RUD}}) \end{bmatrix}^{\text{T}} \quad (3.13a)$$

$$\mathbf{z}_{\text{WFE,FLC},n,\sin} = \begin{bmatrix} \sin(\rho_{\text{WFE}}) & \sin(2\rho_{\text{WFE}}) & \cdots & \sin(n\rho_{\text{WFE}}) \end{bmatrix}^{\text{T}} \quad (3.13b)$$

$$\mathbf{z}_{\text{RUD,FLC},n,\cos} = \begin{bmatrix} \cos(\rho_{\text{RUD}}) & \cos(2\rho_{\text{RUD}}) & \cdots & \cos(n\rho_{\text{RUD}}) \end{bmatrix}^{\text{T}} \quad (3.13c)$$

$$\mathbf{z}_{\text{WFE,FLC},n,\cos} = \begin{bmatrix} \cos(\rho_{\text{WFE}}) & \cos(2\rho_{\text{WFE}}) & \cdots & \cos(n\rho_{\text{WFE}}) \end{bmatrix}^{\text{T}} \quad (3.13d)$$

The Fourier series expansion order  $n$  is selected based on the trade-off between model complexity and approximation accuracy. In this paper, we select  $n = 2$ . Hence, we approximate the nonlinear and complicated real wrist translational  $\mathbf{d}_{\text{wrist}}$  as

$$\mathbf{d}_{\text{wrist}} \approx \mathbf{d}_{\text{wrist,est}}(\boldsymbol{\xi}_{\text{wrist}}) = \mathbf{D}_{\text{wrist},d,\text{linear}} \boldsymbol{\rho}_{\text{wrist,main}} + \mathbf{D}_{\text{wrist},d,\text{FLC}} \mathbf{z}_{\text{wrist,FLC}} \quad (3.14)$$

where  $\mathbf{D}_{\text{wrist},d,\text{linear}} \in \mathbb{R}^{3 \times 2}$  contains parameters for the linear regression component; and  $\mathbf{D}_{\text{wrist},d,\text{FLC}} \in \mathbb{R}^{3 \times ((2n+1)^2 - 1)}$  contains amplitude parameters for the 2D FLC term. Adopting  $\mathbf{d}_{\text{wrist,est}}$  leads to the general regression model for wrist translational displacement

$$\mathbf{d}_{a,\text{end}} \approx \mathbf{d}_{a,\text{end,est}} = \mathbf{d}_{a,1} + \boldsymbol{\Omega}_{a,1} \mathbf{d}_{\text{wrist}} + \boldsymbol{\Omega}_{a,1} \boldsymbol{\Omega}_{\text{wrist}} \mathbf{d}_{a,2} \quad (3.15)$$

The regression model for wrist rotational constraint is designed by modifying the basic quaternion-based constraint from Eq. (3.1), which can be written as

$$r_{\lambda,\text{wrist,est}}(\boldsymbol{\xi}_{\text{wrist}}) = r_{\lambda,\text{wrist},0}(\boldsymbol{\xi}_{\text{wrist}}) + c_{\xi} \sin(\rho_{\text{WFE}}/2) \sin(\rho_{\text{RUD}}/2) + \mathbf{c}_{\text{wrist},\Omega,\text{FLC}}^{\text{T}} \mathbf{z}_{\text{wrist,FLC}} \quad (3.16)$$

where  $c_{\xi}$  is an unknown real parameter; and  $\mathbf{c}_{\text{wrist},\Omega,\text{FLC}} \in \mathbb{R}^{(2n+1)^2 - 1}$  contains amplitude

parameters for the 2D FLC term. Based on Section 3.1.1,  $c_\xi$  can classify the characteristics of identified wrist rotation. Specifically,  $c_\xi \approx 1$  indicates similarity to the first-RUD-then-WFE joint according to Eq. (3.3);  $c_\xi \approx -1$  suggests similarity to the first-WFE-then-RUD joint based on Eq. (3.4); and  $c_\xi \approx -0.5$  indicates similarity to the WFE-RUD-WFE-RUD joint according to Eq. (3.6).

The WKI regression models in Eqs. (3.15, 3.16) contain many unknown translational and rotational parameters, which are collected in the parameter vector  $\mathbf{z}$  written as

$$\mathbf{p}_{\text{wrist}} = \left[ \boldsymbol{\xi}_{a,1}^T \quad c_\xi \quad \mathbf{c}_{\text{wrist},\Omega,\text{FLC}}^T \quad \mathbf{d}_{a,1}^T \quad \mathbf{d}_{a,2}^T \quad \text{vec}^T(\mathbf{D}_{\text{wrist},d,\text{linear}}) \quad \text{vec}^T(\mathbf{D}_{\text{wrist},d,\text{FLC}}) \right]^T \quad (3.17)$$

where  $\boldsymbol{\xi}_{a,1}$ ,  $c_\xi$ ,  $\mathbf{d}_{a,1}$ , and  $\mathbf{d}_{a,2}$  are the primary wrist kinematic parameters. In the next section, we discuss the identification of  $\mathbf{p}_{\text{wrist}}$  via sparsity-promoting extended Kalman filter.

## 3.2 Real-Time Wrist Kinematics Identification

This section explains the real-time WKI algorithm based on the generalized regression model proposed in Section 3.1.3. The online regression is carried out by the Extended Kalman Filter (EKF), which identifies the unknown kinematic parameters of the wrist from movement measurements. We also introduce a sparsity-promoting observable that helps reduce the model redundancy and identify the primary wrist parameters. Finally, we specify the EKF design for WKI based on a lab-developed Wrist Kinematics Measurement Tool (WKMT) that provides data collection.

### 3.2.1 Extended Kalman Filter

To solve the real-time parameter identification problem, the extended Kalman filter (EKF) is employed [62]. The nonlinear discrete-time model for EKF can be generalized as

$$\mathbf{x}_k = \mathbf{f}(t, \mathbf{x}_{k-1}, \mathbf{u}_k, \mathbf{w}_k) \quad (3.18a)$$

$$\mathbf{y}_k = \mathbf{h}(t, \mathbf{x}_k, \mathbf{u}_k, \mathbf{v}_k) \quad (3.18b)$$

where  $t = k/c_{f,s}$  is the time, with  $k$  as discrete time, and  $c_{f,s}$  as the sampling rate of the discrete time system;  $\mathbf{x}_k$  is the internal state vector at discrete time  $k$  (the same notation with  $k$  applies for the other terms);  $\mathbf{u}$  is the input;  $\mathbf{w}$  is the process noise;  $\mathbf{y}$  is the observation;  $\mathbf{v}$  is the observation noise;  $f(t, \mathbf{x}_{k-1}, \mathbf{u}_k, \mathbf{w}_k)$  is the model process function; and  $h(t, \mathbf{x}_k, \mathbf{u}_k, \mathbf{v}_k)$  is the observation function.

In this study, it is assumed that both  $\mathbf{w}$  and  $\mathbf{v}$  are independently stochastic under Gaussian distributions with zero means. The augmented state vector  $\mathbf{z}_k$  and its covariance matrix  $\mathbf{P}_a = \mathbf{P}_a^T > 0$  can be constructed as [174]

$$\mathbf{z}_k = \begin{bmatrix} \mathbf{x}_k \\ \mathbf{w}_k \\ \mathbf{v}_k \end{bmatrix}; \quad \mathbf{P}_{a,k} = \begin{bmatrix} \mathbf{P}_{xx,k} & \mathbf{0} & \mathbf{0} \\ \mathbf{0} & \mathbf{Q} & \mathbf{0} \\ \mathbf{0} & \mathbf{0} & \mathbf{R} \end{bmatrix} \quad (3.19)$$

whose elements are initialized as

$$E(\mathbf{w}\mathbf{w}^T) = \mathbf{Q}; \quad E(\mathbf{v}\mathbf{v}^T) = \mathbf{R} \quad (3.20a)$$

$$E(\mathbf{x}_0) = \bar{\mathbf{x}}_0; \quad E((\mathbf{x}_0 - \bar{\mathbf{x}}_0)(\mathbf{x}_0 - \bar{\mathbf{x}}_0)^T) = \mathbf{P}_{xx,0} \quad (3.20b)$$

where  $\mathbf{Q}$  and  $\mathbf{R}$  are respectively the covariances of  $\mathbf{w}$  and  $\mathbf{v}$ ; and  $\bar{\mathbf{x}}$  and  $\mathbf{P}_{xx} = \mathbf{P}_{xx}^T$  are

respectively the mean/posteriori state estimate and state covariance.

EKF is a nonlinear extension of the standard Kalman filter which estimates the mean and covariance based on the system linearization at  $\bar{\mathbf{x}}$ , which is equivalent to the mean of the current state. The predict process of EKF can be written as

$$\hat{\mathbf{x}}_k = \mathbf{f}(t, \bar{\mathbf{x}}_{k-1}, \mathbf{u}_k, \mathbf{0}); \quad \hat{\mathbf{y}}_k = \mathbf{h}(t, \hat{\mathbf{x}}_k, \mathbf{u}_k, \mathbf{0}); \quad (3.21a)$$

$$\hat{\mathbf{P}}_{xx,k} = \mathbf{F}_{x,k} \mathbf{P}_{xx,k-1} \mathbf{F}_{x,k}^T + \mathbf{F}_{w,k} \mathbf{Q} \mathbf{F}_{w,k}^T \quad (3.21b)$$

$$\hat{\mathbf{P}}_{yy,k} = \mathbf{H}_{x,k} \hat{\mathbf{P}}_{xx,k} \mathbf{H}_{x,k}^T + \mathbf{H}_{v,k} \mathbf{R} \mathbf{H}_{v,k}^T; \quad (3.21c)$$

$$\hat{\mathbf{P}}_{xy,k} = \hat{\mathbf{P}}_{xx,k} \mathbf{H}_{x,k}^T \quad (3.21d)$$

and the update process can be presented as

$$\boldsymbol{\epsilon}_k = \mathbf{y}_k - \hat{\mathbf{y}}_k; \quad \mathbf{K}_k = \hat{\mathbf{P}}_{xy,k} \hat{\mathbf{P}}_{yy,k}^{-1} \quad (3.22a)$$

$$\boldsymbol{\delta}_k = \bar{\mathbf{x}}_k - \hat{\mathbf{x}}_k = \mathbf{K}_k \boldsymbol{\epsilon}_k \quad (3.22b)$$

$$\mathbf{P}_{xx,k} = \hat{\mathbf{P}}_{xx,k} - \mathbf{K}_k \hat{\mathbf{P}}_{xy,k} \mathbf{K}_k^T \quad (3.22c)$$

where  $\hat{\mathbf{x}}$  is the priori estimated state,  $\hat{\mathbf{y}}$  is the priori estimated observation;  $\boldsymbol{\delta}$  is the update step between the posteriori mean  $\bar{\mathbf{x}}$  and priori mean  $\hat{\mathbf{x}}$ ;  $\boldsymbol{\epsilon}$  is the error between the measured observation  $\mathbf{y}$  and estimated observation  $\hat{\mathbf{y}}$ ;  $\hat{\mathbf{P}}_{yy} = \hat{\mathbf{P}}_{yy}^T > 0$  is the priori estimated covariance of  $\mathbf{y}$ ;  $\hat{\mathbf{P}}_{xy} = \hat{\mathbf{P}}_{yx}^T$  is the priori estimated cross covariance between  $\mathbf{x}$  and  $\mathbf{y}$ ;  $\mathbf{K}$  is the approximated optimal Kalman gain; and the Jacobian matrices  $\mathbf{F}$  and  $\mathbf{H}$  are defined as

$$\mathbf{F}_{x,k} = \partial \mathbf{f}(t, \bar{\mathbf{x}}_{k-1}, \mathbf{u}_k, \mathbf{w}_k) / \partial \bar{\mathbf{x}}_{k-1}; \quad \mathbf{F}_{w,k} = \partial \mathbf{f}(t, \bar{\mathbf{x}}_{k-1}, \mathbf{u}_k, \mathbf{w}_k) / \partial \mathbf{w}_k \quad (3.23a)$$

$$\mathbf{H}_{x,k} = \partial \mathbf{h}(t, \hat{\mathbf{x}}_k, \mathbf{u}_k, \mathbf{v}_k) / \partial \hat{\mathbf{x}}_k; \quad \mathbf{H}_{v,k} = \partial \mathbf{h}(t, \hat{\mathbf{x}}_k, \mathbf{u}_k, \mathbf{v}_k) / \partial \mathbf{v}_k \quad (3.23b)$$

Previous studies have demonstrated that Kalman filters can also be used to formulate dynamic (real-time) optimizer [5, 25, 173]. For each propagation, the update  $\delta$  in Eq. (3.22b) carried out with gain and error is a step towards minimizing the cost function

$$\begin{aligned} \mathcal{J}_{\text{EKF}}(\bar{\mathbf{x}}_k) &= ((\mathbf{y}_k - \mathbf{h}(t, \bar{\mathbf{x}}_k, \mathbf{u}_k, \mathbf{0}))^\top (\hat{\mathbf{P}}_{yy,k} - \hat{\mathbf{P}}_{xy,k}^\top \hat{\mathbf{P}}_{xx,k}^{-1} \hat{\mathbf{P}}_{xy,k})^{-1} (\mathbf{y}_k - \mathbf{h}(t, \bar{\mathbf{x}}_k, \mathbf{u}_k, \mathbf{0}))) \\ &\quad + (\bar{\mathbf{x}}_k - \hat{\mathbf{x}}_k)^\top \hat{\mathbf{P}}_{xx,k}^{-1} (\bar{\mathbf{x}}_k - \hat{\mathbf{x}}_k) \end{aligned} \quad (3.24)$$

by optimizing the value of  $\bar{\mathbf{x}}_k = \text{argmin}(\mathcal{J}_{\text{EKF}})$ . This is later used to introduce sparsity-promoting features into the EKF process.

### 3.2.2 Promoting Sparsity in Extended Kalman Filter

Sparsity in model regression is a qualitative measure of states and parameters that appears to be zeros. When correctly designed and implemented, sparse model regression can simplify the identified system features with redundant states and parameters converging to zeros. Sparsity can be promoted by  $l^1$  minimization [5, 25]. To realize  $l^1$  minimization in EKF, we can introduce an additional observable set  $\mathbf{f}_{\text{sp}}(\mathbf{x})$  so that

$$\mathbf{y}_{\text{sp},k} = \begin{bmatrix} \mathbf{y}_k \\ \mathbf{0} \end{bmatrix} = \begin{bmatrix} \mathbf{h} \\ \mathbf{f}_{\text{sp}}(\mathbf{x}_k) + \mathbf{v}_{\text{sp},k} \end{bmatrix}; \quad \mathbf{R}_{\text{sp}} = \begin{bmatrix} \mathbf{R} & \mathbf{0} \\ \mathbf{0} & \mathbf{R}_{\text{sp}} \end{bmatrix} \quad (3.25)$$

By having  $\mathbf{y}_{\text{sp},k}$  as the new observable for the sparsity-promoting EKF (SP-EKF), the cost function can be written as

$$\begin{aligned} \mathcal{J}_{\text{EKF,sp}}(\bar{\mathbf{x}}_k) &= ((\mathbf{y}_k - \mathbf{h}(t, \bar{\mathbf{x}}_k, \mathbf{u}_k, \mathbf{0}))^\top (\mathbf{H}_{v,k} \mathbf{R} \mathbf{H}_{v,k}^\top)^{-1} (\mathbf{y}_k - \mathbf{h}(t, \bar{\mathbf{x}}_k, \mathbf{u}_k, \mathbf{0}))) \\ &\quad + (\bar{\mathbf{x}}_k - \hat{\mathbf{x}}_k)^\top \hat{\mathbf{P}}_{xx,k}^{-1} (\bar{\mathbf{x}}_k - \hat{\mathbf{x}}_k) + \mathbf{f}_{\text{sp}}^\top(\bar{\mathbf{x}}_k) \mathbf{R}_{\text{sp}}^{-1} \mathbf{f}_{\text{sp}}(\bar{\mathbf{x}}_k) \end{aligned} \quad (3.26)$$

The function  $\mathbf{f}_{\text{sp}}(\mathbf{x})$  in Eq. (3.32, 3.26) is designed for increasing the sparsity of the parameters. When correctly designed and implemented, sparse model regression can identify the basis of a signal with the redundant states converging to zero. Sparsity can be promoted by  $l^1$  minimization [5, 25]. For Eq. (3.26), this requires  $\mathbf{f}_{\text{sp}}(\mathbf{x}) = |\mathbf{x}_{\text{sp}} - \mathbf{b}_{\text{sp}}|^{0.5}$  where  $\mathbf{x}_{\text{sp}} \in \mathbf{x}$  is the sparse state vector, and  $\mathbf{b}_{\text{sp}}$  is the user-defined bias introduced because some internal states (e.g., unit quaternions) are unable to reach zeros due to constraints.

Traditional  $l^1$  minimization via Kalman filtering may also require reconstructing the model [5] due to  $|\mathbf{x}_{\text{sp}} - \mathbf{b}_{\text{sp}}|$  being undifferentiable at  $\mathbf{x}_{\text{sp}} = \mathbf{b}_{\text{sp}}$ . Furthermore, with the increase of  $\mathbf{x}_{\text{sp}}$ , the time complexity of the EKF process can become significantly higher. Therefore, we use an alternative  $f_{\text{sp}}(\mathbf{x})$ , which is a non-negative scalar function designed as

$$f_{\text{sp}}(\mathbf{x}) = \left( \text{sum}((\mathbf{a}_{\text{sp}}^2 * (\mathbf{x}_{\text{sp}} - \mathbf{b}_{\text{sp}})^2 + \mathbf{c}_{\text{sp}}^2)^{0.5} - \mathbf{c}_{\text{sp}}) + c_{\text{sp},0} \right)^{0.5} - c_{\text{sp},0}^{0.5} \quad (3.27)$$

whose partial derivative of  $\mathbf{x}$  is

$$\frac{\partial f_{\text{sp}}}{\partial \mathbf{x}_{\text{sp}}} = \frac{(\mathbf{a}_{\text{sp}}^2 * (\mathbf{x}_{\text{sp}} - \mathbf{b}_{\text{sp}}) * (\mathbf{a}_{\text{sp}}^2 * (\mathbf{x}_{\text{sp}} - \mathbf{b}_{\text{sp}})^2 + \mathbf{c}_{\text{sp}}^2)^{-0.5})^T}{2 (f_{\text{sp}} + c_{\text{sp},0}^{0.5})} \quad (3.28)$$

Here,  $\mathbf{a}_{\text{sp}} > 0$  is a constant scaling parameter vector;  $\mathbf{c}_{\text{sp}}$  and  $c_{\text{sp}}$  are small positive constant parameters. Notice that when  $x = 0$ , Eqs. (3.27) and (3.28) both reach zeros; when  $\mathbf{c}_{\text{sp}} \ll |\mathbf{a}_{\text{sp}} * (\mathbf{x}_{\text{sp}} - \mathbf{b}_{\text{sp}})|$ ,  $\mathbf{f}_{\text{sp}}^2(\mathbf{x}, \mathbf{a}_{\text{sp}}, \mathbf{c}_{\text{sp}})$  is approximately identical to the sum of  $|\mathbf{a}_{\text{sp}} * (\mathbf{x}_{\text{sp}} - \mathbf{b}_{\text{sp}})|$ . Therefore,  $\mathbf{a}_{\text{sp}}$  is selected to scale  $(\mathbf{x}_{\text{sp}} - \mathbf{b}_{\text{sp}})$  to proper magnitudes for optimization;  $\mathbf{c}_{\text{sp}}$  and  $c_{\text{sp}}$  are designed as reasonably small numbers compared to  $|\mathbf{a}_{\text{sp}} * (\mathbf{x}_{\text{sp}} - \mathbf{b}_{\text{sp}})|$ . The user can also design  $\mathbf{a}_{\text{sp}}$  and  $\mathbf{R}_{\text{sp}}$  to adjust the weight of the sparsity promoting term in the cost function.

The comparison of  $f_{\text{sp}}(x_{\text{sp}})$  and  $|x_{\text{sp}}|^{0.5}$  for a scalar variable  $x_{\text{sp}}$  is shown in Fig. 3.2. Here, we assign  $\mathbf{a} = \mathbf{1}$ ,  $\mathbf{c}_{\text{sp}} = \mathbf{10}^{-4}$ , and  $c_{\text{sp},0} = 10^{-6}$ . Notice from Fig. 3.2(a) that the two functions

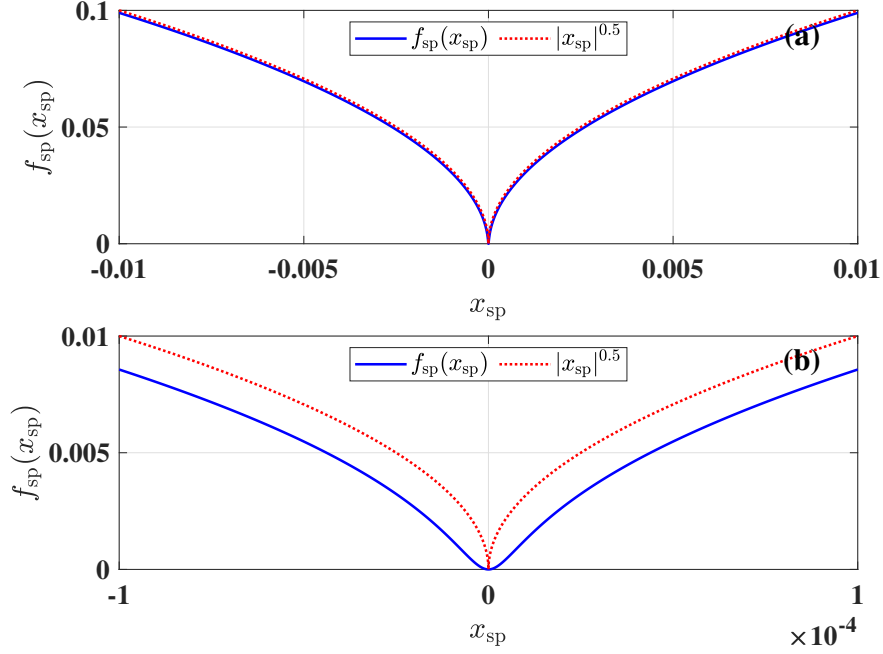


Figure 3.2: Comparison of  $f_{\text{sp}}(x_{\text{sp}})$  and  $|x_{\text{sp}}|^{0.5}$  at different scales and ranges of  $x_{\text{sp}}$ .

are very similar when  $x_{\text{sp}} \in [-10^{-2}, 10^{-2}]$ . When zoomed into  $x_{\text{sp}} \in [-10^{-4}, 10^{-4}]$ , we can observe that  $f_{\text{sp}}(x_{\text{sp}})$  is a smooth function that is differentiable around  $x_{\text{sp}} = 0$ , which is different from  $|x_{\text{sp}}|^{0.5}$ . Hence, the proposed  $f_{\text{sp}}(x_{\text{sp}})$  can directly fit into the EKF as an observation function for  $l^1$  minimization.

### 3.2.3 The 6-DOF Wrist Motion Measurement Tool

The wearable wrist kinematics measurement tool (WKMT) is developed to collect experimental motion data from the user for identification. As shown in Fig. 3.3, WKMT features a 6-DOF rigid linkage mechanism similar to that in TAWE, which connects Frame A1 and Frame A2 and supports any translations and rotations between the two frames within its reachable workspace. Hence, WKMT allows unconstrained and natural wrist movements.

As WKMT has 6 joints, a total of six intermediate (Frames J1 to J6) can be defined. The joint

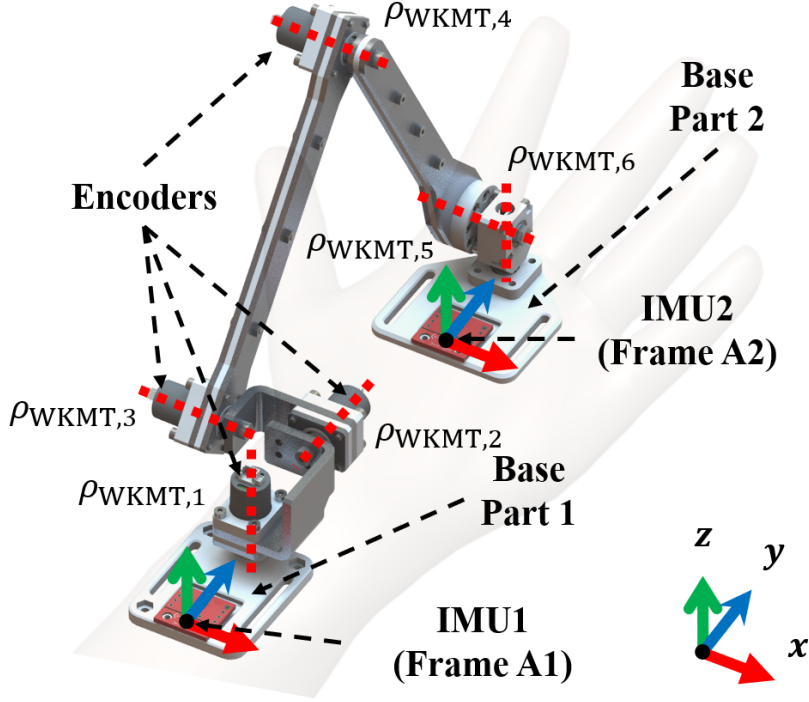


Figure 3.3: The design of WKMT and its approximate location on the right human forearm [176]. The two IMUs on the base parts measure the rotations of Frames A1 and A2, respectively. The joints  $\rho$  are marked around their rotation axes (red dot lines), which are labeled with their sequence numbers and rotation axes in their local frames. Encoders are installed on the first four joints.

angles are defined as  $\boldsymbol{\rho}_{\text{WKMT}} = [\rho_{\text{WKMT},1}, \rho_{\text{WKMT},2}, \rho_{\text{WKMT},3}, \rho_{\text{WKMT},4}, \rho_{\text{WKMT},5}, \rho_{\text{WKMT},6}]^T$ . For convenience, the origins of Frame A1 and Frame A2 are respectively defined to be on the interceptions between base parts and the axes of Joint 1 and Joint 6. The transformations between frames in the exoskeleton kinematic chain are demonstrated in Table 3.1, where the default parameters of the design are also included.

WKMT can adopt various sensor configurations to fully measure the displacement  $\mathbf{d}_{a,\text{end}}$  and rotation  $\boldsymbol{\xi}_{a,\text{end}}$  between Frame A1 and Frame A2 as introduced in Eq. (3.10). Therefore, the measurement input  $\mathbf{u}_{\text{WKI}}$  for the WKI process is defined as

$$\mathbf{u}_{\text{WKI}} = \left[ \boldsymbol{\xi}_{a,\text{end}}^T \quad \mathbf{d}_{a,\text{end}}^T \right]^T \quad (3.29)$$

Table 3.1: Properties of transformations between coordinate frames in the WKMT kinematic system.

From	To	Translation ( $\mathbf{d}$ )	Rotation ( $\mathbf{\Omega}$ )
A1	J1	$\mathbf{d} = [0; 0; 0]$ cm	$\mathbf{\Omega}_{\bar{z}}(\rho_1)$
J1	J2	$\mathbf{d} = [1; 4; 3.5]$ cm	$\mathbf{\Omega}_{\bar{y}}(\rho_2)$
J2	J3	$\mathbf{d}_{\bar{x}} = -0.3$ cm	$\mathbf{\Omega}_{\bar{x}}(\rho_3)$
J3	J4	$\mathbf{d}_{\bar{z}} = 12$ cm	$\mathbf{\Omega}_{\bar{x}}(\rho_4)$
J4	J5	$\mathbf{d}_{\bar{y}} = 12$ cm	$\mathbf{\Omega}_{\bar{x}}(\rho_5)$
J5	J6	$\mathbf{d}_{\bar{z}} = -2$ cm	$\mathbf{\Omega}_{\bar{z}}(\rho_6)$
J6	A2	$\mathbf{d} = [0; 0; 0]$ cm	$\mathbf{I}_3$

Here, we use two inertia measurement units (IMU) (MPU9250) to measure the rotation between Frame A1 and Frame A2, and four absolute encoders (US Digital MAE3) to measure the first four joints ( $\rho_{\text{WKMT},1}$  to  $\rho_{\text{WKMT},4}$ ).

The rotation  $\mathbf{\Omega}_{a,\text{end}}$  (or equivalently the rotation quaternion  $\boldsymbol{\xi}_{a,\text{end}}$  in Eq. (3.10)) between Frame 2 and Frame R can be directly calculated with IMU measurements through sensor fusion [112]. The unmeasured joint angles  $\rho_{\text{WKMT},5}$  and  $\rho_{\text{WKMT},6}$  can be calculated from the equation

$$\begin{aligned} \mathbf{\Omega}_{56} &= \left( \mathbf{\Omega}_{\bar{z}}(\rho_{\text{WKMT},1}) \mathbf{\Omega}_{\bar{y}}(\rho_{\text{WKMT},2}) \mathbf{\Omega}_{\bar{x}}(\rho_{\text{WKMT},3}) \mathbf{\Omega}_{\bar{x}}(\rho_{\text{WKMT},4}) \right)^T \mathbf{\Omega}_{a,\text{end}} \\ &= \mathbf{\Omega}_{\bar{x}}(\rho_{\text{WKMT},5}) \mathbf{\Omega}_{\bar{z}}(\rho_{\text{WKMT},6}) \end{aligned} \quad (3.30)$$

which leads to

$$\rho_5 = \arctan\left(-\frac{z_{56,2,3}}{z_{56,3,3}}\right); \quad \rho_6 = \arctan\left(-\frac{z_{56,1,2}}{z_{56,1,1}}\right) \quad (3.31)$$

where  $z_{56,i,j}$  is the  $i$ th row,  $j$ th column element of  $\mathbf{\Omega}_{56}$ . Later, with the full knowledge of  $\boldsymbol{\rho}_{\text{WKMT}}$ , we can calculate the translational displacement  $\mathbf{d}_{a,\text{end}}$  between Frame A1 and Frame A2 based on kinematic transformations listed in Table 3.1.

### 3.2.4 Wrist Kinematics Regression via Sparsity Promoting EKF

Based on the aforementioned setups, we can formulate the EKF model for WKI. Here we define the state dynamics of the WKI model as

$$\mathbf{x}_{\text{WKI}} = \begin{bmatrix} \mathbf{p}_{\text{wrist}}^T & \boldsymbol{\xi}_{\text{wrist}}^T & \mathbf{x}_{\kappa,\text{int}}^T \end{bmatrix}^T; \quad \mathbf{y}_{\text{WKI}} = \mathbf{0}; \quad \mathbf{u}_{\text{WKI}} = \begin{bmatrix} \boldsymbol{\xi}_{a,\text{end}}^T & \mathbf{d}_{a,\text{end}}^T \end{bmatrix}^T \quad (3.32a)$$

$$\mathbf{w}_{\text{WKI}} = \begin{bmatrix} \mathbf{w}_{\text{WKI},\xi}^T & \mathbf{w}_{\text{WKI},p}^T \end{bmatrix}^T; \quad \mathbf{v}_{\text{WKI}} = \begin{bmatrix} \mathbf{v}_{\text{WKI},d}^T & \mathbf{v}_{\text{WKI},h}^T & v_{\text{WKI},\text{sp}}^T \end{bmatrix}^T \quad (3.32b)$$

$$\mathbf{f}_{\text{WKI}} = \begin{bmatrix} \mathbf{p}_{\text{wrist}} \\ \boldsymbol{\xi}_{a,1}^* \times (\boldsymbol{\xi}_{a,\text{end}} + \mathbf{w}_{\text{WKI},\xi}) \\ \mathbf{x}_{\kappa,\text{int}} + c_{\text{WKI},\text{int}} \mathbf{f}_{\kappa}(\boldsymbol{\xi}_{a,1}^* \times (\boldsymbol{\xi}_{a,\text{end}} + \mathbf{w}_{\text{WKI},\xi})) \end{bmatrix} + \mathbf{w}_{\text{WKI},p} \quad (3.32c)$$

$$\mathbf{h}_{\text{WKI},1} = \begin{bmatrix} r_{\lambda,\text{wrist},\text{est}} \\ \mathbf{d}_{a,\text{end},\text{est}} - \mathbf{d}_{a,\text{end}} - \mathbf{v}_{\text{WKI},d} \end{bmatrix}; \quad \mathbf{h}_{\text{WKI},2} = \begin{bmatrix} \|\boldsymbol{\xi}_{a,1}\| - 1 \\ \mathbf{x}_{\kappa,\text{int}} \end{bmatrix} \quad (3.32d)$$

$$\mathbf{h}_{\text{WKI}} = \begin{bmatrix} \begin{bmatrix} \mathbf{h}_{\text{WKI},1} \\ \mathbf{h}_{\text{WKI},2} \end{bmatrix} + \mathbf{v}_{\text{WKI},h} \\ f_{\text{sp}}(\mathbf{p}_{\text{wrist},\text{sp}}) + v_{\text{WKI},\text{sp}} \end{bmatrix} \quad (3.32e)$$

Here, recall that  $\mathbf{p}_{\text{wrist}}$  is the wrist kinematic parameter vector previously introduced in Eq. (3.17); the wrist rotation  $\boldsymbol{\xi}_{\text{wrist}}$  can be calculated based on Eq. (3.11);  $\mathbf{x}_{\kappa,\text{wrist},\text{int}} \in \mathbb{R}^3$  is the discrete time integral of the Euler angles  $\boldsymbol{\kappa}_{\text{wrist}}$  based on a step size  $c_{\text{WKI},\text{int}} > 0$ , where  $\mathbf{f}_{\kappa}(\cdot)$  converts the estimation of the corresponding quaternion  $\boldsymbol{\xi}_{\text{wrist}}$  into  $\boldsymbol{\kappa}_{\text{wrist}}$ ; and  $\mathbf{p}_{\text{wrist},\text{sp}} = [\mathbf{c}_{\text{wrist},\Omega,\text{FLC}}^T, \text{vec}^T(\mathbf{D}_{\text{wrist},d,\text{linear}}), \text{vec}^T(\mathbf{D}_{\text{wrist},d,\text{FLC}})]^T$  is the sparse parameter state vector. Notice that  $\mathbf{f}_{\text{WKI}}$  implies that the kinematic parameters are expected to be time-invariant. The observation function  $\mathbf{h}_{\text{WKI},1}$  is collected from Eqs. (3.15, 3.16). The additional observation function  $\mathbf{h}_{\text{WKI},2}$  provides better algorithm stability by ensuring that  $\boldsymbol{\xi}_{a,1}$  is a unit quaternion, and the means of  $\boldsymbol{\kappa}_{\text{wrist}}$  are centered around zeros through its discrete-time

integral  $\mathbf{x}_{\kappa,\text{int}}$ . Hence,  $\mathbf{h}_{\text{WKI},2}$  is designed to increase the robustness of regression without significantly affecting parameter identification governed by  $\mathbf{h}_{\text{WKI},1}$ .

The state covariance  $\mathbf{Q}_{\text{WKI}}$  and measurement covariance  $\mathbf{R}_{\text{WKI}}$  for this model are designed as

$$\mathbf{Q}_{\text{WKI}} = \begin{bmatrix} \mathbf{Q}_{\text{WKI},\xi} & \mathbf{0} \\ \mathbf{0} & \mathbf{Q}_{\text{WKI},p} \end{bmatrix}; \quad \mathbf{R}_{\text{WKI}} = \begin{bmatrix} \mathbf{R}_{\text{WKI},d} & \mathbf{0} & \mathbf{0} \\ \mathbf{0} & \mathbf{R}_{\text{WKI},h} & \mathbf{0} \\ \mathbf{0} & \mathbf{0} & R_{\text{WKI},\text{sp}} \end{bmatrix} \quad (3.33)$$

where  $\mathbf{Q}_{\text{WKI},\xi}$  and  $\mathbf{Q}_{\text{WKI},p}$  are respectively corresponding to  $\mathbf{w}_{\text{WKI},\xi}$  and  $\mathbf{w}_{\text{WKI},p}$ ;  $\mathbf{R}_{\text{WKI},d}$ ,  $\mathbf{R}_{\text{WKI},h}$  and  $\mathbf{R}_{\text{WKI},\text{sp}}$  are respectively corresponding to  $\mathbf{v}_{\text{WKI},d}$ ,  $\mathbf{v}_{\text{WKI},h}$ , and  $\mathbf{v}_{\text{WKI},\text{sp}}$ . Specifically,  $R_{\text{WKI},\text{sp}}$  is a scalar since the sparsity-promoting function yields a scalar observable. The design of  $\mathbf{Q}_{\text{WKI}}$  and  $\mathbf{R}_{\text{WKI}}$  can effectively adjust the performance of the WKI algorithm.

In summary, the real-time WKI algorithm is designed based on a sparsity-promoting EKF (SP-EKF), which is expected to reduce the model complexity by prioritizing the primary wrist parameters, and drives the sparse parameters  $\mathbf{p}_{\text{wrist},\text{sp}}$  to zeros. SP-EKF can also potentially improve the robustness of the regression algorithm under noisy conditions. The next two sections verify the findings through simulation and experiment.

### 3.3 Numerical Simulation

This section presents the numerical simulations to demonstrate the theoretical findings and test the performance of the WKI algorithm. The simulations are carried out in MATLAB. The default forearm and wrist parameters are selected as [31]

$$\mathbf{c}_{\text{wrist},d} = \begin{bmatrix} 3 & 2 & 2.5 \end{bmatrix}^T \text{ cm}; \quad \mathbf{d}_{a,1} = \begin{bmatrix} 1 & 12 & -1 \end{bmatrix}^T \text{ cm}; \quad \mathbf{d}_{a,2} = \begin{bmatrix} -2 & 10 & 1 \end{bmatrix}^T \text{ cm} \quad (3.34)$$

We also define the default sequential rotation model as the first-RUD-then-WFE model. Hence,  $\rho_{\text{RUD}}$ ,  $\rho_{\text{wrist},\vec{y}}$ , and  $\rho_{\text{WFE}}$  are respectively equal to  $\kappa_{\text{wrist},\vec{z}}$ ,  $\kappa_{\text{wrist},\vec{y}}$ , and  $\kappa_{\text{wrist},\vec{x}}$  from the intrinsic  $\vec{z}$ - $\vec{y}$ - $\vec{x}$  Euler angles  $\boldsymbol{\kappa}_{\text{wrist}}$ .

### 3.3.1 Solutions of the Ellipsoidal Joint Model

The solutions of the constrained ellipsoidal joint rotation  $\rho_{\text{wrist},\vec{y}}$  and translational displacement  $\mathbf{d}_{\text{wrist}}$  respectively from Eq. (3.2) and Eq. (A.2) in the domain of  $\boldsymbol{\rho}_{\text{wrist},\text{main}}$  are presented in Fig. 3.4. Notice that all of these maps are symmetric and bounded within the domain of  $\boldsymbol{\rho}_{\text{wrist},\text{main}}$ , where  $d_{\text{wrist},\vec{x}}$  and  $d_{\text{wrist},\vec{z}}$  are respectively sensitive to  $\kappa_{\text{wrist},\vec{z}}$  and  $\kappa_{\text{wrist},\vec{x}}$  (i.e.,  $\rho_{\text{RUD}}$  and  $\rho_{\text{WFE}}$ ), and  $d_{\text{wrist},\vec{y}}$  can increase along any rotation directions due to the sliding of the ellipsoid ball in the socket as previously depicted in Fig. 3.1. Figure 3.4(a) also shows that the rotation constrained by Eq. (3.1) is non-orthogonal, as the coupling between RUD and WFE becomes significant when both  $\rho_{\text{RUD}}$  and  $\rho_{\text{WFE}}$  are large.

The wrist kinematics in real life is more complicated than the proposed ellipsoidal joint. In the upcoming WKI simulations, a few references are employed to test the generality of the proposed approach based on Eqs. (3.15, 3.16) in regressing different models and uncertainties. To begin with, three translational displacement references  $\mathbf{d}_{a,\text{end},r,i}$  ( $i = 1, 2, 3$ ) are adopted so that

$$\mathbf{d}_{a,\text{end},r,i}(\boldsymbol{\kappa}) = \mathbf{d}_{a,1} + \boldsymbol{\Omega}_{a,1}\boldsymbol{\Omega}_{\text{wrist}}\mathbf{d}_{a,2} + \boldsymbol{\Omega}_{a,1}\mathbf{d}_{\text{wrist},r,i} \quad (3.35a)$$

$$\mathbf{d}_{\text{wrist},r,1} = \mathbf{0}; \quad \mathbf{d}_{\text{wrist},r,2} = \boldsymbol{\Omega}_{\text{wrist},\text{half}}\mathbf{d}_{a,1,2} \quad (3.35b)$$

$$\mathbf{d}_{\text{wrist},r,3} = \mathbf{d}_{\text{wrist}} + \mathbf{D}_{\text{wrist},d,\text{linear}}\boldsymbol{\rho}_{\text{wrist},\text{main}} \quad (3.35c)$$

so that  $\mathbf{d}_{\text{wrist},r,1}$  is the simplified reference that excludes internal wrist translation;  $\mathbf{d}_{\text{wrist},r,2}$

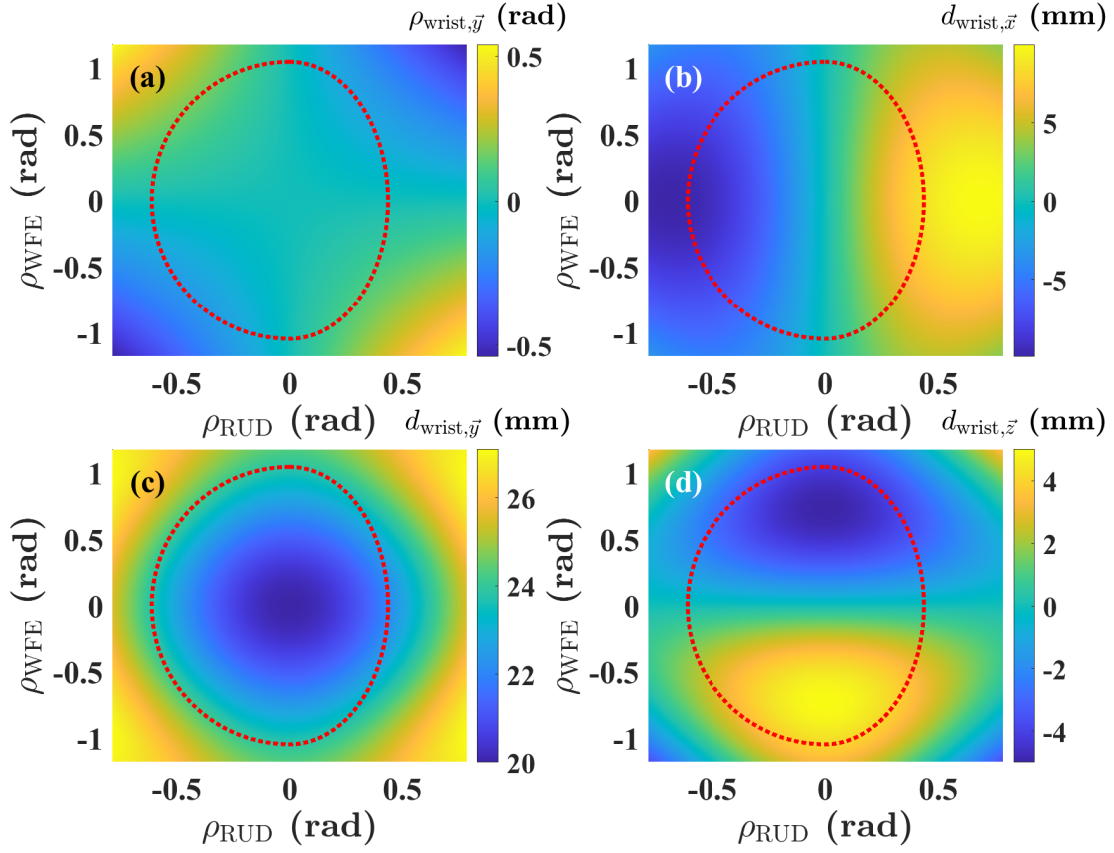


Figure 3.4: The solutions of the constrained rotation  $\rho_{\text{wrist},\bar{y}}$  and translational displacement  $\mathbf{d}_{\text{wrist}}$  from the ellipsoidal joint model in the domain of  $\boldsymbol{\rho}_{\text{wrist},\text{main}}$  [176], where (a) shows the solution of  $\rho_{\text{wrist},\bar{y}}$ ; (b) shows the solution of  $d_{\text{wrist},\bar{x}}$ ; (c) presents the solution of  $d_{\text{wrist},\bar{y}}$ ; and (d) presents the solution of  $d_{\text{wrist},\bar{z}}$ . The range of  $\rho_{\text{RUD}}$  and  $\rho_{\text{WFE}}$  in these plots are respectively  $[-\pi/4, \pi/4]$  and  $[-3\pi/8, 3\pi/8]$ . The red dot contour is the approximate wrist circumduction envelope [141].

is similar as in [55, 71], where a constant translational offset  $\mathbf{d}_{a,1,2}$  divides WFE-RUD-WFE-RUD joint into two halves (recall Eq. (3.5)); and  $\mathbf{d}_{\text{wrist},r,3}$  features the proposed ellipsoid-based translation in Eq. (A.1) along with a term linear with  $\boldsymbol{\rho}_{\text{wrist},\text{main}}$ .

We also respectively adopt three rotation references as the first-RUD-then-WFE model  $\boldsymbol{\Omega}_{\text{wrist},\text{FRTW}}$  from Eq. (2.12), first-WFE-then-RUD model  $\boldsymbol{\Omega}_{\text{wrist},\text{FWTR}}$  from Eq. (2.11), and WFE-RUD-WFE-RUD model  $\boldsymbol{\Omega}_{\text{wrist},\text{WRWR}}$  from Eq. (3.5). The default value of the

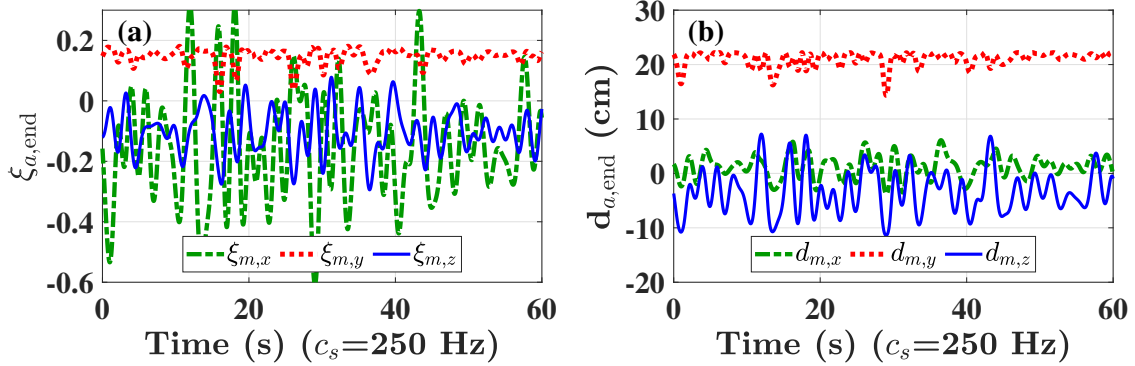


Figure 3.5: The quasi-periodic wrist motions trajectories randomly generated by the simulation reference model, where (a) shows the  $\vec{x}$ ,  $\vec{y}$ , and  $\vec{z}$  components of wrist rotation quaternion  $\xi_{a,\text{end}}$  (note that  $\|\xi_{a,\text{end}}\| = 1$ ), and (b) shows the wrist translation displacement  $\mathbf{d}_{a,\text{end}}$  (where  $\mathbf{d}_{a,\text{end}} = \mathbf{d}_{a,\text{end},r,1}$  based on Eq. (3.35)).

quaternion  $\xi_{a,1}$  that represents the initial rotation  $\Omega_{a,1}$  before the wrist is selected as

$$\xi_{a,1} = \begin{bmatrix} 0.9710 & -0.1539 & 0.1499 & -0.1050 \end{bmatrix}^T \quad (3.36)$$

which is equivalent to the  $\vec{z}$ - $\vec{y}$ - $\vec{x}$  Euler angle  $\kappa_{a,1} = [-20^\circ, 15^\circ, -15^\circ]^T$ . Hence, these reference models generate the trajectories of input  $\mathbf{u}_1$  in Eq. (3.29), which are used as regression data in the following WKI simulations.

### 3.3.2 Parameter Identification via EKF

We use the first simulation to show that EKF is a real-time optimizer, where translational reference is  $\mathbf{d}_{\text{wrist},r,1}$ , and the regression model from Eqs. (3.15, 3.16) is simplified to exclude  $\rho_{\text{wrist},\text{main}}$ -affine and FLC terms. Figure 3.5 shows an example wrist trajectories of  $\xi_{a,\text{end}}$  and  $\mathbf{d}_{a,\text{end}}$  generated by the reference model via quasi-periodic trajectories of  $\rho_{\text{wrist},\text{main}}$ , which are composed by harmonic waves of random amplitudes and phases. The trajectories are sampled at 250 Hz with zero noise added.

To test if EKF can correct large initial guess errors, the WKI simulation starts with all initial parameter estimations as zeros, except that  $\xi_{a,1} = [1, 0, 0, 0]^T$ . The covariance matrices are selected as

$$\mathbf{P}_{xx,0} = 10^{-6}\mathbf{I}_{14}; \quad \mathbf{Q}_{\text{WKI},u} = 10^{-6}\mathbf{I}_4 \quad (3.37a)$$

$$\mathbf{Q}_{\text{WKI},p} = \text{diag}\left(\left[10^{-8}\mathbf{1}_{1 \times 5} \quad 10^{-10}\mathbf{1}_{1 \times 12}\right]\right) \quad (3.37b)$$

$$\mathbf{R}_{\text{WKI},u} = 10^{-6}\mathbf{I}_3; \quad \mathbf{R}_{\text{WKI},h} = \text{diag}\left(\left[10^{-6}\mathbf{1}_{1 \times 5} \quad \mathbf{1}_{1 \times 3}\right]\right) \quad (3.37c)$$

The results are shown in Fig. 3.6. Figures 3.6(a-c) is based on the first-RUD-then-WFE

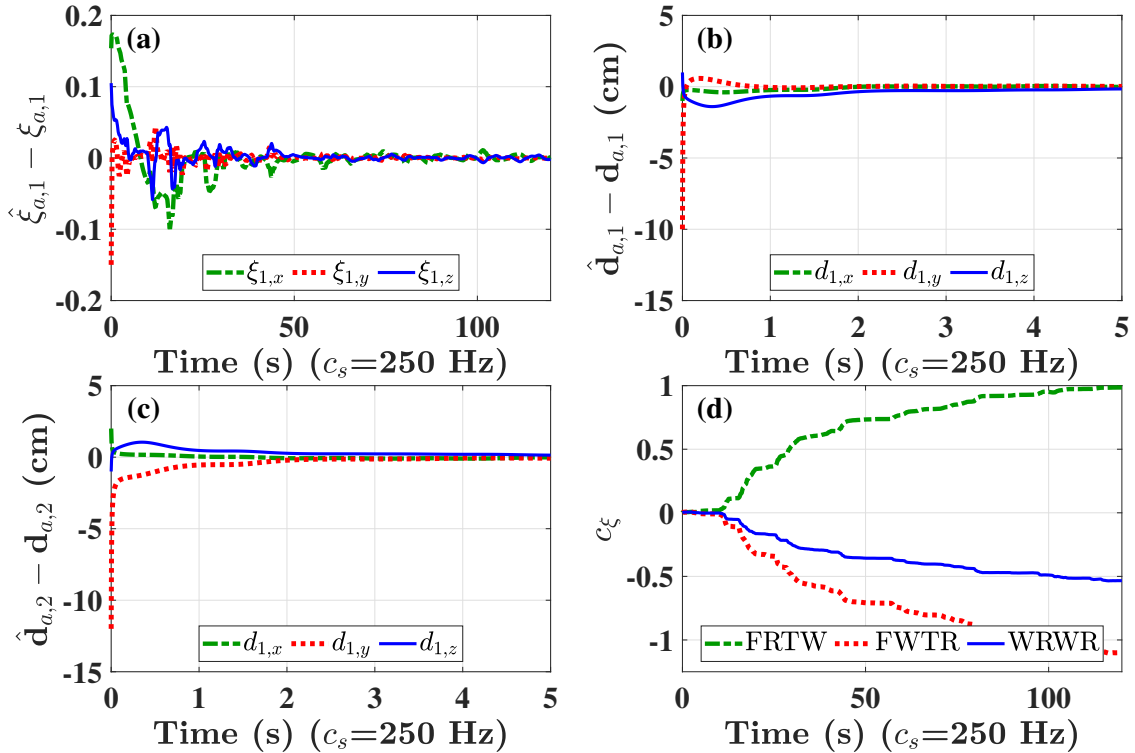


Figure 3.6: Trajectories of parameter estimation errors in the regression of the simplified model via EKF [176], where (a) shows the estimation error of  $\xi_{a,1}$ ; (b) shows the estimation error of  $\mathbf{d}_{a,1}$ ; (c) shows the estimation error of  $\mathbf{d}_{a,2}$ ; and (d) shows the estimation of  $c_\xi$  under different sequential rotation models  $\Omega_{\text{wrist},\text{FRTW}}$ ,  $\Omega_{\text{wrist},\text{FWTR}}$ , and  $\Omega_{\text{wrist},\text{WRWR}}$  from Eqs. (2.12, 2.11, 3.5).

reference model. The estimated parameters  $\hat{\boldsymbol{\xi}}_{a,1}$ ,  $\hat{\mathbf{d}}_{a,1}$ , and  $\hat{\mathbf{d}}_{a,2}$  eventually converge to the close vicinities of their true values. Also, the convergence of translational parameters  $\hat{\mathbf{d}}_{a,1}$  and  $\hat{\mathbf{d}}_{a,2}$  is significantly faster than that of the quaternion parameters  $\hat{\boldsymbol{\xi}}_{a,1}$ . This is likely due to the observation errors being less sensitive to  $\hat{\boldsymbol{\xi}}_{a,1}$ . Finally, Fig. 3.6(d) compares the values of  $c_\xi$  in Eq. (3.16) from the rotation constraint regressions based on different rotation references. The values of  $c_\xi$  converge to approximately 1,  $-1$ , and  $-0.5$  with respect to  $\boldsymbol{\Omega}_{\text{wrist,FRTW}}$ ,  $\boldsymbol{\Omega}_{\text{wrist,FWTR}}$ , and  $\boldsymbol{\Omega}_{\text{wrist,WRWR}}$ , which corroborates the findings in Section 3.1.3 revealing that  $c_\xi$  can approximate and classify different rotation models.

### 3.3.3 Characteristics of FLC and SP-EKF

The previous subsection confirms that EKF is capable of real-time parameter identification. For the simulations involving SP-EKF, we use the full regression model in Eqs. (3.15, 3.16), which contains 119 unknown kinematic parameters. The covariances are selected as

$$\mathbf{P}_{xx,0} = 10^{-6} \mathbf{I}_{119}; \quad \mathbf{Q}_{\text{WKL},p} = \text{diag}\left(\begin{bmatrix} 10^{-8} \mathbf{1}_{1 \times 5} & 10^{-10} \mathbf{1}_{1 \times 114} \end{bmatrix}\right) \quad (3.38)$$

The regression model updated by regular EKF can obtain good approximation of wrist kinematics. However, the FLC in the regression model can lead to redundancy, which leads to poor identification of primary parameters  $\hat{\boldsymbol{\xi}}_{a,1}$ ,  $c_\xi$ ,  $\hat{\mathbf{d}}_{a,1}$ , and  $\hat{\mathbf{d}}_{a,2}$ . Hence, the covariances and parameters introduced by SP-EKF are

$$R_{\text{WKL,sp}} = 1; \quad \mathbf{a}_{\text{sp}} = \mathbf{10}; \quad \mathbf{b}_{\text{sp}} = \mathbf{0}; \quad \mathbf{c}_{\text{sp}} = \mathbf{10}^{-5}; \quad c_{\text{sp},0} = 10^{-5} \quad (3.39)$$

The proposed WKI approach is tested on two reference models. The first reference model adopts  $\mathbf{d}_{\text{wrist},r,2}$  as translation and  $\boldsymbol{\Omega}_{\text{wrist,WRWR}}$  as rotation [55, 71], where  $\mathbf{d}_{a,1,2} = [0.120]$  cm;

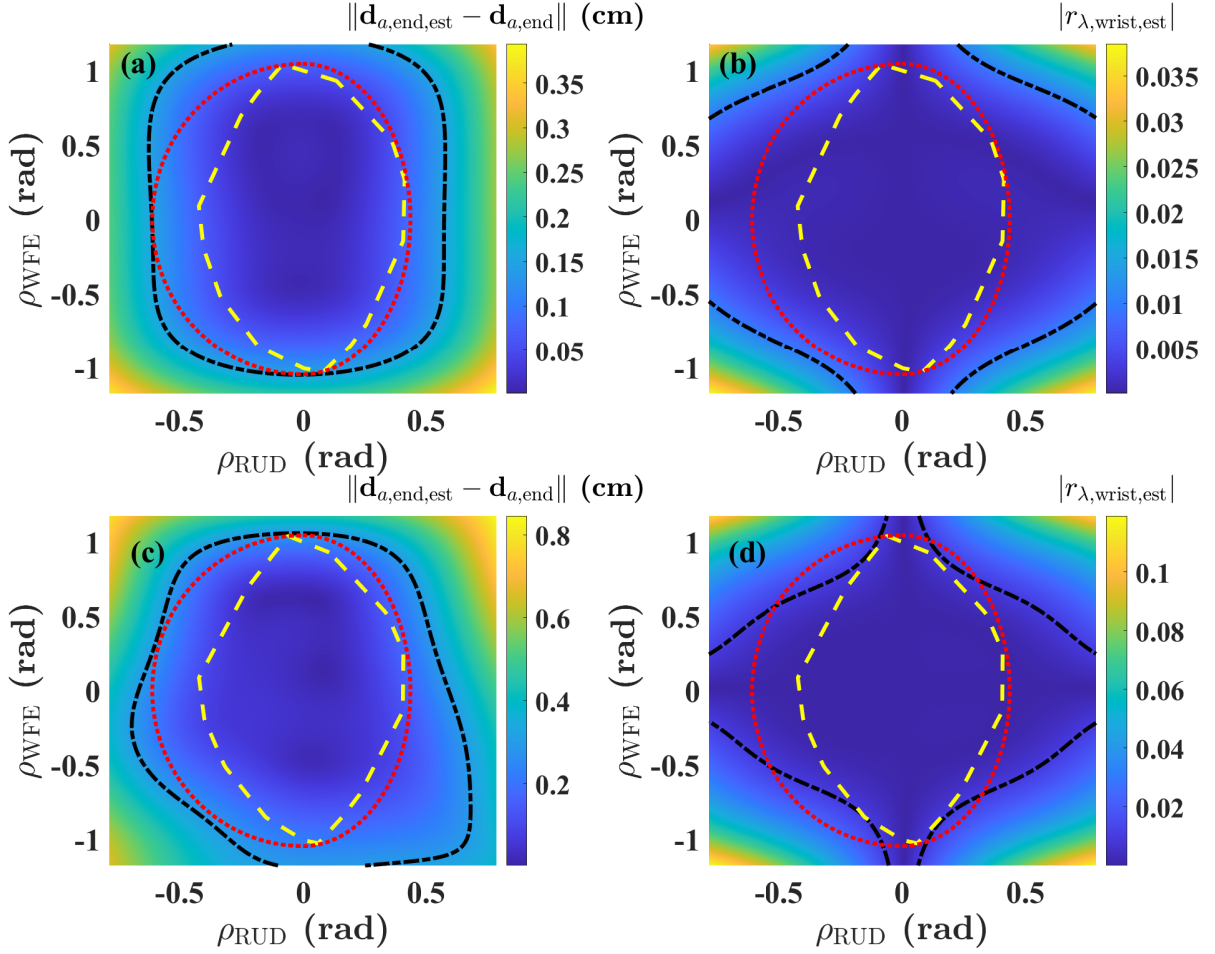


Figure 3.7: The performance of WKI algorithm on regressing two reference models [176], where (a, c) and (b, d) map the norms of estimation errors in translational displacement  $\|\mathbf{d}_{a,\text{end,est}} - \mathbf{d}_{a,\text{end}}\|$  and rotational constraint  $|r_{\lambda,\text{wrist,est}}|$ , respectively. Here, (a, b) are results from the first reference (with  $\mathbf{d}_{\text{wrist},r,2}$  and  $\mathbf{\Omega}_{\text{wrist,WRWR}}$ ); (c, d) are results from the second reference (with  $\mathbf{d}_{\text{wrist},r,3}$  and  $\mathbf{\Omega}_{\text{wrist,FWTR}}$ ). In the maps, the yellow dash contour contains the region traversed by the motion trajectory  $\boldsymbol{\rho}_{\text{wrist,main}}$ ; the red dot contour is the circumduction envelope of the wrist motions [141]. The black dot-dash contours in (a) and (c) contains the regions where  $\|\mathbf{d}_{a,\text{end,est}} - \mathbf{d}_{a,\text{end}}\| \leq 1.5$  mm and  $\|\mathbf{d}_{a,\text{end,est}} - \mathbf{d}_{a,\text{end}}\| \leq 3$  mm, respectively; and the black dot-dash contours in (b, d) contains the regions where  $|r_{\lambda,\text{wrist,est}}| < 0.01$ .

and the second reference model adopts  $\mathbf{d}_{\text{wrist},r,3}$  as translation and  $\mathbf{\Omega}_{\text{wrist,FWTR}}$  as rotation, where  $\mathbf{D}_{\text{wrist},d,\text{linear}} = [0, 0; 0, -2; 0, 0]$  cm. For each case, the SP-EKF updates the regression models for  $3 \times 10^4$  steps within 2 minutes. The norms of translational displacement estimation error  $\|\mathbf{d}_{a,\text{end,est}} - \mathbf{d}_{a,\text{end}}\|$  and rotational constraint estimation error  $|r_{\lambda,\text{wrist,est}}|$

from the updated models are then mapped in the domain of  $\rho_{\text{wrist,main}}$ . As shown in Fig. 3.7, for translational regressions, the envelopes of wrist circumduction movements [141] are contained within the regions of  $\|\mathbf{d}_{a,\text{end,est}} - \mathbf{d}_{a,\text{end}}\| \leq 1.5$  mm for the first reference ( $\mathbf{d}_{a,\text{end}} = \mathbf{d}_{a,\text{end},r,2}$ ), and  $\|\mathbf{d}_{a,\text{end,est}} - \mathbf{d}_{a,\text{end}}\| \leq 3$  mm for the second reference ( $\mathbf{d}_{\text{wrist}} = \mathbf{d}_{a,\text{end},r,3}$ ). These estimation errors are respectively within 1% and 2% of the ranges of  $\|\mathbf{d}_{a,\text{end}}\|$ , which are approximately 15 cm for both cases. The results also indicate that the proposed ellipsoid-based translation  $\mathbf{d}_{\text{wrist}}$  in Eq. (A.1) is relatively more complicated and difficult to model. For rotational regressions, the circumduction envelopes are largely contained within the regions

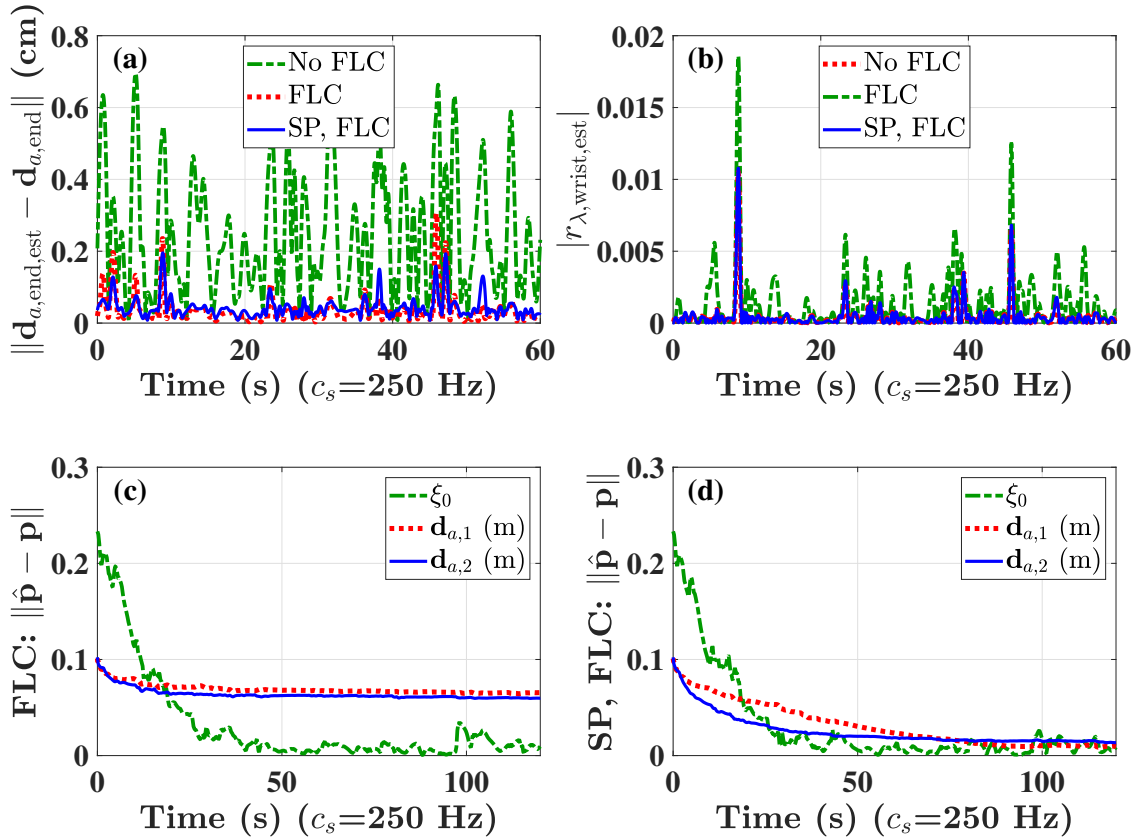


Figure 3.8: The comparison of regression performances using a simplified regression model (no FLC) [176], a full model updated by regular EKF, and a full model updated by SP-EKF, where (a) compares the norm of the translational displacement estimation error  $\|\mathbf{d}_{a,\text{end,est}} - \mathbf{d}_{a,\text{end}}\|$ ; (b) compares the norm of estimated rotation constraint  $|r_{\lambda,\text{wrist,est}}|$  (whose true value is zero); (c) and (d) demonstrates the norm of the primary parameter estimation errors from the regression model with FLC respectively updated by regular EKF and SP-EKF.

of  $|r_{\lambda, \text{wrist, est}}| \leq 0.01$  for both cases, which are within 5% of the range of quaternion-based constraint  $|r_{\lambda, \text{wrist, 0}}|$  as calculated from Eq. (3.1). Hence, the WKI algorithm is general and can approximate various reference models. The second reference (with  $\mathbf{d}_{\text{wrist}, r, 3}$  and  $\mathbf{\Omega}_{\text{wrist}, \text{FWTR}}$ ) is also used in the later simulations.

We then compare three different regression configurations: the simplified regression model (with no FLC) updated by regular EKF, the full model updated by regular EKF, and the full model updated by SP-EKF. From Fig. 3.8(a), we observe that the full regression model excels in translational displacement estimations. This confirms that FLC is effective in modeling the nonlinear kinematics introduced by  $\mathbf{d}_{\text{wrist}}$  from the reference  $\mathbf{d}_{\text{wrist}, r, 3}$ . For quaternion-based constraint regression shown in Fig. 3.8(b), the benefit from FLC is not significant, since the reference rotation  $\mathbf{\Omega}_{\text{wrist}, \text{FWTR}}$  can be closely approximated with the term  $c_{\xi} \sin(\rho_{\text{WFE}}/2) \sin(\rho_{\text{RUD}}/2)$  from Eq. (3.16). While models updated by regular EKF can achieve good approximation, regular EKF cannot prioritize the identification of primary parameters  $\xi_{a,1}$ ,  $c_{\xi}$ ,  $\mathbf{d}_{a,1}$ , and  $\mathbf{d}_{a,2}$  as shown in Fig. 3.8(c). SP-EKF, on the other hand, ensures the convergence of these parameters to the vicinity of their true values as shown in

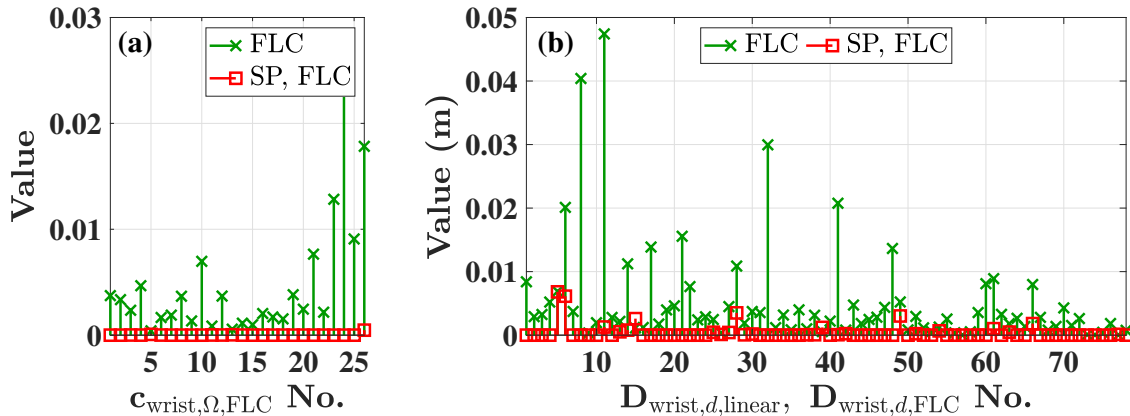


Figure 3.9: The comparison of parameter sparsities (zeros versus non-zeros) of the models respectively updated by regular EKF and SP-EKF [176], where (a) shows the rotational parameter values from  $c_{\text{wrist}, \Omega, \text{FLC}}$ , and (b) presents the translational parameter values from  $\mathbf{D}_{\text{wrist}, d, \text{linear}}$  and  $\mathbf{D}_{\text{wrist}, d, \text{FLC}}$ .

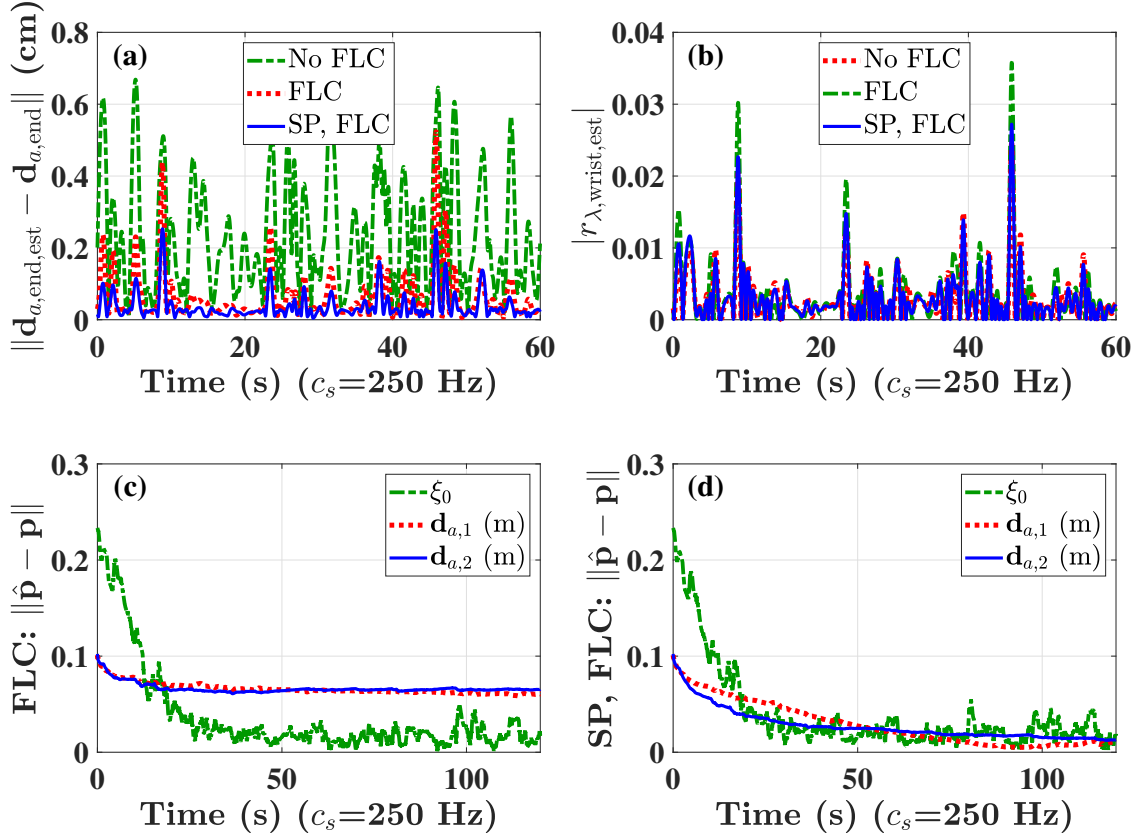


Figure 3.10: The comparison of regression performances using a simplified regression model (no FLC) [176], a full model updated by regular EKF, and a full model updated by SP-EKF based on noisy motion data. The specifications of the subplots are the same as those in Fig. 3.8.

Fig. 3.8(d). Figure 3.9 indicates that SP-EKF also significantly decreases the number of the nonzero parameters, leading to simpler models suitable for further analysis.

SP-EKF also provides robustness towards noises. To demonstrate this, the translational and rotational motion data are overlaid with high-frequency quasi-period noises, whose ranges are  $\pm 2$  mm and  $\pm 2^\circ$ , respectively. In Figs. 3.10(a, b), we observe that SP-EKF yields better regressions under noises, particularly in translational displacement estimations. Figures 3.10(c, d) show that SP-EKF can also identify primary kinematic parameters despite the noises.

The simulations show that the proposed regression model in Eqs. (3.15, 3.16) can approximate various reference models. The potentials of SP-EKF in reducing model complexity, prioritizing the identification of primary parameters, and providing robustness towards noises are also observed. In the next section, experiments are carried out with WKMT to further validate the proposed WKI approach.

### 3.4 Experimental Validation

Experimental validation of the proposed WKI algorithm is carried out based on wrist motion data collected by WKMT. The experimental setup is shown in Fig. 3.11. The wearability of WKMT is similar to that of TAWE. WKMT is attached to the human body through Velcro

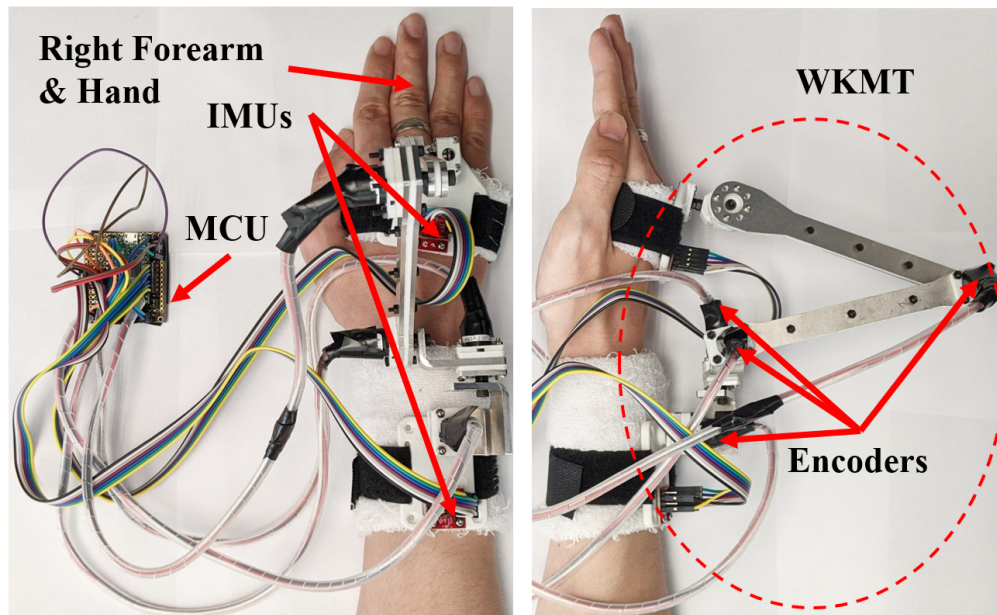


Figure 3.11: The experimental setup [176]: the author wears the WKMT via sleeves/bands and Velcro tapes on his right forearm. The IMU sensors are installed on the base parts attached to the forearm and hand dorsum. The encoder locations on the WKMT are also marked. The sensor data is collected by a microchip processor (MCU), which transmits the data to a computer.

tapes, which indicates that wearing locations can slowly shift over time. Therefore, the wrist kinematic parameter  $\rho_{\text{wrist,main}}$  from Eq. (3.17) is assumed to be slowly time-varying.

The user is asked to keep randomly moving the wrist during data collection. The WKMT samples wrist motions at a rate of  $c_s = 200$  Hz. The measurement noises are eliminated by a 10-Hz low-pass filter. Note that the filter should be carefully selected to avoid distortion of real wrist movements. An example of the processed rotation trajectory of  $\xi_{a,\text{end}}$  is shown in Fig. 3.12(a). The translational displacement  $\mathbf{d}_{a,\text{end}}$  of the wrist in the 3D space is shown in Fig. 3.12(b, c) from different viewing aspects. It is observed that the distribution of the translational displacements are approximately located on a surface, which indicates that it is valid to model the wrist as a 2-DOF joint.

To compare different regression setups, the data are regressed offline. However, the proposed WKI algorithm is efficient for real-time application, and can run at 1100 Hz on a 3.6 GHz Processor (AMD Ryzen 7 1800X). The configurations of EKF and initial estimations are the same as in Section 3.3, except that the covariance matrix  $\mathbf{Q}_{\text{WKI},p}$  has been updated to  $\mathbf{Q}_{\text{WKI},p} = 10^{-10}\mathbf{I}_{119}$  for more steady estimations of  $\xi_{a,1}$  and  $c_\xi$ .

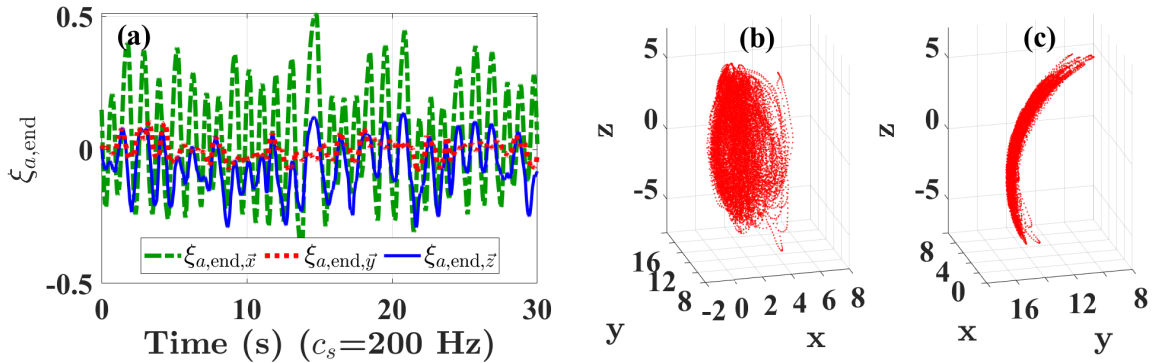


Figure 3.12: The experimental wrist motion data, where (a) shows the  $\vec{x}$ ,  $\vec{y}$ , and  $\vec{z}$  components of  $\xi_{a,\text{end}}$ , and (b, c) presents the translational displacement in a 3D space from different view angles. The axis units in (b, c) are centimeters.

### 3.4.1 Regression Performance

The wrist kinematics estimation performance of a model with FLC updated by SP-EKFs is presented in Fig. 3.13. After 6000 steps of update within 30 seconds, the model closely approximates the translational displacements. The norm of maximum translational estimation error is around 5 mm, which is below 5% of the total range of wrist translational displacement. The absolute value of quaternion-based constraint regression is contained within 0.05.

The consistency of real-time regressions as well as the comparison of different WKI configurations are shown in Figs. 3.14 and 3.15. For each configuration, three 60-second estimation

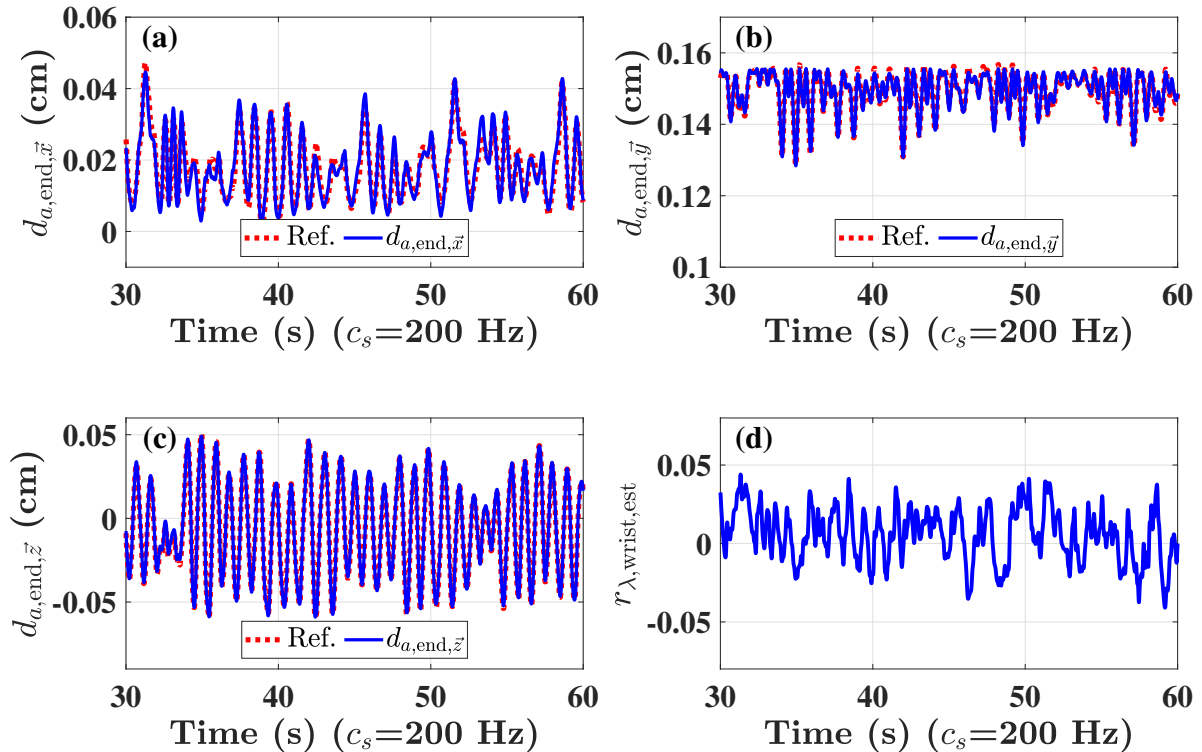


Figure 3.13: The estimation performance of a model with FLC terms updated by SP-EKF based on 30 seconds of experimental motion data (sampling rate  $c_s = 200$ ) [176]. The  $\bar{x}$ ,  $\bar{y}$ , and  $\bar{z}$  components of  $\mathbf{d}_{a,end,est}$  and their references from  $\mathbf{d}_{a,end}$  are shown respectively in (a, b, c); the trajectory of  $r_{\lambda,wrist,est}$  is shown in (d).

tests are carried out, which are respectively based on models updated for 30, 60, and 90 seconds (6000 updates between one model and another). For translational regressions, we respectively adopt a simplified model without FLC, a model with a constant offset amid the rotation (i.e.,  $\mathbf{d}_{\text{wrist},r,2}$  from Eq. (3.35)), and the proposed model updated with SP-EKF. The first two cases yield similar performances as shown Figs. 3.14(a, b), and the proposed model excels in regression accuracy with 50% smaller estimation errors as shown in Fig. 3.14(c).

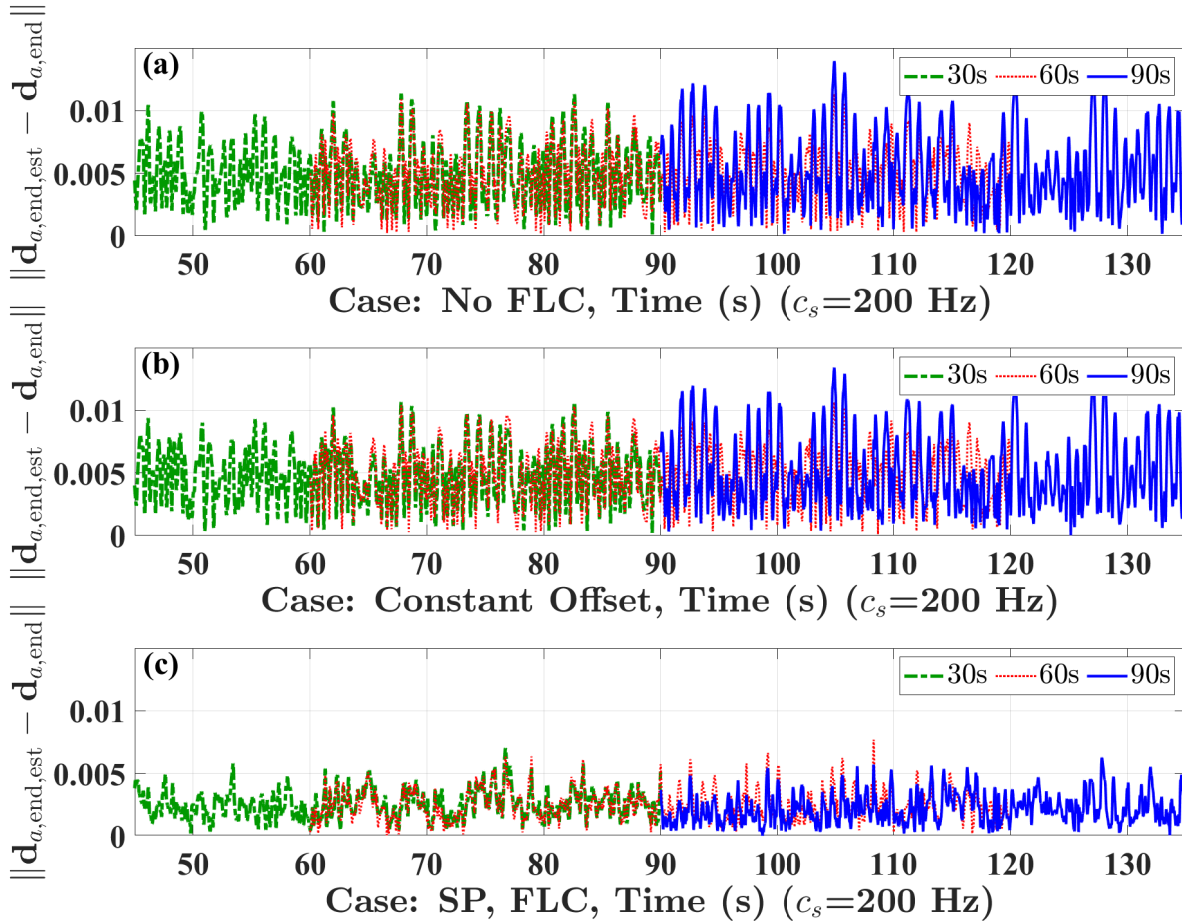


Figure 3.14: The norms of translational displacement estimation errors  $\|\mathbf{d}_{a,\text{end,est}} - \mathbf{d}_{a,\text{end}}\|$  from different WKI setups based on experimental data [176], where (a) uses a simplified model without FLC; (b) adopts a model with a model with a constant offset amid the rotation (i.e.,  $\mathbf{d}_{\text{wrist},r,2}$ ); and (c) uses the proposed model updated with SP-EKF. For each case, three 60-second tests are carried out, which are respectively based on models updated for 30, 60, and 90 seconds.

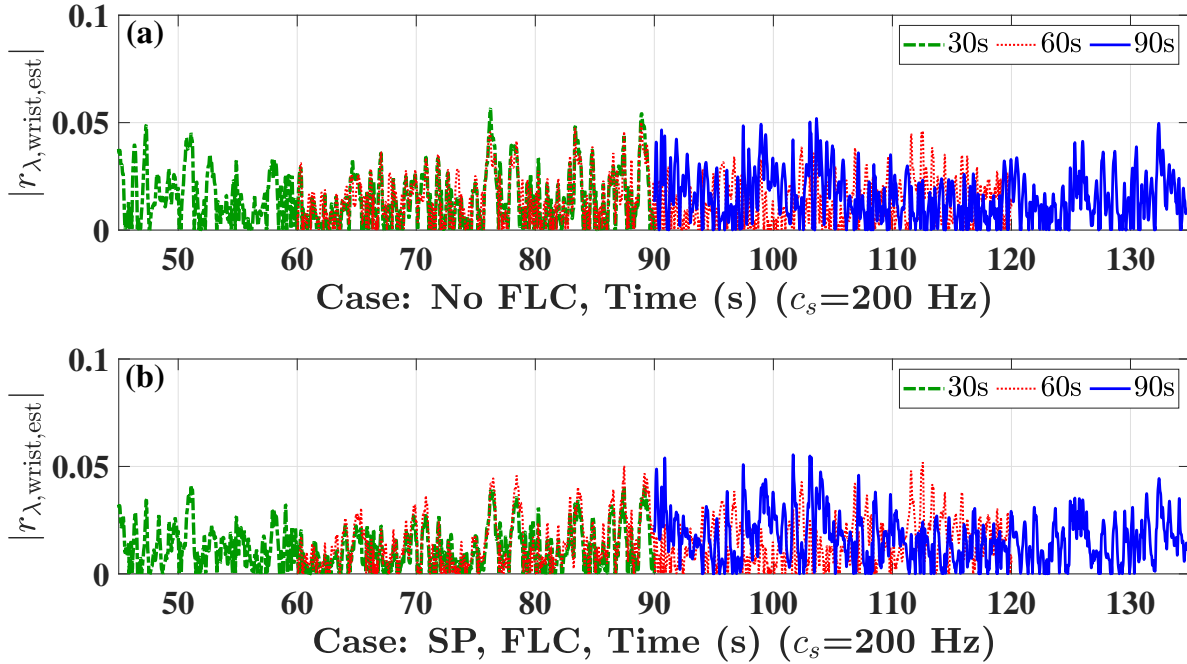


Figure 3.15: The norm of rotational constraint estimation errors  $|r_{\lambda, \text{wrist}, \text{est}}|$  (whose truth is zero) from different WKI setups based on experimental data [176], where (a) uses a simplified model without FLC; (b) uses the proposed model updated with SP-EKF. For each case, three 60-second tests are carried out, which are respectively based on models updated for 30, 60, and 90 seconds.

The rotational constraint estimation errors are compared in Fig. 3.15. Similar to the simulations, FLC does not significantly improve the regression performance. In general, we also observe larger rotational constraint estimation errors from experiments than from simulations. Apart from slowly varying wrist kinematics, the observation also suggests that the real wrist rotation may be much more complicated.

Figures 3.14 and 3.15 also show the real-time adaptability of the WKI algorithm. In the overlapped estimation windows of two models, the model updated with the newer data yields different and potentially smaller estimation errors. This also indicates that the proposed real-time WKI algorithm can keep up with slowly varying kinematic properties.

### 3.4.2 Analysis of the Identified Model

Since the wrist motion data is filtered before regression, the experiments do not distinctively show the robustness of SP-EKF towards noise. However, SP-EKF ensures the identifications of the primary wrist kinematic parameters as shown in Fig. 3.16. The displacements  $\hat{\mathbf{d}}_{a,1}$  and  $\hat{\mathbf{d}}_{a,2}$  are reasonable according to the user forearm profile, especially on the  $\vec{y}$  (distal) direction. The identified  $\hat{c}_\xi$  is close to zero, which suggests no similarity to any sequential rotations (e.g., first-RUD-then-WFE ( $\mathbf{\Omega}_{\text{wrist,FRTW}}$  from Eq. (2.12)), first-WFE-then-RUD ( $\mathbf{\Omega}_{\text{wrist,FWTR}}$ ) from Eq. (2.11)).

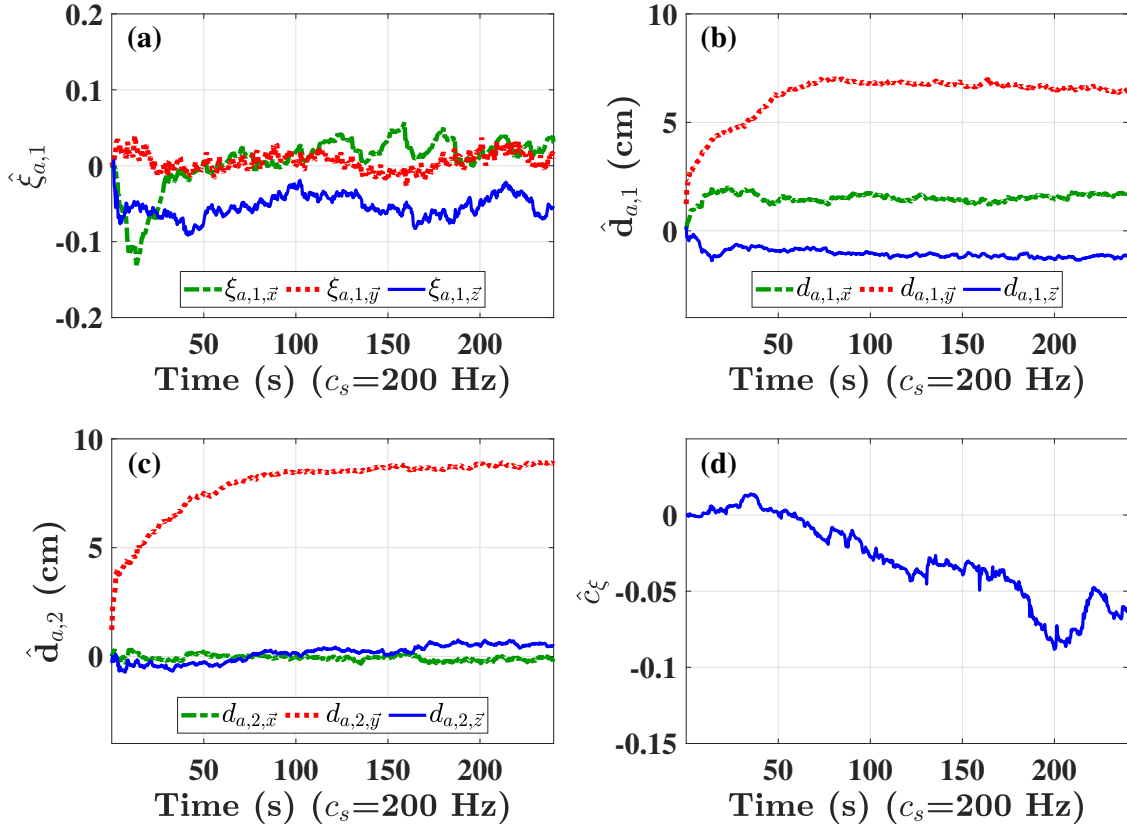


Figure 3.16: The estimated primary parameters from the model with FLC trained by SP-EKF [176], where (a) shows the estimation of the  $\vec{x}$ ,  $\vec{y}$ , and  $\vec{z}$  components of  $\xi_{a,1}$ , (b) presents the estimation  $\hat{\mathbf{d}}_{a,1}$ , and (c) shows the estimation  $\hat{\mathbf{d}}_{a,2}$ , and (d) presents the identification of  $\hat{c}_\xi$ .

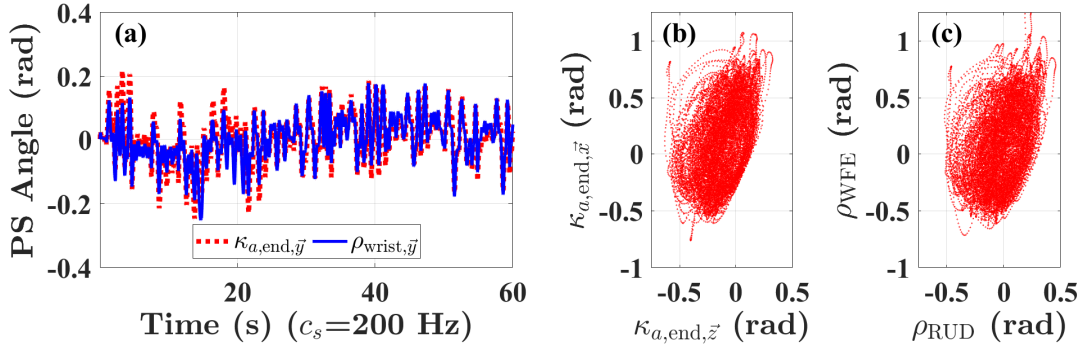


Figure 3.17: The comparison between wrist rotation presented in Frame A1 and Frame W1 [176]. Here, (a) shows the angle  $\kappa_{a,end,\vec{y}}$  and  $\rho_{wrist,\vec{y}}$  on pronation-supnation direction, (b) shows the RUD-WFE trajectory in Frame A1, (c) shows the RUD-WFE trajectory in Frame W1. (Note -  $+\vec{z}$ : radial deviation,  $-\vec{z}$ : ulnar deviation,  $+\vec{x}$  extension,  $-\vec{x}$ : flexion).

The effect of the identified  $\hat{\xi}_{a,1}$  is demonstrated in Fig. 3.17. Here,  $\kappa_{a,end}$  is the  $\vec{z}$ - $\vec{y}$ - $\vec{x}$  Euler angle corresponding to  $\xi_{a,end}$ . As shown in Fig. 3.17(a), on the pronation-supnation (PS) direction, the angle  $\rho_{wrist,\vec{y}}$  measured in Frame W1 is slightly smaller than  $\kappa_{a,end,\vec{y}}$  measured in Frame A1. The WFE-RUD trajectories in Frame A1 and Frame W1 are respectively presented in Fig. 3.17(b, c). Notice that the oblique ellipsoidal shape of the RUD-WFE trajectory is also previously witnessed in other studies [11, 34, 155]. As the observation function  $\mathbf{h}_{WKL,2}$  from Eq. (3.32) drives the mean values of  $\kappa$  to zeros by converging the integral term  $\mathbf{x}_{\kappa,int}$ , the RUD-WFE trajectory in Fig. 3.17(c) is shifted to center around the origin. Note that this does not deny the correctness of Fig. 3.17(b), since Figs. 3.17(b) and (c) respectively display the same wrist rotation in two different frames.

In general, the experimental results corroborate the simulation observations. The proposed WKI algorithm is proven capable of identifying wrist kinematics in real time. The regression model with FLC updated by SP-EKF can approximate the wrist motion with good accuracy, and provide useful wrist kinematic information for analysis.

## 3.5 Summary

This chapter introduced a novel method for real-time wrist kinematics identification (WKI). We designed the regression model based on ellipsoidal joint formulation, which features a quaternion-based constraint that characterizes the constrained wrist rotation. The regression model also employs 2D Fourier linear combiners (FLC) to approximate unmodeled nonlinear wrist kinematic features. Extended Kalman filter (EKF) was implemented to update the model in real time based on wrist motion data. A sparsity-promoting EKF (SP-EKF) was also realized through a smooth  $\ell^1$ -minimization observation function that utilizes the optimality of EKF.

To test the WKI algorithm and compare different regression setups, simulations were carried out using various reference models. Observations from simulations showed that: (1) the proposed model with FLC can accurately approximate various reference models; (2) the quaternion-based constraint can regress and classify different sequential rotational models; and (3) SP-EKF can provide accurate regression with reduced model complexity, and robustness towards the noise. We also developed a wrist kinematic measurement tool (WKMT) to collect wrist motion data for experimental validation. The experimental results corroborated the findings from the simulations. The experiment also showed that the proposed real-time WKI algorithm can adapt to slowly time-varying properties, and identify primary wrist kinematic parameters that are useful for analysis.

While motivated by the development of TAWA, the proposed method can be applied to generic wrist kinematics modeling problems. The framework of the proposed method may also apply to the real-time identifications of other human joints for exoskeleton control. The next chapter will discuss the motion controller design for the exoskeleton to realize tremor alleviation.

# Chapter 4

## Exoskeleton Control for Tremor

### Alleviation

As mentioned in Section 1.3.2, various controllers [16, 17, 22, 63, 183] have been developed for rehabilitation exoskeletons. When provided a reference trajectory, the goal of the controller is to calculate and provide actuation inputs to the human-exoskeleton dynamic system, so that its motion trajectories can converge to and follow the tracking reference.

For tremor alleviation in user-guided operations, the exoskeleton needs to provide both reference tracking and tremor mitigation. A major challenge for controller design is the model uncertainty from the user. The dynamical properties such as inertia and load on the body parts, unless specifically measured, can generally be assumed as unavailable to the control system. Another challenge for exoskeleton control is perturbation/disturbance. Disturbances can come from soft tissue artifacts due to the deformations of skin and muscle (as discussed in Assumption (MA. 1)) [101], and actuation fluctuation from both the user and exoskeleton.

The difference between model uncertainty and disturbance is that there exists a deterministic model that governs the behavior of the former. As previously mentioned, pathological tremors are generally oscillatory and rhythmic. Earlier studies suggest there exists a nonlinear dynamic system that underlies the behavioral patterns of tremors [119, 167, 172, 192]. Hence, it is acceptable for tremors to be considered as a part of the model uncertainty.

The performance and stability of these controllers under model uncertainties, perturbations, and disturbances are crucial to the reliability and safety of exoskeleton operations. This chapter discusses the exoskeleton controller design for tremor alleviation. Specifically, we introduce a robust adaptive controller based on inverse optimality theory [175]. The proposed inverse optimal robust adaptive controller (IO-RAC) can compensate for inertia and load uncertainties as well as provide robustness toward disturbances. The proposed control framework applies to not only TAWÉ, but also other exoskeletons and robotic systems.

The rest of the chapter is arranged as follows. In Section 4.1, we observe and analyze the experimental tremor signals, which leads to assumptions of tremor dynamics for controller design. In Section 4.2, we formulate the problem by establishing the human-exoskeleton control system that incorporates model uncertainties and disturbances. Section 4.3 discusses the model-based controller for tremor suppression, which focuses on the theoretical formulation and design of IO-RAC for rehabilitation exoskeleton. In Section 4.4, the performance of IO-RAC is demonstrated by simulation cases that feature TAWÉ and a stationary exoskeleton. Finally, Section 4.5 summarizes the findings in this chapter. The proofs of stability and optimality for the controllers are discussed in Appendix A.2-A.5. (The study in this chapter has been partially reported in [175].)

## 4.1 Tremor Dynamics and Assumptions

The neuromusculoskeletal dynamics of pathological tremor is extremely complicated. Research indicated that while some tremors originated anew in the central nervous system (CNS), others appear to be the amplification and distortion of physiological tremor [119]. The observations show that tremors are caused by multiple oscillators [133], which may contain components from the central neural oscillator, the peripheral neural feedback/reflex

resonance, and the mechanical resonance [119, 172, 192]. These subsystems in the nervous system are highly coupled. The tremor may be related to the time delays in the system as well [21, 59, 192]. It is noticed that Parkinsonian tremors may involve limit cycle behaviors resembling the effects of time delay [129]. On the other hand, tremor oscillations are not strictly periodic. Previous studies also suggest that the dynamics of tremor is highly stochastic and nonlinear [54, 136, 167].

### 4.1.1 Experimental Tremor Time Series Observation

The observation of tremor signals can lead to insights that are extremely useful to the development of exoskeleton controllers for tremor suppression. In this study, we first observe the dynamics of experimental tremor signals. The “Motus” tremor data set provides multiple experimental measurements of kinetic (e.g., Essential Tremor) and resting (e.g., Parkinso-

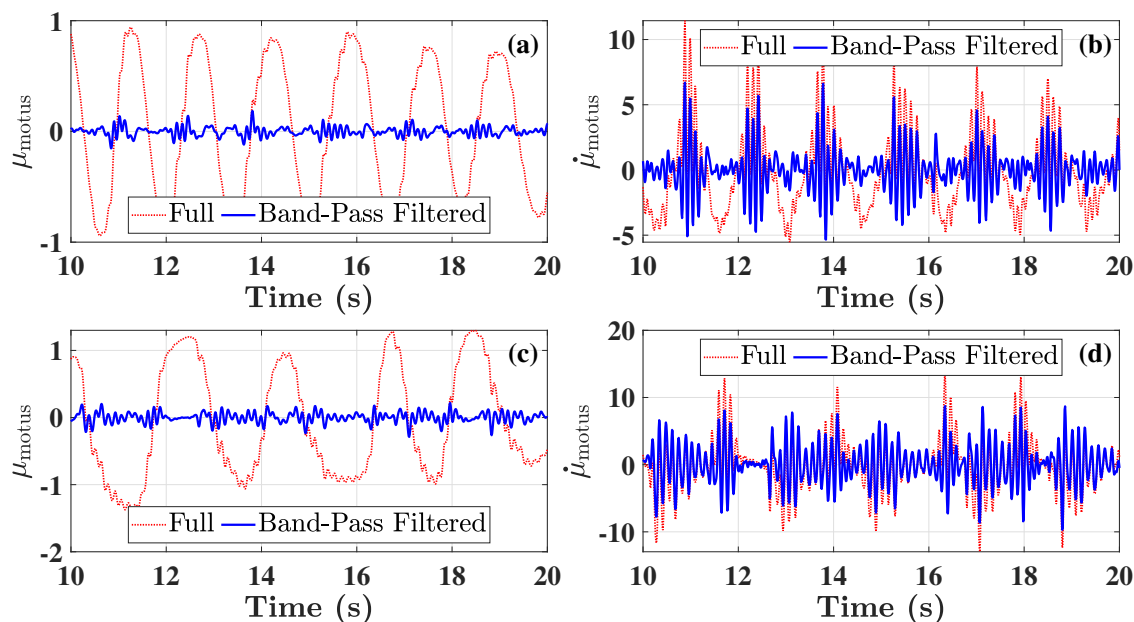


Figure 4.1: Two sets of kinetic tremor time series from the “Motus” tremor data set, where (a, b) show the angle and angular velocities of “Kinetic #1”, respectively; and (c, d) show the angle and angular velocities of “Kinetic #3”, respectively.

nian Tremor) tremor time series [134]. Each time series is 30 seconds long. The original measurements are angular velocities (converted to rad/s) sampled at 100 Hz, which are later numerically integrated to obtain the joint angles.

Some kinetic tremors can show approximately repetitive patterns in their oscillations. Such behavior is particularly noticeable in Fig. 4.1(b), where for every 1.5 seconds the amplitude of the tremor increases and then decreases. To analyze the periodicity, we performed the autocorrelation of the band-pass filtered tremor signals as shown in Fig. 4.2. Notice from Fig. 4.2(b) that for approximately every 1.5 seconds of time shift, the autocorrelation values will reach a local optimum, which matches the result in Fig. 4.1(b).

Here we demonstrate the characteristics of four selected sets of kinetic and rest tremor signals, which are labeled as “Kinetic # $i$ ” and “Resting # $i$ ”, respectively. Two of the active

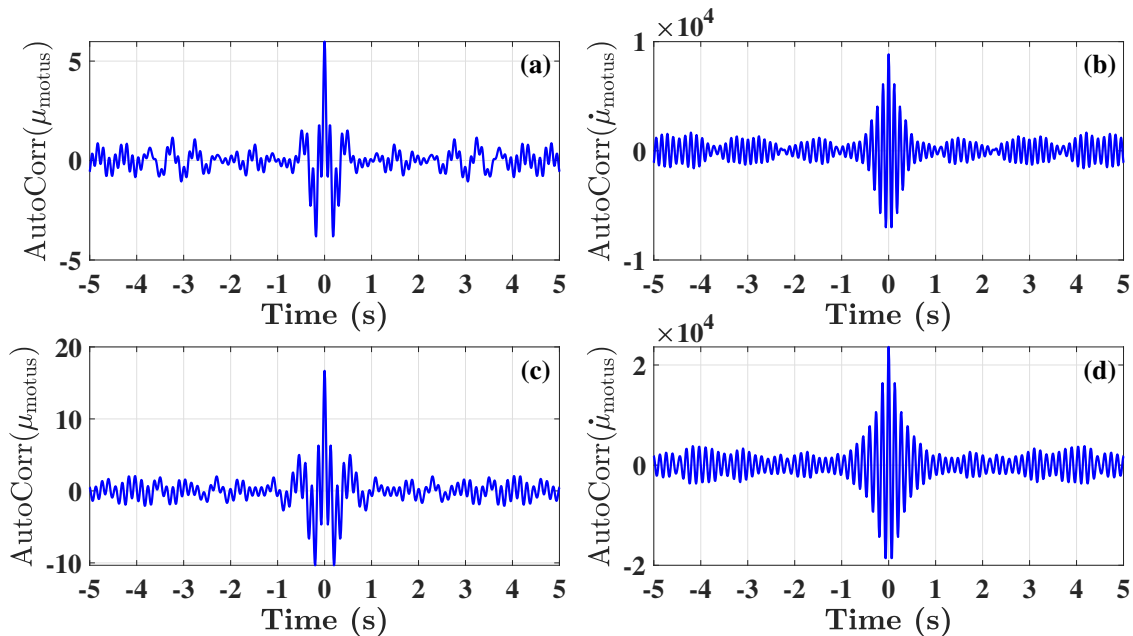


Figure 4.2: Autocorrelation plots for two sets of band-pass filtered kinetic tremor time series from the “Motus” tremor data set, where (a, b) show the autocorrelations of angle and angular velocities for “Kinetic #1”, respectively; and (c, d) show the autocorrelations of angle and angular velocities for “Kinetic #3”, respectively.

tremor time series are demonstrated in Fig. 4.1. In Figs. 4.1(a, c), we can easily observe the low-frequency sinusoidal voluntary movements, which are overlaid with tremors. After filtering the tremor from voluntary movement using a zero-phase 5th-order Butterworth band-pass filter from 1.5 to 20 Hz, we observe that the amplitude of tremor in angular position measurement is smaller than those of the voluntary movements. On the other hand, in the angular velocity measurement, the high-frequency tremor components show larger amplitudes. This suggests that tremor movements, while having small amplitudes in terms of position, can consume a significant amount of power.

Two of the resting tremor time series are demonstrated in Fig. 4.3. It can be easily noticed that the voluntary components in the time series are less insignificant since tremor components dominate the velocity trajectories as shown in Figs. 4.3 (b, d). Compared to kinetic tremors, resting tremors have smaller amplitudes. The patterns of resting tremor amplitude variations are also more irregular and difficult to identify.

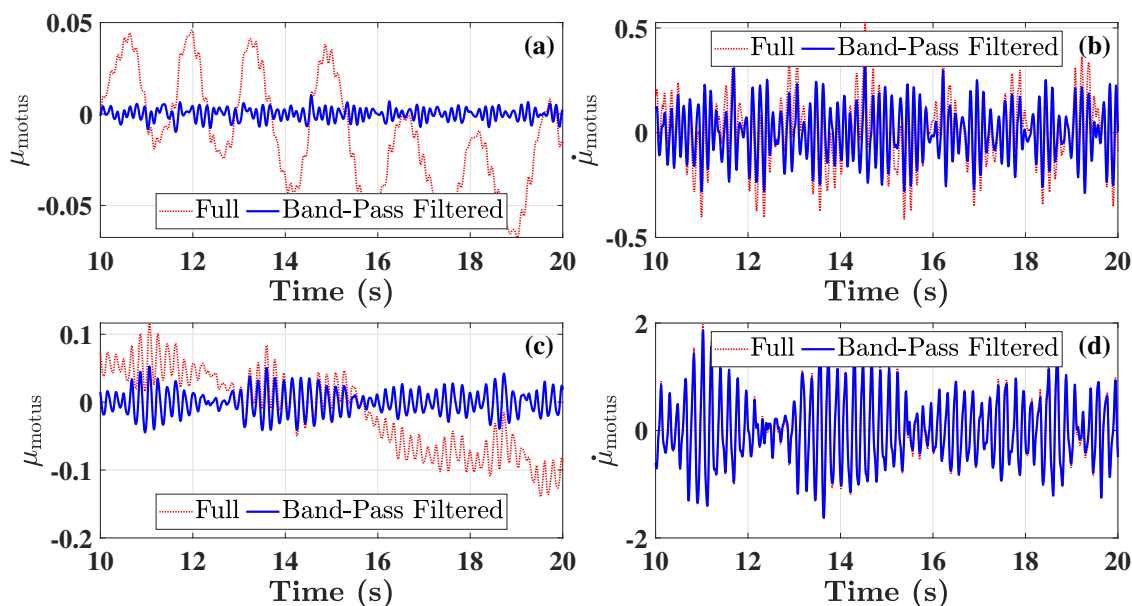


Figure 4.3: Two sets of resting tremor time series from the “Motus” tremor data set, where (a, b) show the angle and angular velocities of “Resting #1”, respectively; and (c, d) show the angle and angular velocities of “Resting #3”, respectively.

### 4.1.2 Frequency Components of Tremor

In the time series plots, the major high-frequency oscillation frequencies in both kinetic and resting tremors are relatively consistent throughout the demonstrated time span. To demonstrate the detailed frequency domain characteristics of kinetic and resting tremors, we present the amplitude spectrums of both kinetic and resting tremor time series in Figs. 4.4 and 4.5. Notice that all tremor signals present multiple frequency components, where the dominant frequency components range from 3 to 10 Hz. The dominant frequencies of resting tremors also appear to be more outstanding than the rest. Throughout the evolution of time, these components of tremors change in amplitude and frequency.

The frequency components indicate the complicated nonlinear dynamics behind pathological tremors [54, 167]. The exact neuromusculoskeletal model of tremor is extremely difficult to

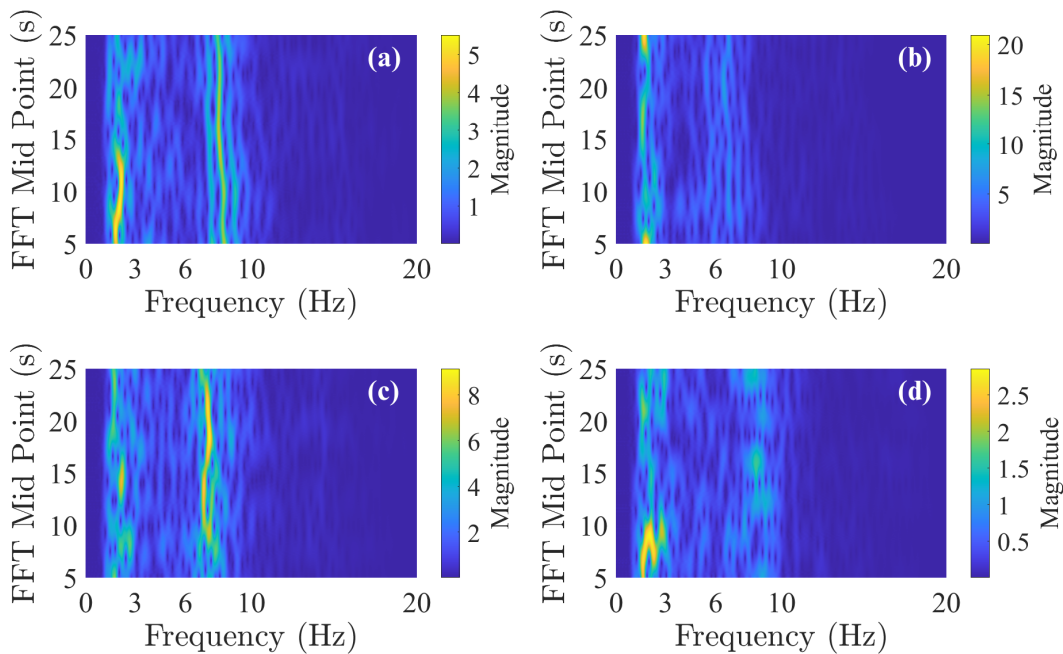


Figure 4.4: Amplitude spectrums of four sets of kinetic tremor time series from the “Motus” tremor data set, where (a-d) show the amplitude spectrums of angular position of “Kinetic #1-4”, respectively.

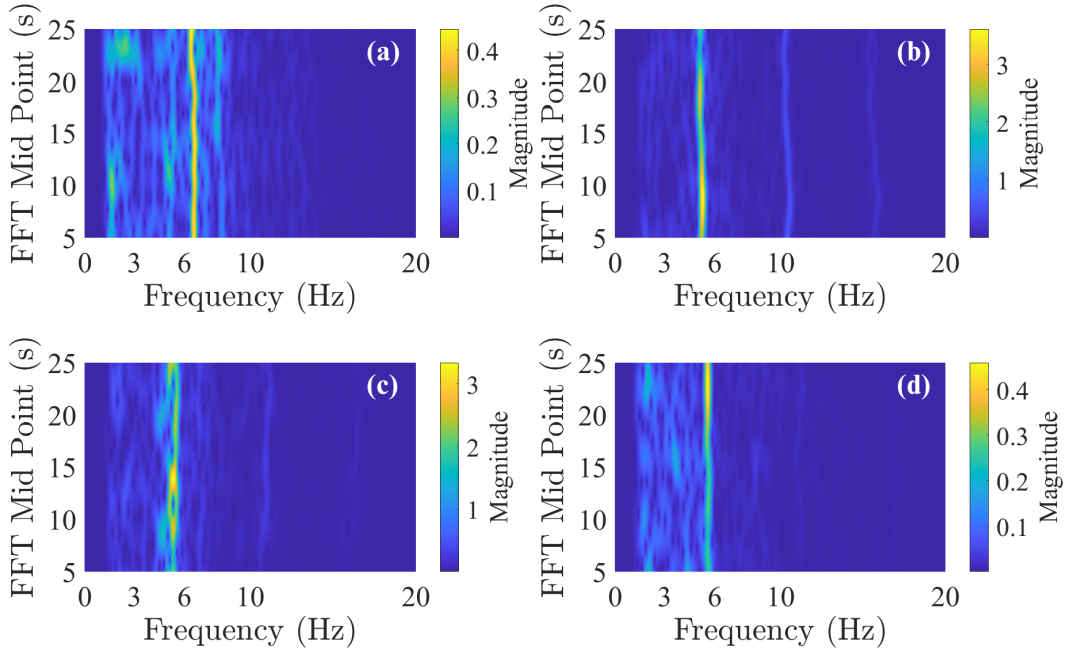


Figure 4.5: Amplitude spectrums of four sets of resting tremor time series from the “Motus” tremor data set, where (a-d) show the amplitude spectrums of angular position of “Resting #1-4”, respectively.

obtain. As discussed in Section 1.2.3, previous studies investigated the regression of tremor signals based on data-driven models such as weighted-frequency Fourier linear combiner [1, 135], band-limited multi-frequency Fourier linear combiner (BMFLC) [171], AR model [163], support vector machine [164], and neural networks [74, 150]. While none of the models can perfectly describe the tremor dynamics, they can effectively approximate or predict tremor signals in a short time window.

In particular, the BMFLC model assumes that tremor signals are combinations of harmonic waves with different frequencies within a certain bandwidth. The structure of a BMFLC model with a total of  $n_{\text{BMFLC}}$  frequency components can be written as

$$\mu_{\text{BMFLC}}(t) = \sum_{i=1}^{n_{\text{BMFLC}}} \left( p_{\mu, \text{BMFLC}, i} \sin(c_{\mu, \text{BMFLC}, i} t) + p_{\mu, \text{BMFLC}, i+n} \cos(c_{\mu, \text{BMFLC}, i} t) \right) \quad (4.1)$$

where  $c_{\mu, \text{BMFLC}, i}$  is the  $i$ th constant frequency, and  $p_{\mu, \text{BMFLC}, i}$  is the  $i$ th uncertain amplitude parameter. The frequencies  $c_{\mu, \text{BMFLC}, 1}$  and  $c_{\mu, \text{BMFLC}, n_{\text{BMFLC}}}$  determines the bandwidth, and  $n_{\text{BMFLC}}$  determines the frequency-domain resolution of model. Notice that all the harmonic terms in BMFLC are combined linearly. Hence, we can obtain the Jacobian matrix  $\mathbf{J}_{p, \text{BMFLC}}$  so that

$$\mathbf{J}_{p, \text{BMFLC}}(t) = \begin{bmatrix} \left[ \begin{array}{c} \sin(c_{\mu, \text{BMFLC}, 1} t) \\ \sin(c_{\mu, \text{BMFLC}, 2} t) \\ \vdots \\ \sin(c_{\mu, \text{BMFLC}, n_{\text{BMFLC}}} t) \end{array} \right]^T & \left[ \begin{array}{c} \cos(c_{\mu, \text{BMFLC}, 1} t) \\ \cos(c_{\mu, \text{BMFLC}, 2} t) \\ \vdots \\ \cos(c_{\mu, \text{BMFLC}, n_{\text{BMFLC}}} t) \end{array} \right]^T \end{bmatrix}^T \quad (4.2a)$$

$$\mu_{\text{BMFLC}} = \mathbf{J}_{p, \text{BMFLC}} \mathbf{p}_{\mu, \text{BMFLC}} \quad (4.2b)$$

Due to the shifting in amplitude and frequency of tremor harmonic components, BMFLC is commonly applied in real-time regression, where the amplitude parameters are adaptively updated online based on regression error. With high enough frequency-domain resolution  $n_{\text{BMFLC}}$ , the BMFLC can accurately describe the dynamics of tremor in a short time window. The BMFLC model will be frequently used in the remaining of this project for both controller design and signal processing.

## 4.2 Human-Exoskeleton Control System

In this study, the human-exoskeleton control system is formulated based on a generic model

$$\begin{aligned} \mathbf{M}(\mathbf{q}, \boldsymbol{\rho}, \mathbf{p}_M) \ddot{\mathbf{q}} = & -\mathbf{C}(\mathbf{q}, \dot{\mathbf{q}}, \boldsymbol{\rho}, \mathbf{p}_M) \dot{\mathbf{q}} - \mathbf{g}(t, \mathbf{q}, \dot{\mathbf{q}}, \boldsymbol{\rho}, \mathbf{p}_M, \mathbf{p}_g) + \mathbf{u}_{\text{user}} \\ & + \mathbf{J}_{u, \text{exo}}^T(\mathbf{q}, \boldsymbol{\rho}) \mathbf{u}_{\text{exo}} + \mathbf{J}_w(\mathbf{q}, \boldsymbol{\rho})^T \mathbf{w} \end{aligned} \quad (4.3)$$

Notice that the control-targeting dynamical model of TAWÉ from Eq. (2.45) fits the structure of this model after a few adjustments. We introduce  $\mathbf{p}_M \in \mathbb{R}^{n_p, M}$  and  $\mathbf{p}_g \in \mathbb{R}^{n_p, g}$ , which are the parameters for inertial and generalized force uncertainties, where  $\mathbf{p}_M$  affects all of the inertial matrix  $\mathbf{M}$ , Coriolis and centripetal matrix  $\mathbf{C}$ , and generalized force  $\mathbf{g}$ , while  $\mathbf{p}_g$  is only involved in  $\mathbf{g}$ .

The previous model assumptions (MA. 1) and (MA. 2) applies to the control system in Eq. (4.3). Similar as in TAWÉ, the controller design also requires the system to be fully actuated, which leads to an additional assumption

(MA. 3) The exoskeleton input  $\mathbf{u}_{\text{exo}} \in \mathbb{R}^{n_{u, \text{exo}}}$  can actuate all the DOFs  $\mathbf{q} \in \mathbb{R}^{n_q}$  within the human-exoskeleton closed kinematic chain. This leads to  $n_{u, \text{exo}} \geq n_q$  and  $\text{rank}(\mathbf{J}_u) = n_q$ .

Finally, note that both  $\mathbf{u}_{\text{user}}$  and  $\mathbf{u}_{\text{exo}}$  are ideal control inputs, which do not involve tremors or disturbances.

### 4.2.1 Control System based on Nonholonomic Outputs

The reference trajectory for exoskeleton tracking control may not directly be the trajectory of generalized coordinate  $\mathbf{q}$ , especially in the cases where there exist nonholonomic states  $\boldsymbol{\rho}$  in the multibody model. we introduce the nonholonomic control output as  $\mathbf{y}$ . The definition of  $\mathbf{y}$  along with its 1st order time-derivatives  $\dot{\mathbf{y}}$  can be written as

$$\dot{\mathbf{y}} = \mathbf{J}_y(\mathbf{q}, \boldsymbol{\rho})\dot{\mathbf{q}}; \quad \ddot{\mathbf{y}} = \mathbf{J}_y\ddot{\mathbf{q}} + \dot{\mathbf{J}}_y\dot{\mathbf{q}} \quad (4.4)$$

This leads to an alternative representation of  $\ddot{\mathbf{q}}$  as

$$\ddot{\mathbf{q}} = \mathbf{J}_y^{-1}\ddot{\mathbf{y}} - \mathbf{J}_y^{-1}\dot{\mathbf{J}}_y\mathbf{J}_y^{-1}\dot{\mathbf{q}} = \mathbf{J}_y^{-1}\ddot{\mathbf{y}} + \dot{\mathbf{J}}_y^{-1}\dot{\mathbf{y}} \quad (4.5)$$

which, by definition, requires  $\dim(\mathbf{y}) = \dim(\mathbf{q})$  and  $\text{rank}(\mathbf{J}_y) = \dim(\mathbf{q})$ . This allow us to convert the dynamical model in Eq. (4.3) into

$$\mathbf{M}_y\ddot{\mathbf{y}} = -\mathbf{C}_y\dot{\mathbf{y}} - \mathbf{g}_y + \mathbf{u}_{\text{user},y} + \mathbf{u}_{\text{exo},y} + \mathbf{J}_{w,y}^{-T}\mathbf{J}_w^T\mathbf{w} \quad (4.6)$$

where

$$\mathbf{M}_y = \mathbf{J}_y^{-T}\mathbf{M}\mathbf{J}_y^{-1}; \quad \mathbf{C}_y = \mathbf{J}_y^{-T}\mathbf{C}\mathbf{J}_y^{-1} + \mathbf{J}_y^{-T}\dot{\mathbf{M}}\dot{\mathbf{J}}_y^{-1}; \quad \mathbf{g}_y = \mathbf{J}_y^{-T}\mathbf{g} \quad (4.7a)$$

$$\mathbf{u}_{\text{user},y} = \mathbf{J}_y^{-T}\mathbf{u}_{\text{user}}; \quad \mathbf{u}_{\text{exo},y} = \mathbf{J}_{u,\text{exo},y}^T\mathbf{u}_{\text{exo}} = \mathbf{J}_y^{-T}\mathbf{J}_{u,\text{exo}}^T\mathbf{u}_{\text{exo}}; \quad \mathbf{J}_{w,y} = \mathbf{J}_w\mathbf{J}_y^{-1} \quad (4.7b)$$

Following (MA. 3), note that the relationship between  $\mathbf{u}_{\text{exo},y}$  and  $\mathbf{u}_{\text{exo}}$  also satisfies

$$\mathbf{u}_{\text{exo}} = (\mathbf{J}_{u,\text{exo},y}\mathbf{J}_{u,\text{exo},y}^T)^{-1}\mathbf{J}_{u,\text{exo},y}\mathbf{u}_{\text{exo},y} = \mathbf{J}_{u,\text{exo},y}^+\mathbf{u}_{\text{exo},y} \quad (4.8)$$

which calculates the  $\mathbf{u}_{\text{exo}}$  that has the smallest  $l^2$  norm according to the Moore-Penrose pseudo inverse. This allows Eq. (4.6) to be applied to over-actuated systems (e.g., cable-driven exoskeletons [115]) as well.

Hence, by defining a tracking reference  $\mathbf{r}_y(t) \in \mathbb{R}^{n_q}$ , the tracking error  $\boldsymbol{\epsilon} \in \mathbb{R}^{n_q}$  and control system state  $\mathbf{x} \in \mathbb{R}^{n_q}$  can be written as

$$\boldsymbol{\epsilon} = \mathbf{y} - \mathbf{r}_y; \quad \mathbf{x} = \begin{bmatrix} \boldsymbol{\epsilon}^T & \dot{\boldsymbol{\epsilon}}^T \end{bmatrix}^T \quad (4.9)$$

It should be noted that  $\mathbf{r}_y$  should be at least a Class  $\mathcal{C}^2$  function of time  $t$  so that continuity of

its 2nd order derivative is guaranteed. In some physiotherapies,  $\mathbf{r}$  can be manually designed by the therapists [17]. The motion planning of  $\mathbf{r}$  may also be realized through the filtering or prediction of voluntary motion [52, 74, 117, 150], which will be further discussed in the next chapter.

Therefore, the control system can be written as

$$\dot{\mathbf{x}} = \mathcal{F}(\mathbf{x}) + \mathcal{G}(t, \mathbf{q}, \dot{\mathbf{q}}, \boldsymbol{\rho}, \mathbf{p}) + \mathcal{U}(\mathbf{q}, \boldsymbol{\rho})(\mathbf{u}_{\text{user},y} + \mathbf{u}_{\text{exo},y}) + \mathcal{W}(\mathbf{q}, \boldsymbol{\rho})\mathbf{w} \quad (4.10)$$

where

$$\begin{aligned} \mathcal{F} &= \begin{bmatrix} \dot{\epsilon} & \mathbf{0} \end{bmatrix}^T; & \mathcal{G} &= \begin{bmatrix} \mathbf{0} & -\ddot{\mathbf{r}}_y - \mathbf{M}_y^{-1}(\mathbf{C}_y\dot{\mathbf{y}} + \mathbf{g}_y) \end{bmatrix}^T; \\ \mathcal{U} &= \begin{bmatrix} \mathbf{0} & \mathbf{M}_y^{-1} \end{bmatrix}^T; & \mathcal{W} &= \begin{bmatrix} \mathbf{0} & \mathbf{M}_y^{-1}\mathbf{J}_{w,y}^T \end{bmatrix}^T \end{aligned} \quad (4.11)$$

Hence, Eq.(4.10) is a time-dependent nonlinear control system affine in terms of  $\mathbf{u}_{\text{user},y}$ ,  $\mathbf{u}_{\text{exo},y}$ , and  $\mathbf{w}$ .

## 4.2.2 Uncertainties and Disturbances

Equation (4.6) involves the model uncertain parameter  $\mathbf{p} \in \mathbb{R}^{n_p}$  (where  $n_p = n_{p,M} + n_{p,g}$ ), which is defined as

$$\mathbf{p} = \begin{bmatrix} \mathbf{p}_M^T & \mathbf{p}_g^T \end{bmatrix}^T \quad (4.12)$$

The uncertain parameter need to satisfy the following conditions

$$\mathbf{M}_y(\mathbf{q}, \boldsymbol{\rho}, \mathbf{p}_M)\mathbf{z}_y = \mathbf{J}_{M,y}^T(\mathbf{q}, \boldsymbol{\rho}, \mathbf{z}_y)\mathbf{p}_M + \mathbf{M}_{y,0}(\mathbf{q}, \boldsymbol{\rho})\mathbf{z}_y \quad (4.13a)$$

$$\mathbf{C}_y(\mathbf{q}, \dot{\mathbf{q}}, \boldsymbol{\rho}, \mathbf{p}_M)\mathbf{z}_y = \mathbf{J}_{C,y}^T(\mathbf{q}, \dot{\mathbf{q}}, \boldsymbol{\rho}, \mathbf{z}_y)\mathbf{p}_M + \mathbf{C}_{y,0}(\mathbf{q}, \dot{\mathbf{q}}, \boldsymbol{\rho})\mathbf{z}_y \quad (4.13b)$$

$$\mathbf{g}_y(t, \mathbf{q}, \dot{\mathbf{q}}, \boldsymbol{\rho}, \mathbf{p}) = \mathbf{J}_{g,y}^T(t, \mathbf{q}, \dot{\mathbf{q}}, \boldsymbol{\rho})\mathbf{p} + \mathbf{g}_{y,0}(t, \mathbf{q}, \dot{\mathbf{q}}, \boldsymbol{\rho}) \quad (4.13c)$$

where  $\mathbf{z}_y \in \mathbb{R}^{n_q}$  is an arbitrary vector;  $\mathbf{J}_M, \mathbf{J}_C \in \mathbb{R}^{n_p, M \times n_q}$ , and  $\mathbf{J}_g \in \mathbb{R}^{n_p \times n_q}$  are Jacobian matrices;  $\mathbf{M}_0, \mathbf{C}_0 \in \mathbb{R}^{n_q \times n_q}$  and  $\mathbf{g}_0 \in \mathbb{R}^{n_q}$  are the known parts of  $\mathbf{M}, \mathbf{C}$ , and  $\mathbf{g}$ , respectively. Specifically, Eq.(4.13) requires  $\mathbf{p}_M$  to be selected as masses and moments of inertia only. These specifications also lead to two more model assumptions:

(MA. 4) The uncertain parameters are constant or slowly time-varying, i.e.,  $\dot{\mathbf{p}} \approx \mathbf{0}$ .

(MA. 5) The unknown kinematic parameters of the system can be estimated in real-time [176], which are directly implemented in the controller design.

Note that for the particular case of TAWÉ, (MA. 5) requires all unknown kinematic properties in the human-exoskeleton system to be identified by the WKI algorithm introduced in Chapter 3. The exclusion of kinematic uncertain parameter from  $\mathbf{p}$  makes it easier to realize the formulation in 4.13.

As previously discussed, the perturbation/disturbance  $\mathbf{w}$  may come from multiple sources and cannot be easily modeled. The control system is susceptible to instability when  $\mathbf{w}$  reaches large amplitude. Here we propose two more assumptions to limit the scope of the controller design

(MA. 6) The disturbance  $\mathbf{w}$  is locally bounded in the domain of  $\mathbf{x}$ .

(MA. 7) The discrepancy between exoskeleton tracking reference and user volition, and error in kinematics identification are bounded and contribute to  $\mathbf{w}$ .

For (MA. 7), it is an understatement that the kinematic identification needs be reliable, and the motion planning of  $\mathbf{r}$  cannot deviate far away from the voluntary intention of user motion (or vice versa), so that  $\mathbf{w}$  is bounded.

To incorporate tremor dynamics into the control system setup, one way is to assume tremor actuation as a part of disturbance  $\mathbf{w}$ . In this case, tremors will not be modeled and actively mitigated, which is suitable for the controller design for passive tremor suppression. However, if we employ BMFLC for the approximation of tremor dynamics, the Jacobian matrix in Eq. (4.2) fits the model condition in Eq. (4.13). Hence, the control system setup in this section lays the foundation for various exoskeleton controller designs, which are explained in detail in the next section.

### 4.3 Model-Based Controller for Tremor Suppression

This section discusses the exoskeleton controller design for passive and active tremor suppression. A controller with an analytical design (i.e., not based on optimization [4, 48, 130]) can be written in the general form of

$$\mathbf{u} = \mathbf{u}_{\text{ff}} + \mathbf{u}_{\text{fb}} \quad (4.14)$$

where  $\mathbf{u}_{\text{ff}}$  is the feedforward component that compensates inertia and loads from model dynamics, and  $\mathbf{u}_{\text{fb}}$  is the feedback component that aims to converge the tracking error between system states and reference trajectories. Passive tremor suppression is commonly handled by  $\mathbf{u}_{\text{fb}}$ , and active tremor suppression is handled by  $\mathbf{u}_{\text{ff}}$ .

#### 4.3.1 Assumptions on User Control Input

Before the design of the exoskeleton controller, the role of the user control input  $\mathbf{u}_{\text{user},y}$  needs to be resolved. Recall that  $\mathbf{u}_{\text{user},y}$  is defined to represent the ideal voluntary control input from the user. Similar to pathological tremors, it is difficult to describe the neuromuscular

dynamics of the user controller analytically. On the other hand, the volitional movement intention is also embedded in the user control input, making it an important part of the human-exoskeleton control system.

In the following part of this work, we propose two final model assumptions on the user controller and voluntary movement

(MA. 8) The tracking reference  $\mathbf{r}_{y,\text{user}}$  that represents the voluntary movement intention of the user is slow in velocity and resides in the low-frequency domain, which leads to  $\dot{\mathbf{r}}_{\text{user}} \approx 0$  and  $\ddot{\mathbf{r}}_{\text{user}} \approx 0$ .

(MA. 9) The user control input, without significant change of the model dynamics, can converge the system trajectory to  $\mathbf{r}_{y,\text{user}}$  without steady state error.

Here, (MA. 8) specifically limits the scope to low-activity user-guided operations, i.e., the voluntary user movement is slow without abrupt changes; (MA. 9) ensures that the user controller can stably converge the system trajectory to a fixed point. In this study, we use PID controller as the hypothetical user controller, which takes the form of

$$\begin{aligned} \mathbf{u}_{\text{user}} &= -K_P(\mathbf{r}_{y,\text{user}} - \mathbf{y}) - K_I \int_0^t (\mathbf{r}_{y,\text{user}} - \mathbf{y}) dt - K_D(\dot{\mathbf{r}}_{\text{user}} - \dot{\mathbf{y}}) \\ &= -K_P \boldsymbol{\epsilon}_{\text{user},P} - K_I \boldsymbol{\epsilon}_{\text{user},I} - K_D \boldsymbol{\epsilon}_{\text{user},D} \end{aligned} \quad (4.15)$$

where  $K_P > 0$ ,  $K_I > 0$ , and  $K_D > 0$  are respectively the proportional, integral, and derivative scalar control gains. The design of this user controller does not take into consideration the exoskeleton inputs, disturbances, or any time-varying generalized forces (i.e., here  $\mathbf{g}_y$  is

state-dependent only). In this case, the control system for the user input can be written as

$$\mathbf{x}_{\text{user},0} = \begin{bmatrix} \boldsymbol{\epsilon}_{\text{user},I} \\ \boldsymbol{\epsilon}_{\text{user},P} \\ \boldsymbol{\epsilon}_{\text{user},D} \end{bmatrix}; \quad \dot{\mathbf{x}}_{\text{user},0} = \begin{bmatrix} \boldsymbol{\epsilon}_{\text{user},P} \\ \boldsymbol{\epsilon}_{\text{user},D} \\ -\ddot{\mathbf{r}}_{\text{user}} - \mathbf{M}_y^{-1}(\mathbf{C}_y \dot{\mathbf{y}} + \mathbf{g}_y) + \mathbf{M}_y^{-1} \mathbf{u}_{\text{user},y} \end{bmatrix} \quad (4.16)$$

whose equilibrium is

$$\mathbf{x}_{\text{user},0} = \begin{bmatrix} -K_I^{-1} \mathbf{g}_y^T & 0 & 0 \end{bmatrix}^T \quad (4.17)$$

The above system stability holds only when the user movement is slow, and the system state is within the vicinity of the tracking reference. The stability proof is provided in Appendix A.2. The convergence of tracking errors  $\boldsymbol{\epsilon}_{\text{user},P}$  and  $\boldsymbol{\epsilon}_{\text{user},D}$  is not guaranteed globally. In the following content, the PID controller  $\mathbf{u}_{\text{user}}$  is used to simulate voluntary actuation, particularly for the full system real-time simulation in Chapter 6.

### 4.3.2 Model Reference Adaptive Controllers for Exoskeletons

For the exoskeleton controller design, we focus on the control model

$$\dot{\mathbf{x}} = \mathcal{F}(\mathbf{x}) + \mathcal{G}(t, \mathbf{q}, \dot{\mathbf{q}}, \boldsymbol{\rho}, \mathbf{p}) + \mathcal{U}(\mathbf{q}, \boldsymbol{\rho}) \mathbf{u}_{\text{exo},y} + \mathcal{W}(\mathbf{q}, \boldsymbol{\rho}) \mathbf{w} \quad (4.18)$$

which is very similar to Eq. (4.10) except that it does not contain the user input  $\mathbf{u}_{\text{user},y}$ . This is because for the various controller design, it would be challenging to guarantee the combined stability of  $\mathbf{u}_{\text{user},y} + \mathbf{u}_{\text{exo},y}$ . Furthermore,  $\mathbf{u}_{\text{user},y}$  can be absent in certain applications, and the proposed PID controller for  $\mathbf{u}_{\text{user},y}$  does not necessarily present dynamics of actual voluntary user control input. Therefore, Eq. (4.18) will be the control system for the exoskeleton controller design hereinafter.

As previously mentioned, two common types of feedback controllers used in the previous study are the PD controller and Sliding Mode Controller (SMC) [17, 22]. By defining two combinations of proportional and derivative errors as

$$\boldsymbol{\chi} = \dot{\boldsymbol{\epsilon}} + \mathbf{K}_\epsilon \boldsymbol{\epsilon}; \quad \boldsymbol{\zeta} = \dot{\mathbf{r}}_y - \mathbf{K}_\epsilon \boldsymbol{\epsilon} \quad (4.19)$$

where  $\mathbf{K}_\epsilon \in \mathbb{R}^{n_q \times n_q}$  is a symmetric positive definite gain matrix, the PD and SMC feedback controllers can be written as

$$\mathbf{u}_{\text{fb,PD}} = -\mathbf{K}_\chi \boldsymbol{\chi}; \quad \mathbf{u}_{\text{fb,SMC}} = -\mathbf{K}_{\text{SMC}} \mathbf{f}_{\text{SMC}}(\boldsymbol{\chi}) - \mathbf{K}_\chi \boldsymbol{\chi}; \quad (4.20)$$

where  $\mathbf{K}_\chi = \mathbf{K}_\chi^T > 0$ , and  $\mathbf{K}_{\text{SMC}}$  is diagonal and positive definite. In  $\mathbf{u}_{\text{fb,SMC}}$ ,  $-\mathbf{K}_{\text{SMC}} \mathbf{f}_{\text{SMC}}(\boldsymbol{\chi})$  is the gain switching controller component, where  $\boldsymbol{\chi}$  is selected so that the sliding surface can be written as

$$\boldsymbol{\chi} = \dot{\boldsymbol{\epsilon}} + \mathbf{K}_\epsilon \boldsymbol{\epsilon} = 0 \quad (4.21)$$

The real-domain function  $\mathbf{f}_{\text{SMC}}$  is designed to approximate the sign function, which satisfies the following conditions:

$$(1): \mathbf{f}_{\text{SMC}}(z) > 0 \text{ for } z > 0; \quad (4.22a)$$

$$(2): \mathbf{f}_{\text{SMC}}(z) = \text{diag}(\text{sign}(z)) \mathbf{f}_{\text{SMC}}(|z|); \quad (4.22b)$$

$$(3): \lim_{|z| \rightarrow \infty} \mathbf{f}_{\text{SMC}}(z) = \text{sign}(z) \quad (4.22c)$$

Hence, in this study, we have selected  $\mathbf{f}_{\text{SMC}}$  as

$$\mathbf{f}_{\text{SMC}}(z) = 2(\text{sigmoid}(c_{\text{SMC}}z) - 0.5) = \frac{1 - e^{-c_{\text{SMC}}z}}{1 + e^{-c_{\text{SMC}}z}} \quad (4.23)$$

where the parameter satisfies  $c_{\text{SMC}} > 0$ . This continuous function approximate the sign function to slightly reduce the common chattering problem caused by the gain switching controller in SMC [168].

The feedforward controller is required to compensate the model properties in  $\mathcal{G}$ , which includes the model uncertainties. Based on Eq. (4.13), we design the feedforward adaptive controller as

$$\mathbf{u}_{\text{ff}} = \mathbf{M}_{y,0}\dot{\boldsymbol{\zeta}} + \mathbf{C}_{y,0}\boldsymbol{\zeta} + \mathbf{g}_{y,0} + \mathbf{J}_p^T \hat{\mathbf{p}}; \quad \mathbf{J}_p = \begin{bmatrix} \mathbf{J}_{M,y}(\mathbf{q}, \dot{\boldsymbol{\zeta}}) + \mathbf{J}_{C,y}(\mathbf{q}, \dot{\mathbf{q}}, \boldsymbol{\zeta}) \\ \mathbf{0} \end{bmatrix} + \mathbf{J}_{g,y}(t, \mathbf{q}, \dot{\mathbf{q}}) \quad (4.24)$$

where  $\mathbf{J}_p^T \hat{\mathbf{p}}$  is the model reference adaptive controller (MRAC) component with  $\hat{\mathbf{p}}$  as the estimation of the uncertain parameters [16, 63, 183]. The update of the uncertain parameters is driven by

$$\dot{\hat{\mathbf{p}}} = -\boldsymbol{\Gamma}^{-1} \mathbf{J}_p \boldsymbol{\chi} \quad (4.25)$$

where  $\boldsymbol{\Gamma} = \boldsymbol{\Gamma}^T > 0$  is the update gain. It should be noted that when  $\hat{\mathbf{p}} = \mathbf{p}$ , the feedforward controller satisfies

$$\mathbf{u}_{\text{ff}} = \mathbf{M}_{y,0}\dot{\boldsymbol{\zeta}} + \mathbf{C}_{y,0}\boldsymbol{\zeta} + \mathbf{g}_{y,0} + \mathbf{J}_p^T \mathbf{p} = \mathbf{M}_y \dot{\boldsymbol{\zeta}} + \mathbf{C}_y \boldsymbol{\zeta} + \mathbf{g}_y \quad (4.26)$$

which indicates the compensation of all model properties after the convergence of  $\hat{\mathbf{p}}$  to  $\mathbf{p}$ .

The feedforward controller with MRAC component Eq. (4.24) can be paired with both PD and SMC controllers in Eq. (4.20). The stability proofs are provided in Appendix A.3. The controllers can stabilize the control system, and compensate the inertia and load in the system. However, while all feedback controllers has a certain level of robustness towards the disturbance, the stability proof of the controllers above did not incorporate the disturbance component  $\mathbf{w}$ . Therefore, in the following subsections, we explain the main focus of controller

development - the robust adaptive controller based on inverse optimality control theory.

### 4.3.3 Inverse Optimal Robust Control Theory

$H_\infty$  controllers are popular optimal controllers with guaranteed robustness towards perturbations and disturbances [50, 96]. For nonlinear systems like exoskeletons, the design of an optimal controller can be challenging as it requires solving a Hamilton-Jacobi-Isaacs equation [3]. The existing algorithms such as the state-dependent Riccati equation cannot guarantee a globally optimal solution [32, 184]. For some problems, this challenge can be resolved by the inverse optimality technique, which produces a stabilizing controller later proven to be the global optimal solution of a meaningful cost function [96, 97]. Previous studies applied the inverse optimality technique to design robust adaptive controllers for spacecraft and robot manipulators [61, 109, 143].

Here we introduce the theory of inverse optimal robust controller (IORC) [96, 97, 109]: For the control system in Eq. (4.18), with the uncertain parameters assumed as known constants  $\mathbf{p} = \mathbf{p}_0 \in \mathbb{R}^{n_p}$ , a smooth function  $\mathcal{V}_0(\mathbf{x}, \mathbf{p}_0)$  is a robust control Lyapunov function, if there exists a controller  $\mathbf{u}_0(t, \mathbf{x}, \mathbf{p}_0) \in \mathbb{R}^{n_u}$  smooth on  $\mathbb{R}^{n_x} \times \mathbb{R}^{n_p}$  that satisfies  $\mathbf{u}_0(\mathbf{0}, \mathbf{p}_0) = \mathbf{0}$ , and a continuous function  $Q_0(\mathbf{x}, \mathbf{p}_0) \geq 0$  ( $Q_0 = 0$  iff.  $\mathbf{x} = \mathbf{0}$ ) so that

$$(\partial\mathcal{V}_0/\partial\mathbf{x})(\mathcal{F} + \mathcal{G} + \mathcal{U}\mathbf{u}_0 + \mathcal{W}\mathbf{w}_0) \leq -Q_0 \quad (4.27)$$

for the auxiliary control system of

$$\dot{\mathbf{x}} = \mathcal{F} + \mathcal{G} + \mathcal{U}\mathbf{u}_0 + \mathcal{W}\mathbf{w}_0 \quad (4.28)$$

where

$$\mathbf{w}_0 = f_\gamma(2\|\mathbf{L}_{\mathcal{W}}\mathcal{V}_0\|)((\mathbf{L}_{\mathcal{W}}\mathcal{V}_0)^T/\|\mathbf{L}_{\mathcal{W}}\mathcal{V}_0\|^2) \quad (4.29)$$

and  $\gamma(\sigma) \in \mathbb{R}_+$  is a class  $\mathcal{K}_\infty$  function, whose derivative  $\gamma'(\sigma) = \partial\gamma/\partial\sigma$  is also a class  $\mathcal{K}_\infty$  function. The function  $f_\gamma(\sigma)$  denotes the Legendre-Fenchel transformation [97, 109]

$$f_\gamma(\sigma) = \sigma(\gamma')^{-1}(\sigma) - \gamma((\gamma')^{-1}(\sigma)) = \int_0^\sigma ((\gamma')^{-1}(z))dz \quad (4.30)$$

and  $\mathbf{L}_{\mathcal{W}}\mathcal{V}_0$  is the Lie derivative of  $\mathcal{V}_0$  in terms of  $\mathcal{W}$  (which is  $\mathbf{L}_{\mathcal{W}}\mathcal{V}_0 = (\partial\mathcal{V}_0/\partial\mathbf{x})\mathcal{W}$ ).

Provided that there exists a matrix  $\mathbf{K}_{R,0}(\mathbf{x}, \mathbf{p}) = \mathbf{K}_{R,0}^T > 0$  so that  $\mathbf{u}_0$  designed as

$$\mathbf{u}_0 = -\mathbf{U}^{-1}\mathbf{g} + \mathbf{u}_{\text{fb},0}; \quad \mathbf{u}_{\text{fb},0} = -c_{R,1}\mathbf{K}_{R,0}^{-1}(\mathbf{L}_{\mathbf{u}}\mathcal{V}_0)^T \quad (4.31)$$

with  $c_{R,1} = 1$  globally asymptotically stabilizes Eq. (4.28) with respect to  $\mathcal{V}_0$ . Then  $\mathbf{u}_0$  solves the inverse optimal  $H_\infty$  control problem of Eq. (4.18) by minimizing the cost function

$$\begin{aligned} \mathcal{J}_0(\mathbf{u}_{\text{exo},y}) = \sup_{\mathbf{w} \in \mathbb{W}} \left\{ \lim_{t \rightarrow \infty} \left[ 2c_{R,1}\mathcal{V}_0 + \int_0^t \left( -2c_{R,1}\mathbf{L}_{\mathcal{F}}\mathcal{V}_0 - c_{R,1}c_{R,2}f_\gamma(2\|\mathbf{L}_{\mathcal{W}}\mathcal{V}_0\|) \right. \right. \right. \\ \left. \left. \left. + c_{R,1}^2\mathbf{L}_{\mathbf{u}}\mathcal{V}_0\mathbf{K}_{R,0}^{-1}(\mathbf{L}_{\mathbf{u}}\mathcal{V}_0)^T + \mathbf{u}_{\text{fb},0}^T\mathbf{K}_{R,0}\mathbf{u}_{\text{fb},0} - c_{R,1}c_{R,2}\gamma\left(\frac{\|\mathbf{w}\|}{c_{R,2}}\right) \right) dt \right] \right\} \quad (4.32) \end{aligned}$$

where  $c_{R,1} \geq 2$  and  $c_{R,2} \in (0, 2]$ , and  $\mathbb{W}$  is the set of locally bounded functions of  $\mathbf{x}$ ; and  $\mathbf{L}_{\mathcal{F}}\mathcal{V}_0$  and  $\mathbf{L}_{\mathbf{u}}\mathcal{V}_0$  are the Lie derivatives:  $\mathbf{L}_{\mathcal{F}}\mathcal{V}_0 = (\partial\mathcal{V}_0/\partial\mathbf{x})\mathcal{F}$  and  $\mathbf{L}_{\mathbf{u}}\mathcal{V}_0 = (\partial\mathcal{V}_0/\partial\mathbf{x})\mathbf{u}$ . For  $l^2$  disturbance attenuation [97, 109], the  $\gamma$  function and its Legendre-Fenchel transformation can be selected as

$$\gamma(\sigma) = f_\gamma(2\sigma) = \sigma^2 \quad (4.33)$$

In summary, the inverse optimal robust control is realized by proving that a stabilizing controller in Eq. (4.31) optimizes a cost function in Eq. (4.32). It is important to show

that the cost function is meaningful for the validity of controller optimality. Also, note that Eq. (4.32) is designed only for IORC, which does not optimize the adaptive control process. During the controller development process in the later subsections, while the above process is referenced, a set of Lyapunov function and cost function is specifically designed for the robust adaptive control problem in Eq. (4.18).

#### 4.3.4 Inverse Optimal Robust Adaptive Controller

A challenge in the synergy of model reference adaptive control and inverse optimal robust control arises from the model limitation. Robust adaptive controllers designed in previous studies [61, 109, 143] via inverse optimality only apply to specific models. Here we present the inverse optimal robust adaptive controller (IO-RAC) for the system in Eq. (4.18), which is realized by designing the robust feedback controller as

$$\mathbf{u}_{\text{fb,IORC}} = -c_{R,1} \mathbf{K}_R^{-1}(\mathbf{q}, \boldsymbol{\rho}) \boldsymbol{\chi} \quad (4.34)$$

where  $\mathbf{K}_R(\mathbf{q}, \boldsymbol{\rho}) \in \mathbb{R}^{n_q \times n_q}$  is defined as

$$\mathbf{K}_R = (\mathbf{J}_{w,y}^T \mathbf{J}_{w,y} + \mathbf{K}_\chi)^{-1} \quad (4.35)$$

with  $\mathbf{K}_\chi = \mathbf{K}_\chi^T > 0$ . By pairing the MRAC feedforward controller from Eq. (4.24) with Eq. (4.34), the full state controller along with parameter update law are explicitly expressed as

$$\mathbf{u}_{\text{exo},y} = \mathbf{u}_{\text{ff}} + \mathbf{u}_{\text{fb,IORC}} = \mathbf{M}_{y,0} \dot{\boldsymbol{\zeta}} + \mathbf{C}_{y,0} \boldsymbol{\zeta} + \mathbf{g}_{y,0} + \mathbf{J}_p^T \hat{\mathbf{p}} - c_{R,1} \mathbf{K}_R^{-1} \boldsymbol{\chi} \quad (4.36a)$$

$$\dot{\hat{\mathbf{p}}} = -\Gamma^{-1} \mathbf{J}_p(t, \mathbf{q}, \dot{\mathbf{q}}) \boldsymbol{\chi} \quad (4.36b)$$

Apart from  $\mathbf{J}_p$  determined by the model uncertainty structure, the performance of IO-RAC is determined by  $c_{R,1}$ ,  $\mathbf{K}_\epsilon$ ,  $\mathbf{K}_\chi$ , and  $\mathbf{J}_{w,y}$ . Specifically,  $c_{R,1}$  scales the whole feedback controller  $\mathbf{u}_{\text{fb,IOIRC}}$ ;  $\mathbf{K}_\epsilon$  determines the ratio between the gains of  $\epsilon$  and  $\dot{\epsilon}$ ;  $\mathbf{K}_\chi$  sets the magnitudes of the fixed gain components; and  $\mathbf{J}_{w,y}$ , which is designed manually or based on system properties, decides the variable gain components for disturbance attenuation. The parameter estimate update rate is determined by  $\mathbf{\Gamma}$ . The proposed controller also does not require acceleration measurement or matrix inversion.

For any control parameters selected that follow their definitions, the proposed controller in Eq. (4.36) is asymptotically stable with respect to the Lyapunov function

$$\mathcal{V}_{\text{IOIRC}}(\mathbf{x}, \hat{\mathbf{p}}) = \frac{1}{2} \mathbf{x}^T \begin{bmatrix} \mathbf{K}_1 + \mathbf{K}_\epsilon \mathbf{M}_y \mathbf{K}_\epsilon & \mathbf{K}_\epsilon \mathbf{M} \\ \mathbf{M}_y \mathbf{K}_\epsilon & \mathbf{M}_y \end{bmatrix} \mathbf{x} + \frac{1}{2} \tilde{\mathbf{p}}^T \mathbf{\Gamma} \tilde{\mathbf{p}} \quad (4.37)$$

where  $\mathbf{K}_1 \in \mathbb{R}^{n_q \times n_q}$  is a positive definite matrix; and  $\tilde{\mathbf{p}} = \hat{\mathbf{p}} - \mathbf{p} \in \mathbb{R}^{n_p}$  is the estimation error. The controller also provides  $l^2$  disturbance attenuation by solving  $H_\infty$  control problem through minimizing a meaningful cost function:

$$\mathcal{J}_{\text{IOIRC}}(\mathbf{u}_{\text{exo},y}) = \sup_{\mathbf{w} \in \mathbb{W}} \left\{ \lim_{t \rightarrow \infty} \left[ 2c_{R,1} \mathcal{V}_{\text{IOIRC}} + \int_0^t \left( z_{J,1} - c_{R,1} c_{R,2} \gamma \left( \frac{\|\mathbf{w}\|}{c_{R,2}} \right) + \mathbf{u}_{\text{fb,IOIRC}}^T \mathbf{K}_R \mathbf{u}_{\text{fb,IOIRC}} \right) dt \right] \right\} \quad (4.38)$$

where

$$z_{J,1}(\mathbf{x}) = -2c_{R,1} z_{J,2}(\mathbf{x}) - c_{R,1} c_{R,2} f_\gamma(2\|\mathbf{L}\mathbf{w}\mathcal{V}_{\text{IOIRC}}\|) + c_{R,1}^2 \mathbf{L}_U \mathcal{V}_{\text{IOIRC}} \mathbf{K}_R^{-1} (\mathbf{L}_U \mathcal{V}_{\text{IOIRC}})^T \quad (4.39a)$$

$$z_{J,2}(\mathbf{x}) = \epsilon \mathbf{K}_1 \dot{\epsilon} = \mathbf{L}_{\mathcal{F}} \mathcal{V}_{\text{IOIRC}} - \chi^T \mathbf{M}_y \mathbf{K}_\epsilon \dot{\epsilon} \quad (4.39b)$$

The cost function penalizes both tracking error  $\mathbf{x}$  and feedback control effort  $\mathbf{u}_{\text{fb,IORC}}$ . Detailed proofs of the stability and optimality of IO-RAC are included in Appendices A.4 and A.5, respectively.

Finally, while IO-RAC is designed to provide stable trajectory tracking for safe exoskeleton operations, the scope of the controller only lies in the dynamics of the human-exoskeleton system. For practical implementation, other safety concerns (e.g., range of motion, maximum velocity/acceleration, and input capacity) should also be taken into consideration during, for example, the motion planning of  $\mathbf{r}_y$ .

### 4.3.5 Passive and Active Tremor Suppression

The PD, SMC, and IO-RAC feedback controllers all can provide passive tremor suppression by emulating the behavior of mechanical impedance as used in the passive and semi-active tremor rehabilitation devices [94, 108, 187]. These controllers all possess control terms involving proportional and derivative errors, which resemble the effect of spring and damper, respectively. If the exoskeleton tracking reference  $\mathbf{r}_y$  aligns with the user voluntary intention  $\mathbf{r}_{y,\text{user}}$ , the feedback controllers can potentially dampen tremor oscillation, particularly when its frequency matches with proper stiffness and damping values.

For active tremor control, the feedforward controller with MRAC will be implemented. As discussed in Section 4.1, by assuming that the tremor excitations follow the structure of a BMFLC model, Eq. (4.2) can be used to construct the uncertain parameter  $\mathbf{p}_g \in \mathbb{R}^{2n_q n_{\text{BMFLC}}}$  as

$$\mathbf{p}_g = \left[ \mathbf{p}_{\mu,\text{BMFLC},1}^T \quad \cdots \quad \mathbf{p}_{\mu,\text{BMFLC},n_q}^T \right]^T \quad (4.40)$$

and the corresponding uncertain parameter Jacobian  $\mathbf{J}_{g,y} \in \mathbb{R}^{n_q \times (2n_q n_{\text{BMFLC}})}$  for generalized

force as

$$\mathbf{J}_{g,y} = \begin{bmatrix} \mathbf{J}_{p,\text{BMFLC}} & \cdots & \mathbf{0} & \cdots & \mathbf{0} \\ \vdots & \ddots & & & \vdots \\ \mathbf{0} & & \mathbf{J}_{p,\text{BMFLC}} & & \mathbf{0} \\ \vdots & & & \ddots & \vdots \\ \mathbf{0} & \cdots & \mathbf{0} & \cdots & \mathbf{J}_{p,\text{BMFLC}} \end{bmatrix} \quad (4.41)$$

This provides active compensation for tremor excitation for all DOFs of the exoskeleton. It should be noted that due to the model assumption (MA. 4), the limitation of BMFLC-based MRAC tremor control is that it cannot adapt to tremor excitations with rapid amplitude and frequency shifts. Finally, since feedback control is indispensable in all exoskeleton controller designs, active and passive tremor suppression will operate simultaneously.

In this section, based on the control model in Eq. (4.10), we have proposed a few model assumptions, which lead to the development of the hypothetical user PID controller, and a few exoskeletons controllers. In particular, we combined the model reference adaptive control and inverse optimal robust control theories, and proposed the inverse optimal robust adaptive controller in Eq. (4.36) that can compensate for the effects of inertia and load uncertainties, as well as providing  $H_\infty$  robustness in  $l^2$  disturbance attenuation by optimizing a meaningful cost function. The proposed controllers apply to not only TAWÉ in tremor suppression, but also other exoskeletons and robotic systems.

## 4.4 Numerical Simulation

This section demonstrates the performance of the robust adaptive controller from Eq. (4.36) through simulations of a stationary upper limb exoskeleton and TAWÉ carried out in MATLAB, whose codes are available [online](#) [175]. For all simulations, the reference  $\mathbf{r}_y$  and dis-

turbance  $\mathbf{w}$  are selected as bounded periodic and quasiperiodic trajectories with multiple harmonic components. The simulation sampling rate is 500 Hz, and the control input update rate is 250 Hz. The gravitational acceleration is along the  $-\bar{z}$  axis of the global frame.

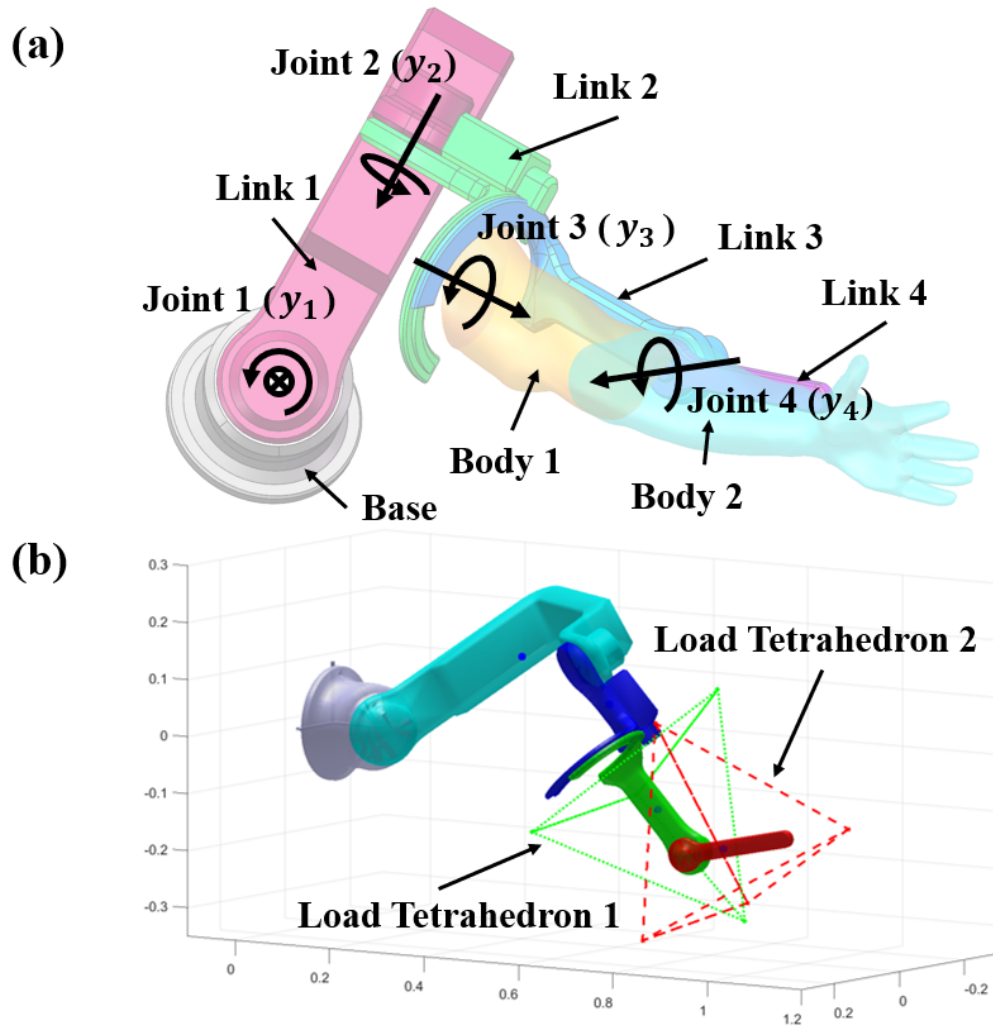


Figure 4.6: The 3D model of the 4-DOF stationary exoskeleton [175] with uncertain inertia and loads from the user is shown in (a). Body 1 and Body 2 are attached to link 3 and link 4, respectively; (b) shows the 3D model in the MATLAB environment, where the load tetrahedrons are used to identify the COM of the unknown bodies.

### 4.4.1 Stationary Exoskeleton

The 4-DOF stationary upper limb exoskeleton dynamical system is presented in Fig. 4.6. The conceptual design adopts a structure similar to the EXO-UL8 exoskeleton [152] without the forearm and wrist actuations. The joint of the  $i$ th link is labeled as  $y_i$ , which is directly actuated by a motor torque input. When the user equips the exoskeleton, inertia and load uncertainties are introduced from the upper arm (Body 1) and forearm (Body 2) to Link 3 and Link 4, respectively. For the  $i$ th load, the unknown parameter  $\mathbf{p}_{\text{body},i} \in \mathbb{R}^7$  can be written as

$$\mathbf{p}_{\text{body},i} = \begin{bmatrix} p_{\text{ma},i} & \mathbf{p}_{\text{mo},i} & \mathbf{p}_{g,i} \end{bmatrix}^T \quad (4.42)$$

where  $p_{\text{ma}}$  is the mass,  $\mathbf{p}_{\text{mo}} = [p_{\text{mo},\bar{x}}, p_{\text{mo},\bar{y}}, p_{\text{mo},\bar{z}}]^T$  includes the moment of inertia elements in the local frame, and  $\mathbf{p}_{g,i} = [p_{g,i,1}, p_{g,i,2}, p_{g,i,3}]^T$  contains gravitational force parameters. To conveniently observe the convergence of parameter estimations, we simplify the inertia tensor to a diagonal matrix. With the center of mass (COM) position of the uncertain body defined as  $\mathbf{d}_{\text{COM},i} = [d_{\text{COM},i,\bar{x}}, d_{\text{COM},i,\bar{y}}, d_{\text{COM},i,\bar{z}}]^T$ ,  $\mathbf{p}_{g,i}$  is introduced so that along with

$$\mathbf{p}_{g,i,4} = p_{\text{ma},i} - (p_{g,i,1} + p_{g,i,2} + p_{g,i,3}) \quad (4.43)$$

Table 4.1: True values of uncertain parameters and default controller parameters for stationary robot simulation. ( $\mathbf{f}_w(t)$  denotes the quasiperiodic function for disturbance.)

$p_{\text{ma},1} = 3.80$ (kg)	$\mathbf{p}_{\text{mo},1} = [0.18; 0.024; 0.17]$ ( $\text{kg}\cdot\text{m}^2$ )
$p_{\text{ma},2} = 4.50$ (kg)	$\mathbf{p}_{\text{mo},2} = [0.87; 0.18; 1.03]$ ( $\text{kg}\cdot\text{m}^2$ )
$\mathbf{d}_{\text{COM},1} = [-5.6; 83; -2.7]$ (mm)	$\mathbf{d}_{\text{COM},2} = [93.6; 174.6; -3.1]$ (mm)
$\mathbf{K}_\epsilon = 4 \mathbf{I}_4$ (1/s)	$\mathbf{K}_\chi = 0.25 \mathbf{I}_4$ ( $\text{N}\cdot\text{m}\cdot\text{s}/\text{rad}$ )
$c_{R,1} = 2$	$\mathbf{\Gamma} = \text{diag}([1, \mathbf{1}_{1\times 3}, 1, \mathbf{1}_{1\times 3}, \mathbf{1}_{1\times 6}])/2$
$\mathbf{w} = \text{diag}([3; 1; 3; 1]) \mathbf{f}_w(t)$	$\mathbf{J}_w = 0.4 \mathbf{J}_{u,\text{exo}} \text{diag}([3; 1; 3; 1])$

each  $p_{g,i,j}$  ( $j$  from 1 to 4) is a point mass that introduces a gravitational force component at a vertex of a load tetrahedron shown in Fig. 4.6(b). The load tetrahedron is located in the local frame of an uncertain body. Since gravitational forces are conservative in the global frame, the sum of gravitational forces on vertices is equal to the total gravitational force, and the weighted average of vertex translational positions is the COM of uncertain body.

The true values of uncertain parameters and default controller parameters are listed in Table 4.1. We first test the controller by assuming no disturbance and only Body 2 is unknown. The initial estimation of  $\mathbf{p}_{\text{body},2}$  is set to  $\hat{\mathbf{p}}_{\text{body},2,t=0} = \mathbf{0}$ . For the feedback controller in Eq. (4.34), we also select  $c_{R,1} = 4$  and  $\mathbf{J}_w = \mathbf{J}_{u,\text{exo}}$  for this simulation. The tracking

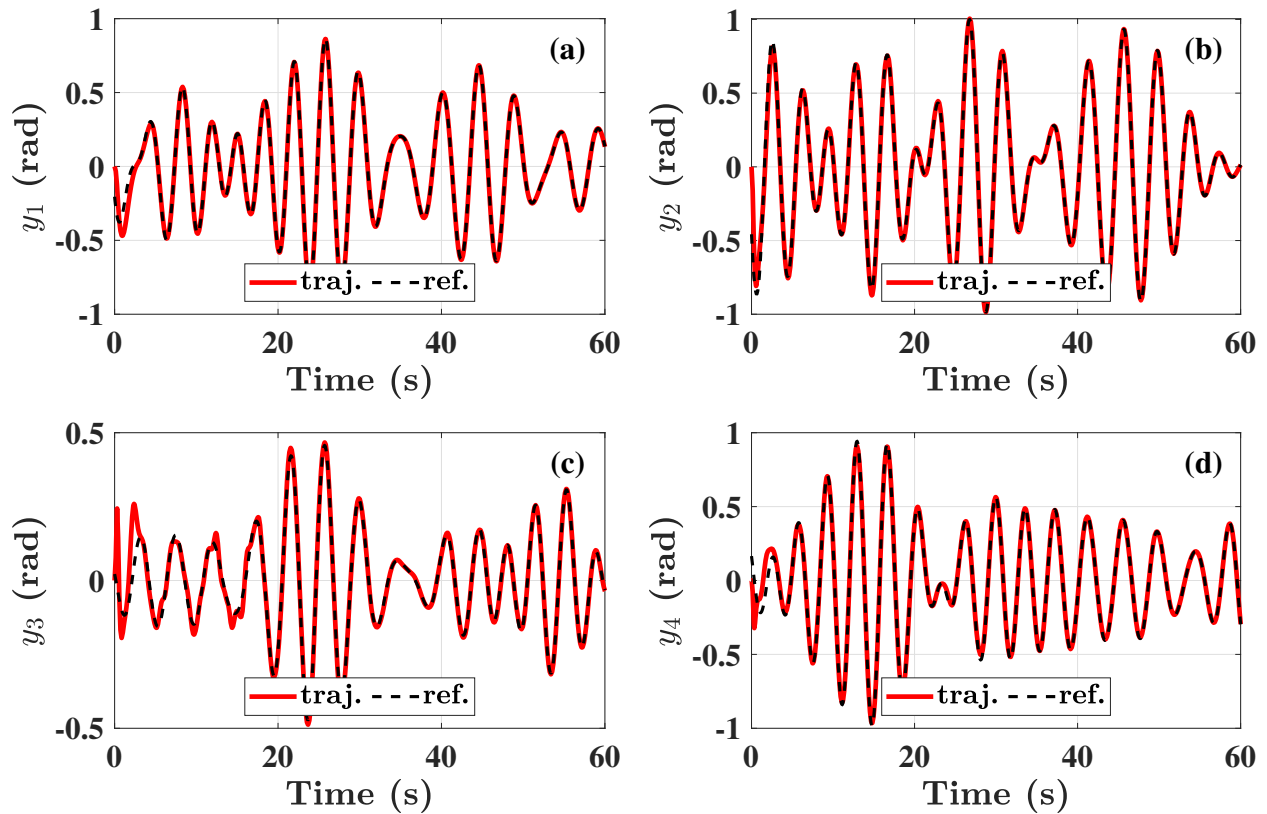


Figure 4.7: Control performance of the stationary exoskeleton with uncertain Body 2 only [175]. The comparisons between tracking trajectories and references of the four joints are shown in (a - d), respectively. respectively.

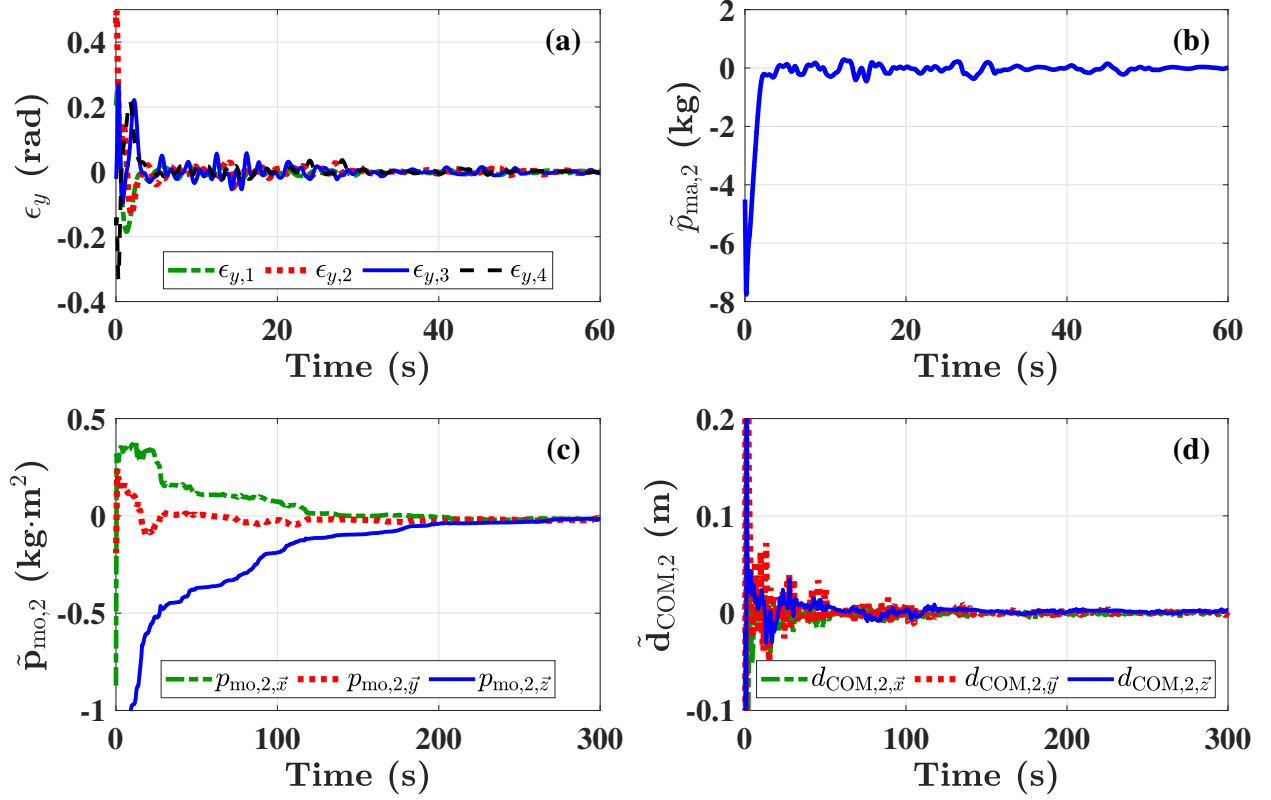


Figure 4.8: Control performance of the stationary exoskeleton with uncertain Body 2 only [175]. The tracking errors  $\epsilon_y$  of the four joints are shown in (a). The estimation errors of uncertain parameters  $p_{ma,2}$ ,  $\mathbf{p}_{mo,2}$ , and  $\mathbf{d}_{COM,2}$  are shown in (b - d), respectively.

and parameter update trajectories are shown in Fig. 4.7. The tracking performances in Fig. 4.7 show that the trajectory can accurately follow the reference. The convergences of tracking errors are presented in Fig. 4.8(a). Note that the startup behaviors of tracking errors can still be affected by model uncertainties since the parameter estimations are yet to converge. In application, this effect can be attenuated through accurate modeling of the known dynamical properties  $\mathbf{M}_{y,0}$ ,  $\mathbf{C}_{y,0}$ , and  $\mathbf{g}_{y,0}$  from Eq. (4.13). Figures 4.8(b - d) show the convergences of all uncertain parameter estimation errors. It should be noted that the parameter update is driven by tracking errors. Since  $p_{ma,2}$  significantly affects the control performance, the quicker convergence of  $\tilde{p}_{ma,2}$  greatly reduces tracking errors, which results in  $\tilde{\mathbf{p}}_{mo,2}$  and  $\tilde{\mathbf{d}}_{COM,2}$  converging at a slower rate.

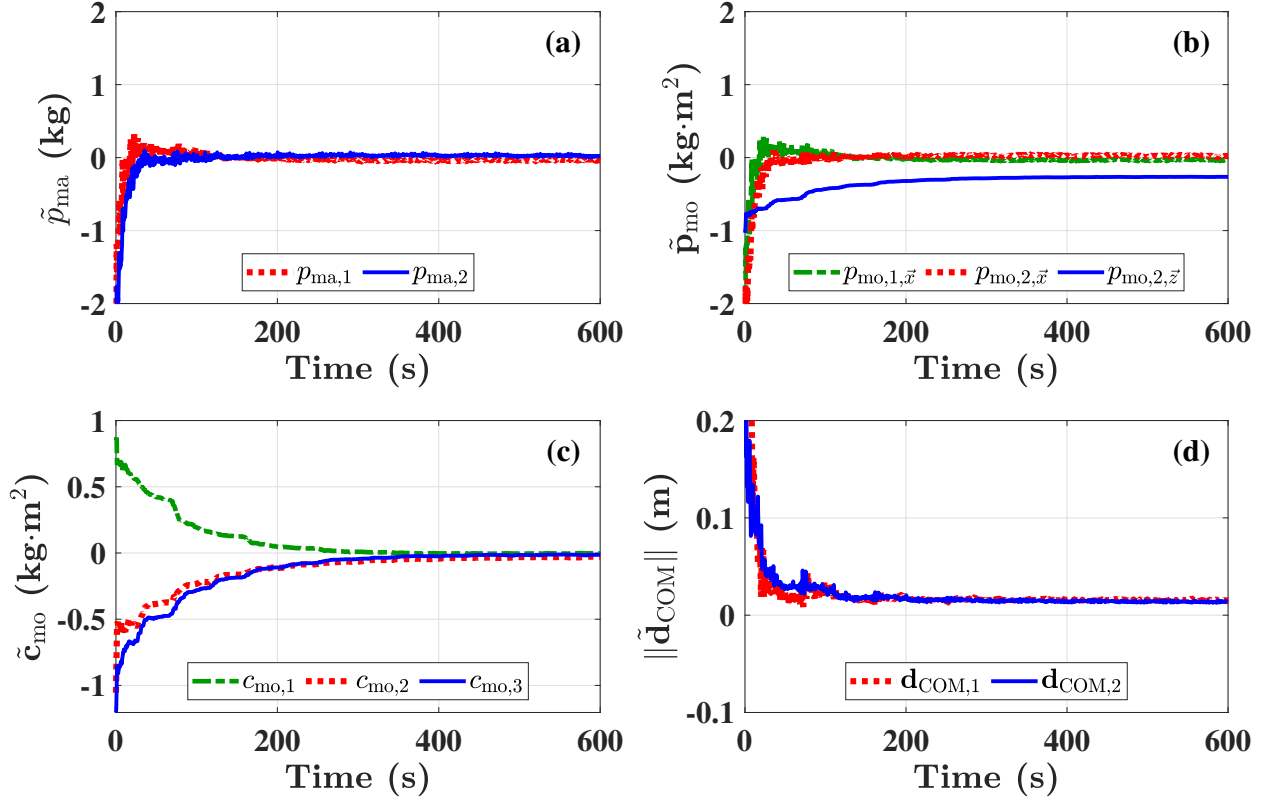


Figure 4.9: Estimation errors of uncertain parameters from Body 1 and Body 2 [175], where (a) presents  $\tilde{p}_{ma,1}$  and  $\tilde{p}_{ma,2}$ , (b) shows  $\tilde{p}_{mo,1,\bar{x}}$ ,  $\tilde{p}_{mo,2,\bar{x}}$ , and  $\tilde{p}_{mo,2,\bar{z}}$ , (c) presents  $\tilde{c}_{mo,1}$ ,  $\tilde{c}_{mo,2}$ ,  $\tilde{c}_{mo,3}$ , and (d) shows the 2-norm of  $\tilde{\mathbf{d}}_{COM,1}$  and  $\tilde{\mathbf{d}}_{COM,2}$ .

When both Body 1 and Body 2 are considered, uncertain parameter estimates do not converge to their true values. Figure 4.9(b) shows that  $\tilde{p}_{mo,2,\bar{z}}$  does not converge to zero. By observing the symbolic structure of the inertia matrix  $\mathbf{M}_y$  for the stationary robot, we notice that  $p_{mo,1,\bar{y}}$ ,  $p_{mo,2,\bar{z}}$ ,  $p_{mo,1,\bar{y}}$ , and  $p_{mo,2,\bar{z}}$  do not distinctly affect  $\mathbf{M}_y$ . Instead,  $\mathbf{M}_y$  is uniquely affected by a linear combination of these terms written as

$$\mathbf{c}_{mo} = \begin{bmatrix} c_{mo,1} \\ c_{mo,2} \\ c_{mo,3} \end{bmatrix} = \begin{bmatrix} p_{mo,2,\bar{y}} - p_{mo,2,\bar{z}} \\ p_{mo,1,\bar{y}} + p_{mo,2,\bar{z}} \\ p_{mo,1,\bar{z}} + p_{mo,2,\bar{z}} \end{bmatrix} \quad (4.44)$$

Therefore, we observe the convergence of  $\tilde{\mathbf{c}}_{mo}$  as shown in Fig. 4.9(c). The error in  $p_{mo,2,\bar{z}}$

also results in other estimates deviating from their truth, as shown in Fig. 4.9(a, d).

The above observations show that uncertain parameter redundancy can result in estimates drifting from their truths. Also, the estimation convergence requires informative tracking references to “trigger” the distinct effects of uncertain parameters. However, the adaptive control term may manage to compensate for manifested model uncertainties without parameter estimation convergence. This can still lead to good tracking performance. In this case, since the estimation is error-driven, the parameter estimation convergence will also be slowed by the reduced tracking errors in return.

In the final test, we introduce the disturbance  $\mathbf{w}$  overlaid on the control input, and adopt the

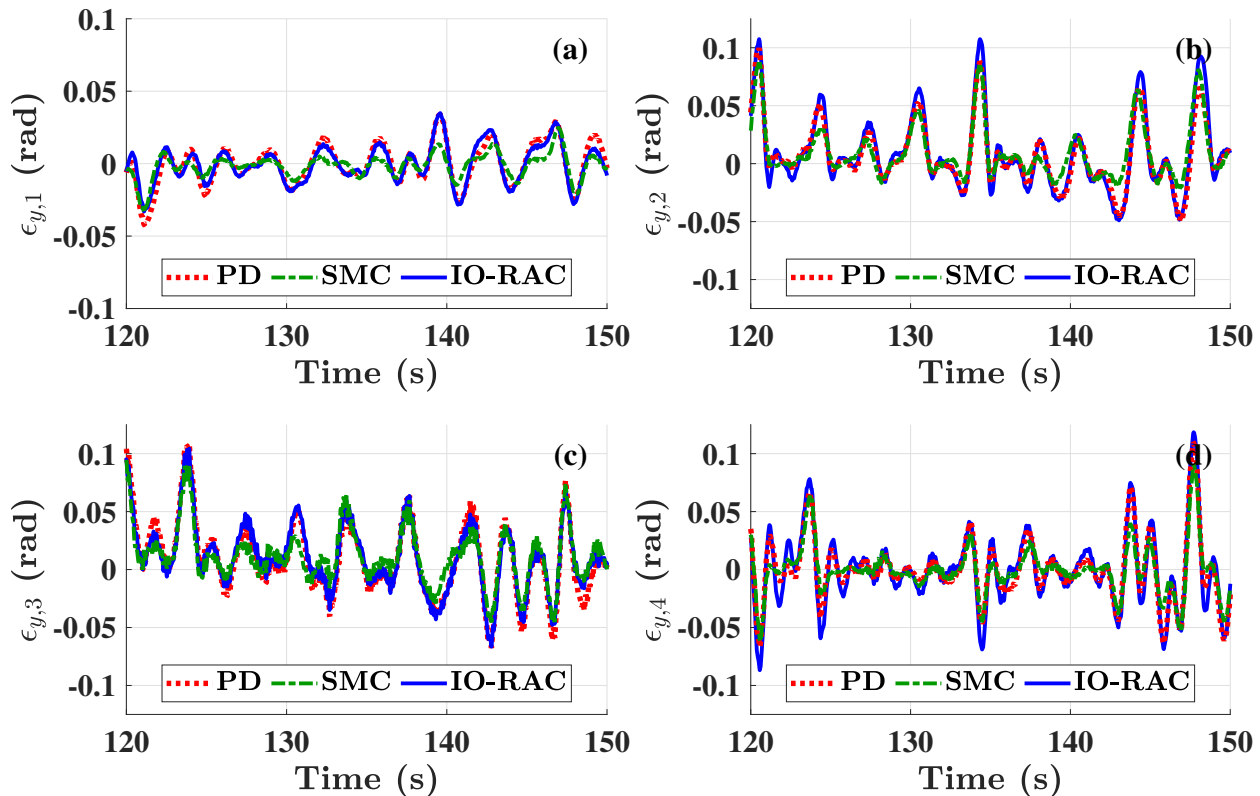


Figure 4.10: Comparison of the stationary exoskeleton tracking controls with different feedback controller designs (i.e., PD, SMC, and IO-RAC) [175]. The time span starts at  $t = 120$  second, so that the transient behaviors at the beginning of the simulation are diminished. The tracking errors  $\epsilon_{y,i}$  of the four joints are shown in (a - d), respectively.

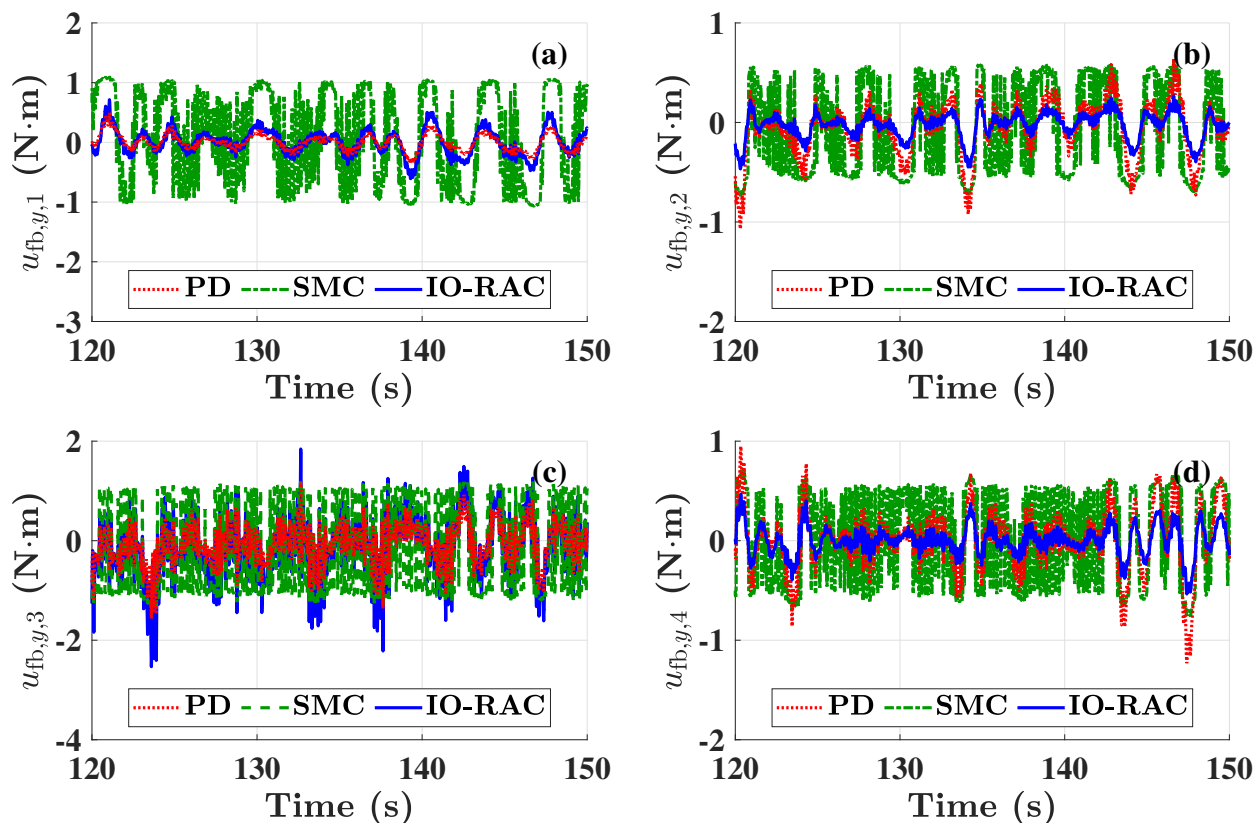


Figure 4.11: Comparison of the stationary exoskeleton tracking controls with different feedback controller designs (i.e., PD, SMC, and IO-RAC) [175]. The time span starts at  $t = 120$  second, so that the transient behaviors at the beginning of the simulation is diminished. The feedback control inputs (i.e.,  $u_{c,y,i}$ ) at the four joints (i.e.,  $y_i$ ) are shown in (a - d), respectively.

default parameters in Table 4.1. Note that the amplitudes of  $\mathbf{f}_w(t) \in \mathbb{R}^4$  are amplified for disturbances on  $y_1$  and  $y_3$ . We compare the performance of IO-RAC with two other adaptive controllers, whose feedback terms  $\mathbf{u}_{fb}$  are respectively selected as a PD and SMC controllers from Eq. (4.20). Since all three controllers may obtain better disturbance attenuation with larger gains, we specifically configure the control parameters so that these controllers have similar performances as shown in Figs. 4.10. However, the feedback inputs from these controllers are significantly different. From Figs. 4.11, we can observe the chattering, i.e., the rapid oscillations of feedback inputs in SMC caused by the gain switching control, which occurs when  $c_{SMC} = 100$  is selected for the sigmoid function that approximates the sign

function in Eq. (4.23). This problem is less significant in the cases of PD and IO-RAC. Also, compared with PD, IO-RAC yields larger feedback inputs for  $y_1$  and  $y_3$ , and significantly smaller input efforts for  $y_2$  and  $y_4$ . This observation is expected since the design of  $\mathbf{J}_w$  in IO-RAC takes into consideration the larger disturbances at  $y_1$  and  $y_3$ , which is unlike the case of PD where simply large control gains are used ( $\mathbf{u}_{fb}$  for PD is designed as  $\mathbf{u}_{fb,PD} = -4c_{R,1}\mathbf{K}_\chi\boldsymbol{\xi}$ ). Therefore, with the reasonable design of  $\mathbf{J}_w$ , IO-RAC can potentially attenuate disturbances at their origins, and prevent them from transmitting to other parts of the system.

The stationary exoskeleton example allows us to observe the fundamental behaviors of IO-RAC. The next case studies the use of IO-RAC in TAWÉ for tremor suppression.

#### 4.4.2 TAWÉ

Figure 4.12 recalls the design of TAWÉ and the geometry of the human-exoskeleton system. Based on the multibody model setup in 2.3, the control system output is selected as  $\mathbf{y} = \boldsymbol{\rho}_{\text{wrist,main}} = [\rho_{\text{WFE}}, \rho_{\text{RUD}}]^T$ . The 2-DOF control input  $\mathbf{u}_{\text{exo}}$  from the exoskeleton can fully

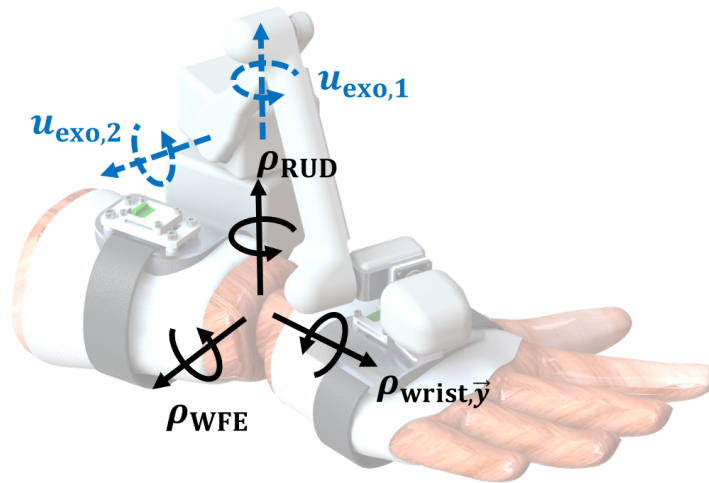


Figure 4.12: The 3D model of TAWÉ system [177] with directions of the wrist angles  $\rho_{\text{RUD}}$ ,  $\rho_{\text{WFE}}$ ,  $\rho_{\text{wrist}, \vec{y}}$  and the control input  $u_{\text{exo},1}$  and  $u_{\text{exo},2}$  are marked.

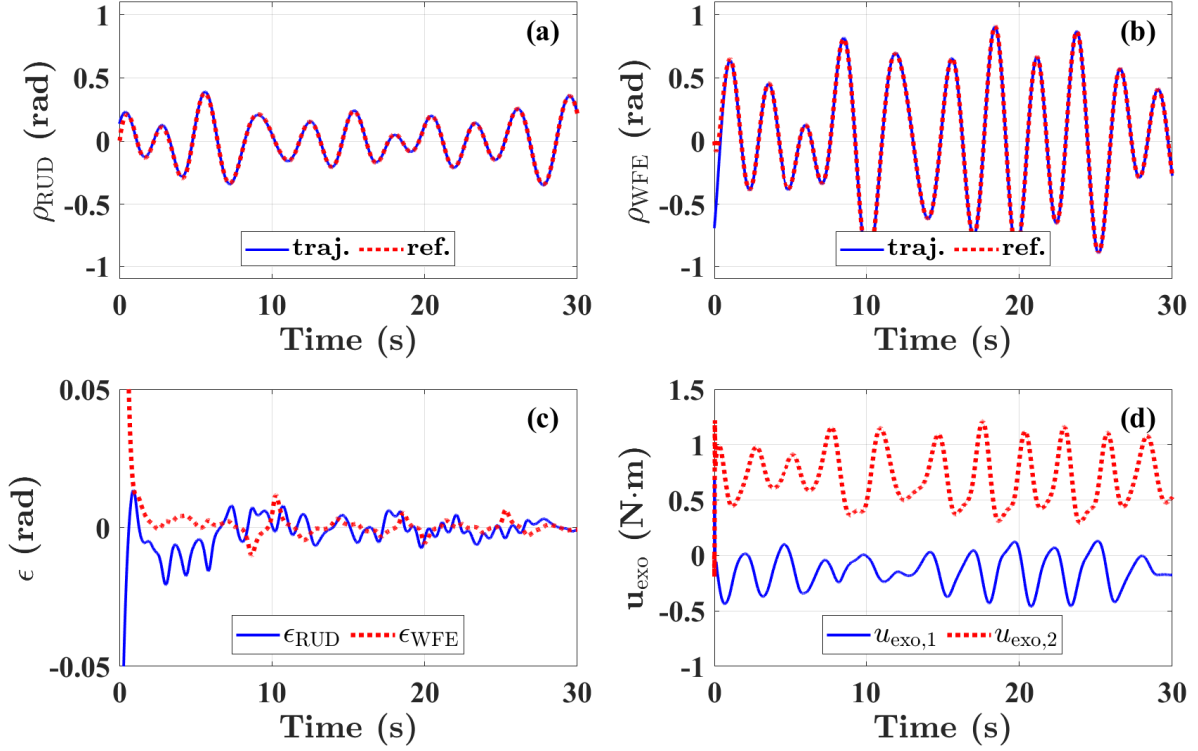


Figure 4.13: The performances of IO-RAC on TAWE with known human kinematics and zero-disturbance [175], where (a - b) compares the tracking trajectories and reference in the wrist angles; (c) shows tracking error; and (d) presents the input efforts.

actuate the control system. It should also be noted that the user control input  $\mathbf{u}_{user,y}$  from Eq. (4.15) is not used in the following simulations. Hence, the tracking reference  $\mathbf{r}_y$  for TAWE is arbitrarily defined and used for all following simulations, and  $\mathbf{u}_{exo,y}$  is required to adaptively compensate for the gravitational load. The inertia of the hand is selected by referencing [31]. For IO-RAC, We also select the feedback control parameters  $c_{R,1} = 2$  and  $\mathbf{J}_{w,y} = 0.25\mathbf{J}_y$  according to Eq. (4.34) in following simulation.

By assuming that the wrist kinematics is known, we first test the tracking performance under zero disturbance shown in Fig. 4.13. Observe from Figs. 4.13(a, b) that the trajectory of  $\mathbf{y}$  is accurately following the tracking reference, and the errors in Fig. 4.13(c) converge quickly to zeros. Furthermore, notice from Fig. 4.13(d) that the control input  $\mathbf{u}_{exo}$  (calculated from

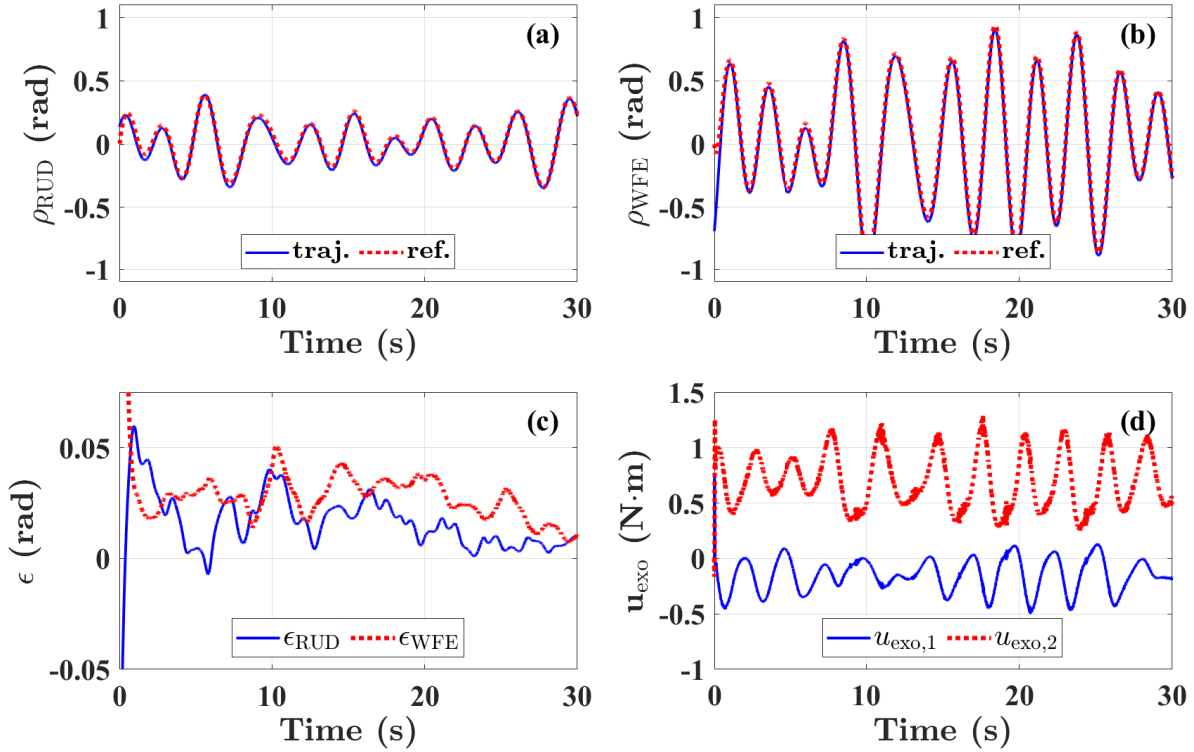


Figure 4.14: The performances of IO-RAC on TAW with unknown human kinematics and disturbance [175], where (a - b) compares the tracking trajectories and reference in the wrist angles; (c) shows tracking error; and (d) presents the input efforts.

$\mathbf{u}_{exo,y}$  based on Eq. (4.8)) is below 2 N·m, which is practically based on the actuator design parameter as discussed in Section 2.1.2. These results confirm that the robust adaptive controller is applicable to the TAW control system.

In practice, wrist kinematics is unknown. Hence, we need to incorporate the WKI algorithm from Section 3.2, which provides crucial information on the closed kinematic chain to the calculation of IO-RAC. The results of the second simulation shown in Figs. 4.15(a - b) indicates that the combination of IO-RAC and WKI algorithm is feasible. In this simulation, the WKI algorithm runs along with IO-RAC in the presence of disturbances and sensor noises. The control system output  $\hat{\mathbf{y}}$  used in the controller is also estimated by the WKI algorithm. Due to both disturbance and estimation errors from WKI, the tracking errors

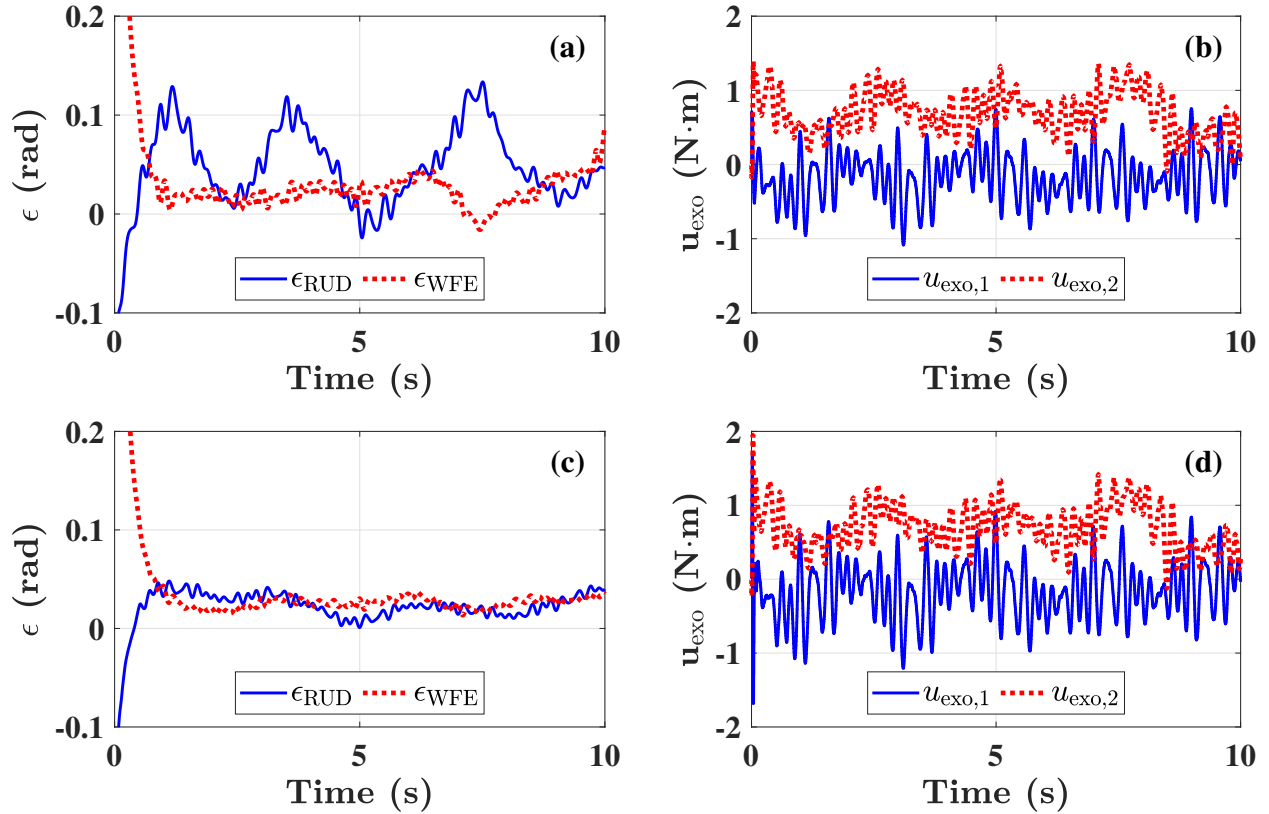


Figure 4.15: The comparison of passive and active tremor suppression with IO-RAC from TAWE simulations [175], where (a, b) show the tracking error and control input from passive tremor suppression, respectively; and (c, d) show the tracking error and control input from active tremor suppression, respectively.

shown in Fig. 4.15(c) have small oscillations. Since the performance is evaluated by the true control system output  $yy$  instead of its estimation, the mean values of error oscillations may also slightly deviate from  $\epsilon = 0$ . Finally, Fig. 4.15(d) demonstrate a similar control input

Finally, we introduce the tremor as model uncertainty. The synthesized tremor excitation is assumed to be a combination of harmonic waves of different frequencies within the 3 - 6 Hz bandwidth, which is similar as observed from Section 4.1. With the use of IO-RAC with the BMFLC model as discussed in Section 4.3.5, we are able to actively compensate for tremor excitations. The comparison between passive (without BMFLC) and active tremor controls in Figs. 4.15(a, c) show that with a good bandwidth resolution, the implementation

of BMFLC through IO-RAC can provide better tremor suppression as the error oscillation amplitudes are reduced. However, it should be noted that the tremor is not fully suppressed, since the frequencies from the BMFLC bandwidth do not fully overlap with that from the synthesized tremor bandwidth. Finally, it can be observed from Fig. 4.15(d) that the adaptive controller introduces high-amplitude and rapidly changing control input behavior in the beginning of the simulation. This is due to the overshoot of the initial uncertain parameter estimation, which can be reduced by tuning the adaptive gain  $\Gamma$  to reduce the step size of parameter update.

In summary, the two simulations demonstrate that the proposed IO-RAC provides good performance and stability in the tracking control of rehabilitation exoskeletons with various model uncertainties and disturbances. The simulations can run faster than 2000 Hz with the robot dynamics simulation and WKI algorithm on a 4.7GHz CPU (Intel i7-11800H), indicating that the proposed model-based controller is real-time applicable.

## 4.5 Summary

This chapter discusses the exoskeleton controller design for tremor suppression. We first observed the dynamics of the experimental tremor time series, which implies that tremor possesses multiple harmonic components with time-varying amplitudes and frequencies, and indicates the nonlinear nature of the neuromusculoskeletal dynamics behind tremor. We then proceed to the generalized exoskeleton controller development. Based on the proposed control model in Eq. (4.10), we have proposed a few model assumptions, which lead to the development of the hypothetical user PID controller, and a few exoskeletons controllers. In particular, we combined the model reference adaptive control and inverse optimal robust control theories, and proposed the inverse optimal robust adaptive controller (IO-RAC) in

Eq. (4.36) that can compensate for the effects of inertia and load uncertainties, as well as providing  $H_\infty$  robustness in  $l^2$  disturbance attenuation by optimizing a meaningful cost function. The proofs of stability and optimality for the controllers are discussed in Appendix A.2-A.5.

We then demonstrated the performance of the proposed controller through two simulations. In the station exoskeleton simulation, we study the fundamental behaviors of IO-RAC in trajectory tracking and uncertain parameter adaptation. It was demonstrated that our controller can compensate for various inertia and load uncertainties, and provide good tracking stability and performance in the presence of disturbances. Later, in the simulation of TAWE, we showcased that the controller can also be combined with the WKI algorithm proposed in Section 3.2, and be applied for active tremor suppression by using the BMLFC model for tremor uncertainty adaptation.

While the IO-RAC can be applied to a family of exoskeletons and other robotic systems, it should be noted that the application conditions must satisfy the model assumptions (MA. 3, 4, 6). Again, IO-RAC does not incorporate input capacity, range of motion, and other safety constraints. The solution to limitations needs to be further investigated in future studies.

Finally, the exoskeleton controller design in this section is carried out under the assumption that the tracking reference is available by default. In user-guided operation, the voluntary movement intention is unknown by default. When overlaid with tremor signal components, the identification of voluntary components has become a challenge. The next Chapter will discuss the real-time estimation of voluntary movement and its application in the exoskeleton control framework for tremor alleviation.

# Chapter 5

## Voluntary Movement Estimation for Exoskeleton Motion Planning

As discussed in Section 4.1, the signal components of pathological tremors mainly come from the high-frequency domain. In earlier studies, the frequency bands of voluntary movements are generally assumed to be lower than those of tremors [137, 164, 171]. Hence, estimations of tremors and voluntary movements can be obtained through band-pass and low-pass filtering, respectively [136]. However, with the common cutoff frequencies selected between 1-2 Hz, these filters also introduce phase shifts that significantly delay or distort the estimations.

Previous studies also proposed various tremor filtering algorithms that can provide voluntary movement estimation (VME). By approximating tremor oscillations as combinations of harmonic components with different frequencies, a few adaptive filtering (AF) techniques adopted Autoregressive models [163], and Fourier linear combiners models (FLC) (e.g., weighted-frequency FLC (WFLC) [14, 135, 137], band-limited multi-frequency FLC (BM-FLC) [171]) for tremor regression. The model parameters are updated in real-time using optimizers including recursive least square and Kalman filter. However, these algorithms (particularly FLC-based) can be sensitive toward the frequency property of tremor, and may not fully remove oscillations or delays. There are also techniques that used data-driven models such as support vector machine [164, 185] and deep neural networks [74, 150] for tremor regression, which can obtain great accuracy and minimal lag in tremor and volun-

tary movement estimation. On the other hand, to realize real-time filtering with increased model complexity, these algorithms may also require high-end processors (e.g., graphic and neural processing units) for calculations.

In this chapter, we explore lightweight data-driven filters for real-time voluntary movement estimation with good precision and little delay. We propose a new data-driven voluntary movement estimator (SVR-VME) that adopts the least square support vector regression (LS-SVR) framework [182], which learns to estimate voluntary components from movement time series with significantly reduced lag. The algorithm also supports the recursive update of the kernel matrix inverse, allowing efficient and adaptive updates based on the latest data. The voluntary movement estimated by SVR-VME will be used for the motion planning of exoskeleton in user-guided operation.

The rest of the chapter is arranged as follows. The need for reduced delay voluntary movement estimation is explained and demonstrated in Section 5.1. Section 5.2 explains the design of the proposed VME algorithm based on LS-SVR. In Section 5.3, the characteristics of the proposed algorithm are compared with those from earlier studies via numerical studies, which are based on synthesized and experimental tremor motion signals with quasiperiodic and transient elements. Finally, Section 5.4 summarizes the findings in this chapter. (The study in this chapter has been partially reported in [182].)

## 5.1 Voluntary movement estimation and Time-Delay

In this work, the following movement data sets are mainly used for the VME study:

- (1) Synthesized tremor signals  $\mu_{\text{synth}}$ , which are non-dimensional signals composed of quasiperiodic (non-repetitive) harmonic waves that made up the voluntary movement (0.1 to

0.2 Hz) and tremor (3 to 6 Hz). Some synthesized signals also contain discrete jumps, i.e., discontinuous changes in signal values.

- (2) “Motus” tremor signals  $\mu_{\text{motus}}$  introduced in Section 4.1 [134], which contains five kinetic tremor time series. The measurements are angular velocities (converted to rad/s), which are also used to obtain the joint angles using numerical integration.

For all data sets, the time series last 30 seconds, and the sampling frequency of the signals is 100 Hz. The signals are also normalized to have an approximate amplitude of 0.5 during regression simulation.

### 5.1.1 Low-Pass Filtering of Voluntary Movement

Following a few earlier studies, we assume that voluntary movement mainly consists of signal components whose frequencies are lower than that of pathological tremors [137, 164, 171]. This is in agreement with the model assumption (MA. 8), which is suitable for low-activity user movements. Therefore, based on the control model in Eq. (4.10), the output measurement  $\mathbf{y}$  from the exoskeleton sensor can be written as

$$\mathbf{y} = \mathbf{y}_{\text{vol}} + \mathbf{y}_{\text{tremor}} \quad (5.1)$$

where the voluntary movement measurement

$$\mathbf{y}_{\text{vol}} = \text{lpf}_0(\mathbf{y}) \quad (5.2)$$

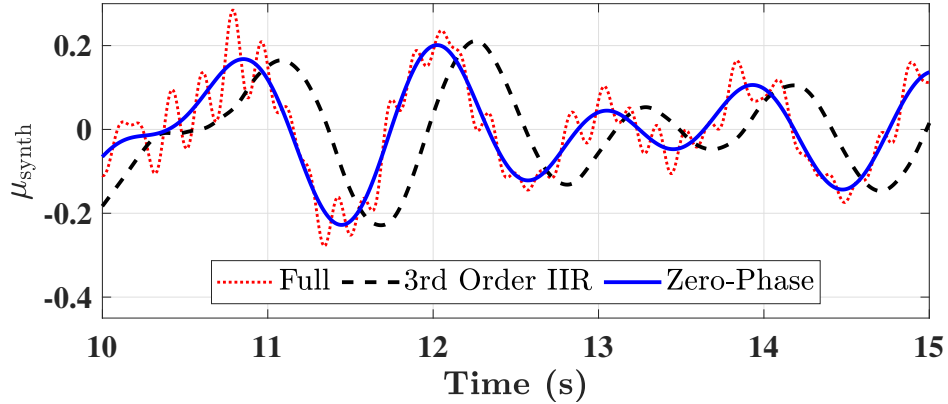


Figure 5.1: Comparison between causal (IIR) and non-causal (zero-phase) low-pass filtering of an example synthesized tremor signal  $\mu_{\text{synth}}$  [182]. Both filter designs are based on a 3rd-order Butterworth low-pass filter with a cutoff frequency of 1.5 Hz, except that the zero-phase filter performed the forward-backward filtering.

is the low-pass filtering of the full movement signal with zero delay. If the tracking reference of the exoskeleton  $\mathbf{r}_y$  is designed as

$$\mathbf{r}_y = \mathbf{f}_{\mathbf{r},y}(t, \mathbf{y}_{\text{vol}}) \quad (5.3)$$

it can be used by the exoskeleton controllers in Section 4.3 as the goal trajectory for passive and active tremor suppression.

Based on the above setup, low-pass filters can extract voluntary components from the tremor movement signals. As shown in Fig. 5.1, causal filters (e.g., Infinite Impulse Response (IIR) filters) can extract voluntary movements with a significant delay. On the other hand, non-causal filtering techniques (e.g., zero-phase filtering) may require forward-backward filtering over a window of movement time series, which may not be efficient for real-time applications. Similarly, real-time application of deep neural networks and other complex models may also require computation hardware that is not applicable in wearable exoskeletons [74, 150].

### 5.1.2 Adaptive Filtering with BMFLC

As previously mentioned, real-time adaptive filtering (e.g., Kalman filter (KF)) [62] based on WFLC and BMFLC models can regress the harmonic components of tremor and provide filtered movement signals. Previous studies also pointed out that BMFLC can outperform WFLC as it can identify multiple harmonic components within a frequency band [164, 171]. Similar to the application of EKF for WKI as discussed in Section 3.2, we assume the discrete-time as  $k = c_{f,s}t$  where  $c_{f,s}$  is the sampling frequency. The difference between the WKI model and the Kalman Filtering with BMFLC (KF-BMFLC) model is that the latter is a linear model where the Jacobian matrices in Eq. (3.23) are independent of the model state  $\mathbf{x}$  and input  $\mathbf{u}$ . Hence, the "extended" version of EKF is not necessary. On the other hand, KF-BMFLC can still follow the formulation of EKF in Section 3.2.1. For filtering one-dimensional movement signals, the KF-BMFLC model can be written as

$$\mathbf{x}_{\text{BMFLC}} = \begin{bmatrix} s \\ \dot{s} \\ \mathbf{p}_{\mu, \text{BMFLC}} \end{bmatrix}; \quad \mathbf{y}_{\text{BMFLC}} = 0; \quad \mathbf{u}_{\text{BMFLC}} = \mu \quad (5.4a)$$

$$\mathbf{f}_{\text{BMFLC}} = \begin{bmatrix} s + \dot{s}/c_{f,s} \\ \dot{s} \\ \mathbf{p}_{\mu, \text{BMFLC}} \end{bmatrix} + \mathbf{w}_x; \quad \mathbf{h}_{\text{BMFLC}} = s + \mathbf{J}_{p, \text{BMFLC}} \mathbf{p}_{\mu, \text{BMFLC}} - \mu + v_\mu \quad (5.4b)$$

where  $s$  is the voluntary signal component,  $\mathbf{p}_{\mu, \text{BMFLC}}$  is the amplitude parameter previously introduced in Eq. (4.1),  $\mathbf{w}_x$  is the process noise of the state,  $\mu$  is the full measurement to be filtered, and  $v_\mu$  is the sensor noise in  $\mu$ . The corresponding covariance matrices of  $\mathbf{w}_x$  and  $v_\mu$  are  $\mathbf{Q}_x$  and  $\mathbf{R}_\mu$ , respectively. It should also be noted that the expression of  $s$  and  $\dot{s}$  follows the design of a  $g$ - $h$  filter, which has been used in earlier studies for one-step voluntary movement prediction [14, 137].

The performance of KF with BMFLC in VME is shown in Fig. 5.2. The frequency band of the default BMFLC is set to 3-13 Hz with a resolution of 0.1 Hz. It is observed from Fig. 5.2(a) that the tremor component from the KF filtered signal is reduced, which also has a very small delay compared to that of the IIR low-pass filter. By adjusting the elements in the covariance matrix  $\mathbf{Q}_x$  corresponding to  $\mathbf{p}_{\mu, \text{BMFLC}}$ , we can tune the quickness of BMFLC amplitude parameter adaptation. From Fig. 5.2(b), notice that quicker update of  $\mathbf{p}_{\mu, \text{BMFLC}}$  results in a smoother trajectory of  $s$  with a more significant delay. On the other hand,

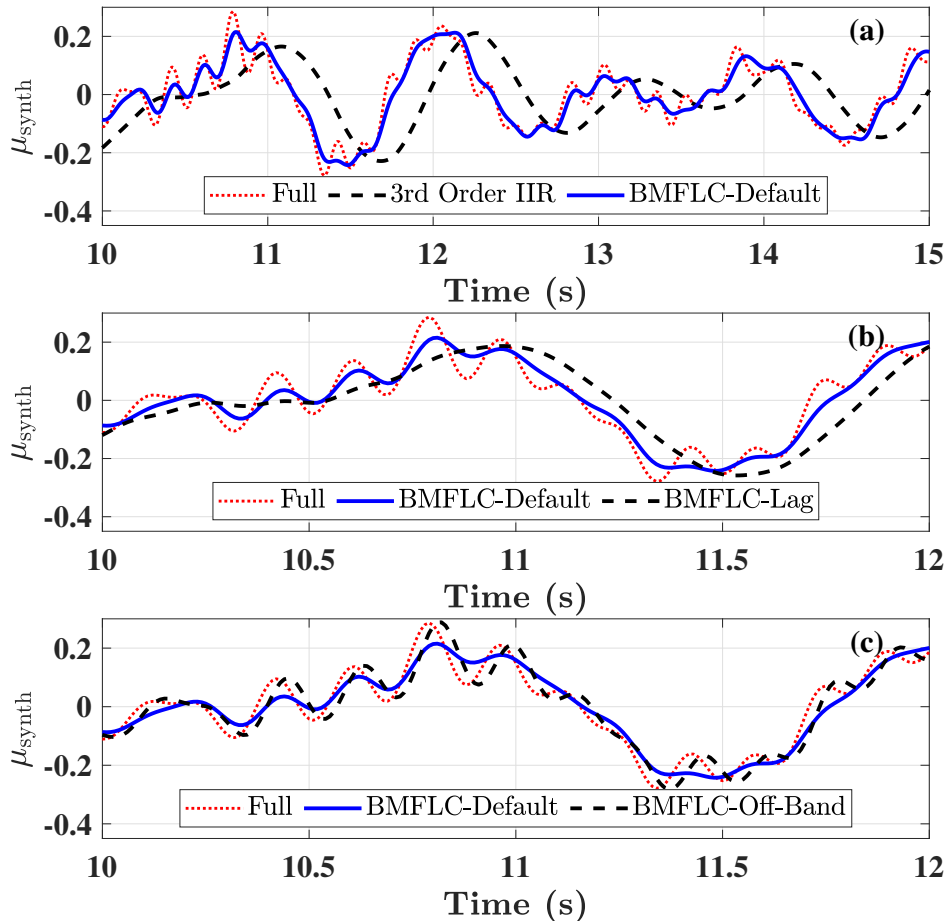


Figure 5.2: The performance of KF-BMFLC in VME [182], where (a) compares KF-BMFLC with IIR filter, (b) compares two KF-BMFLC algorithms with different covariances, and (c) compares the default KF-BMFLC with an alternate one whose frequency band does not match with that of the tremor signal component.

slower update of  $\mathbf{p}_{\mu, \text{BMFLC}}$  allows  $s$  to quickly respond to signal changes, but the tremor components are not fully filtered. Finally, if the frequency band of BMFLC does not match the tremor frequency, KF cannot extract tremor components from the full signal. This is shown in Fig. 5.2(c), where the off-band BMFLC covers 8-13 Hz, which does not match the tremor frequency from the synthesized signal.

In summary, VME is crucial to exoskeleton control for both passive and active tremor suppression. On the other hand, the existing approaches for VME may provide limited performance when applied to the control framework of wearable exoskeletons for tremor alleviation. The major challenge is the time delay in the estimated voluntary movement. In the next section, the theoretical formulation of the proposed SVR-VME algorithm will be explained in detail, which provides a solution to VME with delay reduction and high real-time efficiency.

## 5.2 Voluntary Movement Estimation via Support Vector Regression

This section introduces a novel data-driven VME algorithm for real-time application. Since the full movement measurement contains both voluntary and tremor signal components, we assume that it is possible to approximate the voluntary movement using a nonlinear function  $\beta$  based on a delayed window of full movement time series. Here we introduce the time-delay window  $\ell$  as

$$\ell_{c_l}(\mathbf{z}_k) = \left[ \mathbf{z}_k^T \quad \mathbf{z}_{k-1}^T \quad \cdots \quad \mathbf{z}_{k-c_l}^T \right]^T \quad (5.5)$$

where  $\mathbf{z}$  is the column vector input argument, and  $c_l$  is the length of the window. The function  $\beta$  can be written as

$$\mathbf{s}_k = \beta_k(\boldsymbol{\sigma}, \ell_{m_{\text{lag}}}(\boldsymbol{\mu}_k)) \quad (5.6)$$

where  $\boldsymbol{\sigma}$  is the model parameter, and both input  $\boldsymbol{\mu}$  and output  $\mathbf{s}$  can be multi-dimensional. Based on (Asm. 4), the zero-phase low-pass filtering of  $\mu$  is selected as the voluntary reference  $\mathbf{r}_{\text{vol}}$ . This leads to the definition of estimation error as

$$\mathbf{r}_{\text{vol},k} = \text{lpf}_0(\boldsymbol{\mu}_k); \quad \mathbf{e}_k = \mathbf{s}_k - \mathbf{r}_{\text{vol},k} \quad (5.7)$$

From the above setup, we formulate the optimization problem that aims to minimize the cost function

$$\mathcal{J}_{\text{VME}}(\hat{\boldsymbol{\sigma}}_k) = (\hat{\boldsymbol{\sigma}}_k^T \mathbf{C}_P \hat{\boldsymbol{\sigma}}_k + \ell_{m_{\text{vol}}}^T(\mathbf{e}_k) \mathbf{C}_Q \ell_{m_{\text{vol}}}(\mathbf{e}_k)) / 2 \quad (5.8)$$

subjected to the equality constraint

$$\boldsymbol{\tau} = \ell_{m_{\text{vol}}}(\beta_k(\boldsymbol{\sigma}, \ell_{m_{\text{lag}}}(\boldsymbol{\mu}_k)) - \mathbf{s}_k) = \mathbf{0} \quad (5.9)$$

where  $\mathbf{C}_P$  and  $\mathbf{C}_Q$  are positive-definite weight matrices, and integer scalars  $m_{\text{lag}}$  and  $m_{\text{vol}}$  are the input and output time-delay window lengths, respectively. The goal of optimization is to find the parameter  $\boldsymbol{\sigma}$  so that  $\beta$  can closely approximate the behavior of a low-pass filter with zero delays. It should also be pointed out that, for general applications, the optimization problem can also be modified with additional components in the cost function and constraints, and various methods can be applied to solve this problem. In this study, to carry out this optimization in real-time, we adopt the support vector regression method explained in the following subsections.

### 5.2.1 Least Square Support Vector Regression

Support Vector Regression applies the support vector machine technique in regression [24, 156, 164, 185], which is data-driven and capable of handling nonlinearities. SVM maps the input into a higher-order nonlinear feature space. Linear regression is then performed on the nonlinear projections of input data. Particularly, when the optimization involves a quadratic cost function and equality constraints, it is possible to apply the least square SVR. LS-SVR can rapidly solve for the parameters  $\boldsymbol{\sigma}$ , which is suitable for real-time applications. Therefore, based on the cost function Eq.(5.8), the nonlinear function  $\boldsymbol{\beta}$  is designed as

$$\boldsymbol{\beta}_k = \boldsymbol{\Psi} \boldsymbol{\phi}_k(\ell_{m_{\text{lag}}}(\boldsymbol{\mu}_k)) + \mathbf{b}; \quad \boldsymbol{\Psi} = \begin{bmatrix} \boldsymbol{\sigma}_1 & \boldsymbol{\sigma}_2 & \cdots & \boldsymbol{\sigma}_{n_s} \end{bmatrix}^T \quad (5.10)$$

where  $\boldsymbol{\phi}$  is the nonlinear projection function, and  $\mathbf{b}$  is the bias.  $\boldsymbol{\Psi}$  consists of multiple  $\boldsymbol{\sigma}$  vectors corresponding to all elements within  $\mathbf{s}$  (whose dimension is  $n_s$ ). Hence, based on the cost function and constraint from Eqs. (5.8, 5.9), we can formulate the dual problem with the Lagrange function as

$$\mathcal{L}(\hat{\boldsymbol{\sigma}}_k) = \mathcal{J}_{\text{VME}}(\hat{\boldsymbol{\sigma}}_k) - \boldsymbol{\theta}_k^T \boldsymbol{\tau} \quad (5.11)$$

where  $\boldsymbol{\theta}$  is the Lagrange multiplier corresponding to the constraints.

We also simplify the weight matrices so that  $\mathbf{C}_P = \mathbf{I}$ , and  $\mathbf{C}_Q = (1/c_Q)\mathbf{I}$  with  $c_Q > 0$ . The Karush-Kuhn-Tucker (KKT) conditions is formulated based on Eq.(5.11) as [156]

$$\frac{\partial \mathcal{L}}{\partial \hat{\boldsymbol{\sigma}}_k} = 0 \rightarrow \hat{\boldsymbol{\sigma}}_{j,k} = \boldsymbol{\Phi}_k \boldsymbol{\theta}_{\text{B},j,k}; \quad \frac{\partial \mathcal{L}}{\partial \ell_{m_{\text{vol}}}(\mathbf{e}_k)} = 0 \rightarrow \mathbf{e}_{k-i} = c_Q \boldsymbol{\theta}_{\text{A},i,k} \quad (5.12a)$$

$$\frac{\partial \mathcal{L}}{\partial \hat{\mathbf{b}}_k} = 0 \rightarrow \mathbf{1}_{1,m_{\text{vol}}} \boldsymbol{\theta}_{\text{B},j,k} = \mathbf{0}; \quad \frac{\partial \mathcal{L}}{\partial \boldsymbol{\theta}} = 0 \rightarrow \boldsymbol{\tau}_{k-i} = \mathbf{0} \quad (5.12b)$$

where  $i = 0, 1, \dots, m_{\text{vol}}$ ,  $j = 1, 2, \dots, n_s$ , and the intermediate matrix terms are

introduced as

$$\Phi_k = \begin{bmatrix} \phi_k & \phi_{k-1} & \cdots & \phi_{k-m_{\text{vol}}} \end{bmatrix} \quad (5.13a)$$

$$\theta_k = \begin{bmatrix} \theta_{A,0,k}^T & \theta_{A,1,k}^T & \cdots & \theta_{A,m_{\text{vol}},k}^T \end{bmatrix}^T \quad (5.13b)$$

$$\begin{aligned} \Theta_k &= \begin{bmatrix} \theta_{A,0,k} & \theta_{A,1,k} & \cdots & \theta_{A,m_{\text{vol}},k} \end{bmatrix}^T \\ &= \begin{bmatrix} \theta_{B,1,k} & \theta_{B,2,k} & \cdots & \theta_{B,n_s,k} \end{bmatrix} \end{aligned} \quad (5.13c)$$

Based on the substitutions of  $\sigma$  and  $\theta$ , the KKT conditions yields the least square problem

$$\begin{bmatrix} \mathcal{R}_{\text{vol},k} & \mathbf{0}_{n_s \times 1} \end{bmatrix} \Pi_k^{-1} = \begin{bmatrix} \hat{\Theta}_k^T & \hat{\mathbf{b}}_k \end{bmatrix} \quad (5.14)$$

where

$$\Pi_k = \begin{bmatrix} \Phi_k^T \Phi_k + c_Q \mathbf{I} & \mathbf{1}_{m_{\text{vol}} \times 1} \\ \mathbf{1}_{1 \times m_{\text{vol}}} & 0 \end{bmatrix} \quad (5.15a)$$

$$\mathcal{R}_{\text{vol},k} = \begin{bmatrix} \mathbf{r}_{\text{vol},k} & \mathbf{r}_{\text{vol},k-1} & \cdots & \mathbf{r}_{\text{vol},k-m_{\text{vol}}} \end{bmatrix} \quad (5.15b)$$

The kernel trick is commonly used in SVM [24]. In this work, we employ the radial basis function (RBF) kernel function as

$$\mathcal{K}(\boldsymbol{\mu}_{k-i}, \boldsymbol{\mu}_{k-j}) = \phi_i^T \phi_j = \exp(-\|\boldsymbol{\mu}_{k-i} - \boldsymbol{\mu}_{k-j}\|^2 / c_{\mathcal{K}}^2) \quad (5.16)$$

where  $i, j = 0, 1, \dots, m_{\text{vol}}$  and  $c_{\mathcal{K}} > 0$ . The RBF kernel function serves as a similarity measure that helps identify the patterns of zero-delay low-pass filtering.

Later, we define the prediction horizon as  $m_{\text{future}}$ . Reasonably increasing  $m_{\text{future}}$  can reduce

the time delay in VME. Therefore,  $\beta$  at discrete time  $k + m_{\text{future}}$  is calculated based on the model driven by previous data as

$$\beta_{k+m_{\text{future}}} = \begin{bmatrix} \hat{\Theta}_k \\ \hat{\mathbf{b}}_k^T \end{bmatrix}^T \begin{bmatrix} \Phi_k^T \phi_{k+m_{\text{future}}} \\ 1 \end{bmatrix} = \begin{bmatrix} \hat{\Theta}_k \\ \hat{\mathbf{b}}_k^T \end{bmatrix}^T \begin{bmatrix} \boldsymbol{\eta}_{k+m_{\text{future}}} \\ 1 \end{bmatrix} \quad (5.17)$$

where  $\boldsymbol{\eta}$  is a collection vector of kernel terms

$$\boldsymbol{\eta}_{k+m_{\text{future}}} = \begin{bmatrix} \mathcal{K}(\boldsymbol{\mu}_{k+m_{\text{future}}}, \boldsymbol{\mu}_k) \\ \mathcal{K}(\boldsymbol{\mu}_{k+m_{\text{future}}}, \boldsymbol{\mu}_{k-1}) \\ \vdots \\ \mathcal{K}(\boldsymbol{\mu}_{k+m_{\text{future}}}, \boldsymbol{\mu}_{k-m_{\text{vol}}}) \end{bmatrix}^T \quad (5.18)$$

## 5.2.2 Recursive Kernel Matrix Inversion

The inversion of kernel matrix  $\mathbf{\Pi}$  can be time-consuming with a large number of samples. An advantage of using LS-SVR is that it is possible to calculate the update of  $\mathbf{\Pi}^{-1}$  based on data in a moving window. This makes it possible to obtain  $\boldsymbol{\theta}$  and  $\mathbf{b}$  in real-time [164]. When the data of  $\mathbf{r}_{\text{vol},k+1}$  is available for the calculation of  $\mathbf{s}_{k+1}$ , we obtain an augmented matrix

$$\mathbf{\Pi}_{k,k+1} = \begin{bmatrix} 1 + c_Q & \begin{bmatrix} \phi_{k+1}^T \Phi_k & 1 \end{bmatrix} \\ \begin{bmatrix} \Phi_k^T \phi_{k+1} \\ 1 \end{bmatrix} & \mathbf{\Pi}_k \end{bmatrix} \quad (5.19)$$

By defining an intermediate vector

$$\mathbf{z}_{\mathcal{K},k,i} = \begin{bmatrix} \Phi_k^T \phi_{k-i} \\ 1 \end{bmatrix} \quad (i = -1, 0, 1, \dots, m_{\text{vol}}) \quad (5.20)$$

and based on Schur complement [194], we can obtain

$$\mathbf{\Pi}_{k,k+1}^{-1} = \begin{bmatrix} z_{\Pi,2} & -z_{\Pi,2}\mathbf{z}_{\Pi,1}^T \\ -z_{\Pi,2}\mathbf{z}_{\Pi,1} & \mathbf{\Pi}_k^{-1} + z_{\Pi,2}\mathbf{z}_{\Pi,1}\mathbf{z}_{\Pi,1}^T \end{bmatrix} \quad (5.21)$$

where

$$\mathbf{z}_{\Pi,1} = \mathbf{\Pi}_k^{-1}\mathbf{z}_{\mathcal{K},k,-1}; \quad z_{\Pi,2} = 1/(1 + c_Q - \mathbf{z}_{\mathcal{K},k,-1}^T\mathbf{z}_{\Pi,1}) \quad (5.22)$$

After that, with  $\mathbf{\Pi}_{k,k+1}^{-1}$  alternatively presented via intermediate terms as

$$\mathbf{\Pi}_{k,k+1}^{-1} = \begin{bmatrix} \mathbf{Z}_{\Pi,3} & \mathbf{Z}_{\Pi,4} \\ \mathbf{Z}_{\Pi,4}^T & \mathbf{Z}_{\Pi,5} \end{bmatrix} \quad (5.23)$$

where  $\mathbf{Z}_{\Pi,5}$  is a  $2 \times 2$  matrix. We then obtain

$$\mathbf{Z}_{\Pi,6} = \mathbf{Z}_{\Pi,3} - \mathbf{Z}_{\Pi,4}\mathbf{Z}_{\Pi,5}^{-1}\mathbf{Z}_{\Pi,4}^T \quad (5.24)$$

Finally, the updated  $\mathbf{\Pi}^{-1}$  can be calculated as

$$\mathbf{\Pi}_{k+1}^{-1} = \begin{bmatrix} \mathbf{Z}_{\Pi,6} + z_{\Pi,8}\mathbf{z}_{\Pi,7}\mathbf{z}_{\Pi,7}^T & -z_{\Pi,8}\mathbf{z}_{\Pi,7} \\ -z_{\Pi,8}\mathbf{z}_{\Pi,7}^T & z_{\Pi,8} \end{bmatrix} \quad (5.25)$$

where

$$\mathbf{z}_{\Pi,7} = \mathbf{Z}_{\Pi,6}\mathbf{1}_{m_{\text{vol}} \times 1}; \quad z_{\Pi,8} = -1/(\mathbf{1}_{1 \times m_{\text{vol}}}\mathbf{z}_{\Pi,7}) \quad (5.26)$$

Therefore,  $\mathbf{\Pi}^{-1}$  can be efficiently updated in real-time through the above process. This allows the data-driven model to adapt to dynamic changes in signal patterns. Comparing to directly inverting the kernel matrix using common methods such as Gauss-Jordan Elimination [33], the time complexity of recursive inversion is reduced from  $O(m_{\text{vol}}^3)$  to  $O(m_{\text{vol}}^2)$ .

### 5.2.3 Delay Reduction in Voluntary Movement Estimation

As discussed in Section 5.1, the time delay from causal digital low-pass filtering cannot be avoided. This delay is related to the filter order and cutoff frequency. By assuming that prediction horizon  $m_{\text{future}}$  is also equal to the delay caused by the filter, at discrete time  $k$ , the SVR-VME algorithm estimates the voluntary movement as the zero-lag low-pass filtered value of the full movement measurement. The application of the algorithm based on the aforementioned theoretical setup can be summarized as the following steps

- (1) Based on full movement measurement  $\boldsymbol{\mu}_{k-m_{\text{future}}}$  at discrete time  $k - m_{\text{future}}$ , recursively update from  $\boldsymbol{\Pi}_{k-m_{\text{future}}-1}^{-1}$  to  $\boldsymbol{\Pi}_{k-m_{\text{future}}}^{-1}$  using Eqs. (5.19-5.26)
- (2) Obtain  $\mathbf{r}_{\text{vol},k-m_{\text{future}}}$  from the low pass filter and update  $\mathcal{R}_{\text{vol},k-m_{\text{future}}}$  appeared in Eq. (5.15).
- (3) Calculate  $\hat{\boldsymbol{\Theta}}_{k-m_{\text{future}}}$  and  $\hat{\mathbf{b}}_{k-m_{\text{future}}}$  using Eq. (5.14).
- (4) Obtain  $\boldsymbol{\mu}_k$  from the current measurement, and calculate  $\boldsymbol{\eta}_k$  based on Eq. (5.18)
- (5) Calculate  $\boldsymbol{\beta}_k$  from Eq. (5.17), which is the approximation of  $\mathbf{s}_k$ , i.e., the zero-lag low-pass filtering from  $\boldsymbol{\mu}_k$ .

Note that the above process does not involve any numerical differentiation of time series, making it robust toward digital measurement noise. Additionally, due to the use of time-delay window operator in Eqs. (5.10, 5.12) the initialization of SVR-VME requires a total of  $m_{\text{lag}} + m_{\text{vol}} + m_{\text{future}}$  discrete time steps.

For parameter selections,  $c_Q$  and  $c_{\mathcal{K}}$  both need to be adjusted based on the amplitude and tremor properties in the signal. In general, small  $c_Q$  penalizes the error of estimation, but it may also cause chattering in estimated trajectories; since  $c_{\mathcal{K}}$  sets the similarity measure

threshold, extremely large or small  $c_{\mathcal{K}}$  can cause underfitting and poor estimation performance. The selection of  $m_{\text{vol}}$  depends on the power of the machine. While a larger data set can lead to better performance, it will also increase the time complexity of the algorithm. Finally, the selection of  $m_{\text{lag}}$  depends on the variation of signal dynamics. Small  $m_{\text{lag}}$  will not be able to capture signal patterns, while large  $m_{\text{lag}}$  can slow down adaptation towards dynamical changes. The selection of  $m_{\text{lag}}$  will be further discussed in the next section.

In summary, the SVR-VME algorithm approximates the zero-lag low-pass filtering based on signal pattern similarities. Through the formulation of LS-SVR, the recursive kernel matrix inversion enables the real-time adaption of the data-driven model. The next section will showcase SVR-VME in estimating voluntary movement from synthesized and experimental tremor movement time series, and compare it with previous methods.

### 5.3 Numerical Analysis

This section presents the characteristics and performance of the SVR-VME algorithm in comparison to the earlier method KF-BMFLC through numerical analysis. To compare both real-time algorithms at the same level, we have selected  $m_{\text{vol}} = 200$  so that SVR-VME and KF-BMFLC have the same time complexity. In this case, the kernel matrix inverse update rate of SVR-VME is 50 Hz. Hence,  $m_{\text{vol}} = 200$  implies that the kernel data set spans within a window of 4 seconds. In addition, we have selected the default parameters  $m_{\text{lag}} = 50$ ,  $c_Q = 10^3$ , and  $c_{\mathcal{K}} = 10^{-1}$ . The estimation reference  $\mathbf{r}_{\text{vol}}$  is obtained from the same 3rd order Butterworth low-pass filter used in Fig. 5.1. The prediction horizon is selected as  $n_{\text{future}} = 10$  to compensate for the delay in  $\mathbf{r}_{\text{vol}}$ .

### 5.3.1 Synthesized Tremor Movement Signals

The behavior of SVR-VME is first observed on the synthesized tremor signals  $\mu_{\text{synth}}$ . In Fig. 5.3, the proposed algorithm is tested on the synthetic signal previously used in Figs. 5.1 and 5.2. Notice from Fig. 5.3(a) that SVR-VME cannot fully realize zero-lag low-pass filtering, but the tremor component in the estimation is significantly reduced. Also, notice that SVR-VME yields very little delay compared to the IIR low-pass filter. It is observed from Fig. 5.3(b) that SVR-VME can obtain a similar level of delay reduction as KF-BMFLC (default version). On the other hand, from Fig. 5.3(c), the error between zero-phase low-pass

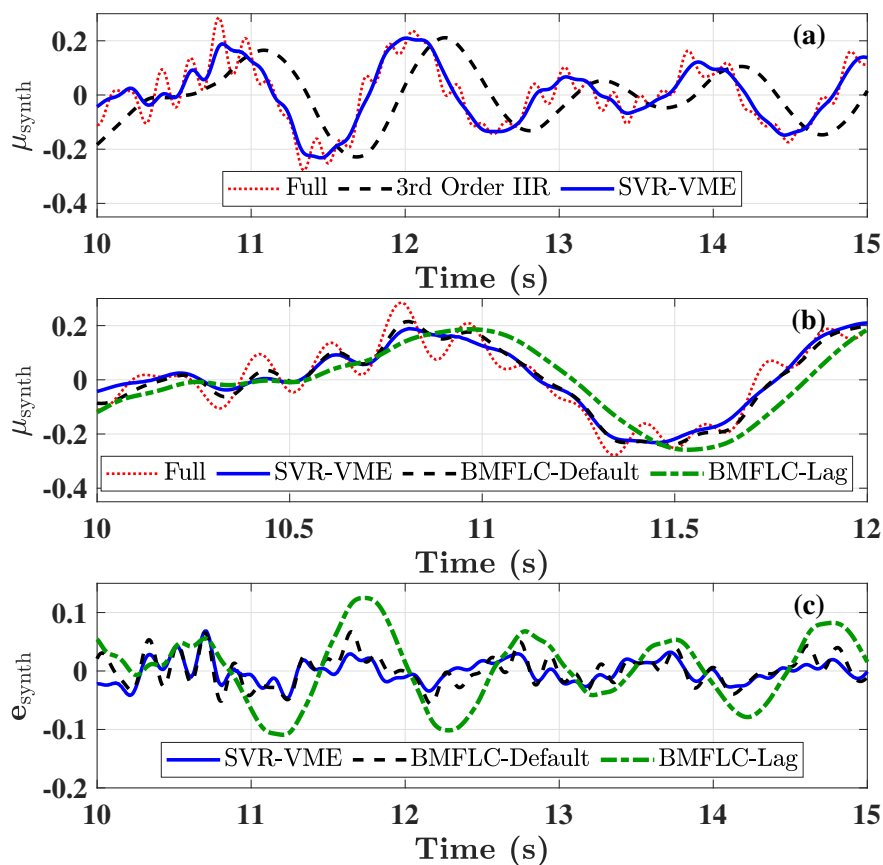


Figure 5.3: The performance of SVR-VME algorithm on synthesized tremor movement signal in comparison with IIR low-pass filter in (a), and KF-BMFLC in (b) [182]. The comparison of estimation errors between SVR-VME and KF-BMFLC algorithms is shown in (c).

filtering and the VME algorithms shows that SVR-VME can produce better tremor removal from the full measurement.

We then performed a quantitative study on the performance of SVR-VME by generating another 49 sets of synthesized tremor signals. The performance is evaluated on the integral of  $\mathbf{e}_{\text{synth}}^2$  and  $\dot{\mathbf{e}}_{\text{synth}}^2$  over a period of 20 seconds. While  $\mathbf{e}_{\text{synth}}$  is a direct reference of estimation error, its derivative  $\dot{\mathbf{e}}_{\text{synth}}$  can highlight the estimation errors related to the relatively high-frequency tremors in the signal. The results are shown in Fig. 5.4, where in both cases of  $\mathbf{e}_{\text{synth}}$  and  $\dot{\mathbf{e}}_{\text{synth}}$ , SVR-VME shows smaller error than KF-BMFLC. It is also interesting to observe that both SVR-VME and BMFLC significantly reduce the high-frequency tremor component from the full measurement.

In some cases, we observe that the errors from both estimators can exceed that from the full measurements. An example is trial No. 9 from Fig. 5.4(a). Figure 5.5 provides a closer

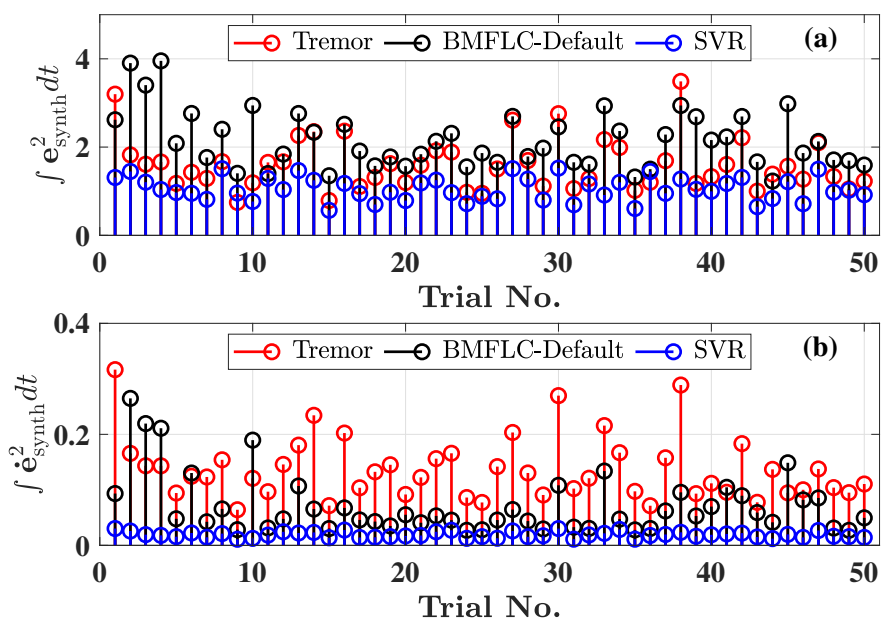


Figure 5.4: Quantitative comparison of errors towards zero-lag low-pass filtering from full measurement, SVR-VME estimations, and KF-BMFLC estimations, respectively, in the cases of synthesized tremor movement signals [182], where (a) shows the time integral of  $\mathbf{e}_{\text{synth}}^2$  for 20 seconds, and (b) shows the time integral of  $\dot{\mathbf{e}}_{\text{synth}}^2$  for 20 seconds.

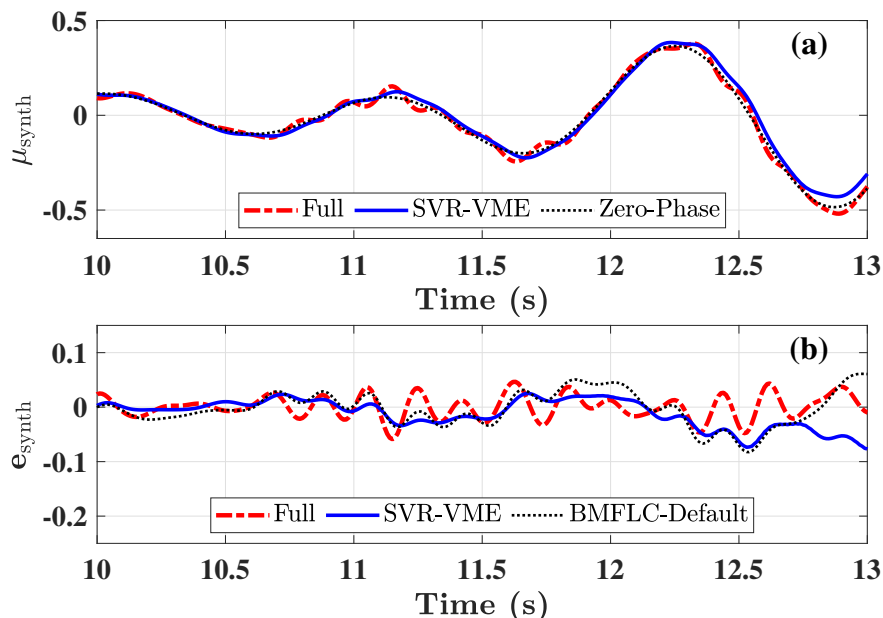


Figure 5.5: The performance of SVR-VME in Trial No. 9 from the quantitative analysis shown in Fig. 5.4, where (a) compares SVR-VME estimation result with zero-phase low-pass filter, and (b) compares the estimation errors between SVR-VME and KF-BMFLC algorithms.

look, where the error between SVR-VME and zero-phase filtering is noticeable in the range close to  $t = 13$  s. This type of error can occur when SVR-VME cannot accurately identify the current pattern of the signal from its database, which can be considered a result of data-driven model discrepancy. From Fig. 5.5(b), the estimation errors show that KF-BMFLC may occasionally have similar errors due to model discrepancy. Also, the removals of tremor elements from the original measurement by both estimators are significant, which matches with the result of Trial No.9 from Fig. 5.4(b).

The prediction horizon is critical to delay reduction in SVR-VME estimations. The comparison between SVR-VME algorithms with prediction horizons of 10 and 5 steps, respectively, is shown in Fig. 5.6. Notice that with a prediction horizon of 5 steps, the delay reduction is significant. On the other hand, a shorter prediction horizon can also produce smoother estimations. The errors shown in Fig. 5.7 also revealed that a longer prediction horizon can

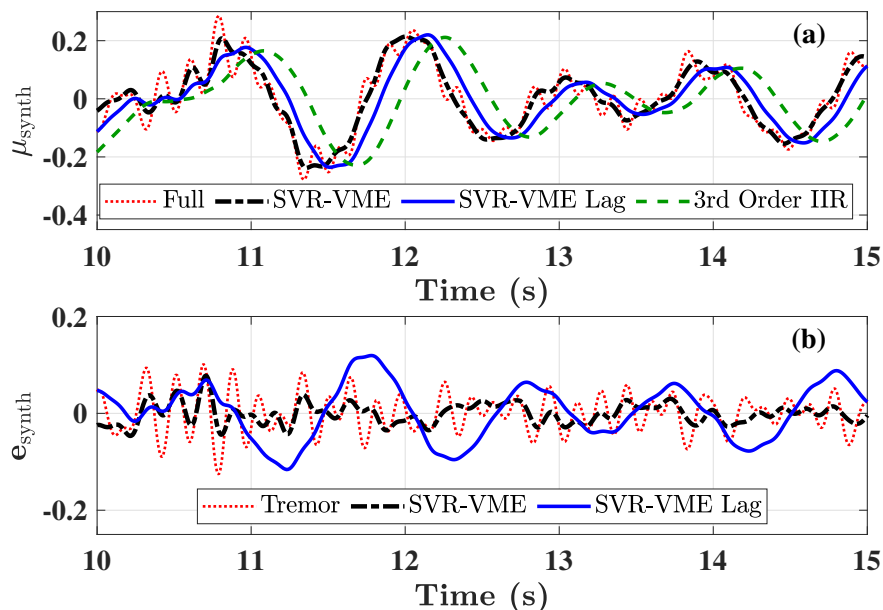


Figure 5.6: Comparison between SVR-VME algorithms with prediction horizons  $n_{\text{future}}$  of 10 steps (SVR-VME) and 5 steps (SVR-VME Lag), respectively [182], where (a) shows the estimations, and (b) shows the estimation errors.

still be preferable, since it yields smaller errors overall.

SVR-VME also possesses robustness against a moderate level of sensor noise. By overlaying uniformly distributed random noise on the previously used synthesized signals, the comparison between SVR-VME and KF-BMFLC is shown in Fig. 5.7. It can be observed that SVR-VME is much less affected by noise. A reason for this outcome is that the input and output of SVR-VME do not contain any numerical derivative, which will benefit the application of SVR-VME in scenarios where sensor noise exists.

In real life, human movements involve transient behaviors. We have synthesized tremor movement signals involving random step functions as transient behaviors. The performance of SVR-VME on synthesized signals with transient behaviors is shown in Fig. 5.8. It can be noticed from Fig. 5.8(a) that the response of SVR-VME is affected by the discrete jumps in the full measurement. Since randomized discrete jumps do not show similar patterns, the estimation of SVR-VME may significantly mismatch the zero-lag low-pass filtering of

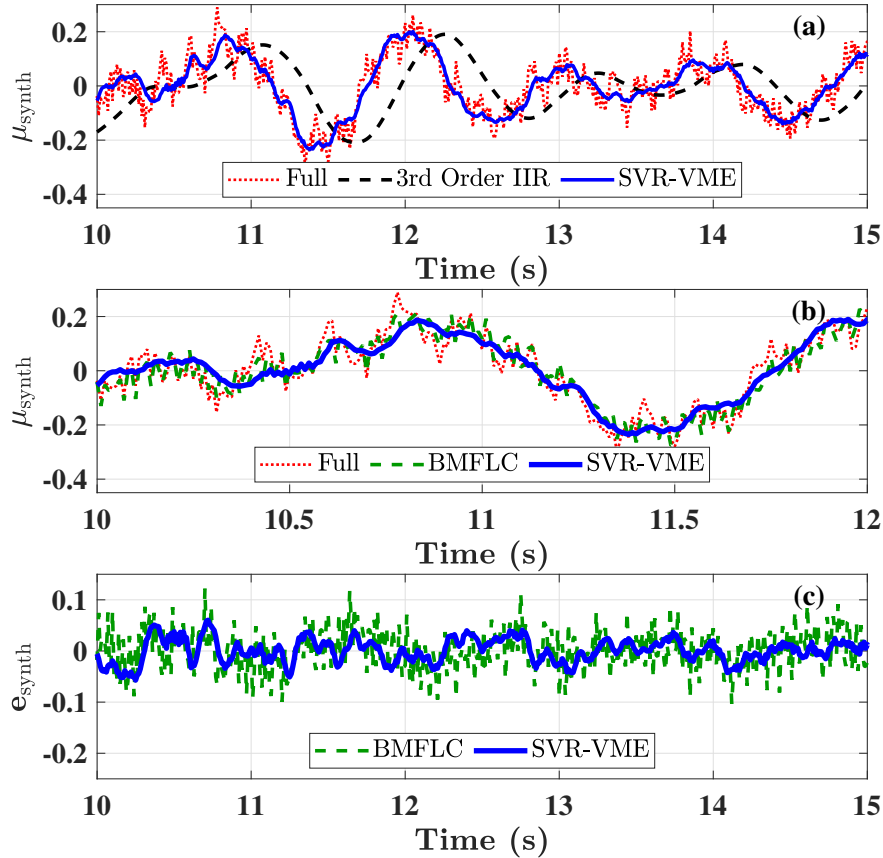


Figure 5.7: The performance of SVR-VME algorithm on a noise overlaid synthesized signal in comparison with IIR low-pass filter in (a), and KF-BMFLC in (b). The comparison of estimation errors between SVR-VME and KF-BMFLC algorithms are shown in (c).

the signals. Furthermore, we notice from Figs. 5.8(b, c) that larger  $m_{\text{lag}}$  can cause more delay in the response of transient behaviors. This matches with the analysis from Section 5.2.3, since larger input delay windows cause the kernel function in Eq. (5.16) to measure the pattern similarity based on more delayed states. In comparison, KF-BMFLC has a quicker response to transient behaviors, even though its estimation is also affected by these abrupt patterns. Therefore, the result suggests that motion signals with transient patterns are generally challenging for voluntary movement estimation.

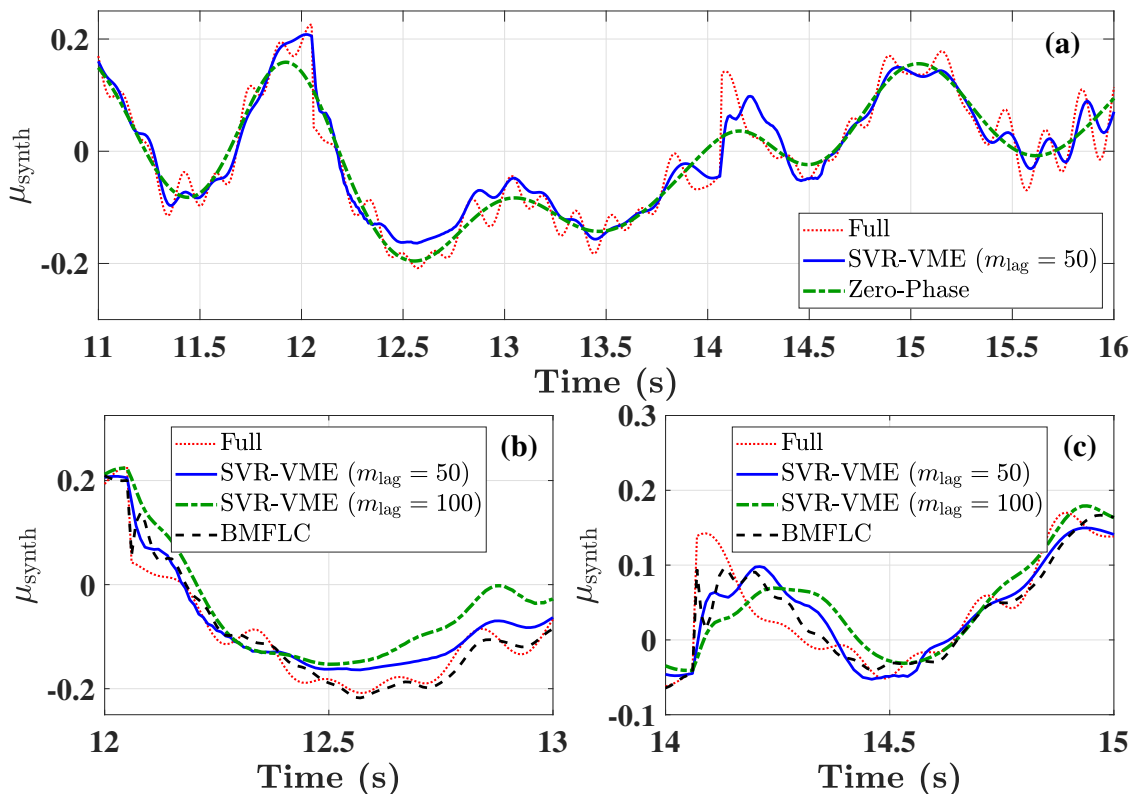


Figure 5.8: The performance of SVR-VME algorithm on synthesized signal in with transient behaviors [182]. Sub-figure (a) compares SVR-VME with IIR low-pass filter; Sub-figure (b) and (c) compare two SVR-VME algorithms of different input delay dimensions  $m_{\text{lag}}$  and KF-BMFLC from the zoomed-in views at  $t = 12$  s and  $t = 14$  s, respectively.

### 5.3.2 Experimental Tremor Movement Signals

The performance of SVR-VME is also tested on the experimental tremor movement measurements  $\mu_{\text{motus}}$ . As mentioned in Section 5.1, a total of five kinetic tremor movements measured in angular velocity are selected from the “Motus” data set. These measurements are also numerically integrated by time to obtain the tremor movement angular position. We then applied the VME algorithms on both normalized velocity and position measurements. Similar to Fig. 5.4, the quantitative comparison of estimation errors with respect to zero-lag low-pass filtering is shown in Fig. 5.9. In general, SVR-VME excels KF-BMFLC when estimating low-pass voluntary components from velocity measurements. This difference be-

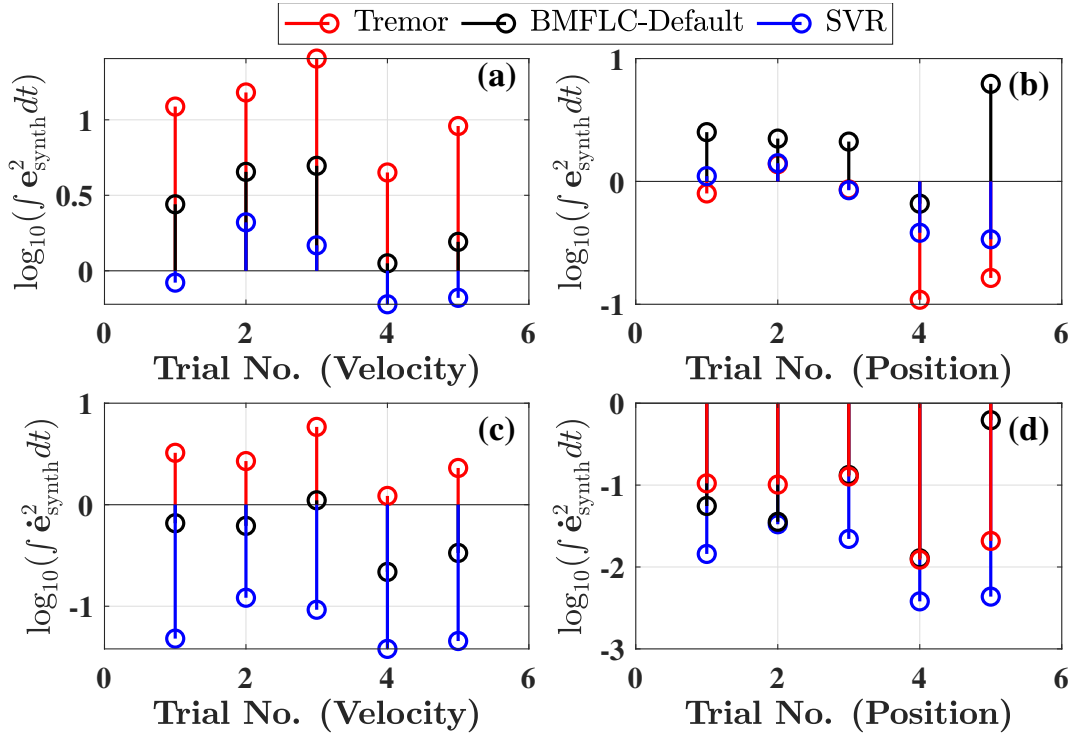


Figure 5.9: Quantitative comparison of errors towards zero-lag low-pass filtering from full measurement, SVR-VME estimations, and KF-BMFLC estimations in the cases of experimental tremor movement signals [182], where (a) and (b) shows the time integral of  $e_{\text{synth}}^2$  for 20 seconds; (c) and (d) show the time integral of  $\dot{e}_{\text{synth}}^2$  for 20 seconds; (a) and (c) are obtained from the velocity of the tremor movement; and (b) and (d) are obtained from the position of the tremor movement.

comes smaller in the cases of position measurements. Specifically, it is observed from Figs. 5.9(c, d) that SVR-VME yields reduced tremor elements in its estimations.

Figure 5.10 provides a detailed look into the performance of SVR-VME on Trial No. 1 from Fig. 5.9. From Fig. 5.10(a), it is easy to notice that the tremor elements are significantly reduced in the low-pass estimation from SVR-VME. Compared to 3rd-order IIR low-pass filtering, the estimation is not as smooth but has a much smaller delay. In Fig. 5.10(b), the estimation error from SVR-VME is smaller than that of KF-BMFLC. Similar performance can also be observed in Fig. 5.11, where the zero-lag low-pass estimation is carried out based on the position measurement. As shown in Fig. 5.11(a), high-frequency tremor elements from

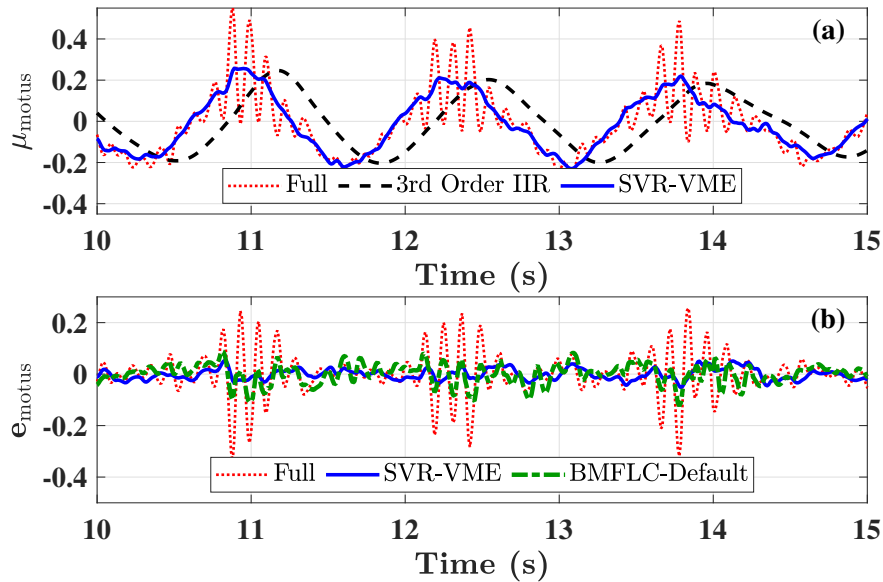


Figure 5.10: The performance of SVR-VME on experimental tremor movement angular velocity signal (Trial No. 1) [182] in comparison with IIR low-pass filter is shown in (a). The comparison of estimation errors between SVR-VME and KF-BMFLC is shown in (b).

position measurements are much smaller in amplitude compared to low-frequency voluntary movements. The estimation from SVR-VME can closely follow the measurement with little

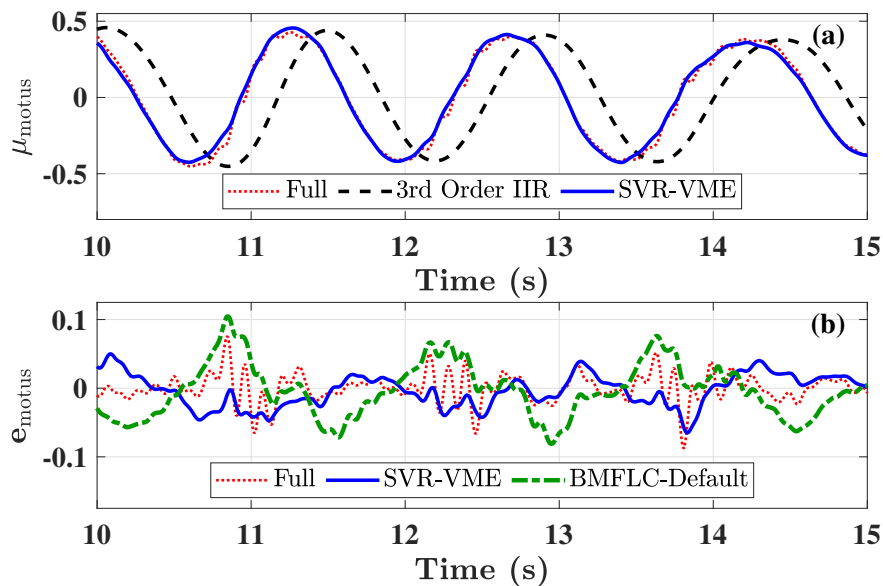


Figure 5.11: The performance of SVR-VME on experimental tremor movement angular position signal (Trial No. 1) [182]. The sub-figure descriptions are the same as in Fig. 5.10.

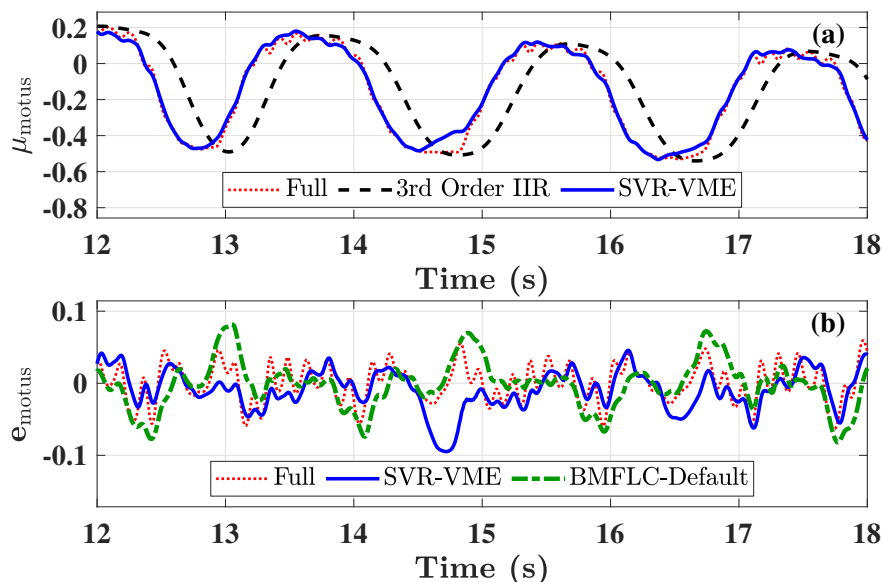


Figure 5.12: The performance of SVR-VME on experimental tremor movement angular position signal (Trial No. 2) [182]. The sub-figure descriptions are the same as in Fig. 5.10.

delay. Figure 5.11(b) shows the effort of SVR-VME in reducing tremor components from its estimations.

Experimental measurements can also pose challenges for SVR-VME. Here we examine Trial No. 2 from Fig. 5.9, where SVR-VME has the lowest performance. Figure 5.12 shows that, in the low-pass estimation of position measurement, SVR-VME fails to identify the signal pattern between  $t = 14.5$  s and  $t = 15$  s, which leads to a spike in estimation error. Therefore, SVR-VME may be limited to application scenarios that do not involve rapid changes of signal patterns.

In summary, the performance of SVR-VME is studied in comparison to other VME algorithms based on synthesized and experimental data. The results show that SVR-VME can significantly reduce tremor elements in its low-pass estimations with very little delay, and it possesses robustness towards a moderate level of noise. On the other hand, SVR-VME has limited performance when there are rapid or unprecedented movement signal patterns.

## 5.4 Summary

In this chapter, we discussed the estimation of voluntary movement from tremorous motion signals. We first examined the problem of voluntary movement filtering, and identified the limitations of existing approaches. In order to reduce the time delay in voluntary movement estimation, we propose a new real-time data-driven voluntary movement estimator based on least square support vector regression. By adopting the radial basis kernel function, SVR-VME models the relationship between the full motion signal and its low-pass filtered version in their time-delay domains based on pattern similarities, and uses the most recent motion data to estimate the low-passed voluntary movement with reduced delay. We also designed the algorithm so that the kernel matrix inverse can be recursively calculated, allowing the efficient update of the model based on the latest motion data in real time.

Numerical analyses are carried out to compare SVR-VME with existing voluntary movement filter methods (i.e., IIR digital low-pass filter and Kalman Filter with frequency-based models (BMFLC)) based on synthesized and experimental kinetic tremor data sets. The results show that SVR-VME can provide good estimations of low-frequency voluntary movement with significantly reduced delay. Compared to Kalman Filters with BMFLC, SVR-VME is less restricted by specific tremor frequency bands, and more robust against measurement noises. On the other hand, we also observe the limitation of SVR-VME in estimating voluntary movement from measurements with unprecedented transient signal patterns.

Finally, SVR-VME aims to provide minimal-delay tracking reference in the exoskeleton control system in user-guided operations. The complete control framework of TAWÉ is established based on the WKI algorithm in Chapter 3, the robust adaptive controller in Chapter 4, and the SVR-VME algorithm in this chapter. In the next chapter, we will discuss the prototyping of TAWÉ, control system integration, and experimental validations.

# Chapter 6

## Prototype, System Integration and Experiment

This chapter discusses the TAWÉ prototype, control system integration, and experimental validations. The studies in Chapters 2 to 5 have provided the theoretical foundations to realize the development of the TAWÉ prototype, whose purpose is to test the feasibility of exoskeleton mechanism, wearability, and hardware selections. The prototype of TAWÉ is realized with 3D printing, standard mechanical parts, and off-the-shelf mechatronics. We then performed preliminary mechanism and wearability tests of TAWÉ on a human subject (author of this dissertation).

The system integration includes the exoskeleton control software development and its interface with the TAWÉ hardware. We developed the control system of TAWÉ based on the ROS2 framework in the C++ environment [110]. The previously proposed algorithms from Chapters 3 to 5 are realized as modules of the control system. ROS2 provides efficient communications among modules, which allows us to perform real-time simulations and hardware interfaces.

Finally, the experimental validations are carried out based on the integrated system. To ensure safety, we performed experiments that involve mechanical loading on a forearm mannequin with an actuated 2-DOF robotic wrist [44]. We partially validated the proposed control framework with a focus on real-time SVR-VME and passive tremor suppression

based on impedance. Experimental validations also identified problems in the current TAWE prototype and control framework, which require solutions in future investigations.

The rest of the chapter is arranged as follows. Section 6.1 introduces the design of the TAWE prototype, and demonstrates its mechanism and wearability through tests on a human subject. We then discuss the control software development of TAWE and real-time simulations of the exoskeleton control system in Section 6.2. The experiments that partially validated TAWE and its control system is explained in Section 6.3. Finally, Section 6.4 summarizes the findings in this chapter. (The study in this chapter has been partially reported in [182].)

## 6.1 Prototype of TAWE

This section discusses the prototype of TAWE, the finalized design of TAWE is shown in Fig. 6.1. The prototyping of this design is fully based on 3D Printing (PLA), standard mechanical parts (screws, bearings, etc.), and off-the-shelf mechatronics. The final design of TAWE excluding battery and passive linkage weighs 315 grams, which is approximately 20% lighter than the conceptual design in Fig. 2.2.

### 6.1.1 Design Updates

A few changes are made in the finalized TAWE design when compared to the preliminary design in Fig. 2.2. For the appearance, the position of the servomotors has been re-positioned from the radial side to the dorsal side of the forearm. This allows the better arrangement of the mechanism and COM distribution. In addition to the active 6-DOF rigid linkage mechanism at the wrist, a 6-DOF passive linkage mechanism is also added that bridges the components on the proximal and distal ends of the forearm. This linkage provides additional

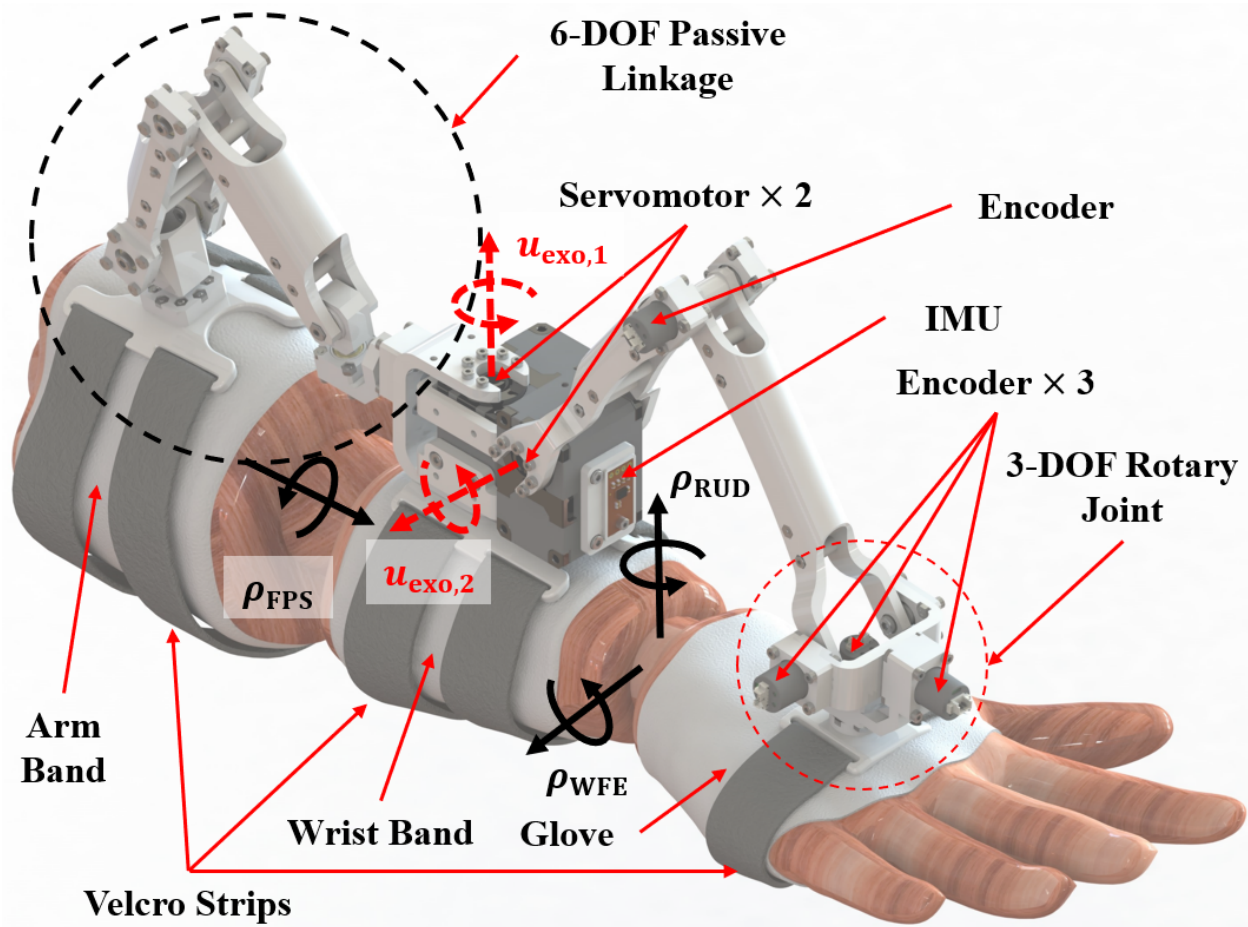


Figure 6.1: The finalized design of the TAWExo Prototype on a right human forearm, where the main design components, directions of forearm movements, and directions of exoskeleton inputs are marked.

wearability support and helps with the organized wiring for the electronics. Similar to the active 6-DOF rigid linkages, the passive linkage mechanism allows unconstrained natural forearm pronation and supination (FPS) motions.

In practice, the IMU of TAWExo is not able to provide accurate 3-DOF orientation measurements due to the magnetic field reading interference in the magnetometer caused by the servomotors. On the other hand, the gyroscopic sensor (for angular velocity) and accelerometer (for acceleration) are unaffected. Hence, absolute encoders are installed on all active rigid linkage joints to provide the full measurement of relative rotation and translational dis-

placement between the distal forearm and hand dorsum ( $\xi_{a,\text{end}}$  and  $\mathbf{d}_{a,\text{end}}$  from Eq. (3.10)), which allows the identification of wrist kinematics as discussed in Section 3.2. We keep one IMU in the design, which measures the tilting of the exoskeleton system around the horizontal axes of the global frame based on the sensor fusion of the gyroscopic sensor and accelerometer.

Finally, a practical concern is raised due to the numerous sensors and actuators in this design. There exists approximately 25 cables/wires (18 from encoders, 4 from the IMU, and 3 from the servomotors) extending to different locations throughout the assembly. Without careful design, the cables can entangle with the exoskeleton mechanism and forearm, restricting their movements and posing potential health risks. Therefore, we designed the linkage parts in both the passive and active mechanisms so that they provide a channel for the wires to go through. All cables and wires are collected and organized along the rigid linkage mechanisms, and exit from the passive linkage to connect with the microcontrollers and drivers.

### 6.1.2 Mechanism and Wearability

We test the mechanism and wearability of the TAWE prototype on a subject (author of this dissertation). In the following test, the exoskeleton is not powered, and the wiring of the sensors is not included. TAWE equipped on the right forearm viewed from different directions is presented in Fig. 6.2. The pose of the forearm and wrist in this view is referred to as the nominal pose (where WFE rotation  $\rho_{\text{WFE}} = 0$  and RUD rotation  $\rho_{\text{RUD}} = 0$ ) hereinafter. Notice that TAWE is attached to the user forearm on three spots - the distal end of the forearm (around the elbow), the proximal end of the forearm, and the dorsum of the hand. While the Velcro strips, arm bands, and gloves help with the easy donning and doffing of TAWE, attaching the device at three different locations can still be difficult for

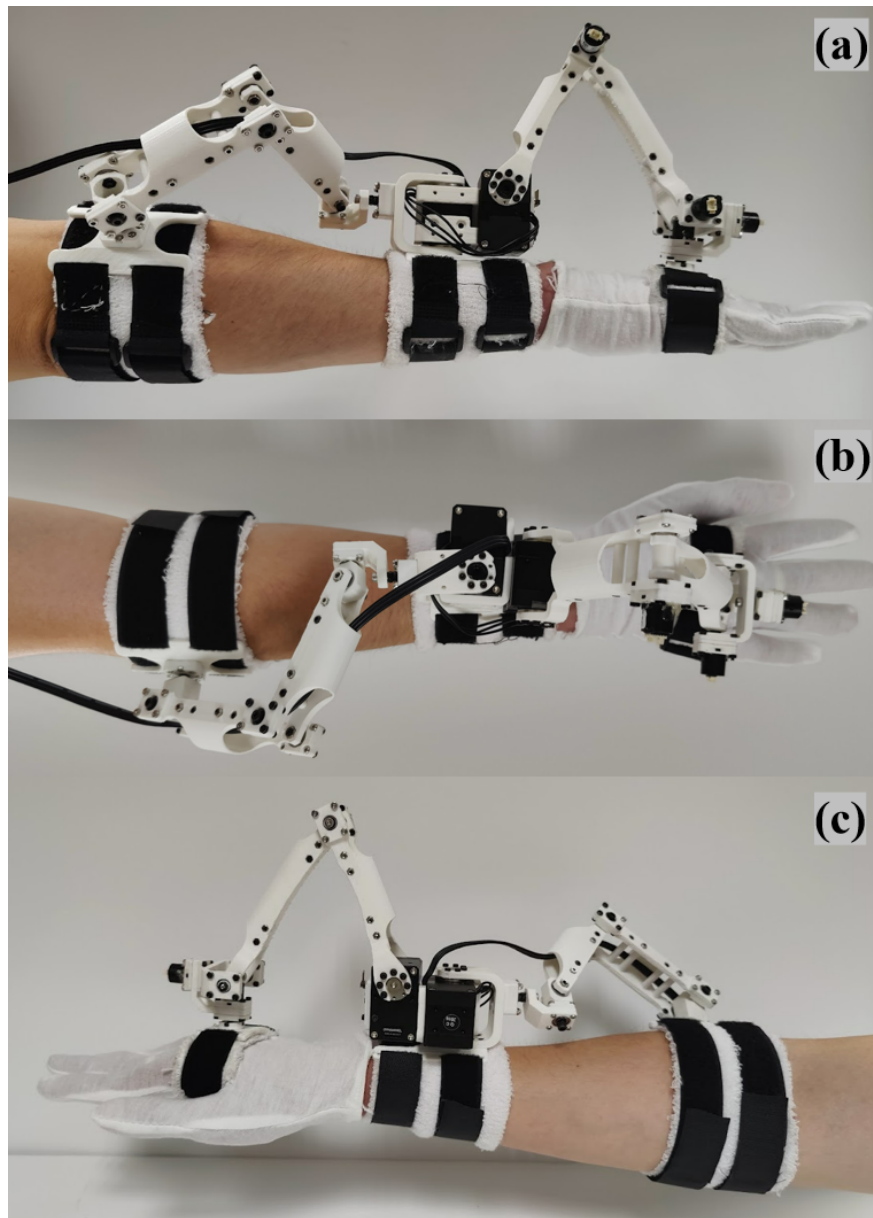


Figure 6.2: The views of the TAWA Prototype attached to the right forearm of a subject (author of this dissertation) from different directions ((a): ulnar, (b): dorsal, and (c): radial), where the wiring of the electronics are not included.

people with limited manipulability. On average, it takes around 40 seconds for the user to fully equip TAWA on the forearm.

The mechanism of the exoskeleton should not be in physical contact with the user body. At

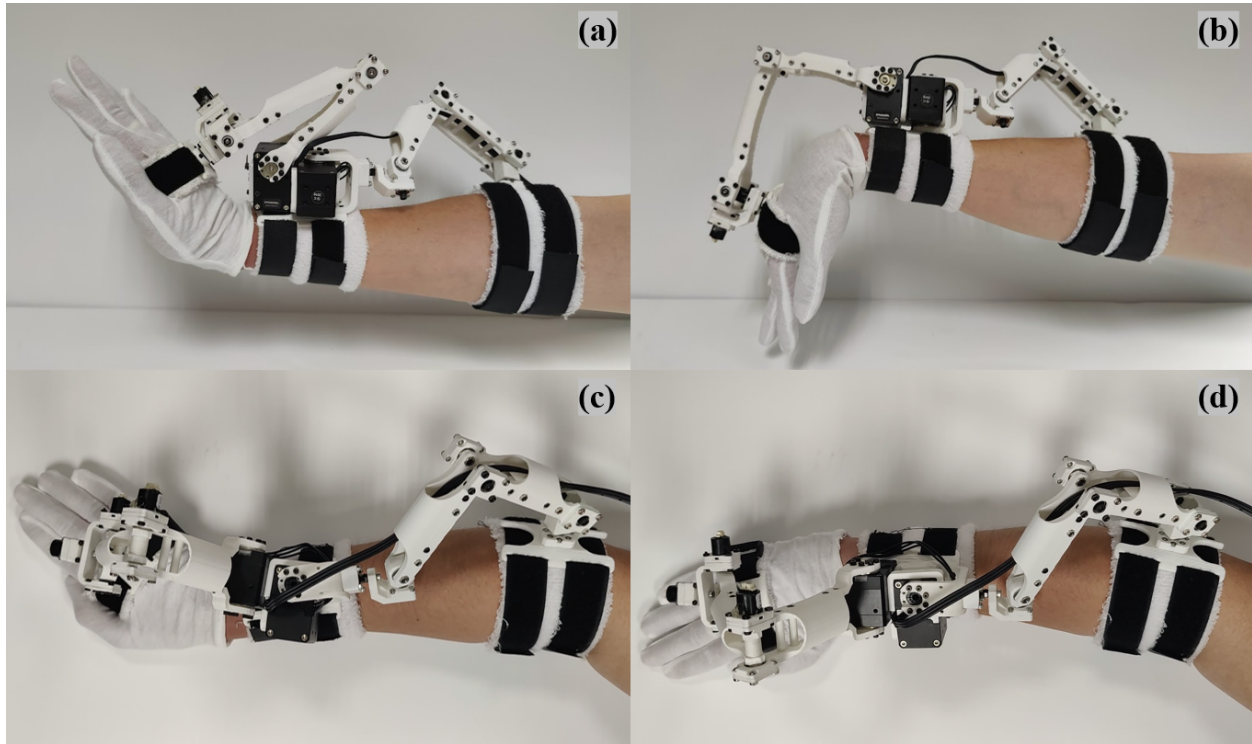


Figure 6.3: The mechanism of TAWE at different natural and unforced wrist poses performed by the subject in Fig. 6.2, where (a) shows the wrist extension at approximately 50 degrees, (b) shows the wrist flexion at approximately 85 degrees, (c) shows the wrist ulnar deviation at approximately 30 degrees, and (d) shows the wrist radial deviation at approximately 15 degrees.

the nominal pose, it can be observed that sufficient clearance exists between the exoskeleton and the forearm. On the other hand, the retraction of the rigid linkage mechanism also causes the exoskeleton parts to significantly extrude in the dorsal direction. This is a potential drawback when TAWE is used in daily activities, since the exoskeleton may be in contact with other body parts and prevent certain movements.

The exoskeleton mechanism is then tested by performing different wrist poses as shown in Fig. 6.3. We observe that the mechanism of TAWE can support both natural WFE and RUD movement, which agrees with the design analysis in Chapter 2. The range of motion of TAWE also covers the wrist circumduction envelope [141], which allows unconstrained

coupled WFE and RUD movements. The feasibility of reaching extreme wrist flexion and extension (approximately 90 degrees for both) is determined by the geometry of both the TAWE mechanism and the user forearm. As shown in Figs. 6.3(a, b), the current rigid linkage mechanism design support extreme wrist flexion by the subject, but failed to allow extreme wrist extension due to the collision of parts. This situation may not appear on other

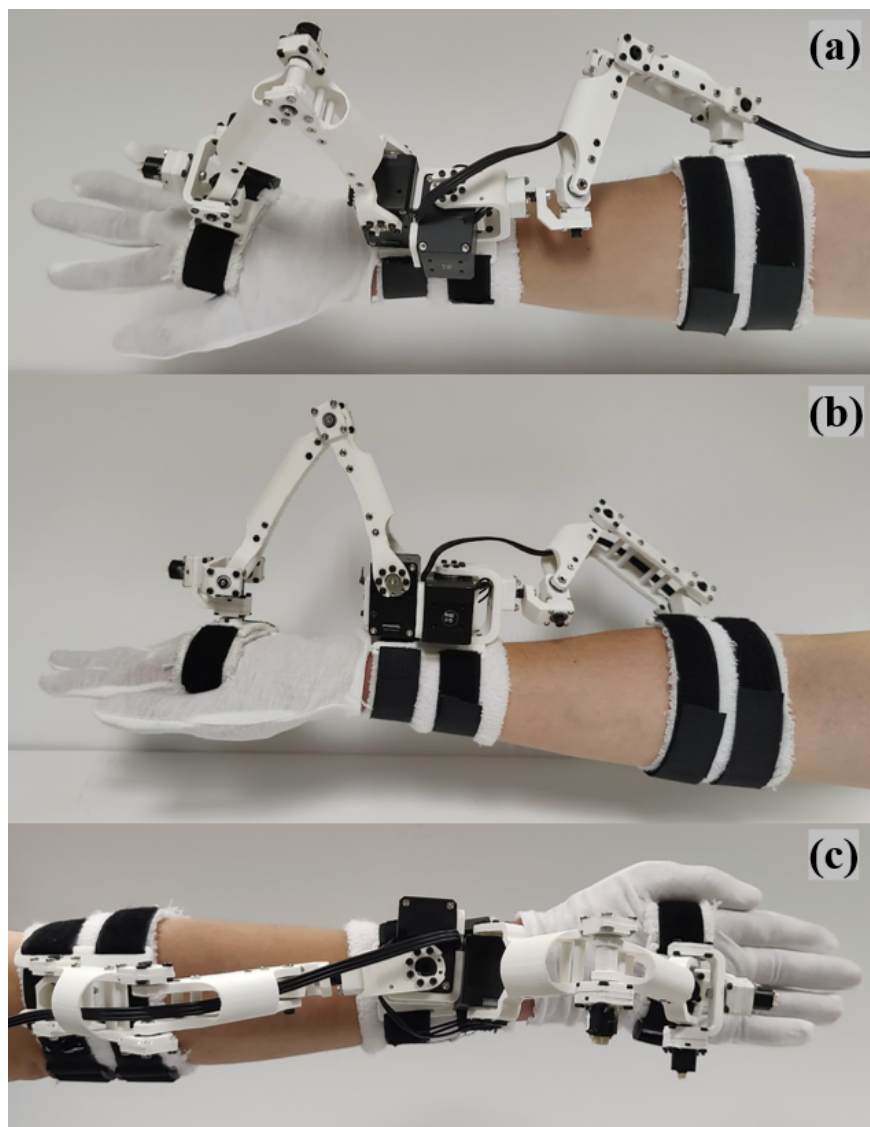


Figure 6.4: The passive linkages of TAWE at different natural forearm rotation poses performed by the subject in Fig. 6.2, where (a) shows pronation, (b) shows the nominal pose, and (c) shows the supination.

users with different forearm profiles. This limitation indicates the importance of easy design customizability so that the exoskeleton is suitable for different users.

Later, we examine the passive linkage mechanism, which is designed to improve the stability of wearability and routing of cables. The forearm pronation-supination movement occurs between the proximal and distal attachment locations of TAWE on the forearm. The passive linkage mechanism at different FPS rotations is shown in Fig. 6.4. It is noticed that, with the 6-DOF mechanism, the passive linkages support the full range of pronation and supination. Since the total combined distance along all linkages of both passive and active exoskeleton mechanisms is approximately constant, the cable and wires going through these mechanisms will not be significantly stretched or twisted. The passive 6-DOF mechanism also proposes a potential solution to extend the exoskeleton for tremor suppression in the FPS motion as future investigation.

When performing different wrist and forearm movements, the subject experience encumbrance due to both the stretching of the upper limb and the weight of the exoskeleton. Muscle fatigue due to encumbrance is mainly experienced in the upper arm and the shoulder, while fatigue in the forearm is insignificant. This result implies that the exoskeleton at the distal end of the limb will more or less increase the burden at the proximal ends. Therefore, TAWE should be further optimized in terms of weights and center of mass distributions.

In summary, the mechanical design of TAWE meets the expectation from the design considerations in Section 2.1.1. The current TAWE is ergonomic in terms of supporting natural forearm movements and non-fixing wearability features. The mechanism and wearability tests also revealed a few limitations. The prototype of TAWE can be further improved in donning-and-doffing simplicity, dimension customizability, and design weight for better ergonomics.

## 6.2 Control System Integration

This section discusses the exoskeleton control system integration. The complete exoskeleton control framework is shown in Fig. 6.5. This framework combines the findings from Chapters 3 to 5. As a review of the framework, TAWÉ measures the states of the human-exoskeleton multibody system in Eq. (2.42) (or equivalently Eq. (4.3)). After filtering and fusing the sensor data, we obtain the measurements of the generalized coordinate  $\mathbf{q}$  and nonholonomic state  $\boldsymbol{\rho}$ . The wrist kinematic identification process from Chapters 3 can be directly carried out based on the measurements. The identified closed kinematic chain in the human-exoskeleton model allows us to formulate the control system in Eq. (4.18) as discussed in Section 4.3. The control system output  $\mathbf{y}$  is then fed into the SVR-VME from Chapter 5 to extract the low-frequency voluntary movements as the tracking reference  $\mathbf{r}_y$  for exoskeleton control. The calculated tracking error  $\boldsymbol{\epsilon}$  is used in the robust adaptive controller in Eq. (4.36), which generated the TAWÉ motor control input  $\mathbf{u}_{\text{exo}}$ . Finally, the exoskeleton and user inputs simultaneously affect the human exoskeleton dynamics. Tremor excitations from the base and forearm muscles are treated as model uncertainties in the human-TAWÉ multibody dynamics.

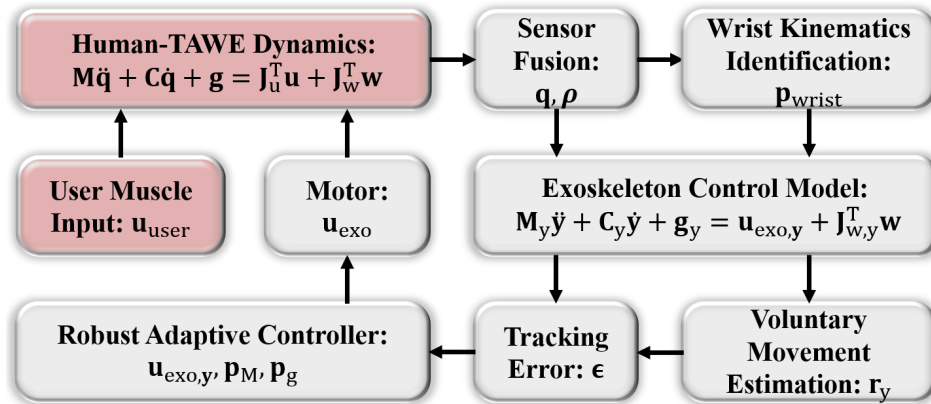


Figure 6.5: The full control framework of TAWÉ, where the pink blocks indicate that the knowledge of the models is not fully known.

### 6.2.1 Mechatronic System of TAWE

The mechatronic system of TAWE is shown in Fig. 6.6, where the control software in Linux machine (`debian` operating system) interfaces with the actuators and sensors through the peripheral electronic components, i.e., motor controller and microcontrollers. The servomotors (Dynamixel XM430 Series) adopted in the design of TAWE come with integrated motor drivers within their casings. The peripheral unit for the communication between the Linux machine and the motor driver is a USB communication converter (U2D2). The motor interface on the Linux machine is designed using the official software development kit library.

A microcontroller (Teensy 4.0 based on Cortex-M7 600 MHz processor) is used for data collection from encoders and IMU. The joint angles from the absolute encoders (US Digital MAE3) are transferred as 12-bit Pulse Width Modulation (PWM) digital signals at 250 Hz. The reading and conversion of PWM signals are realized using digital pin interrupt utilities in the microcontroller. The communication between the IMU (LSM9DS1) and the microcontroller is established based on the I2C protocol at 238 Hz. The microcontroller firmware is designed so that it can stably collect all sensor data without interrupt contention, and transfer them to the Linux machine. The microcontroller interface on the Linux machine is developed based on `ttyUSB` utilities native to `debian` kernel.

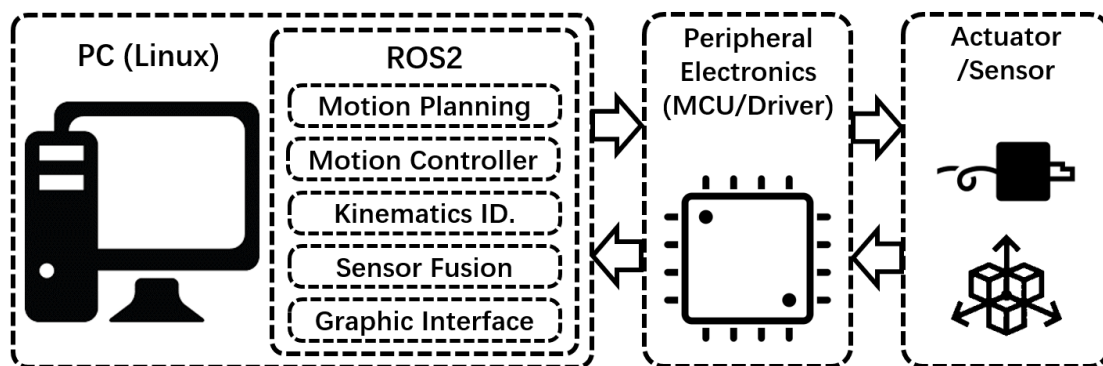


Figure 6.6: The mechatronic system of TAWE.

## 6.2.2 Control Software on ROS2

The TAWE control software is developed in the ROS2 framework [110], which is based on the Data-Distribution Service (DDS) middleware that supports real-time efficient communications between control modules (nodes in the distributed network). The architecture of TAWE control software in ROS2 is presented in Fig. 6.7. In this framework, each block indicates of control module consists of one or multiple ROS2 nodes that realize the algorithms proposed in Chapters 3 to 5 (i.e., WKI, IO-RAC, and SVR-VME).

All algorithms in the TAWE control system are reprogrammed in the C++14 environment to ensure numerical efficiency. The analytical models of human-exoskeleton dynamics and WKI are generated from MATLAB into C++ libraries using MATLAB Coder. To ensure

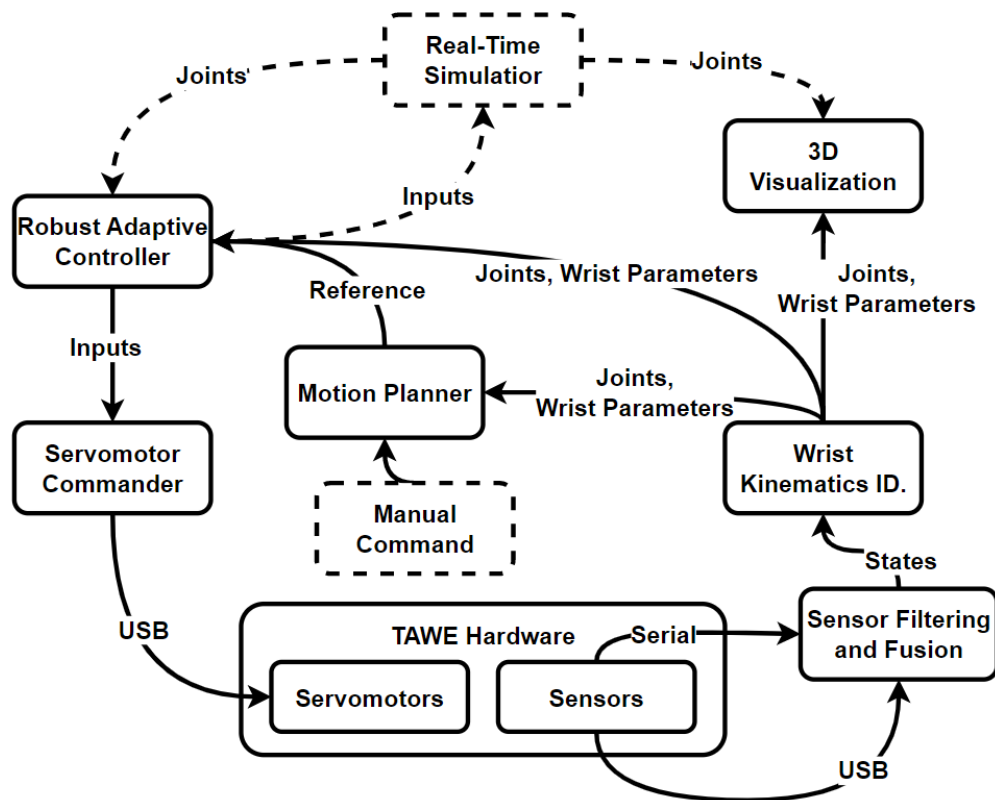


Figure 6.7: The architecture of TAWE control software in ROS2, where the dash-lined blocks and arrows indicate modules used in real-time simulations only.

convenient adaptation of the generated codes into the ROS2 framework. We developed a utility library based on object-oriented design, which includes generic frameworks for robot dynamics simulator, EKF, model-based robotic controller (featuring IO-RAC), and SVR-VME. The utility library also includes common-use toolboxes for linear algebra, digital filters, and serial message encryption. Therefore, the utility library can be applied to not only TAWÉ but also other robotic projects.

For safety considerations, the control modules in the ROS2 network operates based on their hierarchy in the control framework from Fig. 6.5. As an example, IO-RAC requires messages from its upstream modules such as WKI and SVR-VME to function. The IO-RAC module should pause if its communication with the upstream modules abruptly stops. Hence, we designed the operation of control modules based on the availability of upstream communication, which ensures that undesired control behaviors will not be caused by any communication failures or control module malfunctions.

Finally, ROS2 also supports real-time simulations and visualizations. We simulate the human-exoskeleton dynamics based on the generated ODE model from MATLAB. The fixed-

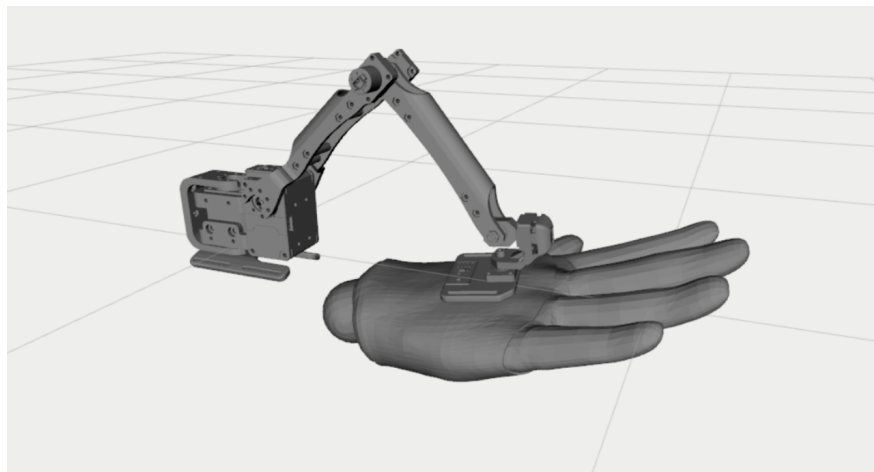


Figure 6.8: Visualization of TAWÉ in Rviz from ROS2, which shows the active 6-DOF linkage mechanism, and the relative position of the hand with respect to the exoskeleton. The forearm and passive linkages in TAWÉ are hidden.

step numerical integration is calculated by Runge-Kutta 4th method. ROS2 can stably simulate the human-exoskeleton dynamics at 1 kHz along with a full control system running at 250 Hz (single-core performance on 4.0 GHz Intel CPUs). The real-time visualization of TAWE can assist in the troubleshooting of both exoskeleton hardware and software, and provide direct observation of the control system performance in sensor fusion, WKI, and tremor suppression.

### 6.2.3 Real-Time Exoskeleton Control Simulation

We carried out the real-time simulation of TAWE in active tremor suppression, which provides insights into the performance of the full control system where the previously proposed

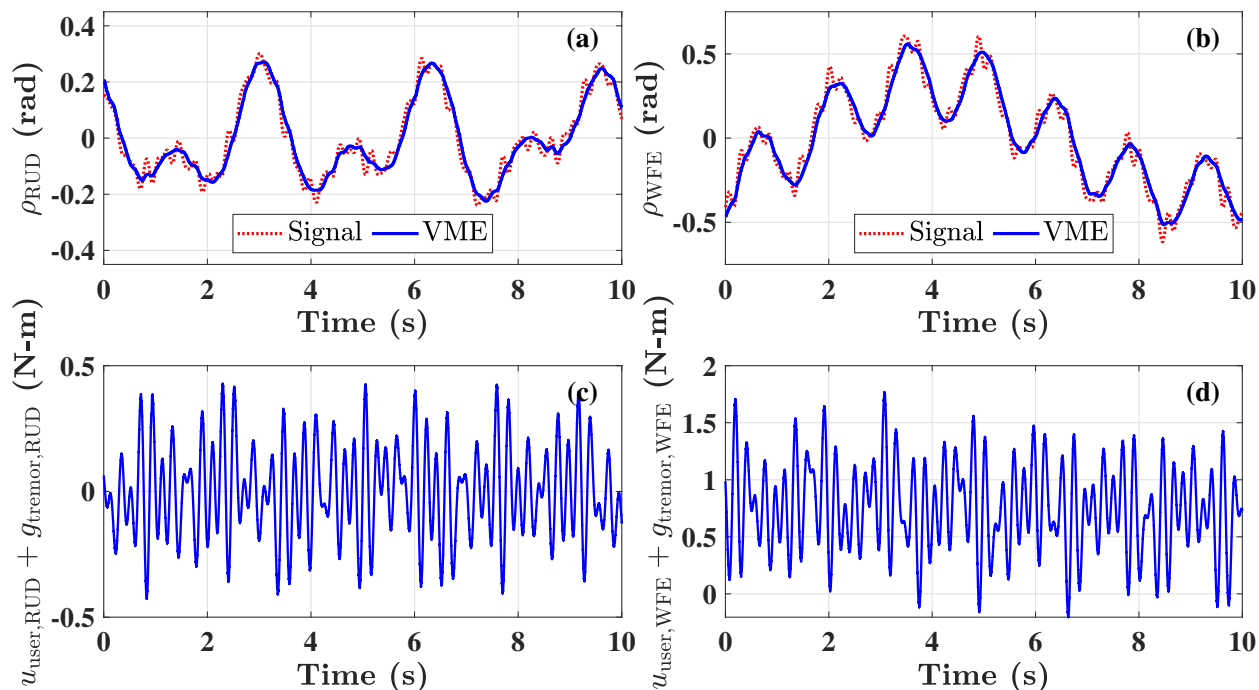


Figure 6.9: Real-time simulation of the human-TAWE system actuated by user control input with fixed-frequency tremor excitation, where (a, b) respectively show the tremorous movement in RUD and WFE with the voluntary component estimated by SVR-VME, and (c, d) show the generalized user control input in RUD and WFE, respectively.

algorithms are executed together. In the simulation, the user control input  $\mathbf{u}_{\text{user}}$  from Fig. 6.5 is emulated by the PID controller from Eq. (4.15), which follows a quasiperiodic reference trajectory. The user control input is then overlaid by tremor excitations  $\gg_{\text{tremor}}$  with three frequency components for each DOF, which range from 3 - 6 Hz and are assumed to be unknown. Since the control system also involves the filtering and fusion of sensor measurements, we also emulated random sensor noises that match the TAWE hardware design to increase the fidelity and challenge in exoskeleton control simulation. The system response without exoskeleton input is shown in 6.9, where the wrist movements in RUD and WFE are estimated by the WKI algorithm. Observe from Figs. 6.9(a, b) that SVR-VME provided good estimations of voluntary movements with little delays. The user excitations in Figs. 6.9(c, d) are mainly composed of tremor elements. Since the user control input also needs to compensate for the gravitational load, the mean value of WFE excitation is around 1 N-m. The exoskeleton controller follows the IO-RAC controller formulation in Eq. (4.36) for active tremor compensation. A BMFLC model with 121 harmonic components uniformly ranging from 3-6 Hz is adopted as the adaptive model for each DOF of the exoskeleton control input. It should be noted that since the tremor excitation frequencies are quasiperiodic, they do not coincide with any particular harmonic components from the BMFLC model. The active suppression of tremor with fixed-frequency harmonic components is shown in Fig. 6.10. It can be observed from Figs. 6.10(a, b) that after the exoskeleton is turned on, the adaptive controller can slowly identify and compensate tremors, reducing their oscillation amplitudes. In Figs. 6.10(c, d), the tremor oscillations come back once the exoskeleton is turned off. These results show the effectiveness of active tremor suppression. It should also be noted that with the reduction of tremor, the VME result can also become smoother since the voluntary component has become more significant in the movement signal. Finally, Figs. 6.10(e, f) shows that the maximum exoskeleton control inputs are approximately 1 N-m,

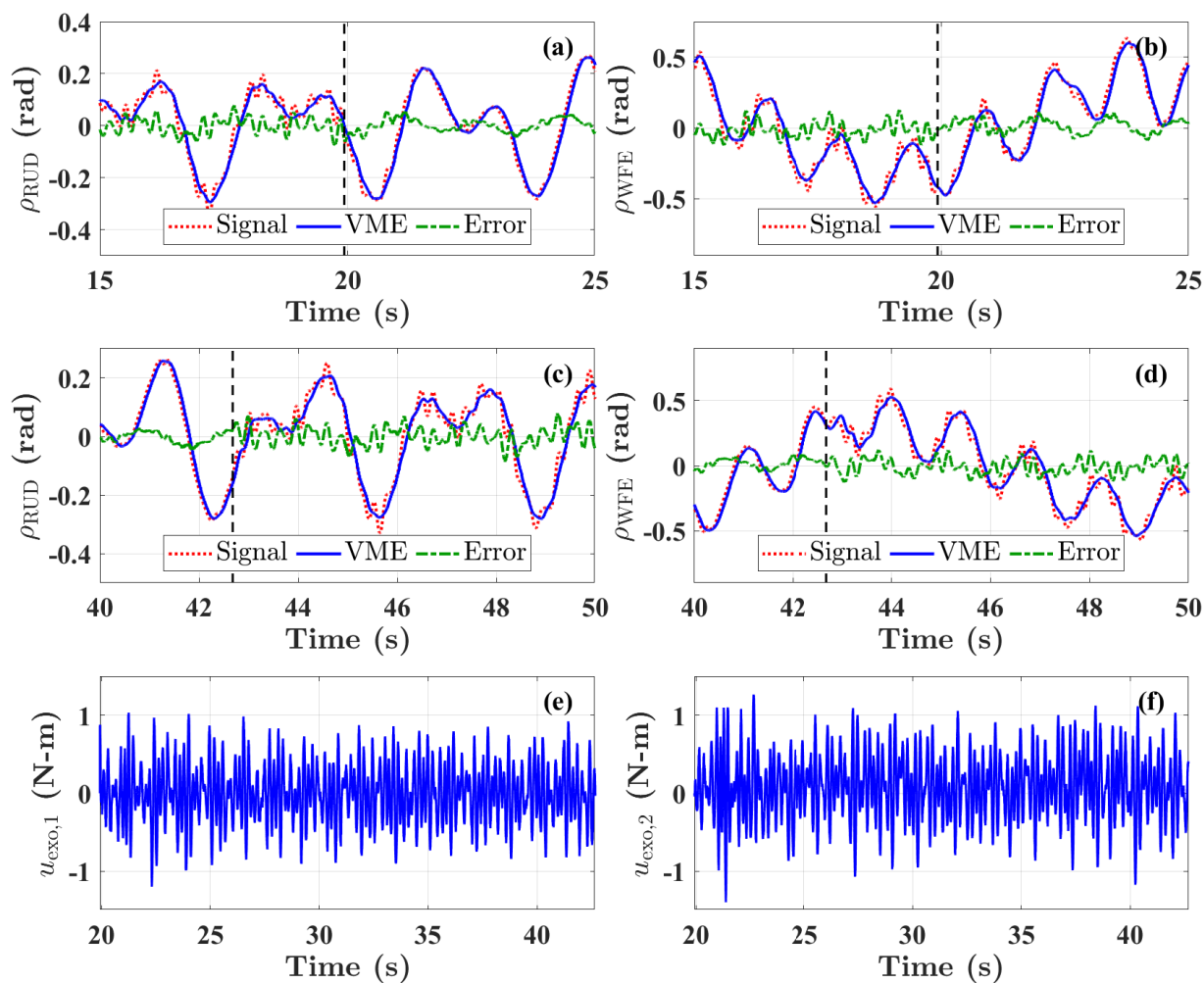


Figure 6.10: Real-time simulation of TAWC on active suppression of tremor with fixed-frequency harmonic components [182], where (a, c) and (b, d) show the tremor suppression in wrist RUD and WFE movements, respectively; the vertical black dash lines in (a, b) and (c, d) indicate the exoskeleton being turned on and off, respectively; and (e, f) show the exoskeleton control inputs.

which is within the capacity of the servomotors.

We then tested the performance of the TAWC control system on active suppression of tremors with varying-frequency harmonic components. In this case, two of the three tremor harmonic components for each DOF have periodically "sweeping" frequency within a small bandwidth

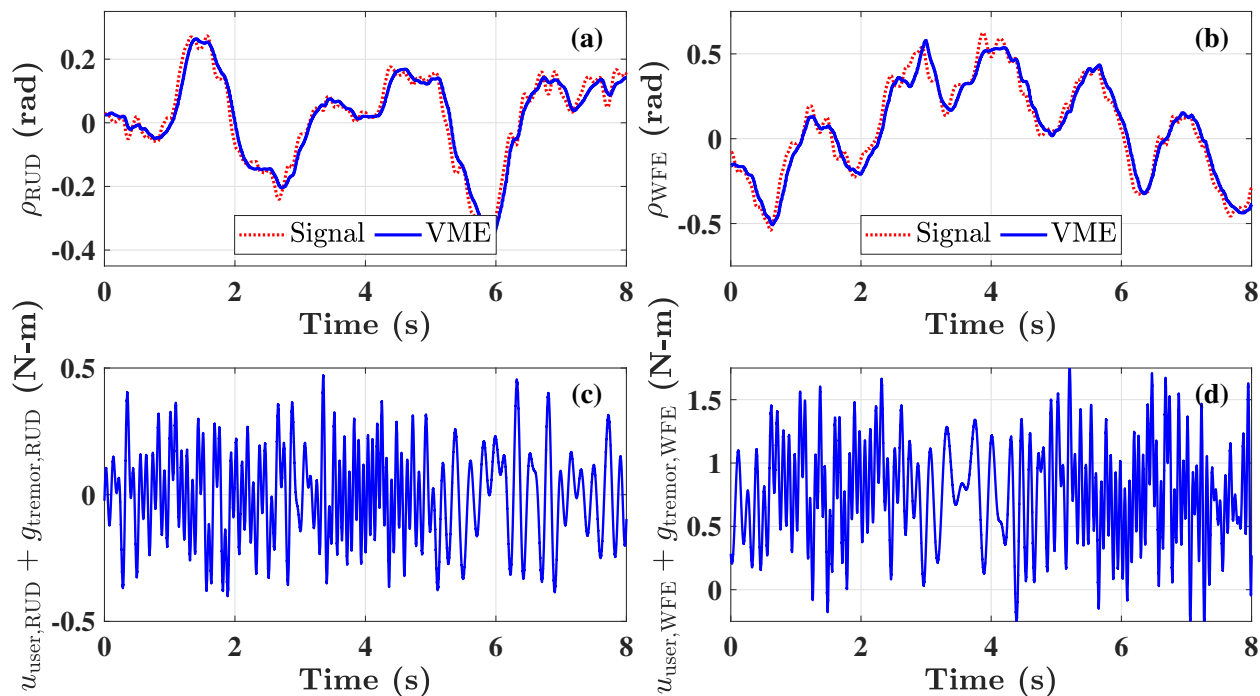


Figure 6.11: Real-time simulation of the human-TAWE system actuated by user control input with fixed-frequency tremor excitation, where the subfigure descriptions are the same as those in Fig. 6.9.

near their original values, so that the frequency bands from harmonic components do not intersect. As shown in Fig. 6.11, with the varying frequencies, the tremor excitation can significantly distort the voluntary components, and make the full movements non-periodic. The distortion of voluntary movement also results in SVR-VME not being able to effectively identify the signal pattern, which leads to less smooth estimated trajectories that contain more tremor components.

The real-time simulation results of TAWE on active suppression of tremor with varying-frequency harmonic components are shown in Fig. 6.12. Both the adaptive controller and SVR-VME are less effective in this simulation due to the varying frequencies of tremors. This is noticed from Figs. 6.12(a - d), where the residue tremors during active tremor suppression are larger. Since the observation of tremor amplitude spectrums from Section 4.1 indicate

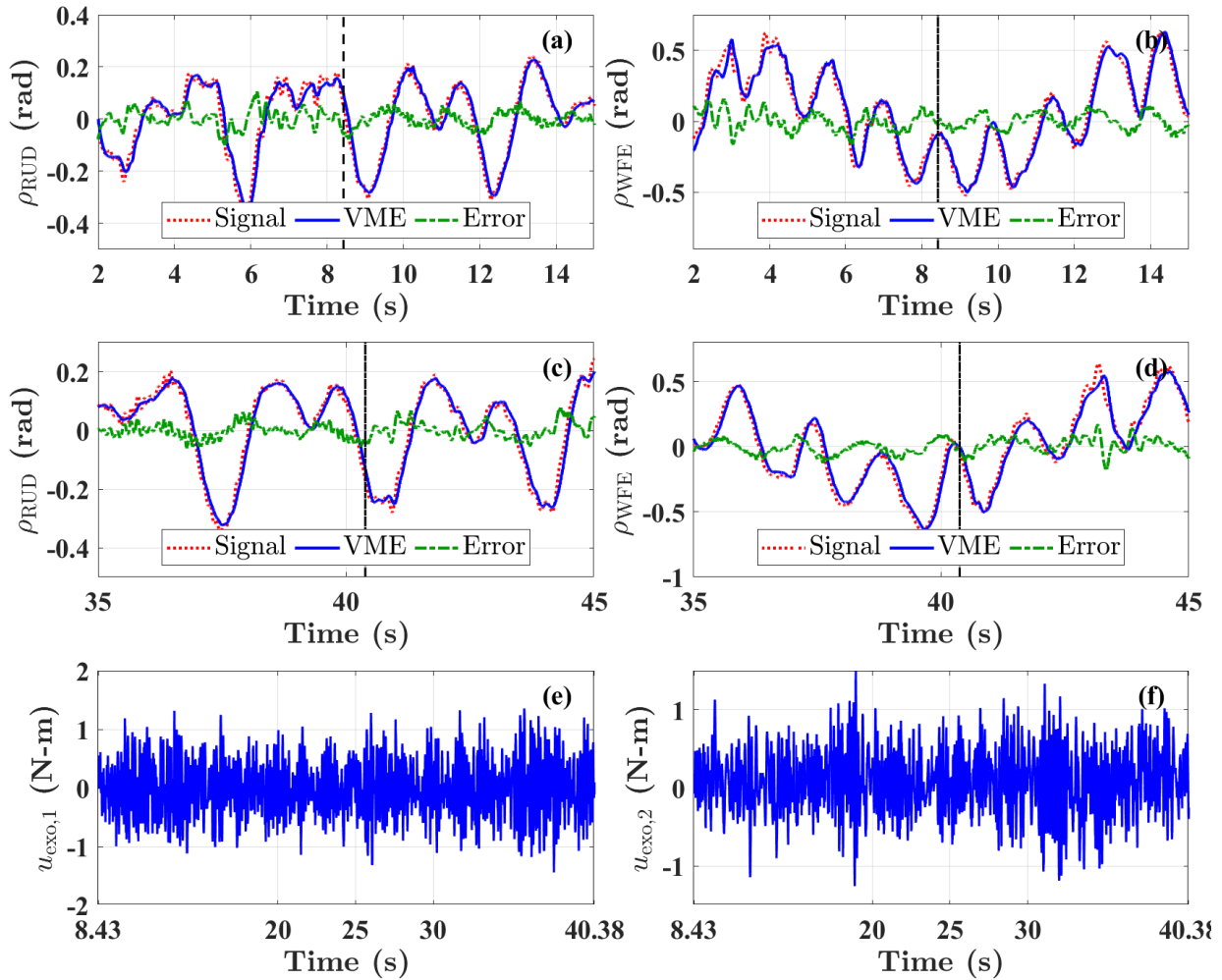


Figure 6.12: Real-time simulation of TAWE on active suppression of tremor with varying-frequency harmonic components [182], where the subfigure descriptions are the same as those in Fig. 6.10.

the possible existence of frequency shifts, these results suggest the need to further improve the proposed active tremor suppression and voluntary movement estimation methods.

In summary, the above simulations show that it is feasible to integrate the WKI, IO-RAC, and SVR-VME algorithms into the exoskeleton control framework. The results also show that the control system efficiently performs in real-time, suppresses fixed-frequency tremor components in wrist movements, and follows user-guided movements. On the other hand,

existing methods are less effective when the tremor has varying frequencies, which requires improvement in future investigations.

## 6.3 Experimental Validations

This section presents the experiments carried out on the TAWÉ prototype, where we partially validated the control framework with a focus on real-time SVR-VME and passive tremor suppression based on impedance.

### 6.3.1 Voluntary Movement Estimation from Real-Time Data

We tested the performance of SVR-VME on real-time experimental movement data collected by the TAWÉ prototype. The experimental setup is shown in Fig. 6.13, where TAWÉ

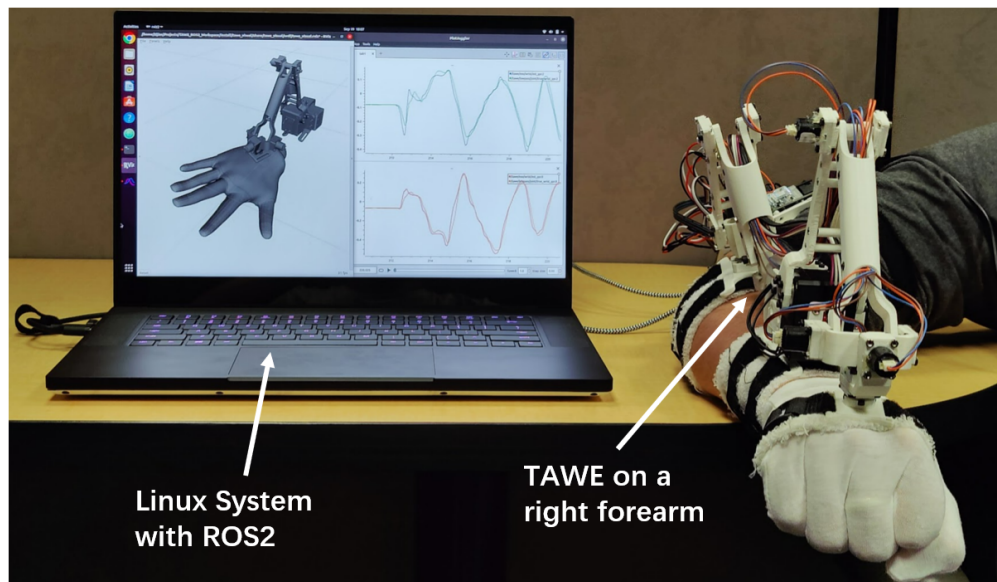


Figure 6.13: Experimental setup for real-time movement data collection using TAWÉ [182], where the measurement and voluntary movement estimation are visualized by ROS2 on the Linux machine.

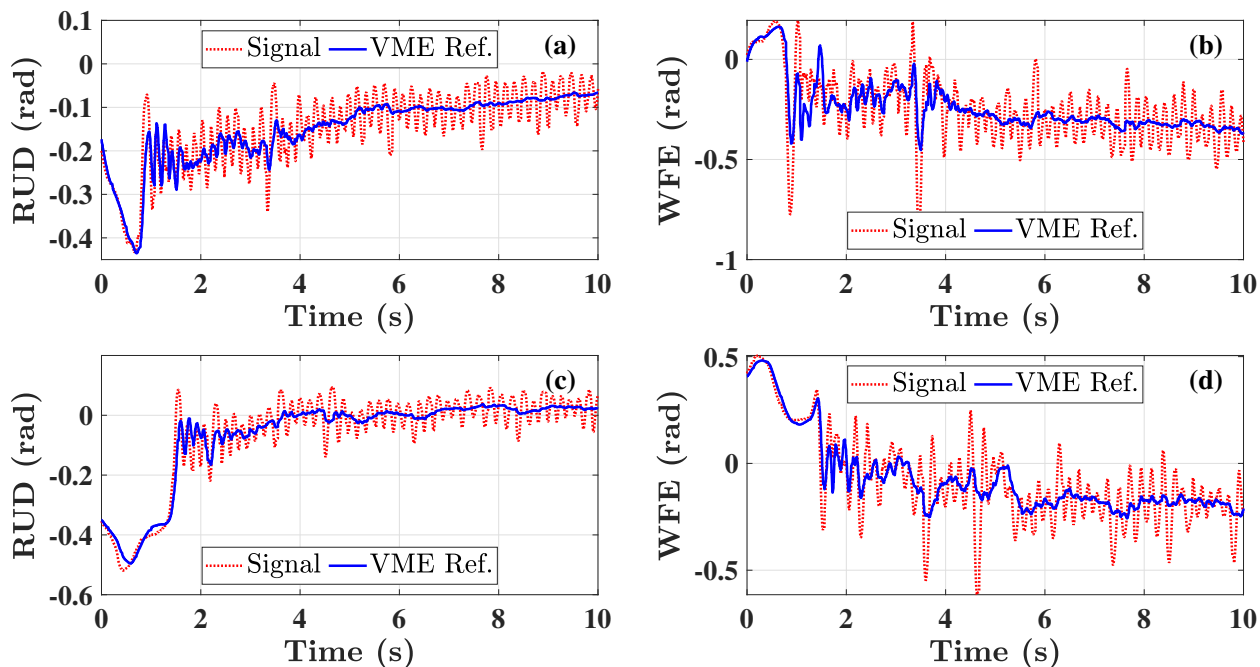


Figure 6.14: Real-time performance of SVR-VME on wrist movements with intentional tremors oscillations shown in two sets of experimental results [182], where (a, b) compare the WFE and RUD measurements with their estimated voluntary movements from result #1, and (c, d) compare those from result #2.

equipped on the right forearm measured the kinematic movement of the wrist. The real-time motion signals are processed by WKI, and the outputs of SVR-VME are visualized on the Linux machine. During data collection, a health subject (author of this dissertation) performed two types of random movements - smooth wrist movement and tremorous movement from intentional excitation (at approximately 6 Hz). It should also be noted that tremor suppression from TAWA is not active in this experiment.

The real-time performance of SVR-VME on the experimental tremorous motion data is shown in Fig. 6.14. In all subfigures, the intentional tremors were triggered abruptly from the original smooth wrist movements. We notice that SVR-VME can effectively filter the tremor elements in the signal. The outcomes of SVR-VME also have small delays and are robust against tremors with varying amplitudes. On the other hand, since the movements

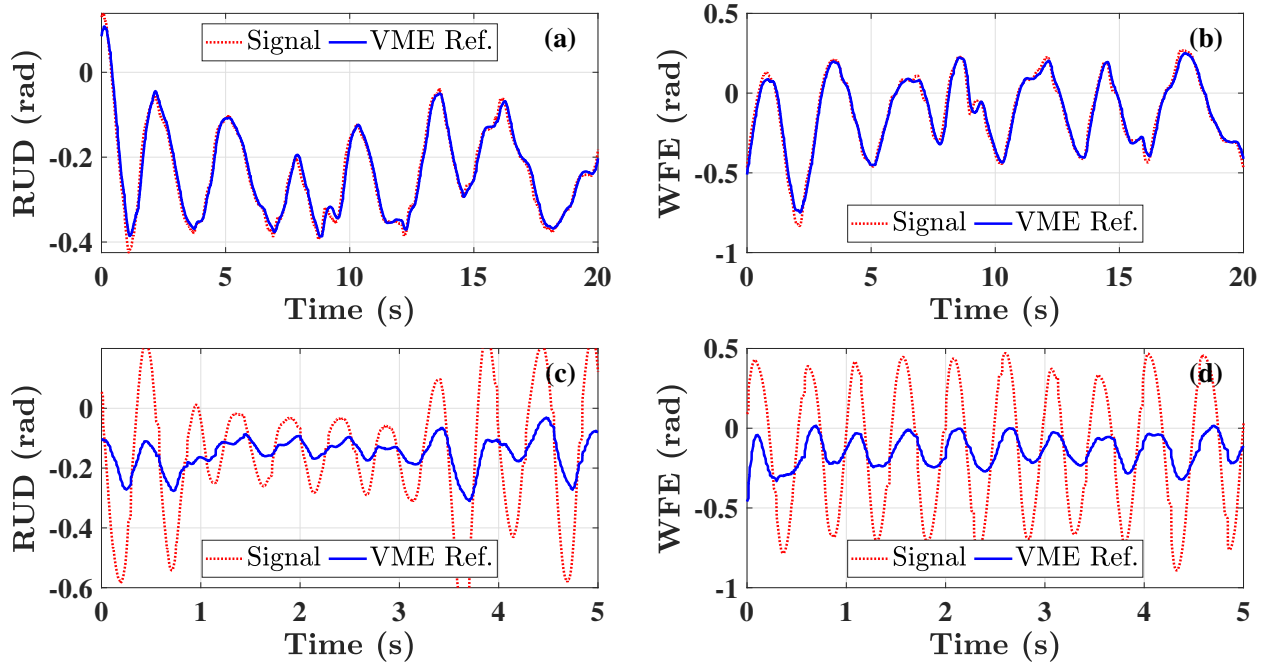


Figure 6.15: Real-time performance of SVR-VME on smooth voluntary wrist movements shown in two sets of experimental results [182], where (a, b) compare the WFE and RUD measurements with their estimated voluntary movements from result #1, and (c, d) compare those from result #2.

before the intentional tremors are voluntary and smooth, we also notice that SVR-VME requires a period (approximately 1 to 2 seconds) to adapt to patterns of tremors. During this transition period, the performance of SVR-VME is limited, which can be a potential problem if pathological tremors behave intermittently in certain scenarios.

The outcomes of SVR-VME on smooth and voluntary wrist movements in Fig. 6.15 revealed a limitation on its application scenarios. As shown in Fig. 6.15(a, b), when the voluntary movement is slow, SVR-VME yields good results despite the fact that the movement pattern is non-periodic. However, if the voluntary movement exhibits patterns in a frequency band close to the cut-off frequency (1.5 Hz). In this case, the IIR low-pass filter cannot distinguish voluntary movement and tremor, which results in SVR-VME being unable to approximate the voluntary movement. This result indicates that the application of SVR-VME requires a

clear separation between the frequency bands of tremor and voluntary movement.

Overall, the performance of SVR-VME on real-time motion data corroborates with the observations from earlier numerical studies in Section 5.3. These cases also revealed the limitations of SVR-VME in processing motion signals and voluntary movements that reside in the frequency band near the cutoff frequency of the low-pass filter. Hence, further investigation is needed to ensure the accurate approximation of high-activity voluntary movements from frequency bands close to those of pathological tremors.

### 6.3.2 Passive Tremor Suppression on Forearm Mannequin

We carried out the experiment on passive tremor suppression based on a forearm mannequin with robotic wrist [44]. The forearm mannequin serves as an experimental test bench for the safe testing of mechanical loading performed by the TAW E prototype. The experimental setup is shown in 6.16. Note that the robotic wrist in the mannequin is actuated by two

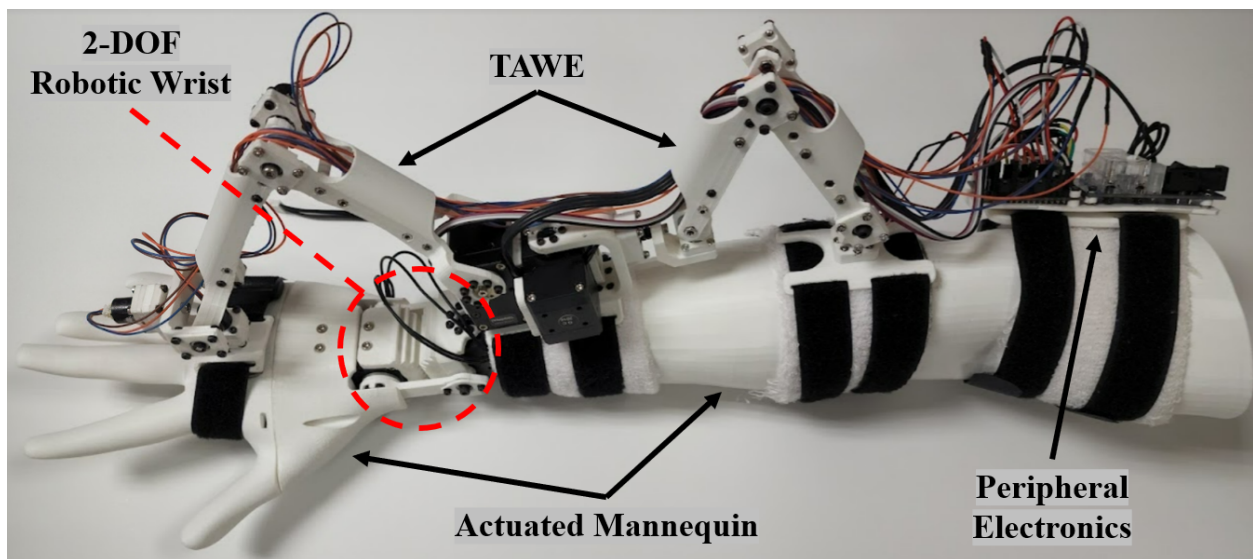


Figure 6.16: TAW E attached to a right forearm mannequin with a 2-DOF robotic wrist actuated by servomotors [44].

servomotors identical to those used in TAWE, which emulate wrist movements that can reach  $-90^\circ$  (flexion) to  $90^\circ$  (extension) in WFE, and  $-20^\circ$  (ulnar deviation) to  $20^\circ$  (radial deviation) in RUD. The FPS motion in the forearm mannequin is fixed. In addition to safety concerns during mechanical loading from TAWE, the use of this mannequin as a test bench also prevented the excessive amount of electronics from being directly attached to the human body.

It should be noted that the current control mode provided by servomotors used in the prototype is designed mainly for fixed-point current tracking. When following a current reference trajectory sampled at 250 Hz, the output current contains time delay (approximately 0.02 to 0.03 seconds) and ripples, which is extremely significant when the sign of the current changes. These behaviors are likely determined by the characteristics of brushed DC motors, the driver circuit design, and the motor control firmware, which are closed-source and cannot be modified. Therefore, current control (for torque control in brushed DC motors [113]) from TAWE is not available in these experiments.

On the other hand, the servomotors in TAWE can provide quick and accurate position control based on linear PID schemes. As previously discussed in Section 4.3.5, PD controllers can emulate spring-damper impedance and lead to passive suppression of tremors. In the following experiments, the servomotors of TAWE are set to current-based position control mode. In this mode, the servomotor will track the reference trajectory in position within the current limits. Therefore, any external load exerted on the motor beyond the current limit can cause it to rotate. Finally, the voluntary movement estimation is carried out directly on the TAWE servomotor rotations.

With the robotic wrist in the forearm mannequin being inactive, we first tested the compliance of TAWE toward user-guided movement. The rotation of servomotors in TAWE is caused by a human operator (author of this dissertation), who manually moved the robotic

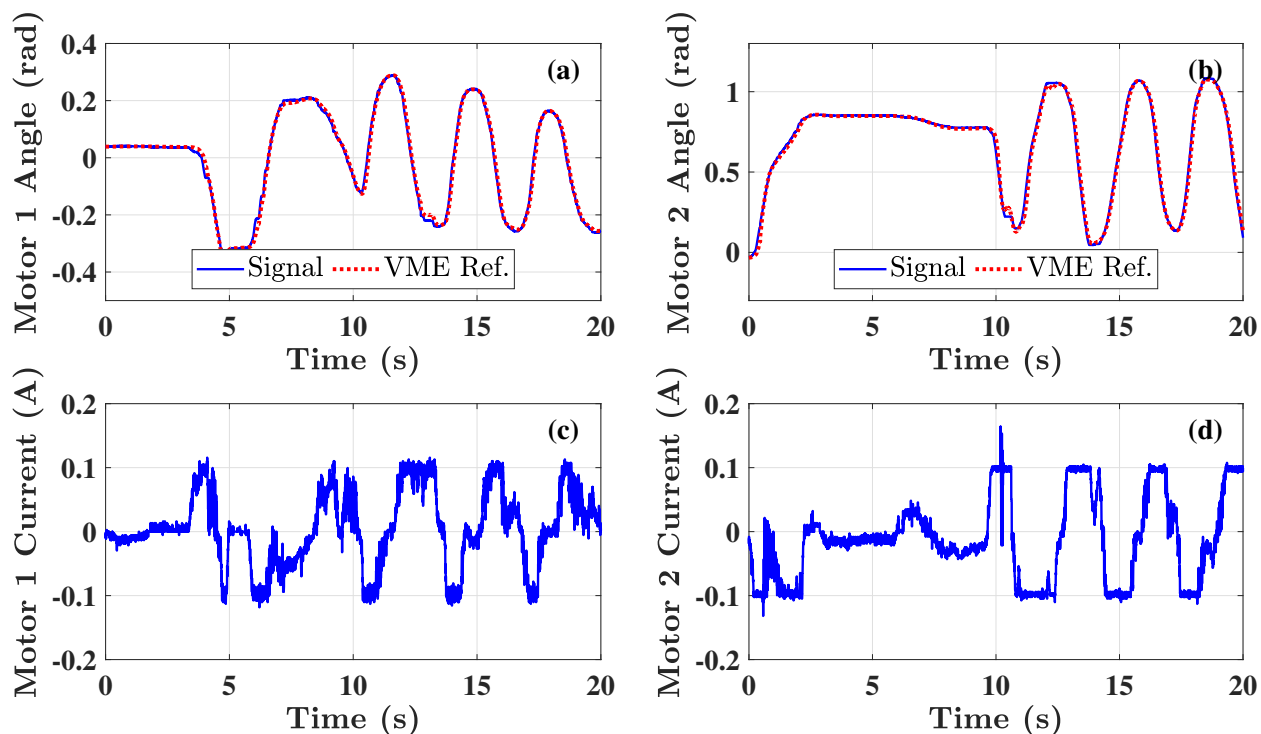


Figure 6.17: The compliance of TAWE towards user-guided movement, where (a, b) show the rotations of motors in TAWE prototype, and (c, d) show the corresponding motor currents.

wrist of the forearm mannequin in a random manner. In this case, the servomotor current limit is set to 0.1 Amps in both directions. The results are shown in Fig. 6.17. It is observed from Figs. 6.17(a, b) that SVR-VME produced the tracking references based on the movement of servomotors due to external voluntary loading. From Figs. (c, d), we notice that the motor currents were contained within 0.1 Amps in magnitude (except the ripples in Fig. (d)). Again, these currents are generated from the PD controller calculated by the servomotor control firmware. Also, Figs. (c, d) show that the trajectories of currents return to the vicinity of zeros whenever the tracking references from SVR-VME match with the motor rotation angles. This outcome is expected since the small tracking errors cause the PD controllers to generate small current outputs. Hence, the results in Fig. 6.17 demonstrate effective user-compliant control based on voluntary references estimated by SVR-VME.

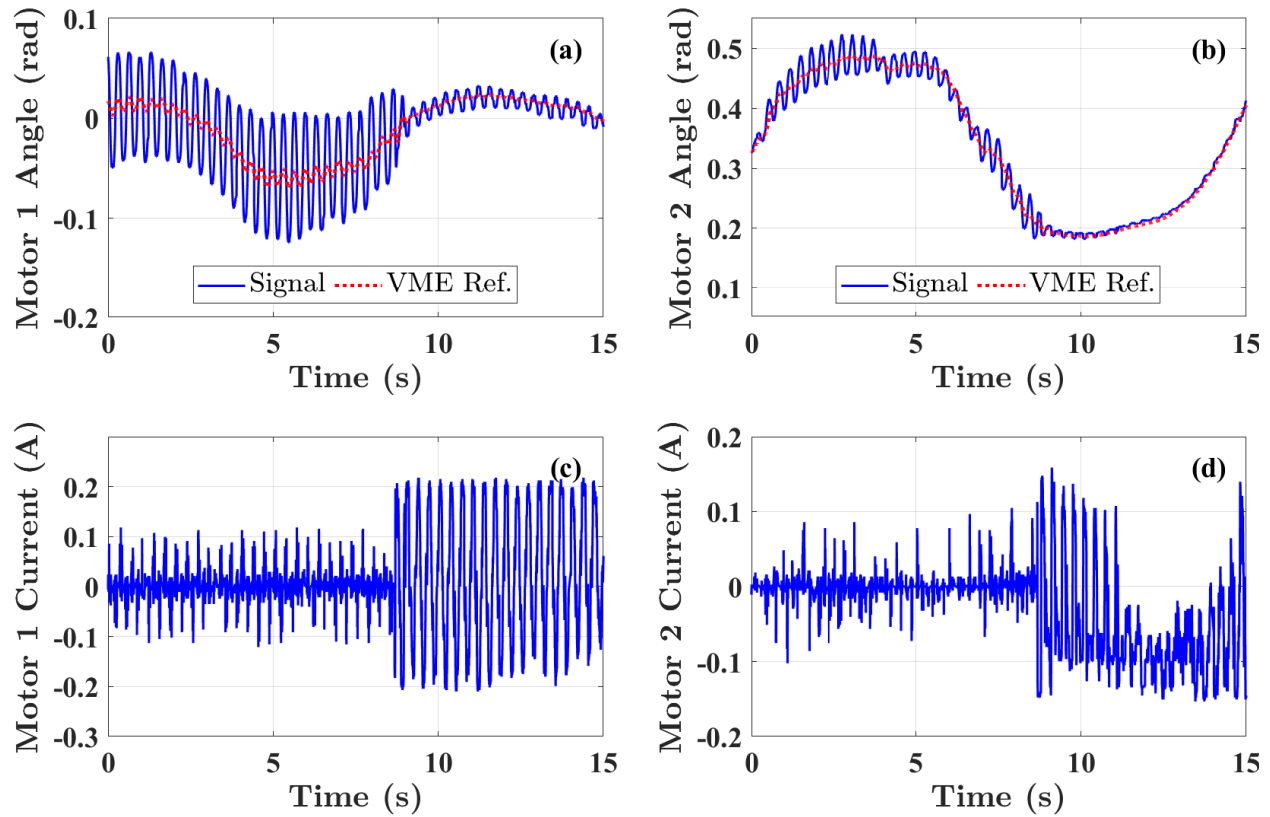


Figure 6.18: TAFE servomotor behaviors in passive tremor suppression experiment, where (a, b) show the rotations of servomotors and their voluntary movement estimation, and (c, d) show the corresponding servomotor currents.

We then activated the forearm mannequin to emulate pathological tremor excitations, which tests the performance of TAFE in passive tremor suppression. In this experiment, the servomotors in the robotic wrist are commanded to output excitation currents. These currents contain low-frequency components (at 0.1 Hz) that emulate voluntary movements, and high-frequency components (at 3 Hz) that emulate pathological tremors. Despite the undesirable ripples in motor currents and the frictions in the robotic wrist mechanism, the robotic wrist was able to generate tremorous movement in both WFE and RUD. The current limits on TAFE servomotors were set to 0.2 Amps for Motor 1 and 0.15 Amps for Motor 2, which are respectively  $u_{\text{exo},1}$  and  $u_{\text{exo},2}$  as marked in Fig. 6.1.

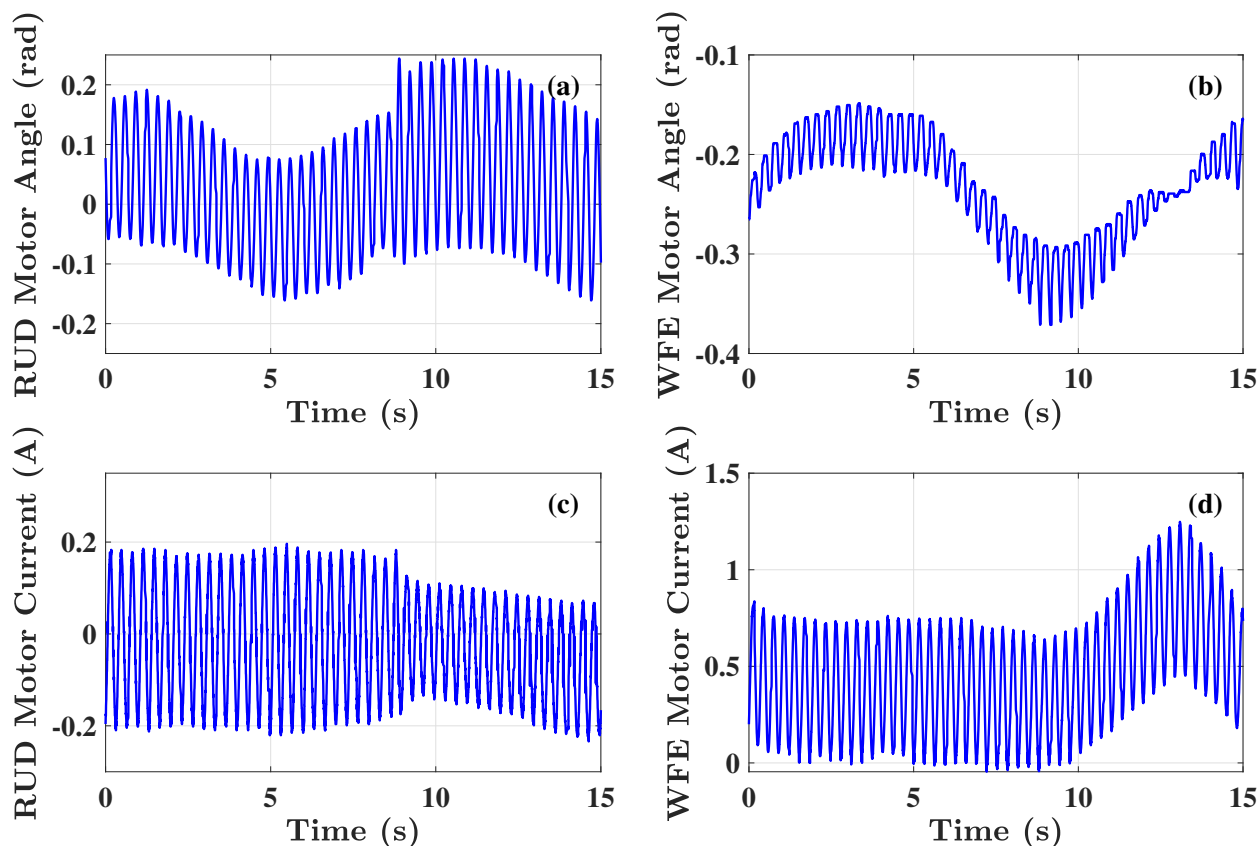


Figure 6.19: Robotic wrist servomotor behaviors in passive tremor suppression experiment, where (a, b) show the rotations of motors in the robotic mannequin, and (c, d) show the servomotor currents that emulates tremorous movements in the forearm mannequin.

The behaviors of servomotors in TAWE are shown in Fig. 6.18. Notice from Figs. 6.18(a, b) that the oscillation amplitudes servomotor rotations are significantly reduced when the servomotors are turned on at approximately  $t = 9$  s. Recall from Fig. 6.1 that these servomotors both reflect movements in WFE and RUD. Therefore, Figs. 6.18(a, b) can be interpreted as the tremors transmitted from WFE and RUD being simultaneously suppressed. In the meantime, the TAWE servomotor can effectively track the low-frequency voluntary components emulated by the robotic wrist without significantly affecting their trajectories. The current responses in Figs. 6.18(c, d) presents the significant effort from TAWE servomotors on tremor suppression. The servomotor currents are also contained within their boundaries.

The behaviors of servomotors in the robotic wrist are presented in Fig. 6.19. Unlike TAWÉ servomotors, the robotic wrist servomotors exhibited increased oscillation amplitudes after TAWÉ is turned on at approximately  $t = 9$  s, which can be observed in Figs. 6.19(a, b). This behavior appears to be resonances caused by the excitation from TAWÉ. Correspondingly, the servomotor currents in Figs. 6.19(c, d) also decreased in amplitudes, which is likely due to reverse currents induced by the increased oscillations in wrist movements.

A possible cause of the opposite behaviors from the TAWÉ and robotic wrist servomotors is the lack of rigidity in the constraints between the exoskeleton and forearm mannequin. Since the forearm mannequin is manufactured by 3D printing, the wearability features in TAWÉ designed for human users cannot firmly attach the exoskeleton to the forearm mannequin. During tremor excitations, we observed rocking motions at the contact points. Such non-rigid behavior in the mechanism likely caused phase shifts during the transmission of exoskeleton actuation, leading to amplified oscillations in the robotic wrist movements due to resonances.

Therefore, the passive tremor suppression demonstrated both the effectiveness and limitation of the current TAWÉ prototype. The emulated tremors are successfully suppressed in the TAWÉ servomotors, which can also simultaneously follow the low-frequency voluntary movement without significantly affecting their trajectories. The increased oscillations in the robotic wrist servomotors indicate the importance of stability in exoskeleton wearability. To ensure expected tremor suppression performance, the rigidity of the exoskeleton mechanism and human-exoskeleton contact must be guaranteed. Any resonance within the system can result in opposite behaviors that further exaggerate pathological tremors. Although TAWÉ can be securely attached to the forearm of a human user, the soft tissue artifacts from human bodies discussed in Assumption (MA. 1) should be seriously investigated and considered during the exoskeleton development for tremor alleviation.

## 6.4 Summary

In this chapter, we presented the prototyping, control software development, and experiment of TAWE. The prototype is manufactured based on 3D printing, standard mechanical parts, and off-the-shelf mechatronics. The mechanism and wearability tests showed that TAWE is ergonomic in terms of supporting natural forearm movements and non-fixing wearability features. The control software of TAWE is developed based on the ROS2 framework. The previously proposed algorithms for WKI, IO-RAC, and SVR-VME are integrated into the control system. We then carried out real-time exoskeleton control simulations on ROS2. The control system can efficiently execute in real-time, suppress fixed-frequency tremor components in wrist movements, and follow user-guided movements. Later, we performed experiments on the TAWE prototype. We validated the performance of SVR-VME on real-time data and realized passive tremor suppression in TAWE during user-guided operation.

The findings in the chapter also revealed a few limitations of the TAWE design. The current design of TAWE can be further improved in donning-and-doffing simplicity, dimension customizability, and design weight for better ergonomics. The control framework is less effective when tremors show varying frequencies, and the SVR-VME is unable to estimate voluntary movements whose frequency band is close to that of tremors. The prototype requires improved actuators to realize torque control, and better wearability/structural rigidity to prevent potential resonance that worsens tremor oscillations in the wrist.

The findings in this chapter conclude the current stage of development of the Tremor Alleviating Wrist Exoskeleton. In the next chapter, we summarize the finding of this project, discuss the limitations of the current approaches, and propose future work.

# Chapter 7

## Conclusion

In this project, we explored the design and control of an ergonomic wearable exoskeleton for full-wrist pathological tremor alleviation. We proposed TAWÉ - a novel wearable exoskeleton that provides tremor suppression in all wrist DOFs. Compared to existing tremor alleviation exoskeletons at the wrist, TAWÉ is a solution with improved ergonomics for its compliance with natural wrist movement and wearability for daily activities.

The analysis of the coupled multibody dynamics of the human-exoskeleton system revealed a few robotic control problems. We investigated and proposed new solutions in the identification of unknown wrist kinematics in the system, robust adaptive exoskeleton control for tremor suppression, and voluntary movement estimation for motion planning. These proposed solutions are real-time efficient, compatible with each other, and individually developed based on generic formulations, making them applicable to other rehabilitation exoskeletons as well.

Later, we developed the hardware prototype and control software of TAWÉ. Simulations and experiments are carried out to validate the proposed methods. The design of TAWÉ meets the expectations in its compliance with natural wrist movement and simple wearability. The exoskeleton control system can execute stably in real-time, identify unknown system kinematics and dynamics, estimate voluntary movements, and suppress tremors in the wrist. The results also revealed a few limitations in the current approaches.

The ultimate goal of TAWÉ is to provide quality-of-life improvements for patients suffering from pathological tremors. This work has laid a solid foundation for the future investigation and improvement of TAWÉ for better tremor suppression performance. The contributions and future directions of the study are summarized in the following sections (Sections 7.1 and 7.2, respectively).

## 7.1 Contribution

This dissertation has reported a few new findings in the development of tremor alleviation exoskeleton for the wrist. This study also established generalized frameworks of exoskeleton modeling, analysis, and control, which apply to not only the proposed tremor alleviation wrist exoskeleton, but also other rehabilitation exoskeletons. The contributions of this work are discussed as follows.

### 7.1.1 The Design of Tremor Alleviating Wrist Exoskeleton

TAWÉ is the first high-DOF wearable exoskeleton designed for full-wrist tremor alleviation. The 6-DOF rigid linkage mechanism in TAWÉ is compliant with the natural movements in the wrist, which is an ergonomic and generic design that can be easily adopted in the rehabilitation exoskeleton at other human joints. The mechanism and wearability design of TAWÉ also provides a potential solution for wearable rehabilitation exoskeleton application in daily activities.

### 7.1.2 Analysis of Coupled Human-Exoskeleton Dynamics

The analysis of coupled human-exoskeleton dynamics is one of the first to investigate human-exoskeleton interactions and tremor behaviors based on generic nonholonomic multibody formulation, which provided preliminary insights into the design feasibility of TAWÉ, and revealed the robotic control problems for later investigations. The framework of nonholonomic multibody analysis is also widely applicable to other rehabilitation exoskeletons and robotic systems.

### 7.1.3 Real-Time Identification of Wrist Kinematic

To identify the unknown wrist kinematics in the human-exoskeleton system, we proposed a novel ellipsoidal joint model, which features a quaternion-based constraint to characterize the constrained 3D rotation of the wrist, and geometric constraints to couple internal wrist translational motions with WFE and RUD rotations. The ellipsoidal joint model can generalize the behaviors of the various sequential rotational wrist models from earlier studies. For real-time WKI, we designed the regression model with additional 2D FLC to compensate for model discrepancies, and applied EKF with sparsity-promoting feature to reduce identified model complexity and improve robustness against noises. Later, simulations and experiments are carried out, which validated the effectiveness of the proposed real-time WKI algorithm. It should be noted that the identification of unknown kinematics in the human-exoskeleton system is not unique to this study. The framework of WKI is transferable to other exoskeleton applications as well.

### 7.1.4 Exoskeleton Controllers for Tremor Suppression

Based on model assumptions (MA. 1, 2 in Section 2.3, MA. 3, 4, 5, 6, 7 in Section 4.2, and MA. 8, 9 in Section 4.3), we developed multiple controllers for the tracking control of the human-exoskeleton system and suppression of pathological tremors. Specifically, we designed a novel robust adaptive controller (IO-RAC) based on model reference adaptive control and inverse optimal robust control theories, which can identify the unknown model inertia and load, and provide stable tracking control under disturbance. The stability and optimality of IO-RAC are proved mathematically.

Simulations were carried out to observe the performance of IO-RAC, which validated its capability in compensating for dynamical model uncertainties and maintaining control stability under disturbance. Based on the observation that pathological tremors possess multiple frequency components, IO-RAC can adopt BMFLC as its adaptive model to provide active tremor suppression. Finally, the IO-RAC formulated based on a generic nonholonomic model can be applied to a family of other rehabilitation exoskeletons and robotic systems.

### 7.1.5 Voluntary Movement Estimation for Motion Planning

The estimation of voluntary movement components from the tremorous motion data provides the reference trajectory for exoskeleton control. A major challenge is the reduction of time delay in the estimated trajectories. We developed a lightweight and data-driven voluntary movement estimator (SVR-VME) based on least square support vector regression, which can estimate low-frequency voluntary movements significantly reduced time delay, and adapt to most recent signal patterns and update the model with real-time efficiency. Simulation and experiments validated the performance of SVR-VME, and demonstrated its robustness to sensor noises and applicability to motion with tremors from different frequency bands.

### 7.1.6 Prototyping, Control Integration and Experiments

We developed the hardware prototype and control software of TAWÉ, and carried out real-time simulations and experiments to validate their performances. Overall, the prototype of TAWÉ meets the expectations in its compliance with natural wrist movement and simple wearability. The exoskeleton control system that integrates all our proposed real-time control solutions can execute stably in real-time, identify unknown system kinematics and dynamics, estimate voluntary movements, and suppress tremors in the wrist. The experiments also showed that the current prototype can realize passive tremor suppression in TAWÉ during user-guided operation. Finally, the results also revealed the limitations in the current approaches, which are crucial to the further improvement of rehabilitation exoskeletons for tremor alleviation.

## 7.2 Future Work

There are spaces for improvement in both the design and control of TAWÉ and other tremor alleviation exoskeletons in general. Based on the limitations of the current methods observed from this study, we propose the following directions for future investigations.

### 7.2.1 Improved Ergonomics in Mechanism and Wearability

While the current design of TAWÉ has taken ergonomics into consideration, we observed a few limitations from the current mechanism and wearability features. The current 6-DOF rigid linkage mechanism significantly extrudes from the forearm in the dorsal direction. By exploring other mechanisms such as parallel linkages or cable-driven mechanisms [115, 127], we can potentially make the mechanism more compact and customizable without losing

compliance with natural movements or efficiency in force/torque transmission. These mechanisms may also allow us to better arrange the COM distribution of exoskeleton along the forearm.

The major challenge in wearability is the contact stability between exoskeleton and human body. The current wearability of TAWÉ also needs improved in donning and doffing. A possible direction is to integrate soft robot elements into the exoskeleton design [75, 149], which ensure ergonomics in human-exoskeleton interfacing without significantly introducing uncertainties in the control system.

### 7.2.2 Reliable Exoskeleton Actuators

The prototyping of TAWÉ revealed the need for reliable actuators for tracking control and active tremor alleviation. The exoskeleton control framework can only be partially validated due to limitations in the servomotors, despite that, they are among the very few options that come with current control and a small form factor for wearability. Therefore, we need to explore more reliable actuators with direct force/torque control for wearable exoskeletons. Potential solutions can be novel series elastic actuators and cable-driven actuators with customized designs specifically for applications in tremor alleviation exoskeletons [27, 57].

### 7.2.3 Nonlinear Analysis of Tremor Dynamics

Pathological tremors originate in the neuromuscular system. However, the existing control system for tremor suppression only uses the knowledge of multibody dynamics and models tremors based on periodicity and similarity patterns. A fundamental understanding of the nonlinear neuromusculoskeletal dynamics can lead to better modeling and control of tremor signals, which can significantly improve voluntary movement estimation and tremor

suppression control performance. A possible direction is to carry out data-driven analysis based on experimentally collected cortical, neuromuscular, and motion measurements from health and tremor-affected subjects. Coherence studies can help us identify and reconstruct tremor-related elements in these signals [69, 70, 124, 125], which leads to the data-driven modeling of neuromusculoskeletal dynamics that provides in-depth analysis of the origins and effects of tremors [178, 192].

#### 7.2.4 Advanced Exoskeleton Control for Tremor Suppression

The existing controller based on RAC, while being able to stably track user movement and suppress tremor, has a few noticeable limitations. A practical problem is that the current control framework cannot conveniently incorporate constraints such as limitations on input force/torque and range of motion. These constraints are crucial to the safety of the user. Another limitation of the current approach is that reference models need to be provided to compensate model uncertainties [76, 98]. The control performance can be challenged when uncertainties do not match with reference models or fit the conditions of disturbances, which likely explains the limited tremor suppression performance in Section 6.2.3 when frequency sweep was considered.

Therefore, we also need to investigate more advanced frameworks to ensure better performance and safety in human-exoskeleton cooperative control. A possible direction is to employ optimization-based control framework [4, 130], which can feature constraints based on human-exoskeleton dynamics, physical safety (e.g., input, range of motion), and control stability conditions. Based on this framework, we may also employ data-driven observers based on kinetic and neural signals for better characterization of tremors and other uncertain dynamical effects from the user [48].

### 7.2.5 Motion Planning with Better Compliance

The current TAWÉ motion planning based on voluntary movement estimation suffers the limitations of being unable to distinguish high-frequency voluntary movements, estimate transient voluntary movements, or predict future voluntary movements. Potential solutions to improve the exoskeleton motion planning in user-guided operation is to employ extra measurements other than motion signals (e.g., force/torque and sEMG measurements), which may allow us to obtain more information on voluntary intentions for multi-step motion planning [80, 153, 196], and leads to better compliance between the exoskeleton and user.

### 7.2.6 Extensive Experimental Validations

Finally, after the abovementioned improvements are made, TAWÉ needs to be thoroughly evaluated through extensive human experiments. We expect to invite volunteer subjects with or without pathological tremors to test the performance of TAWÉ in tremor suppression and compliance with user movements. The data collection and user feedback can provide insights to further optimize the prototype, which can potentially become a valid product to improve the quality of living for people suffering from pathological tremors.

# Bibliography

- [1] Kabita Adhikari, Sivanagaraja Tatinati, Wei Tech Ang, Kalyana C Veluvolu, and Kianoush Nazarpour. A quaternion weighted fourier linear combiner for modeling physiological tremor. *IEEE Transactions on Biomedical Engineering*, 63(11):2336–2346, 2016.
- [2] Bardiya Akhbari, Douglas C Moore, David H Laidlaw, Arnold-Peter C Weiss, Edward Akelman, Scott W Wolfe, and Joseph J Crisco. Predicting carpal bone kinematics using an expanded digital database of wrist carpal bone anatomy and kinematics. *Journal of Orthopaedic Research®*, 2019.
- [3] MDS Aliyu. *Nonlinear H-infinity control, Hamiltonian systems and Hamilton-Jacobi equations*. CRC Press, 2017.
- [4] Aaron D Ames, Xiangru Xu, Jessy W Grizzle, and Paulo Tabuada. Control barrier function based quadratic programs for safety critical systems. *IEEE Transactions on Automatic Control*, 62(8):3861–3876, 2016.
- [5] Aleksandr Y Aravkin, James V Burke, and Gianluigi Pillonetto. Optimization viewpoint on kalman smoothing with applications to robust and sparse estimation. In *Compressed sensing & sparse filtering*, pages 237–280. Springer, 2014.
- [6] Ece Aydoğ, Emel Ekşioğlu, Aytül Çakci, and Özge Yılmaz. Hand deformity in parkinson’s disease: case report. *Rheumatology international*, 25(7):548–549, 2005.
- [7] Julian Benito-Leon and Elan D Louis. Essential tremor: emerging views of a common disorder. *Nature Reviews Neurology*, 2(12):666, 2006.

- [8] A Berardelli, AF Sabra, and M Hallett. Physiological mechanisms of rigidity in parkinson's disease. *Journal of Neurology, Neurosurgery & Psychiatry*, 46(1):45–53, 1983.
- [9] Alfredo Berardelli, JC Rothwell, PD Thompson, and M Hallett. Pathophysiology of bradykinesia in parkinson's disease. *Brain*, 124(11):2131–2146, 2001.
- [10] R Bhidayasiri. Differential diagnosis of common tremor syndromes. *Postgraduate medical journal*, 81(962):756–762, 2005.
- [11] EV Biryukova, A Roby-Brami, AA Frolov, and M Mokhtari. Kinematics of human arm reconstructed from spatial tracking system recordings. *Journal of biomechanics*, 33(8):985–995, 2000.
- [12] Brian Bittner and Koushil Sreenath. Symbolic computation of dynamics on smooth manifolds. In *Algorithmic Foundations of Robotics XII*, pages 336–351. Springer, 2020.
- [13] Antonio Padilha Lanari Bo, Philippe Poignet, and Christian Geny. Pathological tremor and voluntary motion modeling and online estimation for active compensation. *IEEE Transactions on Neural Systems and Rehabilitation Engineering*, 19(2):177–185, 2010.
- [14] Antonio Padilha Lanari Bo, Philippe Poignet, and Christian Geny. Pathological tremor and voluntary motion modeling and online estimation for active compensation. *IEEE Transactions on Neural Systems and Rehabilitation Engineering*, 19(2):177–185, 2011.
- [15] Vincent Bonnet, Claudia Mazza, John McCamley, and Aurelio Cappozzo. Use of weighted fourier linear combiner filters to estimate lower trunk 3d orientation from gyroscope sensors data. *Journal of neuroengineering and rehabilitation*, 10(1):1–8, 2013.
- [16] Brahim Brahmi, Maarouf Saad, Jacqueline Tu Anh Thu Lam, Cristobal Ochoa Luna, Philippe S Archambault, and Mohammad H Rahman. Adaptive control of a 7-dof

- exoskeleton robot with uncertainties on kinematics and dynamics. *European Journal of Control*, 42:77–87, 2018.
- [17] Brahim Brahmi, Abdelkrim Brahmi, Maarouf Saad, Guy Gauthier, and Mohammad Habibur Rahman. Robust adaptive tracking control of uncertain rehabilitation exoskeleton robot. *Journal of Dynamic Systems, Measurement, and Control*, 141(12), 2019.
- [18] Kevin C Brennan, Eva C Jurewicz, Blair Ford, Seth L Pullman, and Elan D Louis. Is essential tremor predominantly a kinetic or a postural tremor? a clinical and electrophysiological study. *Movement disorders: official journal of the Movement Disorder Society*, 17(2):313–316, 2002.
- [19] Daniel Bruder, Brent Gillespie, C David Remy, and Ram Vasudevan. Modeling and control of soft robots using the koopman operator and model predictive control. *arXiv preprint arXiv:1902.02827*, 2019.
- [20] Carmen Camara, Pedro Isasi, Kevin Warwick, Virginie Ruiz, Tipu Aziz, John Stein, and Eduard Bakštein. Resting tremor classification and detection in parkinson’s disease patients. *Biomedical Signal Processing and Control*, 16:88–97, 2015.
- [21] Sue Ann Campbell. Time delays in neural systems. In *Handbook of brain connectivity*, pages 65–90. Springer, 2007.
- [22] Fucheng Cao, Chunfeng Li, and Yuanchun Li. Robust sliding mode adaptive control for lower extremity exoskeleton. In *2015 Chinese Automation Congress (CAC)*, pages 400–405. IEEE, 2015.
- [23] David Case, Behzad Taheri, and Edmond Richer. Dynamic magnetorheological damper for orthotic tremor suppression. *HUIC Mathematics & Engineering*, 2011.

- [24] Yin-Wen Chang, Cho-Jui Hsieh, Kai-Wei Chang, Michael Ringgaard, and Chih-Jen Lin. Training and testing low-degree polynomial data mappings via linear svm. *Journal of Machine Learning Research*, 11(4), 2010.
- [25] Adam S Charles, Aurele Balavoine, and Christopher J Rozell. Dynamic filtering of time-varying sparse signals via l1 minimization. *IEEE Transactions on Signal Processing*, 64(21):5644–5656, 2016.
- [26] Steven K Charles and Neville Hogan. Dynamics of wrist rotations. *Journal of biomechanics*, 44(4):614–621, 2011.
- [27] Tianyao Chen, Rafael Casas, and Peter S Lum. An elbow exoskeleton for upper limb rehabilitation with series elastic actuator and cable-driven differential. *IEEE Transactions on Robotics*, 35(6):1464–1474, 2019.
- [28] Xing Chen, Yan Zeng, and Yuehong Yin. Improving the transparency of an exoskeleton knee joint based on the understanding of motor intent using energy kernel method of emg. *IEEE Transactions on Neural Systems and Rehabilitation Engineering*, 25(6): 577–588, 2016.
- [29] Shankar J Chinta and Julie K Andersen. Dopaminergic neurons. *The international journal of biochemistry & cell biology*, 37(5):942–946, 2005.
- [30] Jakkrapun Chuanasa and Szathys Songschon. Anti-shaker simulation for arm tremor. In *Proceedings of International Conference on Circuits, System and Simulation (ICCSS 2011)*, 2011.
- [31] Charles E Clauser, John T McConville, and John W Young. Weight, volume, and center of mass of segments of the human body. Technical report, Antioch Coll Yellow Springs OH, 1969.

- [32] James R Cloutier. State-dependent riccati equation techniques: an overview. In *American Control Conference, 1997. Proceedings of the 1997*, volume 2, pages 932–936. IEEE, 1997.
- [33] Thomas H Cormen, Charles E Leiserson, Ronald L Rivest, and Clifford Stein. *Introduction to algorithms*. MIT press, 2022.
- [34] Joseph J Crisco, Wendell MR Heard, Ryan R Rich, David J Paller, and Scott W Wolfe. The mechanical axes of the wrist are oriented obliquely to the anatomical axes. *The Journal of Bone and Joint Surgery. American volume.*, 93(2):169, 2011.
- [35] Hao Deng, Weidong Le, and Joseph Jankovic. Genetics of essential tremor. *Brain*, 130(6):1456–1464, 2007.
- [36] G Deuschl, R Wenzelburger, K Löffler, J Raethjen, and H Stolze. Essential tremor and cerebellar dysfunction clinical and kinematic analysis of intention tremor. *Brain*, 123(8):1568–1580, 2000.
- [37] David T Dexter and Peter Jenner. Parkinson disease: from pathology to molecular disease mechanisms. *Free Radical Biology and Medicine*, 62:132–144, 2013.
- [38] Jakob L Dideriksen, Christopher M Laine, Strahinja Dosen, Silvia Muceli, Eduardo Rocon, José L Pons, Julian Benito-Leon, and Dario Farina. Electrical stimulation of afferent pathways for the suppression of pathological tremor. *Frontiers in neuroscience*, 11:178, 2017.
- [39] James Diebel. Representing attitude: Euler angles, unit quaternions, and rotation vectors. *Matrix*, 58(15-16):1–35, 2006.
- [40] Karen M Doherty, Bart P van de Warrenburg, Maria Cecilia Peralta, Laura Silveira-

- Moriyama, Jean-Philippe Azulay, Oscar S Gershanik, and Bastiaan R Bloem. Postural deformities in parkinson's disease. *The Lancet Neurology*, 10(6):538–549, 2011.
- [41] Strahinja Dosen, Silvia Muceli, Jakob Lund Dideriksen, Juan Pablo Romero, Eduardo Rocon, Jose Pons, and Dario Farina. Online tremor suppression using electromyography and low-level electrical stimulation. *IEEE Transactions on Neural Systems and Rehabilitation Engineering*, 23(3):385–395, 2014.
- [42] Sonia Duprey, Alexandre Naaim, Florent Moissenet, Mickaël Begon, and Laurence Cheze. Kinematic models of the upper limb joints for multibody kinematics optimisation: An overview. *Journal of biomechanics*, 62:87–94, 2017.
- [43] M. Freese E. Rohmer, S. P. N. Singh. V-rep: a versatile and scalable robot simulation framework. In *Proc. of The International Conference on Intelligent Robots and Systems (IROS)*, 2013.
- [44] Mohammed El Kihal, Jiamin Wang, and Oumar Barry. Design and modeling of a biomimetic robotic wrist via hybrid mechanism. In *International Design Engineering Technical Conferences and Computers and Information in Engineering Conference*, volume 86281, page V007T07A049. American Society of Mechanical Engineers, 2022.
- [45] Rodger Elble and Günther Deuschl. Milestones in tremor research. *Movement Disorders*, 26(6):1096–1105, 2011.
- [46] Erland Erdmann. Safety and tolerability of beta-blockers: prejudices and reality. *European Heart Journal Supplements*, 11(suppl\_A):A21–A25, 2009.
- [47] Mohammad Esmaeili, Kumudu Gamage, Eugene Tan, and Domenico Campolo. Ergonomic considerations for anthropomorphic wrist exoskeletons: A simulation study

- on the effects of joint misalignment. In *2011 IEEE/RSJ International Conference on Intelligent Robots and Systems*, pages 4905–4910. IEEE, 2011.
- [48] Randall T Fawcett, Kereshmeh Afsari, Aaron D Ames, and Kaveh Akbari Hamed. Toward a data-driven template model for quadrupedal locomotion. *IEEE Robotics and Automation Letters*, 7(3):7636–7643, 2022.
- [49] Domenico Formica, Steven K Charles, Loredana Zollo, Eugenio Guglielmelli, Neville Hogan, and Hermano I Krebs. The passive stiffness of the wrist and forearm. *Journal of neurophysiology*, 108(4):1158–1166, 2012.
- [50] Randy Freeman and Petar V Kokotovic. *Robust nonlinear control design: state-space and Lyapunov techniques*. Springer Science & Business Media, 2008.
- [51] Nicolas Philip Fromme, Martin Camenzind, Robert Riener, and René Michel Rossi. Need for mechanically and ergonomically enhanced tremor-suppression orthoses for the upper limb: a systematic review. *Journal of neuroengineering and rehabilitation*, 16(1):93, 2019.
- [52] Juan A Gallego, Eduardo Rocon, Javier O Roa, Juan C Moreno, and José L Pons. Real-time estimation of pathological tremor parameters from gyroscope data. *Sensors*, 10(3):2129–2149, 2010.
- [53] Juan Álvaro Gallego, Eduardo Rocon, Juan Manuel Belda-Lois, and José Luis Pons. A neuroprosthesis for tremor management through the control of muscle co-contraction. *Journal of neuroengineering and rehabilitation*, 10(1):36, 2013.
- [54] JB Gao. Analysis of amplitude and frequency variations of essential and parkinsonian tremors. *Medical and Biological Engineering and Computing*, 42(3):345–349, 2004.

- [55] Roger V Gonzalez, Thomas S Buchanan, and Scott L Delp. How muscle architecture and moment arms affect wrist flexion-extension moments. *Journal of biomechanics*, 30(7):705–712, 1997.
- [56] Parkinson Study Group. Levodopa and the progression of parkinson’s disease. *New England Journal of Medicine*, 351(24):2498–2508, 2004.
- [57] Yunfei Guo, Wenda Xu, Sarthark Pradhan, Cesar Bravo, and Pinhas Ben-Tzvi. Data driven calibration and control of compact lightweight series elastic actuators for robotic exoskeleton gloves. *IEEE Sensors Journal*, 21(19):21120–21130, 2021.
- [58] Abhishek Gupta, Marcia K O’Malley, Volkan Patoglu, and Charles Burgar. Design, control and performance of ricewrist: a force feedback wrist exoskeleton for rehabilitation and training. *The International Journal of Robotics Research*, 27(2):233–251, 2008.
- [59] David Hajdu, John Milton, and Tamas Insperger. Extension of stability radius to neuromechanical systems with structured real perturbations. *IEEE transactions on neural systems and rehabilitation engineering*, 24(11):1235–1242, 2016.
- [60] Marwan I Hariz, Stig Rehncrona, Niall P Quinn, Johannes D Speelman, and Carin Wensing. Multicenter study on deep brain stimulation in parkinson’s disease: an independent assessment of reported adverse events at 4 years. *Movement disorders: official journal of the Movement Disorder Society*, 23(3):416–421, 2008.
- [61] Rameez Hayat, Marion Leibold, and Martin Buss. Robust-adaptive controller design for robot manipulators using the h-infinity approach. *IEEE Access*, 6:51626–51639, 2018.
- [62] Simon S Haykin. *Adaptive filter theory*. Pearson Education India, 2005.

- [63] Wei He, Zhijun Li, Yiting Dong, and Ting Zhao. Design and adaptive control for an upper limb robotic exoskeleton in presence of input saturation. *IEEE transactions on neural networks and learning systems*, 30(1):97–108, 2018.
- [64] Jae-Hoon Heo, Ji-Won Kim, Yuri Kwon, Sang-Ki Lee, Gwang-Moon Eom, Do-Young Kwon, Chan-Nyeong Lee, Kun-Woo Park, and Mario Manto. Sensory electrical stimulation for suppression of postural tremor in patients with essential tremor. *Bio-medical materials and engineering*, 26(s1):S803–S809, 2015.
- [65] Ayonga Hereid and Aaron D Ames. Frost: Fast robot optimization and simulation toolkit. In *2017 IEEE/RSJ International Conference on Intelligent Robots and Systems (IROS)*, pages 719–726. IEEE, 2017.
- [66] Gil Herrnstadt and Carlo Menon. On-off tremor suppression orthosis with electromagnetic brake. *International Journal of Mechanical Engineering and Mechatronics*, 1(2): 7–24, 2012.
- [67] Gil Herrnstadt and Carlo Menon. Admittance-based voluntary-driven motion with speed-controlled tremor rejection. *IEEE/ASME Transactions on Mechatronics*, 21(4): 2108–2119, 2016.
- [68] Margaret M Hoehn and Melvin D Yahr. Parkinsonism: onset, progression, and mortality. *Neurology*, 17(5):427–427, 1967.
- [69] Aleš Holobar, Marco Alessandro Minetto, Alberto Botter, Francesco Negro, and Dario Farina. Experimental analysis of accuracy in the identification of motor unit spike trains from high-density surface emg. *IEEE Transactions on Neural Systems and Rehabilitation Engineering*, 18(3):221–229, 2010.
- [70] Aleš Holobar, Juan A Gallego, Jernej Kranjec, Eduardo Rocon, Juan P Romero, Julián

- Benito-León, José L Pons, and Vojko Glaser. Motor unit-driven identification of pathological tremor in electroencephalograms. *Frontiers in neurology*, 9:879, 2018.
- [71] Katherine RS Holzbaur, Wendy M Murray, and Scott L Delp. A model of the upper extremity for simulating musculoskeletal surgery and analyzing neuromuscular control. *Annals of biomedical engineering*, 33(6):829–840, 2005.
- [72] Fay B Horak, Diana Dimitrova, and John G Nutt. Direction-specific postural instability in subjects with parkinson’s disease. *Experimental neurology*, 193(2):504–521, 2005.
- [73] Denis Huen, Jindong Liu, and Benny Lo. An integrated wearable robot for tremor suppression with context aware sensing. In *2016 IEEE 13th International conference on wearable and implantable body sensor networks (BSN)*, pages 312–317. IEEE, 2016.
- [74] Anas Ibrahim, Yue Zhou, Mary E Jenkins, Ana Luisa Trejos, and Michael D Naish. Real-time voluntary motion prediction and parkinson’s tremor reduction using deep neural networks. *IEEE Transactions on Neural Systems and Rehabilitation Engineering*, 29:1413–1423, 2021.
- [75] Hyunki In, Brian Byunghyun Kang, Minki Sin, and Kyu-Jin Cho. Exo-glove: A wearable robot for the hand with a soft tendon routing system. *IEEE Robotics & Automation Magazine*, 22(1):97–105, 2015.
- [76] Petros A Ioannou and Jing Sun. *Robust adaptive control*, volume 1. PTR Prentice-Hall Upper Saddle River, NJ, 1996.
- [77] Samay Jain, Steven E Lo, and Elan D Louis. Common misdiagnosis of a common neurological disorder: how are we misdiagnosing essential tremor? *Archives of neurology*, 63(8):1100–1104, 2006.

- [78] Spencer L James, Degu Abate, Kalkidan Hassen Abate, Solomon M Abay, Cristiana Abbafati, Nooshin Abbasi, Hedayat Abbastabar, Foad Abd-Allah, Jemal Abdela, Ahmed Abdelalim, et al. Global, regional, and national incidence, prevalence, and years lived with disability for 354 diseases and injuries for 195 countries and territories, 1990–2017: a systematic analysis for the global burden of disease study 2017. *The Lancet*, 392(10159):1789–1858, 2018.
- [79] Joseph Jankovic. Parkinson’s disease: clinical features and diagnosis. *Journal of neurology, neurosurgery & psychiatry*, 79(4):368–376, 2008.
- [80] Nathanaël Jarrassé, Jamie Paik, Viviane Pasqui, and Guillaume Morel. How can human motion prediction increase transparency? In *2008 IEEE International Conference on Robotics and Automation*, pages 2134–2139. IEEE, 2008.
- [81] Fabian Just, Özhan Özen, Philipp Bösch, Hanna Bobrovsky, Verena Klamroth-Marganska, Robert Riener, and Georg Rauter. Exoskeleton transparency: feed-forward compensation vs. disturbance observer. *at-Automatisierungstechnik*, 66(12):1014–1026, 2018.
- [82] Lorraine V Kalia and Anthony E Lang. Parkinson’s disease. *The Lancet*, 386(9996):896 – 912, 2015. ISSN 0140-6736. doi: [https://doi.org/10.1016/S0140-6736\(14\)61393-3](https://doi.org/10.1016/S0140-6736(14)61393-3). URL <http://www.sciencedirect.com/science/article/pii/S0140673614613933>.
- [83] Thomas R Kane and David A Levinson. *Dynamics, theory and applications*. McGraw Hill, 1985.
- [84] Robert Kaufmann, Jamie Pfaeffle, Brad Blankenhorn, Kathryn Stabile, Doug Robertson, and Robert Goitz. Kinematics of the midcarpal and radiocarpal joints in radioulnar deviation: an in vitro study. *The Journal of hand surgery*, 30(5):937–942, 2005.

- [85] Robert A Kaufmann, H James Pfaeffle, Brad D Blankenhorn, Kathryn Stabile, Doug Robertson, and Robert Goitz. Kinematics of the midcarpal and radiocarpal joint in flexion and extension: an in vitro study. *The Journal of hand surgery*, 31(7):1142–1148, 2006.
- [86] Andrés Kecskeméthy and Manfred Hiller. An object-oriented approach for an effective formulation of multibody dynamics. *Computer Methods in Applied Mechanics and Engineering*, 115(3-4):287–314, 1994.
- [87] Christopher R Kelley and Jeffrey L Kauffman. Exploring dielectric elastomers as actuators for hand tremor suppression. In *Electroactive Polymer Actuators and Devices (EAPAD) 2017*, volume 10163, page 1016322. International Society for Optics and Photonics, 2017.
- [88] Christopher R Kelley and Jeffrey L Kauffman. Tremor-active controller for dielectric elastomer-based pathological tremor suppression. *IEEE/ASME Transactions on Mechatronics*, 25(2):1143–1148, 2020.
- [89] Hassan K Khalil. Nonlinear systems. *Prentice-Hall, New Jersey*, 2(5):5–1, 1996.
- [90] Hassan K Khalil and Jessy W Grizzle. *Nonlinear systems*, volume 3. Prentice hall Upper Saddle River, NJ, 2002.
- [91] Sundeep Khosla and Lorenz C Hofbauer. Osteoporosis treatment: recent developments and ongoing challenges. *The lancet Diabetes & endocrinology*, 5(11):898–907, 2017.
- [92] William C Koller. Pharmacologic treatment of parkinsonian tremor. *Archives of neurology*, 43(2):126–127, 1986.
- [93] William C Koller, Kelly E Lyons, Steven B Wilkinson, Alexander I Troster, and Rajesh Pahwa. Long-term safety and efficacy of unilateral deep brain stimulation of the

- thalamus in essential tremor. *Movement disorders: official journal of the Movement Disorder Society*, 16(3):464–468, 2001.
- [94] Jack Kotovsky and Michael J Rosen. A wearable tremor-suppression orthosis. *Journal of rehabilitation research and development*, 35:373–387, 1998.
- [95] E Kreuzer and W Schiehlen. Neweul—software for the generation of symbolical equations of motion. In *Multibody systems handbook*, pages 181–202. Springer, 1990.
- [96] Miroslav Krstic and Hua Deng. *Stabilization of Nonlinear Uncertain Systems*. Springer London, 1998.
- [97] Miroslav Krstic and Zhong-Hua Li. Inverse optimal design of input-to-state stabilizing nonlinear controllers. *IEEE Transactions on Automatic Control*, 43(3):336–350, 1998.
- [98] Andrew J Kurdila and Pinhas Ben-Tzvi. *Dynamics and Control of Robotic Systems*. John Wiley & Sons, 2019.
- [99] Th Kurz, P Eberhard, C Henninger, and W Schiehlen. From neweul to neweul-m2: symbolical equations of motion for multibody system analysis and synthesis. *Multibody System Dynamics*, 24(1):25–41, 2010.
- [100] Maria Laitenberger, Maxime Raison, Delphine Périé, and Mickael Begon. Refinement of the upper limb joint kinematics and dynamics using a subject-specific closed-loop forearm model. *Multibody System Dynamics*, 33(4):413–438, 2015.
- [101] Alberto Leardini, Lorenzo Chiari, Ugo Della Croce, and Aurelio Cappozzo. Human movement analysis using stereophotogrammetry: Part 3. soft tissue artifact assessment and compensation. *Gait & posture*, 21(2):212–225, 2005.

- [102] Wei Li and Jinling Wang. Effective adaptive kalman filter for mems-imu/magnetometers integrated attitude and heading reference systems. *The Journal of Navigation*, 66(1):99–113, 2013.
- [103] Zhijun Li, Chun-Yi Su, Liangyong Wang, Ziting Chen, and Tianyou Chai. Nonlinear disturbance observer-based control design for a robotic exoskeleton incorporating fuzzy approximation. *IEEE Transactions on Industrial Electronics*, 62(9):5763–5775, 2015.
- [104] Zong-Ming Li, Laurel Kuxhaus, Jesse A Fisk, and Thomas H Christophel. Coupling between wrist flexion-extension and radial-ulnar deviation. *Clinical biomechanics*, 20(2):177–183, 2005.
- [105] Elan D Louis. Essential tremor. *New England Journal of Medicine*, 345(12):887–891, 2001.
- [106] Elan D Louis and Joaquim J Ferreira. How common is the most common adult movement disorder? update on the worldwide prevalence of essential tremor. *Movement Disorders*, 25(5):534–541, 2010.
- [107] Elan D Louis and Ruth Ottman. How many people in the usa have essential tremor? deriving a population estimate based on epidemiological data. *Tremor and other hyperkinetic movements*, 4, 2014.
- [108] Rui CV Loureiro, Juan M Belda-Lois, Eduardo R Lima, Jose L Pons, Javier J Sanchez-Lacuesta, and William S Harwin. Upper limb tremor suppression in adl via an orthosis incorporating a controllable double viscous beam actuator. In *9th International Conference on Rehabilitation Robotics, 2005. ICORR 2005.*, pages 119–122. Ieee, 2005.
- [109] Wencheng Luo, Yun-Chung Chu, and Keck-Voon Ling. Inverse optimal adaptive con-

- trol for attitude tracking of spacecraft. *IEEE Transactions on Automatic Control*, 50 (11):1639–1654, 2005.
- [110] Steven Macenski, Tully Foote, Brian Gerkey, Chris Lalancette, and William Woodall. Robot operating system 2: Design, architecture, and uses in the wild. *Science Robotics*, 7(66):eabm6074, 2022.
- [111] Paweł Maciejasz, Jörg Eschweiler, Kurt Gerlach-Hahn, Arne Jansen-Troy, and Steffen Leonhardt. A survey on robotic devices for upper limb rehabilitation. *Journal of neuroengineering and rehabilitation*, 11(1):3, 2014.
- [112] Sebastian OH Madgwick, Andrew JL Harrison, and Ravi Vaidyanathan. Estimation of imu and marg orientation using a gradient descent algorithm. In *2011 IEEE international conference on rehabilitation robotics*, pages 1–7. IEEE, 2011.
- [113] S Maheriya and P Parikh. A review: Modelling of brushed dc motor and various type of control methods. *Journal for Research*, 1, 2016.
- [114] Paul Jackson Mansfield and Donald A Neumann. *Essentials of kinesiology for the physical therapist assistant e-book*. Elsevier Health Sciences, 2018.
- [115] Ying Mao and Sunil Kumar Agrawal. Design of a cable-driven arm exoskeleton (carex) for neural rehabilitation. *IEEE transactions on robotics*, 28(4):922–931, 2012.
- [116] C Marras, JC Beck, JH Bower, E Roberts, B Ritz, GW Ross, RD Abbott, R Savica, SK Van Den Eeden, AW Willis, et al. Prevalence of parkinson’s disease across north america. *NPJ Parkinson’s disease*, 4(1):21, 2018.
- [117] Yuya Matsumoto, Masatoshi Seki, Takeshi Ando, Yo Kobayashi, Hiroshi Iijima, Masanori Nagaoka, and Masakatsu G Fujie. Tremor frequency based filter to extract voluntary movement of patients with essential tremor. In *2012 4th IEEE RAS & EMBS*

- International Conference on Biomedical Robotics and Biomechatronics (BioRob)*, pages 1415–1422. IEEE, 2012.
- [118] Yuya Matsumoto, Motoyuki Amemiya, Daisuke Kaneishi, Yasutaka Nakashima, Masatoshi Seki, Takeshi Ando, Yo Kobayashi, Hiroshi Iijima, Masanori Nagaoka, and Masakatsu G Fujie. Development of an elbow-forearm interlock joint mechanism toward an exoskeleton for patients with essential tremor. In *2014 IEEE/RSJ International Conference on Intelligent Robots and Systems*, pages 2055–2062. IEEE, 2014.
- [119] JH McAuley and CD Marsden. Physiological and pathological tremors and rhythmic central motor control. *Brain*, 123(8):1545–1567, 2000.
- [120] Jayesh Minase, T-F Lu, B Cazzolato, and S Grainger. A review, supported by experimental results, of voltage, charge and capacitor insertion method for driving piezoelectric actuators. *Precision Engineering*, 34(4):692–700, 2010.
- [121] Douglas C Moore, Joseph J Crisco, Theodore G Trafton, and Evan L Leventhal. A digital database of wrist bone anatomy and carpal kinematics. *Journal of biomechanics*, 40(11):2537–2542, 2007.
- [122] John E Morley, Angela Marie Abbatecola, Josep M Argiles, Vickie Baracos, Juergen Bauer, Shalender Bhasin, Tommy Cederholm, Andrew J Stewart Coats, Steven R Cummings, William J Evans, et al. Sarcopenia with limited mobility: an international consensus. *Journal of the American Medical Directors Association*, 12(6):403–409, 2011.
- [123] Steven Morrison and Karl M Newell. Postural and resting tremor in the upper limb. *Clinical neurophysiology*, 111(4):651–663, 2000.
- [124] M Muthuraman, J Raethjen, H Hellriegel, G Deuschl, and U Heute. Imaging coherent

- sources of tremor related eeg activity in patients with parkinson's disease. In *2008 30th Annual International Conference of the IEEE Engineering in Medicine and Biology Society*, pages 4716–4719. IEEE, 2008.
- [125] Francesco Negro, Silvia Muceli, Anna Margherita Castronovo, Ales Holobar, and Dario Farina. Multi-channel intramuscular and surface emg decomposition by convolutive blind source separation. *Journal of neural engineering*, 13(2):026027, 2016.
- [126] Dan Negrut and Andrew Dyer. Adams/solver primer. *MSC. Software Documentation, Ann Arbor*, 2004.
- [127] Yijun Niu, Zhibin Song, and Jiansheng Dai. Kinematic analysis and optimization of a planar parallel compliant mechanism for self-alignment knee exoskeleton. *Mechanical Sciences*, 9(2):405–416, 2018.
- [128] Rory J O'Connor and Manohar U Kini. Non-pharmacological and non-surgical interventions for tremor: a systematic review. *Parkinsonism & related disorders*, 17(7):509–515, 2011.
- [129] Harish J Palanthandalam-Madapusi and Sachin Goyal. Is parkinsonian tremor a limit cycle? *Journal of Mechanics in Medicine and Biology*, 11(05):1017–1023, 2011.
- [130] Abhishek Pandala, Randall T Fawcett, Ugo Rosolia, Aaron D Ames, and Kaveh Akbari Hamed. Robust predictive control for quadrupedal locomotion: Learning to close the gap between reduced-and full-order models. *IEEE Robotics and Automation Letters*, 7(3):6622–6629, 2022.
- [131] James Parkinson. An essay on the shaking palsy. *The Journal of neuropsychiatry and clinical neurosciences*, 14(2):223–236, 2002.

- [132] Joel C Perry, Jacob Rosen, and Stephen Burns. Upper-limb powered exoskeleton design. *IEEE/ASME transactions on mechatronics*, 12(4):408–417, 2007.
- [133] Jan Raethjen, Michael Lindemann, Holger Schmaljohann, Roland Wenzelburger, Gerd Pfister, and Günther Deuschl. Multiple oscillators are causing parkinsonian and essential tremor. *Movement disorders: official journal of the Movement Disorder Society*, 15(1):84–94, 2000.
- [134] George N Reeke, Roman R Poznanski, Kenneth A Lindsay, Jay R Rosenberg, and Olaf Sporns. *Modeling in the neurosciences: from biological systems to neuromimetic robotics*. CRC Press, 2005.
- [135] Cameron N Riviere, R Scott Rader, and Nitish V Thakor. Adaptive cancelling of physiological tremor for improved precision in microsurgery. *IEEE Transactions on Biomedical Engineering*, 45(7):839–846, 1998.
- [136] E Rocon, JM Belda-Lois, JJ Sanchez-Lacuesta, and Jose L Pons. Pathological tremor management: Modelling, compensatory technology and evaluation. *Technology and Disability*, 16(1):3–18, 2004.
- [137] Eduardo Rocon, JM Belda-Lois, AF Ruiz, Mario Manto, Juan C Moreno, and Jose L Pons. Design and validation of a rehabilitation robotic exoskeleton for tremor assessment and suppression. *IEEE Transactions on neural systems and rehabilitation engineering*, 15(3):367–378, 2007.
- [138] Carlos M Roithmayr and Dewey H Hodges. Dynamics: theory and application of kane’s method, 2016.
- [139] Chad G Rose, Evan Pezent, Claudia K Kann, Ashish D Deshpande, and Marcia K

- O'Malley. Assessing wrist movement with robotic devices. *IEEE Transactions on Neural Systems and Rehabilitation Engineering*, 26(8):1585–1595, 2018.
- [140] G Webster Ross, Helen Petrovitch, Robert D Abbott, James Nelson, William Markesbery, Daron Davis, John Hardman, Lenore Launer, Kamal Masaki, Caroline M Tanner, et al. Parkinsonian signs and substantia nigra neuron density in decedents elders without pd. *Annals of Neurology: Official Journal of the American Neurological Association and the Child Neurology Society*, 56(4):532–539, 2004.
- [141] Patrick Salvia, Laurent Woestyn, José Henri David, Véronique Feipel, Serge Van, Sint Jan, Paul Klein, and Marcel Rooze. Analysis of helical axes, pivot and envelope in active wrist circumduction. *Clinical Biomechanics*, 15(2):103–111, 2000.
- [142] Massimo Sartori, David G Lloyd, and Dario Farina. Neural data-driven musculoskeletal modeling for personalized neurorehabilitation technologies (vol 63, pg 879, 2016). *IEEE Transactions on Biomedical Engineering*, 63(6):1341–1341, 2016.
- [143] Kazuya Sato, Takanori Nakashima, and Kazuhiro Tsuruta. A robust adaptive h-infinity control for robotic manipulators with input torque uncertainties. *International Journal of Advanced Mechatronic Systems*, 1(2):116–124, 2008.
- [144] Andr Schiele and Frans CT Van Der Helm. Kinematic design to improve ergonomics in human machine interaction. *IEEE Transactions on Neural Systems and Rehabilitation Engineering*, 14(4):456–469, 2006.
- [145] P Richard Schuurman, D Andries Bosch, Patrick MM Bossuyt, Gouke J Bonsel, Eus JW Van Someren, Rob MA De Bie, Maruschka P Merkus, and Johannes D Speelman. A comparison of continuous thalamic stimulation and thalamotomy for suppression of severe tremor. *New England Journal of Medicine*, 342(7):461–468, 2000.

- [146] Masatoshi Seki, Yuya Matsumoto, Takeshi Ando, Yo Kobayashi, Masakatsu G Fujie, Hiroshi Iijima, and Masanori Nagaoka. Development of robotic upper limb orthosis with tremor suppressibility and elbow joint movability. In *2011 IEEE International Conference on Systems, Man, and Cybernetics*, pages 729–735. IEEE, 2011.
- [147] Ajay Seth, Michael Sherman, Peter Eastman, and Scott Delp. Minimal formulation of joint motion for biomechanisms. *Nonlinear dynamics*, 62(1-2):291–303, 2010.
- [148] Ajay Seth, Jennifer L Hicks, Thomas K Uchida, Ayman Habib, Christopher L Dembia, James J Dunne, Carmichael F Ong, Matthew S DeMers, Apoorva Rajagopal, Matthew Millard, et al. Opensim: Simulating musculoskeletal dynamics and neuromuscular control to study human and animal movement. *PLoS computational biology*, 14(7): e1006223, 2018.
- [149] Talha Shahid, Darwin Gouwanda, Surya G Nurzaman, and Alpha A Gopalai. Moving toward soft robotics: A decade review of the design of hand exoskeletons. *Biomimetics*, 3(3):17, 2018.
- [150] Soroosh Shahtalebi, Seyed Farokh Atashzar, Rajni V Patel, and Arash Mohammadi. Hmfp-dbrnn: Real-time hand motion filtering and prediction via deep bidirectional rnn. *IEEE Robotics and Automation Letters*, 4(2):1061–1068, 2019.
- [151] Mohammed Shamroukh, Ihtisham Qasim Kalimullah, Alan Chacko, Shreya Sharad Barlingay, V Kalaichelvi, and Adhir Baran Chattopadhyay. Evaluation of control strategies in semi-active orthosis for suppression of upper limb pathological tremors. In *2017 International Conference on Innovations in Electrical, Electronics, Instrumentation and Media Technology (ICEEIMT)*, pages 75–80. IEEE, 2017.
- [152] Yang Shen, Peter Walker Ferguson, Ji Ma, and Jacob Rosen. Chapter 4 - upper limb wearable exoskeleton systems for rehabilitation: State of the art re-

- view and a case study of the exo-ul8—dual-arm exoskeleton system. In Raymond Kai-Yu Tong, editor, *Wearable Technology in Medicine and Health Care*, pages 71–90. Academic Press, 2018. ISBN 978-0-12-811810-8. doi: <https://doi.org/10.1016/B978-0-12-811810-8.00004-X>. URL <https://www.sciencedirect.com/science/article/pii/B978012811810800004X>.
- [153] Yang Shen, Jianwei Sun, Ji Ma, and Jacob Rosen. Admittance control scheme comparison of exo-ul8: A dual-arm exoskeleton robotic system. In *2019 IEEE 16th International Conference on Rehabilitation Robotics (ICORR)*, pages 611–617. IEEE, 2019.
- [154] Michael A Sherman, Ajay Seth, and Scott L Delp. Simbody: multibody dynamics for biomedical research. *Procedia Iutam*, 2:241–261, 2011.
- [155] Harvinder P Singh, Joseph J Dias, Harm Slijper, and Steven Hovius. Assessment of velocity, range, and smoothness of wrist circumduction using flexible electrogoniometry. *The Journal of hand surgery*, 37(11):2331–2339, 2012.
- [156] Alex J Smola and Bernhard Schölkopf. A tutorial on support vector regression. *Statistics and computing*, 14(3):199–222, 2004.
- [157] Tümay Sözen, Lale Özişik, and Nursel Çalık Başaran. An overview and management of osteoporosis. *European journal of rheumatology*, 4(1):46, 2017.
- [158] Lee Swallow and Elias Siores. Tremor suppression using smart textile fibre systems. *Journal of Fiber Bioengineering and Informatics*, 1(4):261–266, 2009.
- [159] Behzad Taheri. *Real-time pathological tremor identification and suppression in human arm via active orthotic devices*. PhD thesis, Southern Methodist University, 2013.

- [160] Behzad Taheri, David Case, and Edmond Richer. Adaptive suppression of severe pathological tremor by torque estimation method. *IEEE/ASME Transactions on Mechatronics*, 20(2):717–727, 2014.
- [161] M Takanokura, R Sugahara, N Miyake, K Ishiguro, T Muto, and K Sakamoto. Upper-limb orthoses implemented with air dashpots for suppression of pathological tremor in daily activities. In *ISB conference July*, pages 3–4, 2011.
- [162] Ronald R Tasker, M Munz, FSCK Junn, ZHT Kiss, K Davis, JO Dostrovsky, and AM Lozano. Deep brain stimulation and thalamotomy for tremor compared. In *Advances in Stereotactic and Functional Neurosurgery 12*, pages 49–53. Springer, 1997.
- [163] Sivanagaraja Tatinati, Kalyana C Veluvolu, Sun-Mog Hong, Win Tun Latt, and Wei Tech Ang. Physiological tremor estimation with autoregressive (ar) model and kalman filter for robotics applications. *IEEE Sensors Journal*, 13(12):4977–4985, 2013.
- [164] Sivanagaraja Tatinati, Kalyana C Veluvolu, and Wei Tech Ang. Multistep prediction of physiological tremor based on machine learning for robotics assisted microsurgery. *IEEE transactions on cybernetics*, 45(2):328–339, 2014.
- [165] Mary Ann Thenganatt and Joseph Jankovic. The relationship between essential tremor and parkinson’s disease. *Parkinsonism & related disorders*, 22:S162–S165, 2016.
- [166] Mary Ann Thenganatt and Elan D Louis. Distinguishing essential tremor from parkinson’s disease: bedside tests and laboratory evaluations. *Expert review of neurotherapeutics*, 12(6):687–696, 2012.
- [167] Jens Timmer, Siegfried Häußler, Michael Lauk, and C-H Lücking. Pathological tremors: Deterministic chaos or nonlinear stochastic oscillators? *Chaos: An Interdisciplinary Journal of Nonlinear Science*, 10(1):278–288, 2000.

- [168] Vadim Utkin and Hoon Lee. Chattering problem in sliding mode control systems. In *International Workshop on Variable Structure Systems, 2006. VSS'06.*, pages 346–350. IEEE, 2006.
- [169] Frederiek Van Den Bos, Arlene D Speelman, Monique Samson, Marten Munneke, Bastiaan R Bloem, and Harald JJ Verhaar. Parkinson’s disease and osteoporosis. *Age and ageing*, 42(2):156–162, 2012.
- [170] Arjan J Van Der Schaft and Hans Schumacher. *An introduction to hybrid dynamical systems*, volume 251. springer, 2007.
- [171] Kalyana C Veluvolu and Wei Tech Ang. Estimation of physiological tremor from accelerometers for real-time applications. *Sensors*, 11(3):3020–3036, 2011.
- [172] Carlijn A Vernooij, Raymond F Reynolds, and Martin Lakie. A dominant role for mechanical resonance in physiological finger tremor revealed by selective minimization of voluntary drive and movement. *Journal of neurophysiology*, 109(9):2317–2326, 2013.
- [173] Eric A Wan and Alex T Nelson. Dual extended kalman filter methods. *Kalman filtering and neural networks*, 123, 2001.
- [174] Eric A Wan and Rudolph Van Der Merwe. The unscented kalman filter for nonlinear estimation. In *Proceedings of the IEEE 2000 Adaptive Systems for Signal Processing, Communications, and Control Symposium (Cat. No. 00EX373)*, pages 153–158. Ieee, 2000.
- [175] © 2021 IEEE. Reprinted, with permission, from Jiamin Wang and Oumar Barry. Inverse optimal robust adaptive controller for upper limb rehabilitation exoskeletons with inertia and load uncertainties. *IEEE Robotics and Automation Letters*, 2021.

- [176] © 2021 IEEE. Reprinted, with permission, from Jiamin Wang and Oumar R Barry. Real-time identification of wrist kinematics via sparsity-promoting extended kalman filter based on ellipsoidal joint formulation. *IEEE Transactions on Biomedical Engineering*, 69(2):1003–1015, 2021.
- [177] Jiamin Wang and Oumar Barry. Multibody analysis and control of a full-wrist exoskeleton for tremor alleviation. *Journal of Biomechanical Engineering*, 2020.
- [178] Jiamin Wang and Oumar R Barry. Exploring data-driven modeling and analysis of nonlinear pathological tremors. *Mechanical Systems and Signal Processing*, 156:107659, 2021.
- [179] Jiamin Wang, Oumar Barry, Andrew J Kurdila, and Sujith Vijayan. On the dynamics and control of a full wrist exoskeleton for tremor alleviation. In *ASME 2019 Dynamic Systems and Control Conference*. American Society of Mechanical Engineers Digital Collection, 2017.
- [180] Jiamin Wang, Vinay R Kamidi, and Pinhas Ben-Tzvi. A multibody toolbox for hybrid dynamic system modeling based on nonholonomic symbolic formalism. In *ASME 2018 Dynamic Systems and Control Conference*, pages V003T29A003–V003T29A003. American Society of Mechanical Engineers, 2018.
- [181] Jiamin Wang, Sunit K. Gupta, and Oumar Barry. Modeling analysis of the wrist dynamics via an ellipsoidal joint. In *(To Appear) Dynamic Systems and Control Conference*. American Society of Mechanical Engineers, 2020.
- [182] Jiamin Wang, Zijian Ding, and Oumar Barry. Delay reduction in voluntary movement estimation for tremor alleviation via wearable exoskeletons. *(Submitted Manuscript)*, 2022.

- [183] Xiaofeng Wang, Xing Li, Jianhui Wang, Xiaoke Fang, and Xuefeng Zhu. Data-driven model-free adaptive sliding mode control for the multi degree-of-freedom robotic exoskeleton. *Information Sciences*, 327:246–257, 2016.
- [184] Ming Xin and SN Balakrishnan. A new method for suboptimal control of a class of non-linear systems. *Optimal Control Applications and Methods*, 26(2):55–83, 2005.
- [185] Chenguang Yang, Jing Luo, Yongping Pan, Zhi Liu, and Chun-Yi Su. Personalized variable gain control with tremor attenuation for robot teleoperation. *IEEE Transactions on Systems, Man, and Cybernetics: Systems*, 48(10):1759–1770, 2017.
- [186] Ningbo Yu and Chang Xu. An improved wrist kinematic model for human-robot interaction. *arXiv preprint arXiv:2002.05790*, 2020.
- [187] Ahmad Zahedi, Bin Zhang, Andong Yi, and Dingguo Zhang. A soft exoskeleton for tremor suppression equipped with flexible semiactive actuator. *Soft robotics*, 2020.
- [188] Amir Hosein Zamanian and Edmond Richer. Adaptive disturbance rejection controller for pathological tremor suppression with permanent magnet linear motor. In *ASME 2017 Dynamic Systems and Control Conference*. American Society of Mechanical Engineers Digital Collection, 2017.
- [189] Amir Hosein Zamanian and Edmond Richer. Adaptive notch filter for pathological tremor suppression using permanent magnet linear motor. *Mechatronics*, 63:102273, 2019.
- [190] Theresa A Zesiewicz, Abinaya Chari, Israt Jahan, Amber M Miller, and Kelly L Sullivan. Overview of essential tremor. *Neuropsychiatric disease and treatment*, 6:401, 2010.

- [191] Dingguo Zhang and Wei Tech Ang. Reciprocal emg controlled fes for pathological tremor suppression of forearm. In *2007 29th Annual International Conference of the IEEE Engineering in Medicine and Biology Society*, pages 4810–4813. IEEE, 2007.
- [192] Dingguo Zhang, Philippe Poignet, Antonio PL Bo, and Wei Tech Ang. Exploring peripheral mechanism of tremor on neuromusculoskeletal model: A general simulation study. *IEEE Transactions on Biomedical Engineering*, 56(10):2359–2369, 2009.
- [193] Dingguo Zhang, Philippe Poignet, Ferdinan Widjaja, and Wei Tech Ang. Neural oscillator based control for pathological tremor suppression via functional electrical stimulation. *Control Engineering Practice*, 19(1):74–88, 2011.
- [194] Fuzhen Zhang. *The Schur complement and its applications*, volume 4. Springer Science & Business Media, 2006.
- [195] Zhongkai Zhang, Jeremie Dequidt, Alexandre Kruszewski, Frederick Largilliere, and Christian Duriez. Kinematic modeling and observer based control of soft robot using real-time finite element method. In *2016 IEEE/RSJ International Conference on Intelligent Robots and Systems (IROS)*, pages 5509–5514. IEEE, 2016.
- [196] Yves Zimmermann, Emek Baris KüçükTABAK, Farbod Farshidian, Robert Riener, and Marco Hutter. Towards dynamic transparency: Robust interaction force tracking using multi-sensory control on an arm exoskeleton. In *IEEE/RSJ International Conference on Intelligent Robots and Systems (IROS 2020)(virtual)*, pages TuDT8–4, 2020.

# Appendices

# Appendix A

## Mathematical Proofs and Results

This appendix presents detailed and extensive mathematical proofs and results related to the work in this project.

### A.1 Explicit Solution of Translational Displacement in the Ellipsoidal Joint Wrist Model

The explicit solution of  $\mathbf{d}_{\text{wrist}}$  in terms of  $\boldsymbol{\xi}_{\text{wrist}}$  and  $\mathbf{c}_{\text{wrist},d}$  is

$$\mathbf{d}_{\text{wrist}} = \begin{bmatrix} z_{\text{wrist},d,1}/z_{\text{wrist},d,4} \\ z_{\text{wrist},d,2} \\ z_{\text{wrist},d,3}/z_{\text{wrist},d,4} \end{bmatrix} \quad (\text{A.1})$$

where

$$\begin{aligned} z_{\text{wrist},d,1} = & - \left[ c_{\text{wrist},d,3}^2 \cos(z_{\text{wrist},\Omega,\bar{x}}) \left( \sin(z_{\text{wrist},\Omega,\bar{x}}) \sin(z_{\text{wrist},\Omega,\bar{y}}) \right. \right. \\ & - c_{\text{wrist},d,1}^2 \sin(z_{\text{wrist},\Omega,\bar{x}}) \sin(z_{\text{wrist},\Omega,\bar{y}}) \\ & + (c_{\text{wrist},d,1}^2 - c_{\text{wrist},d,2}^2) \sin(z_{\text{wrist},\Omega,\bar{x}}) \sin(z_{\text{wrist},\Omega,\bar{y}}) \cos^2(z_{\text{wrist},\Omega,\bar{z}}) \\ & \left. \left. + (c_{\text{wrist},d,2}^2 - c_{\text{wrist},d,1}^2) \cos(z_{\text{wrist},\Omega,\bar{y}}) \sin(z_{\text{wrist},\Omega,\bar{z}}) \cos(z_{\text{wrist},\Omega,\bar{z}}) \right) \right] \quad (\text{A.2a}) \end{aligned}$$

$$\begin{aligned}
z_{\text{wrist},d,2} = & \left( c_{\text{wrist},d,3}^2 \sin^2(z_{\text{wrist},\Omega,\bar{x}}) - c_{\text{wrist},d,1}^2 \sin^2(z_{\text{wrist},\Omega,\bar{z}}) \sin^2(z_{\text{wrist},\Omega,\bar{x}}) \right. \\
& + c_{\text{wrist},d,1}^2 \sin^2(z_{\text{wrist},\Omega,\bar{z}}) + c_{\text{wrist},d,2}^2 \sin^2(z_{\text{wrist},\Omega,\bar{z}}) \sin^2(z_{\text{wrist},\Omega,\bar{x}}) \\
& \left. - c_{\text{wrist},d,2}^2 \sin^2(z_{\text{wrist},\Omega,\bar{z}}) - c_{\text{wrist},d,2}^2 \sin^2(z_{\text{wrist},\Omega,\bar{x}}) + c_{\text{wrist},d,2}^2 \right)^{0.5} \quad (\text{A.2b})
\end{aligned}$$

$$\begin{aligned}
z_{\text{wrist},d,3} = & - \left[ c_{\text{wrist},d,3}^2 \cos(z_{\text{wrist},\Omega,\bar{x}}) \left( \cos(z_{\text{wrist},\Omega,\bar{y}}) \sin(z_{\text{wrist},\Omega,\bar{x}}) \right. \right. \\
& - c_{\text{wrist},d,1}^2 \cos(z_{\text{wrist},\Omega,\bar{y}}) \sin(z_{\text{wrist},\Omega,\bar{x}}) \\
& + (c_{\text{wrist},d,1}^2 - c_{\text{wrist},d,2}^2) \cos(z_{\text{wrist},\Omega,\bar{y}}) \sin(z_{\text{wrist},\Omega,\bar{x}}) \cos^2(z_{\text{wrist},\Omega,\bar{z}}) \\
& \left. \left. + (c_{\text{wrist},d,1}^2 - c_{\text{wrist},d,2}^2) \sin(z_{\text{wrist},\Omega,\bar{z}}) \sin(z_{\text{wrist},\Omega,\bar{y}}) \cos(z_{\text{wrist},\Omega,\bar{z}}) \right) \right] \quad (\text{A.2c})
\end{aligned}$$

$$\begin{aligned}
z_{\text{wrist},d,4} = & \left( - c_{\text{wrist},d,3}^2 \cos^2(z_{\text{wrist},\Omega,\bar{x}}) + c_{\text{wrist},d,3}^2 - c_{\text{wrist},d,1}^2 \cos^2(z_{\text{wrist},\Omega,\bar{z}}) \cos^2(z_{\text{wrist},\Omega,\bar{x}}) \right. \\
& \left. + c_{\text{wrist},d,1}^2 \cos^2(z_{\text{wrist},\Omega,\bar{x}}) + c_{\text{wrist},d,2}^2 \cos^2(z_{\text{wrist},\Omega,\bar{z}}) \cos^2(z_{\text{wrist},\Omega,\bar{x}}) \right)^{0.5} \quad (\text{A.2d})
\end{aligned}$$

Here,  $\mathbf{z}_{\text{wrist},\Omega} = [z_{\text{wrist},\Omega,\bar{x}}, z_{\text{wrist},\Omega,\bar{y}}, z_{\text{wrist},\Omega,\bar{z}}]^T$  is the  $y$ - $x$ - $z$  sequenced Euler angles that satisfies

$$\mathbf{\Omega}_{\text{wrist}} = \mathbf{\Omega}_{\bar{y}}(z_{\text{wrist},\Omega,\bar{y}}) \mathbf{\Omega}_{\bar{x}}(z_{\text{wrist},\Omega,\bar{x}}) \mathbf{\Omega}_{\bar{z}}(z_{\text{wrist},\Omega,\bar{z}}) \quad (\text{A.3})$$

## A.2 Lyapunov Stability of User PID Controller

The stability of Eq. (4.16) can be obtained locally in the vicinity of its equilibrium (where  $\mathbf{y} \approx \dot{\mathbf{r}}_{\text{user}}$ ). Based on (MA. 8) which states the low activity of voluntary movement, we assume that  $\ddot{\mathbf{r}}_{\text{user}} \approx \mathbf{0}$  and  $\dot{\mathbf{y}} \approx \mathbf{0}$ , which leads to a modified control system

$$\mathbf{x}_{\text{user}} = \begin{bmatrix} \boldsymbol{\epsilon}_{\text{user},I} + K_I^{-1} \mathbf{g}_y \\ \boldsymbol{\epsilon}_{\text{user},P} \\ \boldsymbol{\epsilon}_{\text{user},D} \end{bmatrix}; \quad \dot{\mathbf{x}}_{\text{user},0} \approx \dot{\mathbf{x}}_{\text{user}} = \begin{bmatrix} \boldsymbol{\epsilon}_{\text{user},P} \\ \boldsymbol{\epsilon}_{\text{user},D} \\ \mathbf{M}_y^{-1}(\mathbf{u}_{\text{user},y} - \mathbf{g}_y) \end{bmatrix} = \mathbf{A}_{\text{user}} \mathbf{x}_{\text{user}} \quad (\text{A.4})$$

where the state matrix  $\mathbf{A} \in \mathbb{R}^{3n_q \times 3n_q}$  is defined as

$$\mathbf{A}_{\text{user}} = \begin{bmatrix} \mathbf{0} & \mathbf{I} & \mathbf{0} \\ \mathbf{0} & \mathbf{0} & \mathbf{I} \\ -K_I \mathbf{M}_y^{-1} & -K_P \mathbf{M}_y^{-1} & -K_D \mathbf{M}_y^{-1} \end{bmatrix} \quad (\text{A.5})$$

Hence, the local stability of Eq. (A.4) at  $\mathbf{x}_{\text{user}} = \mathbf{0}$  can be obtained via Lyapunov Stability [89]. Here, we design a Lyapunov-like function  $\mathcal{V}_{\text{user}}(\mathbf{x}_{\text{user}})$  as

$$\mathcal{V}_{\text{user}}(t) = \mathbf{x}_{\text{user}}^T \mathcal{P} \mathbf{x}_{\text{user}} \quad (\text{A.6})$$

where  $\mathcal{P} = \mathcal{P}^T > 0$  so that  $\mathcal{V}_{\text{user}} \geq 0$ , and  $\mathcal{V}_{\text{user}} = 0$  iff.  $\mathbf{x}_{\text{user}} = \mathbf{0}$ . The 1st order time derivative  $\dot{\mathcal{V}}_{\text{user}}$  can be written as

$$\dot{\mathcal{V}}_{\text{user}} = \mathbf{x}_{\text{user}}^T (\mathbf{A}_{\text{user}}^T \mathcal{P} + \mathcal{P} \mathbf{A}_{\text{user}}) \mathbf{x}_{\text{user}} \quad (\text{A.7})$$

In order to find a matrix  $\mathcal{Q} = \mathcal{Q}^T \geq 0$  so that

$$\mathbf{A}_{\text{user}}^T \mathcal{P} + \mathcal{P} \mathbf{A}_{\text{user}} = -\mathcal{Q} \quad (\text{A.8})$$

which leads to  $\dot{\mathcal{V}}_{\text{user}} \leq 0$  (where  $\dot{\mathcal{V}}_{\text{user}} = 0$  iff.  $\mathbf{x}_{\text{user}} = \mathbf{0}$ ) and thus system stability,  $\mathbf{A}$  is required to be a Hurwitz matrix. Since  $\mathbf{M}_y = \mathbf{M}_y^T > 0$ , the eigenvalues  $z_A$  of  $\mathbf{A}$  can be solved from a total of  $n_q$  characteristic equations

$$z_{M,y,i} z_A^3 + K_D z_A^2 + K_P z_A + K_I = 0 \quad (i = 1, 2, \dots, n_q) \quad (\text{A.9})$$

where  $z_{M,y,i} > 0$  is the  $i$ th eigenvalue of  $\mathbf{M}_y$ . The Routh-Hurwitz Criterion for  $\mathbf{A}_{\text{user}}$  requires that the control parameters satisfy  $K_P K_D > K_I z_{M,y,i}$  for every characteristic equation. This

requirement can be easily fulfilled if the human-exoskeleton system has small inertia.

### A.3 Lyapunov Stability of PD and SMC Controllers

The feedforward controller with MRAC component Eq. (4.24) can be paired with both PD and SMC controllers in Eq. (4.20). The stability proofs is carried out under the condition that there is no disturbance in the system, i.e.,  $\mathbf{w} = \mathbf{0}$ .

For both control systems, we adopt the Lyapunov-like function  $\mathcal{V}_{\text{MRAC}}(\mathbf{x}, \hat{\mathbf{p}})$  defined as

$$\begin{aligned} \mathcal{V}_{\text{MRAC}}(\mathbf{x}, \hat{\mathbf{p}}) &= \frac{1}{2} \mathbf{x}^T \begin{bmatrix} \mathbf{K}_1 + \mathbf{K}_\epsilon \mathbf{M}_y \mathbf{K}_\epsilon & \mathbf{K}_\epsilon \mathbf{M}_y \\ \mathbf{M}_y \mathbf{K}_\epsilon & \mathbf{M}_y \end{bmatrix} \mathbf{x} + \frac{1}{2} \tilde{\mathbf{p}}^T \mathbf{\Gamma} \tilde{\mathbf{p}} \\ &= (\boldsymbol{\chi}^T \mathbf{M}_y \boldsymbol{\chi} + \boldsymbol{\epsilon}^T \mathbf{K}_1 \boldsymbol{\epsilon} + \tilde{\mathbf{p}}^T \mathbf{\Gamma} \tilde{\mathbf{p}}) / 2 \end{aligned} \quad (\text{A.10})$$

where  $\mathbf{K}_1 \in \mathbb{R}^{n_q \times n_q}$  is a positive definite matrix; and  $\tilde{\mathbf{p}} = \hat{\mathbf{p}} - \mathbf{p} \in \mathbb{R}^{n_p}$  is the estimation error. Hence  $\mathcal{V}_{\text{MRAC}}(\mathbf{x}, \hat{\mathbf{p}})$  satisfies  $\mathcal{V}_{\text{MRAC}}(\mathbf{x}, \hat{\mathbf{p}}) \geq 0$ , and  $\mathcal{V}_{\text{MRAC}}(\mathbf{x}, \hat{\mathbf{p}}) = 0$  iff.  $\mathbf{x} = \mathbf{0}$  and  $\hat{\mathbf{p}} = \mathbf{p}$ . Since it is assumed in (MA. 4) that  $\dot{\mathbf{p}} \approx \mathbf{0}$ , taking the first order time derivative of  $\mathcal{V}_{\text{MRAC}}$  yields

$$\dot{\mathcal{V}}_{\text{MRAC}} = \boldsymbol{\chi}^T (-\mathbf{M}_y \ddot{\mathbf{r}}_y - \mathbf{C}_y \dot{\mathbf{y}} - \mathbf{g}_y + \mathbf{u}_{\text{user}} + \mathbf{M}_y \mathbf{K}_\epsilon \dot{\boldsymbol{\epsilon}}) + (\boldsymbol{\chi}^T \dot{\mathbf{M}}_y \boldsymbol{\chi}) / 2 + \boldsymbol{\epsilon}^T \mathbf{K}_1 \dot{\boldsymbol{\epsilon}} + \tilde{\mathbf{p}}^T \mathbf{\Gamma} \dot{\tilde{\mathbf{p}}} \quad (\text{A.11})$$

After incorporating the error related terms in Eq. (4.19), the feedforward controller design

with MRAC in Eq. (4.24), and the relationship in Eq. (4.26), we obtain

$$\begin{aligned}
\dot{\mathcal{V}}_{\text{MRAC}} &= \boldsymbol{\chi}^T(-\mathbf{M}_y\dot{\boldsymbol{\zeta}} - \mathbf{C}_y\boldsymbol{\zeta} - \mathbf{g}_y + \mathbf{M}_{y,0}\dot{\boldsymbol{\zeta}} + \mathbf{C}_{y,0}\boldsymbol{\zeta} + \mathbf{g}_{y,0} + \mathbf{J}_p^T\hat{\mathbf{p}} + \mathbf{C}_y\boldsymbol{\zeta} - \mathbf{C}_y\dot{\mathbf{y}} + \mathbf{u}_{\text{user,fb}}) \\
&\quad + (\boldsymbol{\chi}^T\dot{\mathbf{M}}_y\boldsymbol{\chi})/2 + \boldsymbol{\epsilon}^T\mathbf{K}_1\dot{\boldsymbol{\epsilon}} + \tilde{\mathbf{p}}^T\boldsymbol{\Gamma}\dot{\tilde{\mathbf{p}}} \\
&= \boldsymbol{\chi}^T(-\mathbf{J}_p^T\mathbf{p} + \mathbf{J}_p^T\hat{\mathbf{p}} - \mathbf{C}_y\boldsymbol{\chi} + \mathbf{u}_{\text{user,fb}}) + (\boldsymbol{\chi}^T\dot{\mathbf{M}}_y\boldsymbol{\chi})/2 + \boldsymbol{\epsilon}^T\mathbf{K}_1\dot{\boldsymbol{\epsilon}} + \tilde{\mathbf{p}}^T\boldsymbol{\Gamma}\dot{\tilde{\mathbf{p}}} \\
&= \boldsymbol{\chi}^T\mathbf{u}_{\text{user,fb}} + \boldsymbol{\epsilon}^T\mathbf{K}_1\dot{\boldsymbol{\epsilon}} + (\boldsymbol{\chi}^T(\dot{\mathbf{M}}_y - 2\mathbf{C}_y)\boldsymbol{\chi})/2 + \tilde{\mathbf{p}}^T\boldsymbol{\Gamma}(\dot{\tilde{\mathbf{p}}} + \boldsymbol{\Gamma}^{-1}\mathbf{J}_p\boldsymbol{\chi}) \tag{A.12}
\end{aligned}$$

For a multibody system,  $\dot{\mathbf{M}}_y - 2\mathbf{C}_y$  is a skew matrix so that  $\boldsymbol{\chi}^T(\dot{\mathbf{M}}_y - 2\mathbf{C}_y)\boldsymbol{\chi} = 0$  [17]. Based on the uncertain parameter update law in Eq. (4.26), we can eliminate two of the terms in  $\dot{\mathcal{V}}_{\text{MRAC}}$ , which leads to

$$\dot{\mathcal{V}}_{\text{MRAC}} = \boldsymbol{\chi}^T\mathbf{u}_{\text{user,fb}} + \boldsymbol{\epsilon}^T\mathbf{K}_1\dot{\boldsymbol{\epsilon}} \tag{A.13}$$

From here, the stability proof branches into the cases for PD and SMC controllers:

(1) In the case of PD feedback controller where  $\mathbf{u}_{\text{user,fb}} = \mathbf{u}_{\text{fb,PD}}$  from Eq. (4.20), we have

$$\begin{aligned}
\dot{\mathcal{V}}_{\text{MRAC,PD}} &= -\boldsymbol{\chi}^T\mathbf{K}_\chi\boldsymbol{\chi} + \boldsymbol{\epsilon}^T\mathbf{K}_1\dot{\boldsymbol{\epsilon}} \\
&= -\boldsymbol{\chi}^T(\mathbf{K}_\chi - \mathbf{K}_2)\boldsymbol{\chi} - \dot{\boldsymbol{\epsilon}}^T\mathbf{K}_2\dot{\boldsymbol{\epsilon}} - \boldsymbol{\epsilon}^T(2\mathbf{K}_2\mathbf{K}_\epsilon - \mathbf{K}_1)\dot{\boldsymbol{\epsilon}} - \boldsymbol{\epsilon}^T\mathbf{K}_\epsilon\mathbf{K}_2\mathbf{K}_\epsilon\boldsymbol{\epsilon} \\
&= -\boldsymbol{\chi}^T(\mathbf{K}_\chi - \mathbf{K}_2)\boldsymbol{\chi} - \dot{\boldsymbol{\epsilon}}^T\mathbf{K}_2\dot{\boldsymbol{\epsilon}} - \boldsymbol{\epsilon}^T\mathbf{K}_\epsilon\mathbf{K}_2\mathbf{K}_\epsilon\boldsymbol{\epsilon} \tag{A.14}
\end{aligned}$$

where  $\mathbf{K}_2 = \mathbf{K}_2^T > 0$ . It is required that  $(\mathbf{K}_\chi - \mathbf{K}_2) > 0$ , and: (1)  $\mathbf{K}_2 = \mathbf{I}_{n_q}/2$  for  $\mathbf{K}_\epsilon = \mathbf{K}_1$ ; or (2)  $\mathbf{K}_2 = \mathbf{K}_\epsilon^{-1}\mathbf{K}_1/2 = \mathbf{K}_1\mathbf{K}_\epsilon^{-1}/2$  for diagonal  $\mathbf{K}_\epsilon$  and  $\mathbf{K}_1$  matrices. Thus, there exists a smooth function  $Q_{\text{PD}}(\mathbf{x}) \geq 0$  ( $Q = 0$  iff.  $\mathbf{x} = \mathbf{0}$ ) so that

$$\dot{\mathcal{V}}_{\text{MRAC,PD}} \leq -Q_{\text{PD}} \tag{A.15}$$

and  $\dot{\mathcal{V}}_{\text{MRAC,PD}} = -Q_{\text{PD}}$  iff.  $\mathbf{x} = \mathbf{0}$ .

(2) In the case of SMC feedback controller where  $\mathbf{u}_{\text{user,fb}} = \mathbf{u}_{\text{fb,SMC}}$  from Eq. (4.20), we have

$$\begin{aligned}\dot{\mathcal{V}}_{\text{MRAC,SMC}} &= -\boldsymbol{\chi}^T \mathbf{K}_{\text{SMC}} \mathbf{f}_{\text{SMC}}(\boldsymbol{\chi}) - \boldsymbol{\chi}^T \mathbf{K}_{\boldsymbol{\chi}} \boldsymbol{\chi} + \boldsymbol{\epsilon}^T \mathbf{K}_1 \dot{\boldsymbol{\epsilon}} \\ &= -(|\boldsymbol{\chi}|)^T \mathbf{K}_{\text{SMC}} \mathbf{f}_{\text{SMC}}(|\boldsymbol{\chi}|) - \boldsymbol{\chi}^T (\mathbf{K}_{\boldsymbol{\chi}} - \mathbf{K}_2) \boldsymbol{\chi} - \dot{\boldsymbol{\epsilon}}^T \mathbf{K}_2 \dot{\boldsymbol{\epsilon}} - \boldsymbol{\epsilon}^T \mathbf{K}_{\boldsymbol{\epsilon}} \mathbf{K}_2 \mathbf{K}_{\boldsymbol{\epsilon}} \boldsymbol{\epsilon}\end{aligned}\tag{A.16}$$

where  $\mathbf{K}_2 = \mathbf{K}_2^T > 0$ . Similar to the previous case of PD controller, it is required that  $(\mathbf{K}_{\boldsymbol{\chi}} - \mathbf{K}_2) > 0$ , and: (1)  $\mathbf{K}_2 = \mathbf{I}_{n_q}/2$  for  $\mathbf{K}_{\boldsymbol{\epsilon}} = \mathbf{K}_1$ ; or (2)  $\mathbf{K}_2 = \mathbf{K}_{\boldsymbol{\epsilon}}^{-1} \mathbf{K}_1/2 = \mathbf{K}_1 \mathbf{K}_{\boldsymbol{\epsilon}}^{-1}/2$  for diagonal  $\mathbf{K}_{\boldsymbol{\epsilon}}$  and  $\mathbf{K}_1$  matrices. Finally, for the gain switching term, since  $\mathbf{K}_{\text{SMC}}$  is positive definite and diagonal, based on the conditions in Eq. (4.22c), we obtain that  $-(|\boldsymbol{\chi}|)^T \mathbf{K}_{\text{SMC}} \mathbf{f}_{\text{SMC}}(|\boldsymbol{\chi}|) < 0$  for any  $\boldsymbol{\chi} \neq \mathbf{0}$ . Thus, there exists a smooth function  $Q(\mathbf{x}) \geq 0$  ( $Q = 0$  iff.  $\mathbf{x} = \mathbf{0}$ ) so that

$$\dot{\mathcal{V}}_{\text{MRAC,SMC}} \leq -Q_{\text{SMC}}\tag{A.17}$$

and  $\dot{\mathcal{V}}_{\text{MRAC,SMC}} = -Q_{\text{SMC}}$  iff.  $\mathbf{x} = \mathbf{0}$ .

Hence, both  $\mathbf{u}_{\text{fb,PD}}$  and  $\mathbf{u}_{\text{fb,SMC}}$  from Eq. (4.20), when paired with feedforward controller with MRAC  $\mathbf{u}_{\text{ff}}$  in Eq. (4.24) are asymptotically stabilizing controllers.

## A.4 Lyapunov Stability of IO-RAC

The Lyapunov function in Eq. (4.37) is positive except  $\mathcal{V}_{\text{IORAC}}(\mathbf{0}, \mathbf{p}) = 0$ , which can be shown by rearranging  $\mathcal{V}$  as

$$\mathcal{V}_{\text{IORAC}} = (\boldsymbol{\chi}^T \mathbf{M}_y \boldsymbol{\chi} + \boldsymbol{\epsilon}^T \mathbf{K}_1 \boldsymbol{\epsilon} + \tilde{\mathbf{p}}^T \boldsymbol{\Gamma} \tilde{\mathbf{p}})/2\tag{A.18}$$

Notice that the Lyapunov function is designed by utilizing the symmetric positive definiteness of  $\mathbf{M}_y$ . To obtain asymptotic stability, it is required that the time-derivative  $\dot{\mathcal{V}}_{\text{IORAC}} < 0$  except that  $\dot{\mathcal{V}}_{\text{IORAC}}(\mathbf{0}, \mathbf{p}) = 0$ . Since it is assumed in (MA. 4) that  $\dot{\mathbf{p}} \approx \mathbf{0}$ , the time-derivative  $\dot{\mathcal{V}}_{\text{IORAC}}$  can be calculated as

$$\dot{\mathcal{V}}_{\text{IORAC}} = \boldsymbol{\chi}^T \mathbf{M}_y \dot{\boldsymbol{\chi}} + (\boldsymbol{\chi}^T \dot{\mathbf{M}}_y \boldsymbol{\chi})/2 + \boldsymbol{\epsilon}^T \mathbf{K}_1 \dot{\boldsymbol{\epsilon}} + \tilde{\mathbf{p}}^T \boldsymbol{\Gamma} \dot{\tilde{\mathbf{p}}} \quad (\text{A.19})$$

Based on Eq. (4.18), Eq. (A.19) can be transformed into

$$\begin{aligned} \dot{\mathcal{V}}_{\text{IORAC}} = & \boldsymbol{\chi}^T (-\mathbf{M}_y \ddot{\mathbf{r}}_y - \mathbf{C}_y \dot{\mathbf{q}} - \mathbf{g}_y + \mathbf{u}_{\text{exo},y} + \mathbf{J}_{w,y}^T \mathbf{w} + \mathbf{M}_y \mathbf{K}_\epsilon \dot{\boldsymbol{\epsilon}}) \\ & + (\boldsymbol{\chi}^T \dot{\mathbf{M}}_y \boldsymbol{\chi})/2 + \boldsymbol{\epsilon}^T \mathbf{K}_1 \dot{\boldsymbol{\epsilon}} + \tilde{\mathbf{p}}^T \boldsymbol{\Gamma} \dot{\tilde{\mathbf{p}}} \end{aligned} \quad (\text{A.20})$$

According to the Eq. (4.11) and Eq. (4.37), the Lie derivative of  $\mathcal{V}$  with respect to  $\boldsymbol{\mathcal{W}}$  and  $\boldsymbol{\mathcal{U}}$  are respectively calculated as

$$\frac{\partial \mathcal{V}_{\text{IORAC}}}{\partial \mathbf{x}} = \mathbf{x}^T \begin{bmatrix} \mathbf{K}_1 + \mathbf{K}_\epsilon \mathbf{M}_y \mathbf{K}_\epsilon & \mathbf{K}_\epsilon \mathbf{M}_y \\ \mathbf{M}_y \mathbf{K}_\epsilon & \mathbf{M}_y \end{bmatrix} \quad (\text{A.21a})$$

$$\mathbf{L}_{\boldsymbol{\mathcal{W}}} \mathcal{V}_{\text{IORAC}} = \boldsymbol{\chi}^T \mathbf{J}_{w,y}^T; \quad \mathbf{L}_{\boldsymbol{\mathcal{U}}} \mathcal{V}_{\text{IORAC}} = \boldsymbol{\chi}^T \quad (\text{A.21b})$$

Based on the auxiliary system in Eq. (4.28) and the gamma function selection from Eq. (4.33), the  $l^2$  perturbation/disturbance attenuation assumes that the perturbation/disturbance  $\mathbf{w}_{0,l2}$  is bounded by  $\mathbf{x}$  through

$$\mathbf{w}_{0,l2} = f_\gamma(2\|\mathbf{L}_{\boldsymbol{\mathcal{W}}} \mathcal{V}_{\text{IORAC}}\|) ((\mathbf{L}_{\boldsymbol{\mathcal{W}}} \mathcal{V}_{\text{IORAC}})^T / \|\mathbf{L}_{\boldsymbol{\mathcal{W}}} \mathcal{V}_{\text{IORAC}}\|^2) = \mathbf{J}_{w,y} \boldsymbol{\chi} \quad (\text{A.22})$$

Hence, bringing  $\mathbf{u}_{\text{exo},y}$  from Eq. (4.36a) and  $\mathbf{w} = \mathbf{w}_{0,l2}$  from Eq. (A.22) into Eq. (A.20)

yields

$$\begin{aligned}\dot{V}_{\text{IORAC}} &= \boldsymbol{\chi}^T(-c_{R,1}\mathbf{K}_R^{-1} + \mathbf{J}_{w,y}^T\mathbf{J}_{w,y})\boldsymbol{\chi} + (\boldsymbol{\chi}^T(\dot{\mathbf{M}}_y - 2\mathbf{C}_y)\boldsymbol{\chi})/2 \\ &\quad + \boldsymbol{\epsilon}^T\mathbf{K}_1\dot{\boldsymbol{\epsilon}} + \tilde{\mathbf{p}}^T\boldsymbol{\Gamma}(\dot{\tilde{\mathbf{p}}} + \boldsymbol{\Gamma}^{-1}\mathbf{J}_p\boldsymbol{\chi})\end{aligned}\tag{A.23}$$

Again, for a multibody system,  $\dot{\mathbf{M}}_y - 2\mathbf{C}_y$  is a skew matrix [17] so that  $\boldsymbol{\chi}^T(\dot{\mathbf{M}}_y - 2\mathbf{C}_y)\boldsymbol{\chi} = 0$ . Finally, by inserting the expressions of  $\dot{\tilde{\mathbf{p}}}$  and  $\mathbf{K}_R^{-1}$  respectively from Eq. (4.36b) and Eq. (4.35), Eq. (A.23) is transformed into

$$\begin{aligned}\dot{V}_{\text{IORAC}} &= \boldsymbol{\chi}^T\mathbf{J}_{w,y}^T\mathbf{J}_{w,y}\boldsymbol{\chi} + \boldsymbol{\epsilon}^T\mathbf{K}_1\dot{\boldsymbol{\epsilon}} - c_{R,1}\boldsymbol{\chi}^T\mathbf{K}_R^{-1}\boldsymbol{\chi} \\ &= -(c_{R,1} - 1)\boldsymbol{\chi}^T\mathbf{J}_{w,y}^T\mathbf{J}_{w,y}\boldsymbol{\chi} - c_{R,1}\boldsymbol{\chi}^T(\mathbf{K}_\chi - \mathbf{K}_2/c_{R,1})\boldsymbol{\chi} \\ &\quad - \dot{\boldsymbol{\epsilon}}^T\mathbf{K}_2\dot{\boldsymbol{\epsilon}} - \boldsymbol{\epsilon}^T\mathbf{K}_\epsilon\mathbf{K}_2\mathbf{K}_\epsilon\boldsymbol{\epsilon}\end{aligned}\tag{A.24}$$

where  $\mathbf{K}_2 \in \mathbb{R}^{n_q \times n_q}$ . It is required that  $(\mathbf{K}_\chi - \mathbf{K}_2/c_{R,1}) > 0$ , and: (1)  $\mathbf{K}_2 = \mathbf{I}_{n_q}/2$  for  $\mathbf{K}_\epsilon = \mathbf{K}_1$ ; or (2)  $\mathbf{K}_2 = \mathbf{K}_\epsilon^{-1}\mathbf{K}_1/2 = \mathbf{K}_1\mathbf{K}_\epsilon^{-1}/2$  for diagonal  $\mathbf{K}_\epsilon$  and  $\mathbf{K}_1$  matrices. Thus, with any  $c_{R,1} \geq 2$ , there exists a smooth function  $Q_{\text{IORAC}}(\mathbf{x}) \geq 0$  ( $Q_{\text{IORAC}} = 0$  iff.  $\mathbf{x} = \mathbf{0}$ ) so that

$$\dot{V}_{\text{IORAC}} \leq -Q_{\text{IORAC}}\tag{A.25}$$

and  $\dot{V}_{\text{IORAC}} = -Q_{\text{IORAC}}$  iff.  $\mathbf{x} = \mathbf{0}$ . Hence, IO-RAC from Eq. (4.36) asymptotically can stabilize the control system in Eq. (4.18) by converging the Lyapunov function in Eq. (4.37).

## A.5 Optimality of IO-RAC

The cost function  $\mathcal{J}_{\text{IORAC}}$  in Eq. (4.38) is slightly different from  $\mathcal{J}_0$  in Eq. (4.32). The difference lies in  $z_{J,2}$  from Eq. (4.39b), where the term  $\boldsymbol{\chi}^T\mathbf{M}_y\mathbf{K}_\epsilon\dot{\boldsymbol{\epsilon}}$  originally contained in

$L_{\mathcal{F}}\mathcal{V}_{\text{IORAC}}$  is compensated by the adaptive control term. However, the  $\mathcal{J}_{\text{IORAC}}$  can still be proved meaningful. Based on Eq. (4.33) and Eq. (A.21b), it can be observed from Eq. (A.24) that

$$\dot{\mathcal{V}}_{\text{IORAC}} = z_{J,2} + f_{\gamma}(2\|L\mathbf{w}\mathcal{V}_{\text{IORAC}}\|) - c_{R,1}L\mathbf{u}\mathcal{V}_{\text{IORAC}}\mathbf{K}_R^{-1}(L\mathbf{u}\mathcal{V}_{\text{IORAC}})^{\text{T}} \quad (\text{A.26})$$

With  $c_{R,1} \geq 2$  and  $c_{R,2} \in (0, 2]$ , according to Eq. (4.39a) and Eq. (A.25), we obtain

$$\begin{aligned} z_{J,1}(\mathbf{x}) &= -2c_{R,1}\dot{\mathcal{V}}_{\text{IORAC}} + c_{R,1}(2 - c_{R,2})f_{\gamma}(2\|L\mathbf{w}\mathcal{V}_{\text{IORAC}}\|) \\ &\quad + c_{R,1}(c_{R,1} - 2)L\mathbf{u}\mathcal{V}_{\text{IORAC}}\mathbf{K}_R^{-1}(L\mathbf{u}\mathcal{V}_{\text{IORAC}})^{\text{T}} \geq Q_{\text{IORAC}} \end{aligned} \quad (\text{A.27})$$

and  $z_{J,1} = 0$  iff.  $\mathbf{x} = \mathbf{0}$ . Therefore,  $\mathcal{J}_{\text{IORAC}}$  is a meaningful cost function [97, 109], since the positive definite term  $z_{J,1}$  penalizes large tracking error  $\mathbf{x}$ , and the positive definite term  $\mathbf{u}_{\text{fb,IORC}}^{\text{T}}\mathbf{K}_R\mathbf{u}_{\text{fb,IORC}}$  penalizes large feedback control effort  $\mathbf{u}_{\text{fb,IORC}}$ . The trade-off between tracking error and input effort can be adjusted by control parameters (i.e.,  $\mathbf{K}_{\epsilon}$ ,  $\mathbf{K}_{\chi}$ , and  $\mathbf{J}_{w,y}$ ).

To prove that the proposed controller in Eq. (4.36) optimizes the cost function  $\mathcal{J}_{\text{IORAC}}$ , based on  $\boldsymbol{\chi}^{\text{T}}(\dot{\mathbf{M}}_y - 2\mathbf{C}_y)\boldsymbol{\chi} = 0$ , we first obtain from Eq. (4.36) and Eq. (A.20) that

$$\begin{aligned} z_{J,2} &= (\dot{\mathcal{V}}_{\text{IORAC}} - \boldsymbol{\chi}^{\text{T}}(-\mathbf{M}_y\boldsymbol{\zeta} - \mathbf{C}_y\boldsymbol{\zeta} - \mathbf{g}_y + \mathbf{u}_{\text{ff}} + \mathbf{u}_{\text{fb,IORC}} + \mathbf{J}_{w,y}^{\text{T}}\mathbf{w}) - \tilde{\mathbf{p}}^{\text{T}}\boldsymbol{\Gamma}\dot{\hat{\mathbf{p}}}) \\ &= \dot{\mathcal{V}}_{\text{IORAC}} - \boldsymbol{\chi}^{\text{T}}(\mathbf{u}_{\text{fb,IORC}} + \mathbf{J}_{w,y}^{\text{T}}\mathbf{w}) \end{aligned} \quad (\text{A.28})$$

With Eq. (4.33), Eq. (A.21b), and Eq. (A.28), Eq. (4.38) can be transformed into

$$\begin{aligned}
\mathcal{J}_{\text{IORAC}}(\mathbf{u}_{\text{exo},y}) &= \sup_{\mathbf{w} \in \mathbb{W}} \left\{ \lim_{t \rightarrow \infty} \left[ 2c_{R,1} \mathcal{V}_{\text{IORAC}} + \int_0^t \left( -2c_{R,1} \dot{\mathcal{V}}_{\text{IORAC}} - \frac{c_{R,1} \mathbf{w}^T \mathbf{w}}{c_{R,2}} \right. \right. \right. \\
&\quad \left. \left. + 2c_{R,1} \boldsymbol{\chi}^T (\mathbf{u}_{\text{fb,IORC}} + \mathbf{J}_{w,y}^T \mathbf{w}) - c_{R,1} c_{R,2} \boldsymbol{\chi}^T \mathbf{J}_{w,y}^T \mathbf{J}_{w,y} \boldsymbol{\chi} \right. \right. \\
&\quad \left. \left. + c_{R,1}^2 \boldsymbol{\chi}^T \mathbf{K}_R^{-1} \boldsymbol{\chi}^T + \mathbf{u}_{\text{fb,IORAC}}^T \mathbf{K}_R \mathbf{u}_{\text{fb,IORAC}} \right) dt \right] \right\} \\
&= 2c_{R,1} \mathcal{V}_{\text{IORAC}}(\mathbf{x}_{t=0}, \hat{\mathbf{p}}_{t=0}) + \sup_{\mathbf{w} \in \mathbb{W}} \left\{ \lim_{t \rightarrow \infty} \left[ \int_0^t \left( z_{J,3} \right. \right. \right. \\
&\quad \left. \left. - c_{R,1} c_{R,2} \left\| \frac{\mathbf{w}}{c_{R,2}} - \mathbf{w}_{0,l2} \right\|^2 \right) dt \right] \right\} \tag{A.29}
\end{aligned}$$

where

$$z_{J,3} = (\mathbf{u}_{\text{fb,IORC}} + c_{R,1} \mathbf{K}_R^{-1} \boldsymbol{\chi})^T \mathbf{K}_R (\mathbf{u}_{\text{fb,IORC}} + c_{R,1} \mathbf{K}_R^{-1} \boldsymbol{\chi}) \tag{A.30}$$

With  $\mathbf{u}_{\text{fb,IORC}}$  from Eq. (4.34), we can obtain  $z_{J,3} = 0$ . Equation (A.29) also shows that the maximum value of Lyapunov function  $\mathcal{V}(\mathbf{x}_{t=0}, \hat{\mathbf{p}}_{t=0})$  is obtained at  $t = 0$ , which indicates the convergence of  $\mathcal{V}$  over time. Finally, it can be proved that

$$\Upsilon = \sup_{\mathbf{w} \in \mathbb{W}} \left\{ \int_0^\infty \left( -c_{R,1} c_{R,2} \left\| \frac{\mathbf{w}}{c_{R,2}} - \mathbf{w}_{0,l2} \right\|^2 \right) dt \right\} \leq 0 \tag{A.31}$$

and  $\Upsilon$  reaches  $\Upsilon = 0$  iff.  $\mathbf{w} = c_{R,2} \mathbf{w}_{0,l2} = c_{R,2} \mathbf{J}_{w,y} \boldsymbol{\chi}$ , which is the worst-case disturbance [97, 109]. Hence, IO-RAC from Eq. (4.36) can provide  $l^2$  disturbance attenuation by solving  $H_\infty$  control problem through minimizing the cost function  $\mathcal{J}_{\text{IORAC}}$ .

# Appendix B

## Symbolic-Numerical Formalism of Multibody Dynamics

The multibody dynamics in this paper follows a symbolic-numerical formalism, where the models are established following intuitive symbolic formulations, and multibody properties are numerically evaluated through efficient codes. This formalism has led to the development of ANDY - a multibody toolbox in MATLAB [180]. ANDY allows the modeling of constrained and nonholonomic multibody dynamics, provides analytical solutions of dynamical properties (e.g., inertia matrix, generalized forces), and generates pre-compiled codes for fast simulations and real-time control.

Note that ANDY is also capable of modeling hybrid systems, i.e., systems consisting of multiple continuous flows governed by different sets of kinematic constraints, and discrete jumps that project the dynamical states (i.e., generalized coordinates and nonholonomic states) from one flow manifold to another based on triggering conditions. However, this feature in the toolbox will not be explained, and we will focus on the parts that are relevant to this study.

The remaining of this appendix is arranged as follows. The multibody formalism through recursive kinematics and Kane's Method is explained in Section B.1. The software design of ANDY is then introduced in Section B.2, along with a brief discussion on the modeling of the human-TAWE system.

## B.1 Recursive Kinematics and Kane's Method

The majority of existing multibody and robotics engines/toolboxes adopt numerical formalism [43, 126, 154], which has been designed and optimized to provide reliable simulations and support real-time applications. On the other hand, symbolic expressions of dynamical properties are more useful for the in-depth analysis of multibody systems. The development of symbolic mathematics engines [12, 65, 86, 95, 99] has enabled the modeling of minimal state-space multibody dynamics through analytical formulations.

Many existing symbolic multibody toolboxes do not support the modeling of nonholonomic constraints, such as 3D systems with rolling-without-slipping and floating-base features. However, multibody systems in biomechanics and robotics often involve nonholonomic constraints  $\mathbf{r}_\lambda$  governed by complicated expressions in the form of

$$\mathbf{r}_\lambda = \mathbf{J}_\lambda(\mathbf{q}, \boldsymbol{\rho})\dot{\mathbf{q}} \quad (\text{B.1})$$

based on generalized coordinate  $\mathbf{q}$ , and nonholonomic state “ $\mathfrak{B}$ ”. The Jacobian matrix  $\mathbf{J}_\lambda$  holds crucial information for analysis and controller design. In this case, numerical formalism lacks the flexibility to obtain  $\mathbf{J}_\lambda$  from arbitrary nonholonomic constraints,

Our solution is the symbolic-numerical formalism based on recursive kinematics and Kane's method [83, 138], which realizes a balance between analytical informativeness and numerical efficiency. In a multibody system, the unconstrained kinematics follows a multi-node tree topology, where the coordinate frames are nodes, and the transformations are edges. The root of the kinematic tree is the global frame, which is an inertial frame undergoing no acceleration. For each pair of parent-child frames (not necessarily immediate), by labeling the parent and child respectively as “ $p$ ” and “ $c$ ”, the global kinematic properties, i.e., translational displacement  $\mathbf{d}$ , rotation  $\boldsymbol{\Omega}$ , velocity ( $\dot{\mathbf{d}}$  and  $\boldsymbol{\omega}$ ), acceleration ( $\ddot{\mathbf{d}}$  and  $\dot{\boldsymbol{\omega}}$ ), and Jacobian

( $\mathbf{J}_d$  and  $\mathbf{J}_\omega$ ) of the child calculated based on parent frame properties can be written as

$$\mathbf{d}_c = \mathbf{d}_p + \Omega_p \mathbf{d}_{c,p} \quad (\text{B.2a})$$

$$\Omega_c = \Omega_p \Omega_{c,p} \quad (\text{B.2b})$$

$$\dot{\mathbf{d}}_c = \dot{\mathbf{d}}_p + \Omega_p \dot{\mathbf{d}}_c + \text{skew}(\boldsymbol{\omega}_p) \Omega_p \mathbf{d}_{c,p} \quad (\text{B.2c})$$

$$\boldsymbol{\omega}_c = \boldsymbol{\omega}_p + \Omega_p \boldsymbol{\omega}_{c,p} \quad (\text{B.2d})$$

$$\ddot{\mathbf{d}}_c = \ddot{\mathbf{d}}_p + \Omega_p \ddot{\mathbf{d}}_{c,p} + \text{skew}(\dot{\boldsymbol{\omega}}_p \Omega_p \mathbf{d}_{c,p}) + \text{skew}(\boldsymbol{\omega}_p) (2\Omega_p \dot{\mathbf{d}}_{c,p} + \text{skew}(\boldsymbol{\omega}_p) \Omega_p \mathbf{d}_{c,p}) \quad (\text{B.2e})$$

$$\dot{\boldsymbol{\omega}}_c = \dot{\boldsymbol{\omega}}_p + \Omega_p \dot{\boldsymbol{\omega}}_{c,p} + \text{skew}(\boldsymbol{\omega}_p) \Omega_p \boldsymbol{\omega}_{c,p} \quad (\text{B.2f})$$

$$\mathbf{J}_{d,c} = \mathbf{J}_{d,p} + \Omega_p \mathbf{J}_{d,c,p} - \text{skew}(\Omega_p \mathbf{d}_{c,p}) \mathbf{J}_{\omega,p} \quad (\text{B.2g})$$

$$\mathbf{J}_{\omega,c} = \mathbf{J}_{\omega,p} + \Omega_p \mathbf{J}_{\omega,c,p} \quad (\text{B.2h})$$

where the subscript “ $c, p$ ” indicates the transformation from the child frame to the parent frame. Specifically, the variables in the Jacobian matrices only include the generalized coordinate  $\mathbf{q}$ , and the nonholonomic state  $\boldsymbol{\rho}$  governed by

$$\dot{\boldsymbol{\rho}} = \mathbf{J}_\rho(\mathbf{q}, \boldsymbol{\rho}) \dot{\mathbf{q}} \quad (\text{B.3})$$

Hence, following Eqs. (B.2), we can calculate the global kinematic properties of each frame in a recursive manner.

The above process applies to both symbolic and numerical formulations, and provides the information for solving the dynamical properties via Kane’s Method. For a Body labeled as “ $j$ ” in the system, provided that its mass  $m_j$  and moment of inertia  $\boldsymbol{\Phi}_j$  ( $\boldsymbol{\Phi}_j = \boldsymbol{\Phi}_j^T > 0$ ) are established at the local frame labeled as “ $i$ ”, then we can derive the left and right inertia

components respectively as

$$\mathbf{J}_{l,j} = \begin{bmatrix} m_j \mathbf{J}_{d,i} \\ \boldsymbol{\Omega}_i \boldsymbol{\Phi}_j \boldsymbol{\Omega}_i^T \mathbf{J}_{\omega,i} \end{bmatrix}; \quad \mathbf{J}_{r,j} = \begin{bmatrix} \mathbf{J}_{d,i} \\ \mathbf{J}_{\omega,i} \end{bmatrix} \quad (\text{B.4})$$

so that the inertia and Coriolis & centripetal matrices of Body  $j$  are respectively written as

$$\mathbf{M}_j = \mathbf{J}_{l,j}^T \mathbf{J}_{r,j}; \quad \mathbf{C}_j = \mathbf{J}_{l,j}^T \dot{\mathbf{J}}_{r,j} + \mathbf{J}_{\omega,i}^T \text{skew}(\boldsymbol{\omega}_i) \boldsymbol{\Omega}_i \boldsymbol{\Phi}_j \boldsymbol{\Omega}_i^T \mathbf{J}_{\omega,i} \quad (\text{B.5})$$

The generalized forces in the system can also be evaluated individually in a similar manner.

As an example, for a scalar force input  $u_k$  heading towards the  $-z$  direction of Frame  $i$ , the input Jacobian matrix  $\mathbf{J}_{u,k}$  and generalized force  $\mathbf{h}_{u,k}$  can be respectively calculated as

$$\mathbf{J}_{u,k} = \begin{bmatrix} 0 & 0 & -1 \end{bmatrix} \mathbf{J}_{d,i}; \quad \mathbf{h}_{u,k} = \mathbf{J}_{u,k}^T u_k \quad (\text{B.6})$$

The total inertia matrix, Coriolis & centripetal, and generalized forces are respectively the sums of these properties from individual bodies and forces. This leads to the generic structure of the multibody model as introduced in earlier chapters

$$\mathbf{M}(\mathbf{q}, \boldsymbol{\rho}) \ddot{\mathbf{q}} = -\mathbf{C}(\mathbf{q}, \dot{\mathbf{q}}, \boldsymbol{\rho}) \dot{\mathbf{q}} - \mathbf{h}(t, \mathbf{q}, \dot{\mathbf{q}}, \boldsymbol{\rho}) + \mathbf{J}_u^T(\mathbf{q}, \boldsymbol{\rho}) \mathbf{u} + \mathbf{J}_\lambda^T(\mathbf{q}, \boldsymbol{\rho}) \boldsymbol{\lambda} \quad (\text{B.7a})$$

$$\dot{\boldsymbol{\rho}} = \mathbf{J}_\rho(\mathbf{q}, \boldsymbol{\rho}) \dot{\mathbf{q}} \quad (\text{B.7b})$$

where the constraint forces are enforced by the Lagrange multiplier  $\boldsymbol{\lambda}$ . The constraint Jacobian matrix  $\mathbf{J}_\lambda$  is acquired from the nonholonomic kinematic constraint previously defined in Eq. (B.1). We can also derive the time-derivative of Eq. (B.1) as

$$\ddot{\mathbf{r}}_\lambda = \mathbf{J}_\lambda \ddot{\mathbf{q}} + \dot{\mathbf{J}}_\lambda \dot{\mathbf{q}} = 0 \quad (\text{B.8})$$

A general approach to calculate the constraint force is by substituting  $\ddot{\mathbf{q}}$  from Eq.(B.7a) into  $\ddot{\mathbf{r}}_\lambda$  from Eq.(B.8)

$$\boldsymbol{\lambda} = \boldsymbol{\Lambda}_\lambda^{-1}(\mathbf{J}_\lambda \mathbf{M}^{-1}(\mathbf{C} + \mathbf{h} - \mathbf{J}_u^T \mathbf{u}) - \dot{\mathbf{J}}_\lambda \dot{\mathbf{q}}) \quad (\text{B.9})$$

where  $\boldsymbol{\Lambda}_\lambda = \mathbf{J}_\lambda \mathbf{M}^{-1} \mathbf{J}_\lambda^T$  is defined as the constraint decoupling matrix. Note that this approach is suitable for numerical simulations of constrained models, while it does not convert the system into the minimal state-space form.

To summarize, the above multibody formulation process allows efficient calculation of the system properties both symbolically and numerically. The overall framework can be demonstrated through the flow chart in Fig. B.1(a). This lays the foundation for the development of ANDY. The next section will introduce the software design of ANDY, and the modeling of the human-TAWE system.

## B.2 Software Design of ANDY

ANDY is designed in MATLAB using its symbolic math and object-oriented programming features. The software architecture is presented in Fig. B.1(b). In ANDY, the `System` is the base object for the multibody system, which serves as a “factory” that produces the other dynamical objects. All object classes inherit the hash-map data structure `jDic`, which allows quick searching and indexing of system information. Before the formulation of kinematics or dynamics, the system variables are declared, where `Param`, `Input`, and `Disc` are time-undifferentiable model parameters, while `Cont` and `NHSignal` are time-dependent system states for  $\mathbf{q}$  and  $\boldsymbol{\rho}$  respectively.

Next, the kinematic tree is formulated, where `Space` is the graph object containing `Frame`

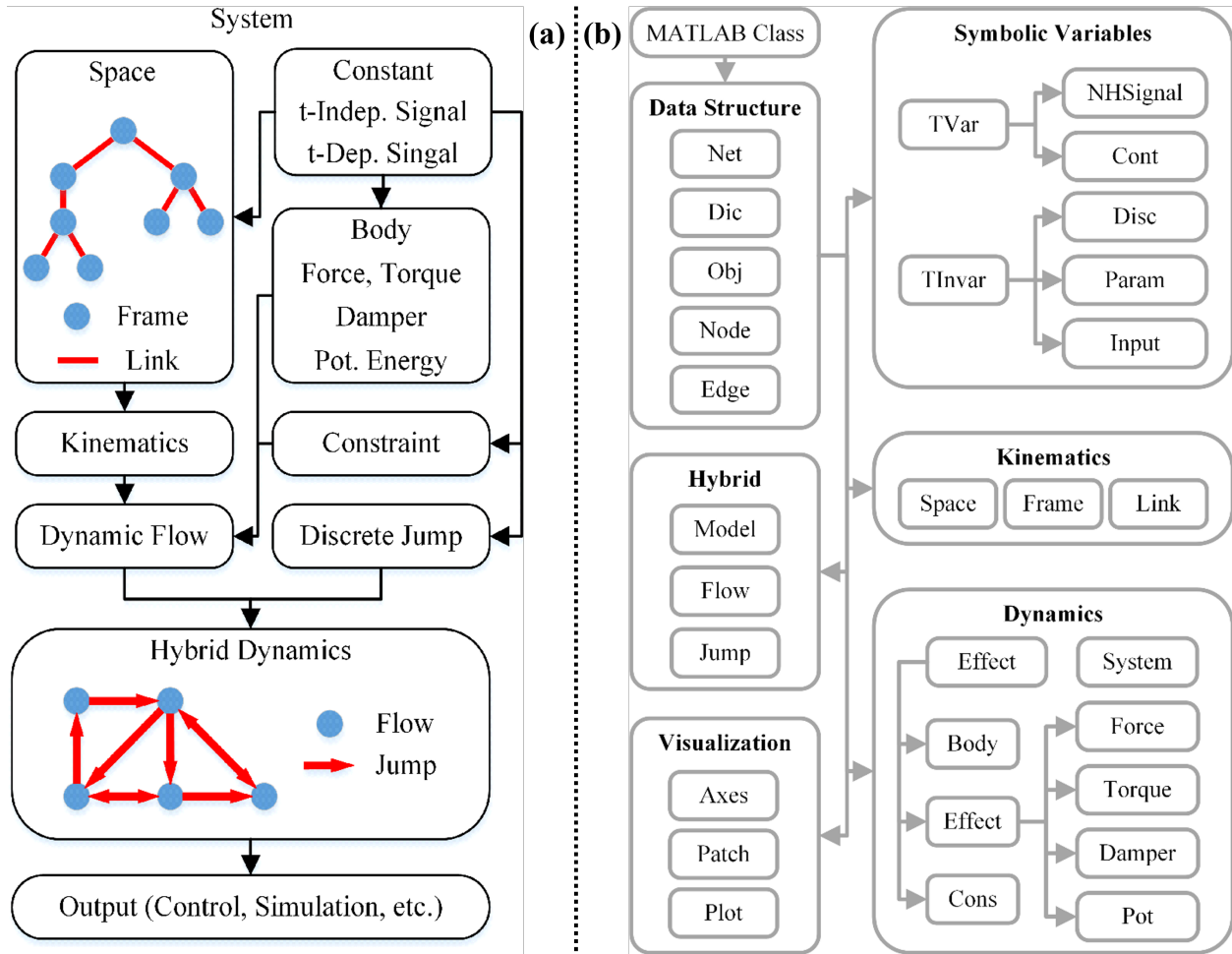


Figure B.1: The multibody formulation framework is shown in (a); the software architecture of TAWÉ is shown in (b) [180].

and **Link** objects as the nodes (coordinate frames) and edges (transformations), respectively. Basic dynamical elements in ANDY include **Body**, **Force**, **Torque**, **Damper** and **Potential Energy Pot**. All of these properties can be conveniently established on the coordinate frames. The unconstrained system dynamics can then be generated following the previously explained approach.

Constraints **Cons** are separated from the basic system elements since they will introduce loss of DOFs to a system based on an open kinematic chain. Since the constraint combinations in a model have also been modularized, the constrained dynamics can be generated simply

based on the unconstrained model and the selected sets of constraints.

As mentioned earlier, ANDY is also capable of modeling hybrid dynamics [65, 170]. The hybrid automata object `Model` is another structure based on graph theory, which contains `Flow` as its nodes and `Jump` as its edges. The jump objects contain the guard and reset maps to switch the system in between flows based on triggering conditions.

With all parts of the system defined, ANDY will then organize the codes and generate pre-compiled codes based on pre-defined templates for simulations and control applications (in both MATLAB and C++). While it will provide symbolic information about the model, the pre-compiled codes solve the dynamical properties via numerical calculation instead of using the fully combined symbolic expression. Hence, the toolbox can model complex multibody and robotic systems featuring nonholonomic states without failing the compilation stage due to symbolical complexity.

While ANDY does not have any graphic user interface, the modeling process is interactive. The toolbox provides information for the user to check the correctness of their models, and feeds back the compilation detail. Finally, visualization object `Axes` provides `Patch` and `Plot` for 3D model animation and animated 3D trajectory printing, respectively. As an example, the visualization of TAWÉ dynamics is shown in Fig. 2.6.

In this project, ANDY is extensively used for system modeling and simulations. The C++ codes generated by ANDY can also be used in control applications during experiments, where the control software is developed based on embedded systems and Robotic Operating System 2 (ROS2). The development of the control software is discussed in Section 6.2.